Ultrafast Nonlinear Optics of Bulk and Two-Dimensional Materials for Infrared Applications

Giorgos Demetriou

Submitted for the degree of Doctor of Philosophy

School of Engineering and Physical Sciences

Heriot-Watt University

June – 2016

Abstract

This thesis presents the results of an experimental study into the nonlinear optical properties of novel nonlinear materials at infrared regions of the electromagnetic spectrum for the realisation of nonlinear optical devices in the near- and mid-infrared. Because of its exceptional nonlinear optical properties and its promise of implementation in a range of mid-infrared applications graphene had a prominent place in this research. Extensive investigations in the nonlinear optical properties of single and multilayer chemical vapour deposition (CVD) graphene are presented. This study revealed that graphene presents a nonlinear phase shift due to a negative, irradiance-dependent nonlinear refraction. The high peak powers available enabled the study of both saturable absorption (SA) and two-photon absorption (2PA), identifying the irradiance limits at which the contribution of two-photon absorption exceeded that of saturable absorption. Moreover, the nonlinear optical properties of graphene-polyvinyl alcohol (G-PVA) composite films were studied. The results indicate the thermal damage of the host polymer due to graphene heating and temperature transfer.

Studies in the third order nonlinear optical properties of chalcogenide glasses with the perspective of integration with graphene for the development of mid-infrared devices and applications are also performed. Of all the glasses investigated, gallium lanthanum sulphide (GLS) was found to have the most interesting nonlinear optical properties. Its optical Kerr nonlinearity was found to be approximately 35 times higher than silica and the upper limit of its two-photon absorption coefficient was the lowest of all the chalcogenide glasses analysed, implying that GLS would be an excellent candidate for ultrafast all-optical switching. Subsequently GLS was chosen as the host material for optical waveguide and device fabrication via ultrafast laser inscription (ULI). Near- and mid-infrared waveguides were successfully fabricated; fundamental features such as, refractive index profiles and material dispersion were investigated. The Zero Dispersion Wavelength (ZDW) of GLS was experimentally measured for the first time; the ZDW was determined to be between 3.66-3.71 μm for the waveguides and about 3.61 μm for the bulk. Single mode directional couplers at 1550 nm were also developed and their ultrafast all-optical switching properties were investigated, leading to the assessment of the nonlinear refractive index n_2 of the ULI modified area. Furthermore, waveguides in Er^{3+} doped GLS were successfully fabricated and the infrared transitions at 1550 and 2750 nm were detected opening the potential for GLS waveguide lasers.

Acknowledgements

First and foremost, I would like to express my deepest gratitude and appreciation to my supervisor, Professor Ajoy Kar. His advice, honesty and support have been tremendous during my PhD pursuit. I would like to thank him for his constant encouragement, his inspiring enthusiasm for research and for the overwhelming trust he showed in me from the first day of my PhD, ingredients which allowed me to grow as a researcher.

I would also like to thank all the members of the nonlinear optics group both past and present. I would like to thank all those who provided me help and training in the beginning of my PhD; Dr Henry Bookey for training me in how to use the complicated OPA laser system and perform Z-scan measurements, Dr Graeme Brown for the training and help he provided me in ultrafast laser inscription and Dr John Macdonald for the help and training on waveguide characterisation techniques. Special thanks to the current members of the NLO group not only for the harmonic collaboration and generous help they provided each time I met any research-related problems but also for tolerating me as their office mate for the last three years.

I am also deeply grateful to Dr Eitan Abraham and Dr Fabio Biancalana for all the time they dedicated, despite being very busy with their own research, to help me by performing comprehensive theoretical and thermal analyses supporting my experimental results regarding the nonlinear optical characterisation of graphene samples. The insightful discussions we had over the past few months no only gave me valuable lessons on how to engage and collaborate with other professionals but also led to high quality publications in peer reviewed journals.

I would like to thank all the friends and colleagues that I have met in Edinburgh the past three years. Special thanks to Giorgos Arnaoutakis, Marios Therisits, Daniel Rylatt and Panos Alevras even for the (mostly) non-research related conversations over a pint of beer!

Finally, special thanks goes to my family, especially my parents as well as two brothers and sister for their support and encouragement over the years.

Publications by the author

Peer reviewed journal articles by the author

1. R. Yingying, G. Brown, R. Mary, **G. Demetriou**, D. Popa, F. Torrisi, A. C. Ferrari, C. Feng, and A. K. Kar, "7.8-GHz Graphene-Based 2-μm Monolithic Waveguide Laser," Selected Topics in Quantum Electronics, IEEE Journal of **21**, 395-400 (2015).

2. **G. Demetriou**, J.-P. Bérubé, R. Vallée, Y. Messaddeq, C. R. Petersen, D. Jain, O. Bang, C. Craig, D. W. Hewak, and A. K. Kar, "Refractive index and dispersion control of ultrafast laser inscribed waveguides in gallium lanthanum sulphide for near and mid-infrared applications," Opt. Express **24**, 6350-6358 (2016).

3. **G. Demetriou**, H. T. Bookey, F. Biancalana, E. Abraham, Y. Wang, W. Ji, and A. K. Kar, "Nonlinear optical properties of multilayer graphene in the infrared," Opt. Express **24**, 13033-13043 (2016).

4. **G. Demetriou**, F. Biancalana, E. Abraham, Y. Wang, W. Ji and A. K. Kar, "Nonlinear refraction in single layer graphene," (Under preparation)

5. **G. Demetriou**, E. Abraham, G. Wang, K. Wang, S. Higgins, W. J. Blau and A. K. Kar, "Laser induced damage in graphene polyvinyl alcohol composite films," (Under preparation)

6. **G. Demetriou**, C. Craig, D. W. Hewak and A. K. Kar, "Study of nonlinear refraction in ultrafast laser inscribed gallium lanthanum sulphide," (Under preparation)

Conference papers by the author

1. **G Demetriou**, H.T Bookey and A.K Kar. "Z-scan investigation of nonlinear optical properties of a graphene Poly-Vinyl alcohol composite", Nonlinear Photonics symposia, Photon 14, 2014, London, UK.

2. D. Milanese, J. Lousteau, D. Pugliese, P. Janicek, N. G. Boetti, E. Ceci-Ginistrelli, **G. Demetriou**, A. K. Kar, and H. T. Bookey, "Novel tellurite core and cladding glasses for high numerical aperture optical fibre: Prospects for a supercontinuum optical fibre source," in *Transparent Optical Networks (ICTON), 2015 17th International Conference on*, 2015), 1-4.

3. **G. Demetriou**, F. Biancalana, H. T. Bookey, and A. Kar, "Nonlinear Optical Properties Of A Graphene-Polyvinyl Alcohol Composite From 1550 nm To 2400 nm," in *CLEO: 2015*, OSA Technical Digest (online) (Optical Society of America, 2015), JTu5A.29.

4. **G. Demetriou**, F. Thorburn, A. Lancaster, C. Craig, E. Weatherby, D. W. Hewak, and A. Kar, "Fluorescence in Erbium Doped Gallium Lanthanum Sulphide: Potential for mid-IR Waveguide Laser," in *CLEO: 2015*, OSA 2015), STh1G.2.

5. J. Morris, **G. Demetriou**, A. Lancaster, A. Kar, and H. Bookey, "3D Optical Waveguides in $Ge_{22}As_{20}Se_{58}$ Glass - a Highly Nonlinear Material for the Mid-IR," in *Conference on Lasers and Electro-Optics*, OSA Technical Digest (online) (Optical Society of America, 2016), JTh2A.82.

Table of Contents

List of figures

List of tables

List of abbreviations

ADM	Adomian Decomposition Method
AlGaAs	Aluminium Gallium Arsenide
AOM	Acousto-Optic Modulator
AOS	All-optical switching
AR	Antireflective
BBO	Barium borate
CaF_2	Calcium fluoride
ChGs	Chalcogenide glasses
CNTs	Carbon Nanotubes
CPA	Chirped pulse amplification
Cr:ZnSe	chromium doped Zinc Selenide
CVD	Chemical vapour deposition
CW	Continuous wave
DC	Direct current
DFG	difference frequency generation
EDFA	Erbium doped fiber amplifier
EM	Electromagnetic
Er^{3+}:GLS	Erbium doped gallium lanthanum sulphide
FCPA	Fibre chirped pulse amplification
FFT-BPM	Fast Fourier Transform Beam Propagation Method
FWM	four wave mixing
G-PVA	graphene poly-vinyl alcohol
$Ge_{22}As_{20}Se_{58}$	Germanium Arsenic Selenide
GLS	Gallium lanthanum sulphide
KLM	Ker-lens mode-locking

LPE	Liquid Phase Exfoliation
MFD	Mode field diameter
MPA	multi-photon absorption
ND	Neutral density
Nd:YAG	Neodymium yttrium aluminium garnet
Nd:YLF	Neodymium yttrium lithium fluoride
NOR	nonlinear optical rectification
OL	optical limiting
OPA	optical parametric amplifier
OPO	optical parametric oscillator
QPM	Quantitative phase microscopy
RIP	refractive index profile
SA	saturable absorption
SESAM	Semiconductor Saturable Absorber Mirror
SFG	sum frequency generation
SHG	second harmonic generation
SLG	Single layer graphene
SPDC	spontaneous parametric down conversion
SPM	Self-phase modulation
THG	third harmonic generation
THz	Terahertz
TPA	two-photon absorption
ULI	ultrafast laser inscription
UV	Ultraviolet
YAG	Yttrium aluminium garnet
ZDW	zero dispersion wavelength
ZnSe	Zinc Selenide

3PA	Three-photon absorption
4PA	Four-photon absorption

Chapter 1. Introduction

1.1. Motivation

There is currently a great deal of interest in developing integrated optics which operate in the mid-infrared region of the electromagnetic spectrum (2-25 μm). This growing interest creates a need for new host materials suitable for optical devices operating in this important region. The two main research fields that are closely intertwined with the realisation of nonlinear optical mid-infrared applications are the fields of materials technology and nonlinear optics. The development and characterisation of novel materials consistently leads to the exploitation of their nonlinear optical properties enabling both, the growth of nonlinear optics and the realisation of nonlinear relevant applications.

The motivation behind this work is precisely that necessity to explore the nonlinear optical properties of novel materials and in combination with existing technologies as well as fabrication methods to assess their capabilities towards implementation in infrared applications. The research undertaken here focusses on the investigation of the nonlinear optical properties of graphene, which during the last decade has emerged as a novel material with exceptional nonlinear optical properties bearing the promise of implementation in a range of mid-infrared applications. However, due to graphene being a pure two-dimensional material, approaches towards realising graphene-based optoelectronic devices require its integration with other nonlinear bulk materials, which can serve as hosts for the fabrication of embedded devices. A very attractive candidate for device fabrication for mid-infrared applications are chalcogenide glasses due to their excellent mid-infrared transparency and high optical nonlinearities. Following the study of graphene's nonlinearities, the nonlinear optical properties of a series of bulk chalcogenide glasses are explored. Special emphasis was given to gallium lanthanum sulphide (GLS), which was chosen as the host material for waveguide and device fabrication. The objective of this work is to influence the integration of graphene with bulk dielectrics, such as chalcogenide glasses, in order to fully exploit their potential in the development of graphene-based optoelectronic applications.

1.1.1. Graphene

Graphene, a single layer of carbon atoms arranged in a hexagonal (honeycomb) lattice is the first truly two-dimensional atomic crystal. Graphene as a concept has been around for a long time and had been studied theoretically as early as 1947 [1]. Graphite was well known to consist of hexagonal carbon sheets stacked on top of each other, but it was believed that a single sheet could not be produced in an isolated form such that electrical and optical measurements could be performed. It therefore, came as a surprise to the physics community when in 2004, Konstantin Novoselov, Andre Geim and their collaborators [2] showed that a single layer of graphene could be isolated and transferred to another substrate. This achievement, not only obtained them the Nobel Prize in physics in 2010 [3], but also sparked enormous interest in the graphene research field, making graphene along with its products some of the most widely studied materials of the last decade.

Graphene has a number of remarkable optoelectronic properties resulting from its unique band structure, which presents zero band-gap at the Dirac point where the valence meets the conduction band. Due to this particular band structure it can absorb photons with the same efficiency, $\pi\alpha \approx 2.3\%$ of the incident light for each layer, over a wide range of wavelengths; ($\pi\alpha$ is a universal constant absorption coefficient, with α being the fine structure constant). The massless bandgap structure of graphene has led to the prediction of strong nonlinear optical effects associated with saturable absorption (SA) [4], optical limiting (OL) [5], frequency mixing [6] and frequency multiplication [7].

Saturable absorption is a consequence of Pauli blocking, when carriers generated because of strong optical excitation lead to the depletion of the valence band and the filling of the conduction band, preventing additional absorption. This property made graphene very popular amongst nonlinear optics groups since it has led to the utilisation of graphene as a saturable absorber gain medium for mode-locked and Q-switched lasers [8, 9]. Moreover, under laser illumination graphene presents a strong nonlinear phase shift due to the optical nonlinear Kerr effect. Broadband four-wave mixing in graphene [6] allowed the determination of the absolute value of the third order susceptibility for a single graphene layer, $\left|\chi_{gr}^{(3)}\right| \simeq 1.5 \times 10^{-7}$ esu, approximately 8 orders of magnitude larger than

bulk dielectrics. Similarly, typical Z-scan measurements have revealed that graphene presents a giant nonlinear refraction in the orders of $\sim 10^{-13} - 10^{-11} m^2 W^{-1}$ [10, 11]. This exceptionally large value leads to an irradiance dependence of the nonlinear optical refraction in graphene. The large value of the nonlinear refraction suggests that the figure of merit (FOM) of graphene for nonlinear switching applications may be highly favourable; thus it was extensively investigated in this thesis.

1.1.2. Chalcogenide glasses

Chalcogenide glasses are an important class of amorphous semiconductors, they contain as their main constituent one or more of the chalcogen elements S, Se and Te, covalently bonded to network formers such as As, Ge, Sb, Ga, Si or P. Chalcogenide glasses are very attractive candidates for mid-infrared applications and devices due to their excellent mid-infrared transparency. They provide high optical nonlinearities which, coupled with their mid-infrared transparency, define them as excellent hosts for supercontinuum generation mid-infrared sources for sensing applications [12, 13]. Furthermore chalcogenides possess low phonon energies, which allows them to be readily doped with rare earth elements giving rise to mid-infrared transitions opening the potential for laser sources operating in this important wavelength region [14]. In addition to their aforementioned properties, they also offer high nonlinear refractive index (up to ~500 times that of silica), low multiphoton absorption and high photosensitivity. Properties which allow for switching devices with shorter interaction lengths, lower switching thresholds and higher figures of merit, defining chalcogenide glasses as a good platform for ultrafast nonlinear optics and also a key technology for future optical communications systems. Of all chalcogenides, GLS is a particularly attractive one; it is a radically new chalcogenide glass and a much-awaited alternative to toxic arsenic-based chalcogenides. GLS present broad optical transparency extending from the visible to the infrared up to 10 μm [15] and thermal stability up to 550^{o}C [15]. In addition, GLS can be melted on a large scale without the requirement for a sealed ampoule environment, making production and processing safer, easier and more economical, further removing barriers to adoption and along with its non-toxicity establishing GLS among the most popular chalcogenides.

1.2. Background

In optics, one is interested in the interaction of light with matter and more specifically the response of atoms and molecules to applied electromagnetic (EM) fields. Optics proceeded quite successfully for many years on the assumption that the response of optical materials was linear in respect with the applied field *E*. This belief of linearity served as a good approximation for such a long period primarily because the electric field strengths that scientists were able to deploy in those early years, before the invention of the laser, were far weaker than the fields inside atoms and molecules. However, it is now very well established that as the electric field strength is increased, approaching that of the materials inter atomic field strength the optical response of the material can become nonlinear, i.e. material properties such as transmission and refraction can become dependent on the applied field strength.

It was not until the 1870's that John Kerr, a lecturer at the Free Church Training College in Glasgow, demonstrated that the refractive index of a number of solids and liquids can be slightly changed by the application of a strong DC field [16].This phenomenon was the first nonlinear optical effect to be observed and it is now known as the DC Kerr effect. The first all optical nonlinear effect, two-photon absorption (TPA), was described theoretically in 1931 by Maria Goeppert-Mayer [17]. However up to then, and for the next 30 years, the advances in the field of nonlinear optics were minimal. Due to the large field intensities required further progress had to wait for a source that would provide them; that source was the laser. With the arrival of the laser in 1960, which provided the required high electric field intensities, the field of nonlinear optics underwent a great revival and has been continuously growing ever since. The first experimental demonstration of a nonlinear optical process of the laser era was reported in 1961 by Franken et.al. [18]. In that experiment a ruby laser was focused onto a quartz crystal demonstrating frequency doubling of the incident light. Soon after this first demonstration a plethora of other nonlinear optical processes was experimentally demonstrated as more research groups gained access to first generation laser systems.

Following the advent of the laser in the 1960's the story has been of the fields of laser physics and nonlinear optics growing in parallel, each fertilising the other, with

technological advances in one field always enabling progress in the other. The technique known as Kerr-lens mode-locking (KLM) [19] is a perfect example of this synergy. KLM along with a number of other nonlinear optical techniques is based on the optical Kerr effect. This effect is the origin of the intensity-dependent refractive index. The spatial properties of a propagating beam in a nonlinear medium are altered by the optical Kerr effect because the refractive index near the beam axis, where the intensity is higher, is increased relative to that of the beam periphery. This causes the beam periphery to travel faster than the beam axis due to the fact that it experiences a lower refractive index, leading to a self-focussing effect of the beam. The self-focussing effect will be more intense for higher intensities. If an aperture is placed somewhere in the beam path at such position that the beam size decreases as the intensity increases, the transmission through the aperture will be greatest at the peak of the pulse, which is exactly the recipe for passive mode-locking. This technique is widely used today in mode-locking Ti:Sapphire lasers and enables pulses shorter than 10 fs to be generated [20]. Such ultrashort pulses carry extremely high peak powers, which is exactly what is needed to excite and investigate optical nonlinearities. A mode-locked Ti:Sapphire system delivering ~100 fs pulses seeding an optical parametric amplifier (OPA) was extensively used for nonlinear measurements throughout the work presented in this thesis.

The progress in materials technology through years, like the growth of ultrahigh purity crystals, had a great impact in the evolution of nonlinear optics. The case of the optical parametric oscillators (OPOs) and amplifiers (OPAs) is a very good illustration of this relationship. OPOs and OPAs are based on the principle of splitting a pump photon ω_p into two other photons, the signal photon ω_s and the idler photon ω_i such that energy is conserved i.e., $\omega_p = \omega_s + \omega_i$ (and $\omega_p > \omega_i$). They offer extremely broad wavelength tuneability, as changing the phase-matching conditions alters the signal and idler wavelengths. Each of the three different wavelengths involved in this process will experience slightly different refractive indices. In order to achieve wavelength conversion the phase-matching conditions, $n_p\omega_p = n_s\omega_s + n_i\omega_i$ where n is the refractive index, must be satisfied. By changing the direction of propagation in the nonlinear crystal one alters the refractive index the wavelengths experience. Therefore, in order for the phase-matching conditions to be satisfied, the signal and idler wavelengths are altered as well, leading to the wavelength tuneability of OPOs and OPAs. The possibility of generating

tuneable coherent light using OPOs was understood as early as 1962 [21], remarkably only two years after the advent of the laser, and the first OPO was experimentally demonstrated in 1965 [22]. But OPO and OPA research proceeded very slowly for the next 20 years primarily because the nonlinear materials required to create viable devices were not available. However, as materials technology progressed, by the 1980's the necessary fabrication techniques had been developed and sophisticated OPO and OPA sources based on high-grade crystals are now in widespread use [23-25].

The field of nonlinear optics has grown enormously the last 50 years and is still flourishing with unabated pace. But still remains a field with even greater potential, having a significant volume of its capabilities still unexplored. This is the reason that a multitude of research groups around the world focusses in nonlinear optics. The two cases of KLM and OPAs, briefly described here, reveal the close interdependence between the fields of materials technology, nonlinear optics and laser physics. Most importantly they underline exactly that necessity to keep investigating new materials so in conjunction with technological advances and novel fabrication techniques to enable further progress and growth in these three closely related fields, which will ultimately lead to the realisation of relevant applications.

1.3 Aims and objectives of the project

The aims and objectives of the project on the ultrafast nonlinear optics of bulk and two-dimensional materials are stated below. The results and details of the research undertaken towards these aims are described in detail in this thesis.

- To assess the potential of graphene for nonlinear optical applications by performing an in-depth investigation in its nonlinear optical properties.
- To demonstrate an application by integrating graphene with a bulk material. A graphene film was used as a saturable absorber to mode-lock a waveguide laser.
- To choose a suitable substrate material for optical waveguide and device fabrication via ultrafast laser inscription. The chosen substrate material was GLS.
- To assess the potential of GLS for all-optical switching applications by fabricating and characterising optical waveguides and devices.

- To assess the potential of GLS for active applications by fabricating and characterising optical waveguides in rare earth doped GLS substrates.

1.4. Thesis outline

The work in this thesis addresses the investigation of the nonlinear optical properties of graphene. The saturable absorption, two-photon absorption and nonlinear refraction of CVD single as well as multilayer graphene are investigated for potential use in nonlinear photonic applications. Special emphasis is given to saturable absorption because of its promise of utilising graphene as a gain medium for laser mode-locking. One important finding is that graphene presents giant nonlinear refraction in the order of $\sim 10^{-9} cm^2 W^{-1}$, suggesting that the figure of merit of graphene for nonlinear switching applications may be highly favourable. Moreover this nonlinear refraction effect is found to be irradiance dependent with a negative origin indicating graphene as a promising medium for nonlinear optics applications related to solitons [26, 27] or imaging [28]. Moreover, the same nonlinear optical properties were studied in graphene-polyvinyl alcohol (G-PVA) composite films, which for certain applications, can be advantageous over deposited graphene on a substrate. By using femtosecond pulses the thermal damage of the host polymer due to graphene heating is also studied in order to assess the potential of using such G-PVA films as saturable absorbers for ultrafast laser mode-locking. Following the investigation of graphene's nonlinearities, the need for a bulk nonlinear material with which graphene could be integrated for the development of nonlinear applications emerged. In order to choose a suitable host material for device fabrication an investigation in the nonlinear optical properties of certain chalcogenide glasses was performed. Of these chalcogenides a particularly attractive one was GLS; hence it was chosen as the host material for waveguide and device fabrication via the ultrafast laser inscription (ULI) technique. Fundamental features of the GLS waveguides, such as refractive index profiles and material dispersion were measured. Ultrafast all-optical switching demonstrated in GLS directional couplers enabled the estimation of the nonlinear refractive index n_2 of the modified by the laser area. Furthermore, the successful fabrication of waveguides in erbium doped GLS (Er^{3+}: GLS) was demonstrated. The infrared transitions at 1550 and 2750 nm were detected, revealing the potential for Er^{3+}: GLS waveguide lasers.

Chapter 2 begins with a discussion of the theoretical principles behind optical nonlinearities and the derivation of the expressions for the nonlinear optical coefficients. This is followed by a detailed description of the femtosecond laser system used throughout this thesis for Z-scan measurements, which is in turn followed by a comprehensive description of the Z-scan experimental technique. The Z-scan technique is a highly effective method, used to characterise the nonlinear optical coefficients of a given material using a single beam, offering both great simplicity and very high sensitivity. Finally, chapter 2 concludes with a detailed description of the ultrafast laser inscription method used for waveguide and device fabrication.

Chapter 3 will present the optical characterisation of CVD single and multilayer graphene. First an introduction into graphene's nonlinear optical properties is presented. The nonlinear optical measurements acquired with the Z-scan technique are used for the characterisation of single and multilayer graphene. The high peak powers available enabled the study of both saturable absorption and two-photon absorption occurring in the same sample simultaneously. Furthermore, the Z-scan results revealed a giant negative irradiance-dependent nonlinear refraction for both single and multilayer graphene. This irradiance-dependent nonlinear refraction is discriminated from the conventional nonlinear refraction coefficient n_2, which is not irradiance dependent. At which point a theoretical analysis arising from the conductivity of the graphene monolayer follows, with special emphasis given to the interpretation of the irradiance dependence and the negative origin of the nonlinear refraction. The experimental results obtained for multilayer graphene were combined with the theoretical analysis and published to Optics Express [10]. Finally the characterisation of a multilayer graphene sample, which was used as a saturable absorber to mode-lock a waveguide Tm:YAG laser [9], is presented.

Chapter 4 is concerned with nonlinear optical measurements performed on graphene poly-vinyl alcohol composite films. First a discussion about graphene composites and their advantages over multilayer graphene for certain applications is performed. The nonlinear optical coefficients of various G-PVA composite films derived from the Z-scan measurements are presented. These results are then followed by the investigation of the thermal damage in G-PVA composites. Graphene presents excellent thermal

conductivity, therefore under laser illumination undergoes a temperature rise due to absorption of light. Subsequently there will be heat interchange with the host polymer leading to its temperature rise and eventually thermal damage. Finally, chapter 4 closes by presenting a theoretical thermal analysis aiming to study the heat accumulation effects in graphene and the temperature interchange between graphene and its host polymer.

Chapter 5 focusses on the investigation of the nonlinear optical properties of certain chalcogenide glasses using the nonlinear optical measurements acquired with the Z-scan technique. Chalcogenide glasses are very attractive candidates for nonlinear optical devices for mid-infrared applications, due to their excellent mid-infrared transparency and high optical nonlinearities. Initially a short review of chalcogenide glasses is performed, pointing out their advantages for mid-infrared device fabrication, followed by the presentation of the nonlinear optical measurements for various chalcogenide bulk glass samples. Finally, the nonlinear optical coefficients derived from the Z-scan results are discussed and the potential of the studied chalcogenides for use in nonlinear optical switching applications is assessed.

In chapter 6 the development of chalcogenide waveguides by utilising the ULI technique is addressed. In the beginning a discussion on the importance of the fabrication parameters with regards to material modification of chalcogenides is performed, demonstrating how the ULI technique may be easily utilised to fabricate single-mode guiding structures for near- and mid-infrared wavelengths. The refractive index profile (RIP) measurements of GLS waveguides are then presented followed by the results of material dispersion measurements, for both the GLS waveguides and bulk substrate. These dispersion measurements are performed over a wide range of wavelengths in the near and mid-infrared region of the electromagnetic spectrum spanning from ~1.3 to 4.5 μm. This work enabled the determination of the zero dispersion wavelength (ZDW) for both, the waveguides and the GLS bulk substrate. The results obtained from the refractive index profiling and dispersion measurements were combined and published in Optics Express [29].

Chapter 7 is concerned with the fabrication of buried nonlinear directional couplers in GLS substrates again by utilising the ULI technique. This will include a brief overview

of ultrafast all-optical switching theory in guided wave formats. Following this, single-mode directional couplers at 1550 nm embedded in GLS substrates are presented. Ultrafast all-optical switching is demonstrated in these ULI structures with the use of ~100 fs ultrashort pulses available from an OPA seeded by a Ti:sapphire mode-locked laser. The ultrafast switching of light in the GLS directional couplers enabled the estimation of the nonlinear refractive index n_2 of the modified by the laser area.

Chapter 8 focusses on the study of rare earth doped GLS glasses revealing their potential for mid-infrared waveguide lasing applications. Firstly, an introduction into rare earth doped glasses with a specific focus on erbium doped GLS is provided. The absorption spectrum of Er^{3+}: GLS along with the energy levels of Er^{3+} indicating the possible mid-infrared transitions are presented. The inscription technology applied in GLS was used for successful fabrication of waveguides in Er^{3+}: GLS. Subsequently presented, are the infrared transitions at 1550 and 2750 nm, detected after exciting the Er^{3+} ions at 980 nm.

Finally, chapter 9 draws conclusions and suggests future research prospects for the field of mid-infrared nonlinear optics. This includes proposed designs for mid-infrared nonlinear applications exploiting the combination of the nonlinearities of graphene and chalcogenide glasses like GLS, both studied in the main body of this work.

1.5. Summary

The work carried out in this thesis is focussed on the ultrafast nonlinear optics of bulk and two-dimensional materials in the near and mid-infrared. Encompassed in this research is the study of optical nonlinearities of graphene for mid-infrared applications, such as saturable absorbers for laser mode-locking or graphene detectors. Moreover, this study revealed very important features of graphene, like a negative irradiance-dependent nonlinear refraction. Thereupon the nonlinear characterisation of various chalcogenide bulk glass samples followed, leading to the selection of gallium lanthanum sulphide for waveguide and device fabrication by the ultrafast laser inscription technique. Features of the fabricated structures, such as refractive index profiles and material dispersion over a broad wavelength range were evaluated. Nonlinear ultrafast all-optical switching in GLS directional couplers was also presented. Furthermore, waveguides in Er^{3+}: GLS were

successfully fabricated and the infrared transitions at 1550 and 2750 nm were detected after exciting the Er^{3+} ions at 980 nm. The study of rare earth doped GLS glasses revealed their potential for mid-infrared waveguide lasing applications.

Chapter 2. Nonlinear Experimental Techniques

2.1. Introduction

This chapter gives an overview of the main experimental techniques employed in this work. The Z-scan technique was used for the study of the optical nonlinearities of bulk and two-dimensional materials. Whereas the ultrafast laser inscription technique was utilised for the fabrication of waveguides and devices. Before these two experimental techniques are presented, it is useful to discuss the origin of the nonlinear optical behaviour in a material. This gives insight in the main nonlinear processes involved with the two aforementioned techniques. Starting from the nonlinear polarisation, the third order nonlinear optical coefficients are derived and the irradiance dependent refractive index is discussed. Following the discussion in optical nonlinearities, a description of the femtosecond laser system used throughout this thesis for Z-scan measurements is given. This is then followed by a comprehensive description of the Z-scan technique and experimental setup. Finally, the chapter concludes with the presentation of the ultrafast laser inscription technique, also performing a detailed description of the ULI experimental setup and a discussion on the key inscription parameters.

2.2. The origin of nonlinear optical behaviour

In order to understand the nonlinear optical behaviour of materials we consider the case of an electromagnetic field applied on a dielectric. For a nonconducting and nonmagnetic material, the applied field will polarise the dielectric, displacing the charges away from their equilibrium positions. This may be understood in terms of a simple Lorentz model, in which the dipole-moment is given by [30],

$$p = -er \tag{2.1}$$

where e is the charge of an electron and r the displacement due to the applied field. If the restoring elastic force is proportional to the displacement i.e. if Hooke's law is satisfied the displacement r from the equilibrium position is proportional to the applied electric field $\boldsymbol{E}$. Consequently, the total macroscopic polarisation $\boldsymbol{P}$, which can be expressed as a

sum of these dipole-moments with N dipoles per unit volume is proportional to $\boldsymbol{E}$. Therefore, the medium exhibits linear behaviour, with the polarisation $\boldsymbol{P}$ given by the relation [30],

$$\boldsymbol{P} = \sum p = Np = \varepsilon_0(\varepsilon - 1)\boldsymbol{E} = \varepsilon_o x^{(1)}\boldsymbol{E} \tag{2.2}$$

where ε is the dielectric constant, $x^{(1)}$ is the dimensionless linear first order susceptibility, ε_o is the free space permittivity and $\boldsymbol{E}$ the applied electric field.

However, relationship 2.2 holds only for low irradiances. Under strong electromagnetic fields and specifically when the strength of the applied field approaches that of the materials interatomic field strength the response of the dielectric becomes nonlinear. Therefore, the total polarisation $\boldsymbol{P}$ is no longer linear with the electric field $\boldsymbol{E}$, but rather described by the following relation [31],

$$\boldsymbol{P} = \varepsilon_0(x^{(1)}.\boldsymbol{E} + x^{(2)}:\boldsymbol{EE} + x^{(3)} \vdots \boldsymbol{EEE} + \ldots) \tag{2.3}$$

where $x^{(2)}$ is the second order nonlinear susceptibility and $x^{(3)}$ is the third order nonlinear susceptibility [32]. The cases of linear polarisation, as well as quadratic and cubic nonlinearities are presented in figure 2.1. The linear case is represented with the dashed straight line (a), showing that the response of the polarisation $\boldsymbol{P}$ is proportional to the applied electric field $\boldsymbol{E}$; this linear relationship obeys equation 2.2. Whereas curves (b) and (c) depict the presence of the second and third order terms of the susceptibility respectively causing the response of the polarisation to become nonlinear to the applied electric field.

The linear susceptibility $x^{(1)}$ is much greater than the higher order nonlinear terms of the susceptibility, such as $x^{(2)}$ and $x^{(3)}$, therefore the contribution of the later terms is only measurable at high field amplitudes or over long interaction lengths.

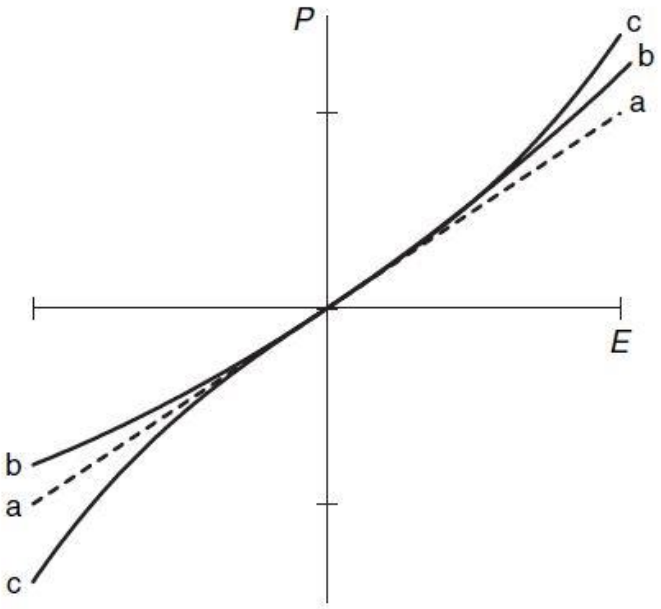

Figure 2.1. Linear and nonlinear response of polarisation P to the applied electric field E: (a) linear case (dashed), (b) quadratic nonlinearity, (c) cubic nonlinearity (Reproduced from [31]).

Now we consider the effect of an intense monochromatic laser beam propagating through a nonlinear medium. The characteristics of the propagating beam can be described by Maxwell's equations. The wave equation describing the propagation of light can be expressed as [30],

$$\nabla^2 \boldsymbol{E} = -\frac{\varepsilon}{c^2}\left(\frac{\partial^2 \boldsymbol{E}}{\partial t^2}\right) \tag{2.4}$$

where c is the speed of light and ∇^2 is the Laplace operator defined as,

$$\nabla^2 = \left(\frac{\partial^2}{\partial x^2} + \frac{\partial^2}{\partial y^2} + \frac{\partial^2}{\partial z^2}\right) \tag{2.5}$$

Under the assumption that the field is propagating as a plane wave in the positive z direction then 2.4 becomes,

$$\frac{\partial^2 \boldsymbol{E}}{\partial z^2} = -\frac{\varepsilon}{c^2}\left(\frac{\partial^2 \boldsymbol{E}}{\partial t^2}\right) \tag{2.6}$$

and a possible solution to 2.6 is the oscillation [33],

$$\boldsymbol{E}(z,t) = \boldsymbol{E}_0 \cos(\omega t - kz) \tag{2.7}$$

where *k* is defined as the propagation constant. By substituting 2.7 to 2.3 and using trigonometric identities we get the nonlinear polarisation as,

$$\boldsymbol{P} = \varepsilon_0 x^{(1)} \boldsymbol{E}_0 \cos(\omega t - kz) + \frac{1}{2}\varepsilon_0 x^{(2)} \boldsymbol{E}_0^2 [1 + \cos(2kz - 2\omega t)]$$

$$+\varepsilon_0 x^{(3)} \boldsymbol{E}_0^3 \left[\tfrac{1}{4}\cos(kz - \omega t) + \tfrac{3}{4}\cos(3kz - 3\omega t)\right] \tag{2.8}$$

Inspecting equation 2.8 one can see that new frequency terms are introduced due to the second and third order susceptibility terms. For materials that present inversion symmetry such as gasses, liquids and amorphous glasses the second order nonlinear susceptibility, $x^{(2)}$, is zero [32]. This is because in a centrosymmetric material, opposite directions are equivalent and the polarisation must change sign when an optical field is reversed. This condition is only satisfied if $x^{(2)}$ is zero. In the case of materials where $x^{(2)}$ is nonzero the second term of equation 2.8 is also nonzero, therefore giving rise to second order nonlinear effects. The new frequency term that has frequency twice that of the input field is responsible for the generation of a second harmonic (SHG) [34]. The second order nonlinear susceptibility is also responsible for nonlinear optical rectification (NOR) [35, 36], sum and difference frequency generation (SFG and DFG) [34, 37], optical parametric amplification and oscillation (OPA and OPO) [34, 38] and spontaneous parametric down conversion (SPDC) [39].

The last term of equation 2.8 demonstrates the contribution of the third order susceptibility. This term is responsible for the third harmonic generation (THG) [40], four wave mixing (FWM) [41], two-photon absorption (TPA) [17, 42], multi-photon absorption (MPA) [43] and nonlinear refraction [44]. The 3ω term can be seen as responsible for THG while the ω term is responsible for the irradiance dependence of the refractive index or as more commonly known, nonlinear refraction. The later

phenomenon along with nonlinear absorption do not require phase-matching conditions to be met and as such are the most readily observable in optical nonlinear materials.

2.3. The third order nonlinear optical coefficients

In this section, the optical coefficients associated with the third order susceptibility are discussed. The nonlinear refractive index is derived from the nonlinear polarisation of a material. Furthermore, the nonlinear absorption is discussed and the irradiance dependent nonlinear absorption coefficient is presented.

2.3.1. Irradiance dependent refractive index

In materials that present inversion symmetry $x^{(2)} = 0$, so equation 2.3 can be simplified to [44],

$$\boldsymbol{P} = \varepsilon_0\left(x^{(1)}.\boldsymbol{E} + x^{(3)} \vdots \boldsymbol{EEE}+\ldots\right) = \varepsilon_0\left(x^{(1)} + x^{(3)}\boldsymbol{E^2}\right)\boldsymbol{E} \tag{2.9}$$

The effective electrical susceptibility is given by the bracketed term equation 2.9 and can be expressed as [44],

$$x_{eff} = x^{(1)} + x^{(3)}\boldsymbol{E^2} \tag{2.10}$$

Also the expression of the refractive index of a material is [33],

$$\varepsilon = n^2 = 1 + x_{eff} \tag{2.11}$$

Similarly, the expression for the linear term of the refractive index which is related only to the linear first order susceptibility, presented in equation 2.2, can be written as [45],

$$n_0^2 = 1 + x^{(1)} \tag{2.12}$$

By re-arranging equations 2.11 and 2.12, substituting x_{eff} and $x^{(1)}$ into equation 2.10 and solving for *n* we get,

$$n = n_0\sqrt{1 + \frac{x^{(3)}\boldsymbol{E}^2}{n_0^2}} \tag{2.13}$$

since the term $\frac{x^{(3)}\boldsymbol{E}^2}{n_0^2} \ll 1$ relation 2.13 can be simplified to,

$$n \approx n_0\left(1 + \frac{x^{(3)}\boldsymbol{E}^2}{2n_0^2}\right) = n_0 + \frac{x^{(3)}\boldsymbol{E}^2}{2n_0} \tag{2.14}$$

The irradiance of the incident field is defined as [46],

$$I = 2\varepsilon_0 c n_0 \boldsymbol{E}^2 \tag{2.15}$$

Therefore, by considering 2.14 we reach to the equation,

$$n = n_0 + n_2 I \tag{2.16}$$

with n_2 being defined as,

$$n_2 = \frac{x^{(3)}}{4cn_0^2\varepsilon_0} \tag{2.17}$$

Relation 2.16 emphasises the dependence of the refractive index on the irradiance of the incident light.

The n_2 term is called the nonlinear refractive index coefficient and as can be seen from equation 2.17 it is related to the real part of the third order susceptibility. This is the coefficient that is responsible for the irradiance dependence of the refractive index. This irradiance dependence of the refractive index gives rise to the effects of self-focussing [47, 48], self-de-focussing [48], self-phase modulation (SPM) [49] and is responsible for

a range of important applications such as the KLM technique [50] for generating femtosecond pulses and optical bistability [47].

2.3.2. Nonlinear absorption

Linear absorption is the process during which a material exposed to light absorbs one photon causing one electron to be promoted from the valence to the conduction band. In this case, the energy of the photon must be larger than the bandgap of the material otherwise linear absorption cannot occur. However, in the case of strong electromagnetic fields, as discussed earlier, nonlinear absorption processes take place. An atom can simultaneously absorb two photons allowing for an electron to be promoted from the valence to the conduction band. This nonlinear process is called two-photon absorption (TPA) [17, 42]. Similarly, other processes can occur with the simultaneous absorption of more than two photons until the bandgap is reached in order for an electron to be excited from its ground state. The later process is called multi-photon absorption (MPA) [43]. A schematic showing linear absorption and MPA processes is presented in figure 2.2.

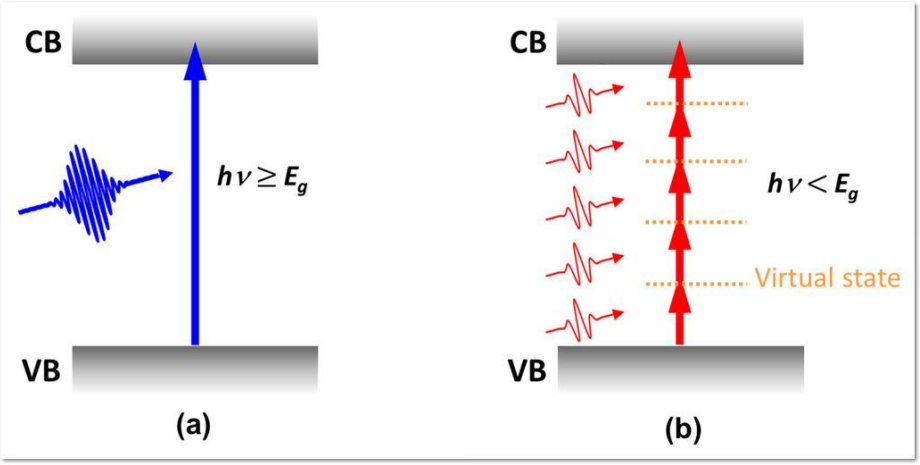

Figure 2.2. (a) Linear absorption process showing a photon with energy bigger than the bandgap being absorbed and exciting an electron from the valence to the conduction band. (b) MPA process showing 5 photons with energy smaller than the bandgap being simultaneously absorbed in order for the bandgap to be reached and excite an electron from the valence to the conduction band. The later process is also called Five-photon absorption.(Reproduced from [51])

The extend of absorption as light passes through a material can be expressed as [52],

$$\frac{dI}{dz} = -a(I) \times I \tag{2.18}$$

where the derivative dI/dz represents the change in transmitted irradiance as the material is translated through a focus in the z direction. This can be seen to be a function of the negative product of the irradiance and the irradiance dependent absorption coefficient which is defined as [33],

$$a(I) = a + \beta I + \gamma I^2 + \delta I^3 + \cdots \tag{2.19}$$

where α, β, γ, δ are the linear absorption coefficient and the nonlinear two-, three- and four-photon absorption coefficients respectively. The nonlinear absorption coefficient used depends on the multi-photon absorption edge of the material. If the dominant process is two-photon absorption the coefficient β would be used. The transmittance through a nonlinear material is obtained by solving the differential equation 2.18 after considering the total nonlinear absorption coefficient $a(I)$ according to the materials absorptive nonlinearities. The propagation equation, 2.18, was numerically solved and extensively used for the fitting of data acquired from Z-scan measurements throughout this work.

2.4. The Z-Scan experimental technique

Many experimental techniques have been developed in order to observe the third order optical behaviour of nonlinear materials and measure the associated coefficients. Some of these include wave mixing [53] or interferometric techniques [54]. Wave mixing techniques exploit the FWM process arising from the 3rd order susceptibility in order to gain information about the 3rd order nonlinearities. Besides their complexity, when using these methods it is not possible to obtain the sign of $x^{(3)}$, or observe both the real and imaginary parts at the same time. On the other hand, interferometric methods enable the determination of the sign of the nonlinearity but the magnitude cannot be directly measured; this can only be estimated from the input irradiance, leading to large errors and uncertainties.

A more elegant approach for studying the optical nonlinearities of a material is the Z-scan experimental technique [55]. Z-scan is based on the principle of spatial beam distortion to measure both, nonlinear absorption and refraction of a material, offering the advantages of great simplicity as well as very high sensitivity. This technique is extensively used in this thesis to study the optical nonlinearities of bulk and two-dimensional materials. A schematic of the basic principle of the Z-scan technique, also illustrating its simplicity, is shown below in figure 2.3.

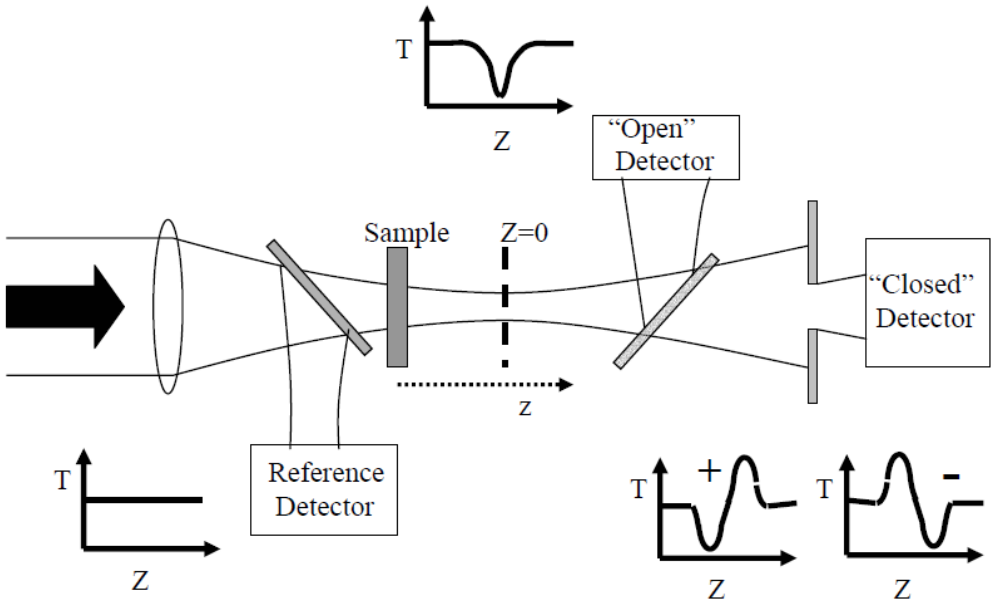

Figure 2.3. Z-scan configuration showing also schematics of the transmission T.

The test sample is translated through the focus of a beam, while continually monitoring the transmittance in the far-field. When far from focus the power per unit area is low therefore the absorption and refraction of the sample are due to linear effects which give a non-varying transmittance. As the sample approaches the focus, the irradiance will be much higher, thus the materials nonlinear properties will affect the propagation of the beam. In figure 2.3 a beam splitter is positioned after the focus tapping a percentage of the beam on a second detector enabling the simultaneous collection of open- and closed-aperture Z-scan traces. The open- and closed-aperture Z-scan regimes are discussed in detail in the following paragraphs.

First we consider the case of nonlinear refraction; this is illustrated in figure 2.3 with the "closed" detector. The effect upon the transmittance in the far field is measured using the "closed" detector which means that an aperture is placed in front of the detector allowing only a percentage of the beam to get through. The far field condition is defined as $d \gg Z_0$ where d is the distance of the aperture from the focus and Z_0 is the Rayleigh range [55]. By assuming a sample with positive nonlinear refractive index and in the absence of any absorptive nonlinearities, as this approaches the focal point it will induce a self-focussing effect to the beam otherwise known as Kerr lensing. This self-focussing effect will cause the beam to focus earlier and become more divergent in the far-field. This effect becomes stronger as the sample approaches the focus. Due to the aperture placed in front of the detector this divergence will lead to a drop in transmittance creating a "valley" on the reading of the detector. Then, as the sample is translated immediately past the focal point, collimation of the beam occurs, which leads to an increase in transmittance as more light is able to pass through the aperture thus creating a "peak" on the reading of the detector. As the sample is transferred further behind the focus the irradiance lowers because the power per unit area is low and only linear effects are observed. Therefore, materials with positive nonlinear refractive index will yield a distinct Z-scan trace with a "valley" in transmittance followed by a "peak" as the sample is translated through the focus of the beam. On the other hand, a material with negative nonlinear refractive index first tends to collimate and then diverge the beam as it is translated through the focus producing a Z-scan trace of a "peak" followed by a "valley". This "valley"-"peak" (or "peak"-"valley") variation will be symmetric about the focus provided there is no nonlinear absorption. Therefore, the sign and the magnitude of a materials nonlinear refractive index can be readily obtained from a Z-scan trace. This technique known as "closed-aperture Z-scan". The characteristics of the "closed-aperture Z-scan" as a material with positive nonlinear refractive index is translated through the focus of a beam are illustrated in figure 2.4.

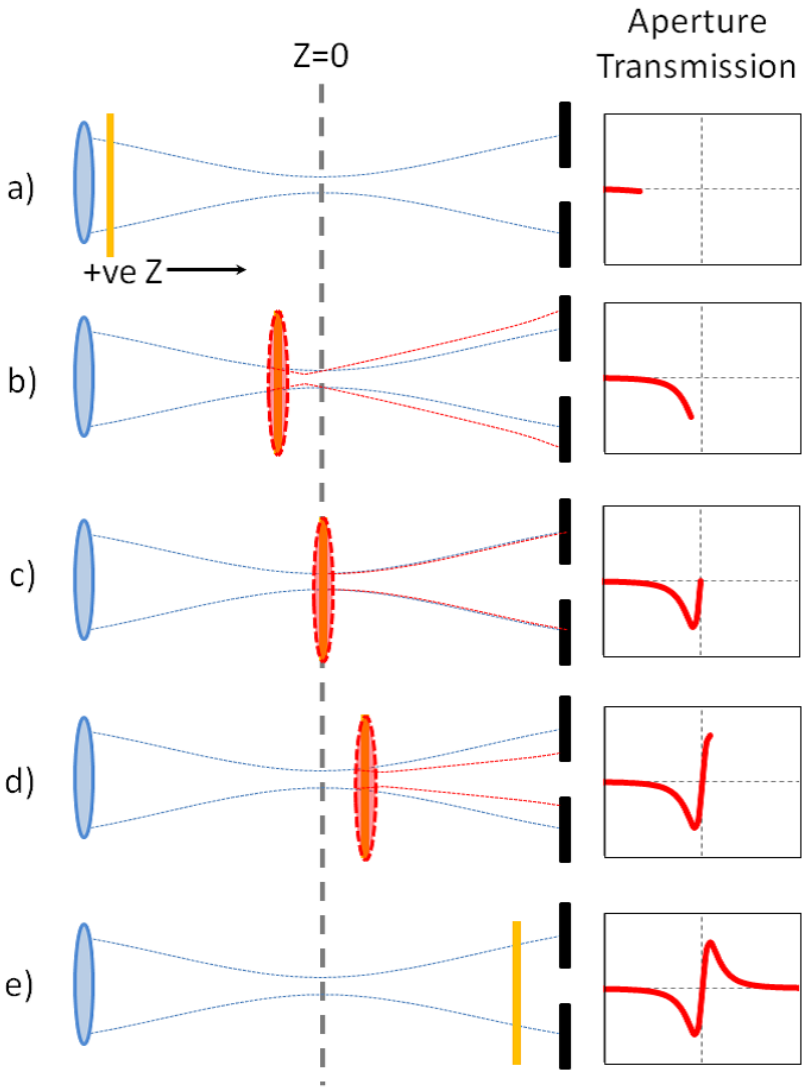

Figure 2.4. Translation of a material with a positive nonlinear refractive index through the focus of an intense laser beam illustrating the principle of the closed-aperture Z-scan, assuming no absorptive nonlinearities are present (reproduced from [33]).

The effect of nonlinear absorption can also be observed by employing a technique known as "open-aperture Z-scan". In this regime no aperture is placed in front of the detector in the far field allowing the whole of beam to be collected. Therefore, this "open" detector is insensitive to the effects relating to nonlinear refraction and only effects relating to nonlinear absorption can affect the measured transmittance. As the sample is translated through the laser beam the absorption will be greatest at the focus where the irradiance is higher. Consequently, a "valley" in the transmittance will be created symmetrically around the focus. In the case of materials that present saturable absorption, such as graphene, the open-aperture Z-scan traces, in contrast to the case of MPA will present a

symmetric peak around the focus. Saturable absorption will be discussed in detail in later chapters, when presenting the work performed on graphene. As discussed earlier, usually in experimental setups a beam splitter is positioned after the focus tapping a percentage of the beam on a second detector enabling the simultaneous collection of open- and closed-aperture Z-scan traces. This configuration provides better accuracy since it assures that the open- and closed-aperture Z-scans are performed at the same pulse energy, as well as offering the advantage of saving time since it does not require the execution of two different scans to acquire the open- and closed Z-scan traces.

However, when using a beam splitter to observe both open- and closed-aperture Z-scans simultaneously, and in the case that the sample presents both nonlinear absorption and refraction, the effect of nonlinear absorption will be present in the closed-aperture trace too. In order to isolate the effect of nonlinear refraction from that of nonlinear absorption the closed-aperture trace can be divided by the open-aperture trace as explained by Sheik-Bahae in [55]. This yields a typical closed-aperture Z-scan trace, one that would be obtained in the absence of any absorptive nonlinearities.

The Z-scan method can clearly capture the effects of nonlinear absorption and refraction of the sample in question. Thereupon, in order to deduce the magnitude of the nonlinear coefficients theoretical fits are applied to the collected data. For a small phase change, $(|\Delta\Phi| \ll 1)$, and in the presence of only TPA simplified empirical formulas can be employed to obtain the values for the nonlinear coefficients [56]:

$$T_{open}(Z) = 1 - \frac{\beta I_0 L}{2\sqrt{2(1+x^2)}} \tag{2.20}$$

$$T_{closed}(Z) \cong 1 + \frac{4x(\Delta\Phi)(1-S)^{0.25}}{(1+x^2)(9+x^2)} \tag{2.21}$$

where $x = {}^{Z}/_{Z_0}$, z is the sample distance from the focus and z_0 is the Rayleigh range defined as $z_0 = \pi\omega_0^2/\lambda$; ω_0 is the beam radius at the focus and λ is the wavelength. S is the aperture transmission, I_0 is the peak on-axis irradiance, L is the sample thickness and $\Delta\Phi$ is the time-averaged on-axis phase change, defined by the equation [47],

$$\Delta\Phi = \frac{2\pi L n_2 I_0}{\lambda} \tag{2.22}$$

The numerical value of β and n_2 coefficients can be obtained by varying these two parameters in equations (2.20) and (2.21) until the experimental data and the theoretical fits come in good agreement. When using this fitting method to determine nonlinear refractive index of a material, no multi-photon absorption effects can be present on the closed-aperture Z-scan.

In the case of MPA or for large phase shifts equations 2.20 and 2.21 do not hold, therefore in order to accurately model the effects of nonlinear absorption and nonlinear refraction from a single Z-scan, other more analytical methods must be deployed. A Fast Fourier Transform Beam Propagation Method (FFT-BPM) [57] can be used. The FFT-BPM divides the sample into a number of thin 'slices', each of which are then treated as a thin lens. The strength of each lens is determined by the *slice* nonlinearity. This method calculates the nonlinear effects by considering the beam size and radius of curvature as the light enters, passes through and exits each slice. The Adomian Decomposition Method (ADM) was developed by George Adomian during the 1980's [58] and has attracted a lot of attention as an effective tool for solving differential equations. This method does not require to fully solve the propagation differential equation, rather a recurrence formula can be used to calculate quickly all the components of the solution of the equation. Ultimately the sum of all these components will approach to the exact solution of the propagation equation. Due to the fact that it does not require to fully solve the propagation equation, ADM offers the advantage of being time effective over other methods that require full propagation of the beam in order to extract the analytical solution. This method was used to fit the experimental data in the case of graphene which presents both SA and TPA [59]. These properties of graphene are extensively discussed later in this thesis.

When fitting Z-scan traces either using the simplified or the accurate formulas there are a number of important experimental parameters that need to be recorded in order to obtain reliable values for the nonlinear coefficients. Such parameters are the pulse duration, the pulse energy, the beam waist at the focal spot and the aperture transmission value. Additionally, for the simplified empirical formulas 2.20 and 2.21 to hold the sample thickness must be less than the Rayleigh range of the beam [55].

While Z-scan is a powerful and fundamental characterisation technique which can clearly capture the nonlinear refraction and absorption effects of the sample in question and measure the associated coefficients, it fails to measure some other aspects of the nonlinearity such as the temporal response of the carrier dynamics. One method that has the ability of studying the temporal response of the ultrafast relaxation phenomena after photo-induced excitation is the pump-probe technique [60]. The general principle of this technique is the following. The sample in question is irradiated by a strong pump pulse, which generates some kind of excitation. After an adjustable time delay a weaker probe pulse, which can be of the same or different wavelength as the pump pulse, is sent on the sample and its transmission or reflection is measured. By monitoring the probe signal as a function of the time delay, it is possible to obtain information on the decay of the generated excitation, or on other processes initiated by the pump pulse. The temporal resolution of this technique is only limited by the pulse duration of the pump and probe pulses. Ultrafast pump-probe spectroscopy has been extensively used to study photo-excited ultrafast carrier dynamics in graphene [61, 62], which are discussed in detail later in section 3.2.1 of the thesis. More recently pump-probe techniques have been used to study the dielectric permittivity of metamaterials close to the epsilon-near-zero wavelength as a function of the optical pump power [63, 64], pointing out another useful application of pump-probe techniques.

The pump-probe and Z-scan techniques can be seen as complementary. The information regarding the temporal response of the carrier dynamics acquired via pump-probe can be combined with the nonlinear optical coefficients acquired via Z-scan providing this way all the necessary information for fully understanding and characterising all the photo-induced processes in the material in question.

2.5. Femtosecond laser system

The laser system used to investigate nonlinear optical effects throughout this thesis was a regeneratively amplified Ti:Sapphire femtosecond laser system which seeded an Optical Parametric Amplifier. The ultrashort pulses made available from this laser system allowed for the high irradiances required to observe nonlinear behaviour. All the laser

systems were manufactured by Spectra-Physics. A schematic of the laser system is shown in figure 2.5.

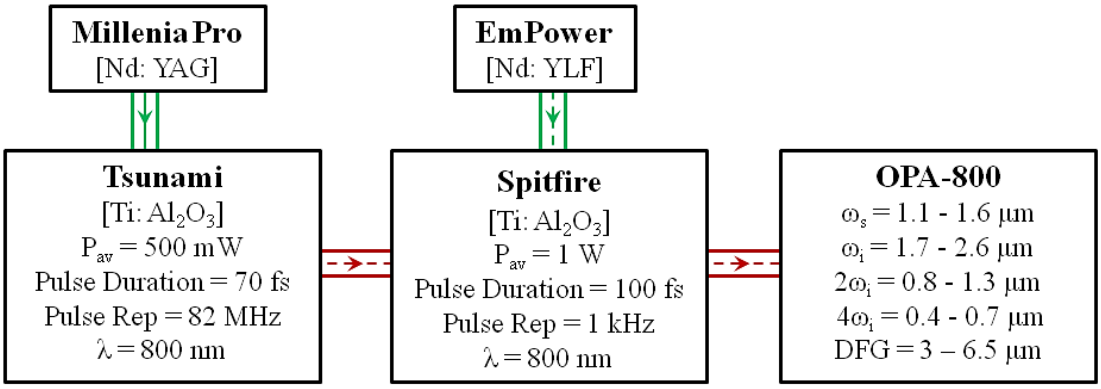

Figure 2.5. Femtosecond optical parametric amplifier seeded by a regeneratively amplified Ti:Sapphire laser system. ω_s and ω_i are the signal and idler photons generated in the OPA, the generation process for ω_s and ω_i is explained in section 2.5 (reproduced from [33]).

A Millenia Pro diode-pumped frequency doubled Nd:YAG laser with a continuous wave output of 5 W at a wavelength of 532 nm is used to optically pump a Tsunami Ti:Sapphire laser. The laser emission wavelength is chosen to be 800 nm. An intra-cavity Acousto-Optic Modulator (AOM) is used to mode-lock the Ti:Sapphire laser. When mode-locked the Tsunami provides an average power of 500 mW at a repetition rate of 82 MHz and pulse widths in the orders of 70 fs.

The output of the Tsunami is then directed to the "Spitfire" chirped pulse amplification (CPA) [65] system which is pumped by an Empower Q-switched Nd:YLF laser. In order to pump the Ti:Sapphire rod within the CPA cavity the Empower is operated at a wavelength of 527 nm, with a pulse duration of 300 ns at a repetition rate of 1 kHz and an average power of 7 W. Before being amplified, the pulse train is directed through a diffraction grating, thus dramatically increasing the pulse duration and consequently decreasing the peak powers. After amplification, the pulses are compressed by passing through a grating which has a complementary dispersion to that of the input grating. At

the output of the Spitfire the pulses then have a duration of 100 fs with a repetition rate of 1 kHz and an average power of 1 W.

The output from the Spitfire is then directed into the Optical Parametric Amplifier. The OPA makes use of second order nonlinear frequency conversion processes in a nonlinear type-II BBO crystal to split an input pump photon ω_p into two other photons, the signal photon ω_s and the idler photon ω_i such that energy is conserved i.e., $\omega_p = \omega_s + \omega_i$ (and $\omega_p > \omega_i$) or in terms of wavelength $\frac{1}{\lambda_p} = \frac{1}{\lambda_s} + \frac{1}{\lambda_i}$. Upon entering the OPA, the input beam is split into two separate beams, one beam that carries 99% of the power and one that carries the remaining 1%; first the 1% is used to generate a white light continuum by focussing onto a sapphire plate. The remaining 99% is split again, 15% of which is spatially and temporally overlapped inside the BBO crystal generating the signal and idler wavelengths; this is known as the pre-amplification stage. The generated signal (ω_s) and idler (ω_i) beams are then passed again through the BBO crystal this time spatially and temporally overlapped with the remaining pump pulse. This greatly intensifies the amount of power generated in the signal and idler wavelengths; this is known as the power amplification stage. The signal and idler wavelengths can then be separated by using a Bragg mirror at the output of the OPA. By tuning the crystal, it is possible to generate signal wavelengths between 1100-1600 nm and idler wavelengths between 1600-2600 nm. Typical un-attenuated output powers are 50-100 mW and 15-60 mW for the signal and idler outputs respectively, depending on the selected wavelength. In terms of pulse energies, values of 50-100 μJ and 15-60 μJ are achieved, since the system is operating at a repetition rate of 1 kHz.

2.6. Z-scan Experimental system

The femtosecond laser system described above was used for Z-scan measurements offering the advantages of ultrashort pulses and broad wavelength tuneability spanning almost 2 μm. Furthermore, the low repetition rate of 1 kHz ensures the absence of thermal contributions when performing Z-scans.

2.6.1. Z-scan experimental setup

The configuration of the experimental setup used for Z-scan measurements is shown in figure 2.6. First Schott RG850 filters were placed at the outputs of the OPA in order to remove any unwanted residual light that may have been co-propagating with the signal and idler beams. After passing through the RG850 filters the beam is directed by two silver coated mirrors (M1 and M2) through a spatial filter. The spatial filter consists of two 200 mm focal length achromatic doublets placed 2-f apart either side of a 100 μm diamond pinhole. The pinhole is held under vacuum to eliminate the creation of plasma which could occur at the focus. The spatial filter is used to "filter" the beam in order to ensure the beam profile is as close to a pure Gaussian as possible. The 100 μm spatial filter typically reduces the laser power by about 40%. After passing through the spatial filter the beam is directed by M3 and M4 through two irises (not shown in figure) to ensure that the beam axis is co-linear with the movement of the translation stage. A beam splitter, BS1, taps off ≈ 4% of the beam before being collected with detector D1, which is used as a reference signal reading. The remaining 96% of the beam is focused with an anti-reflection (AR) coated calcium fluoride (CaF_2) lens, L4, which has a focal length of 200 mm; this is the lens used to focus the beam for the actual Z-scan measurement. Another beam splitter, BS2, positioned in the far field well after the focal spot of L4 reflects ≈ 4% of the signal which is collected with detector D2, the open-aperture detector. Finally, the remaining signal is passed through a variable aperture, I1, before being collected by detector D3, the closed-aperture detector.

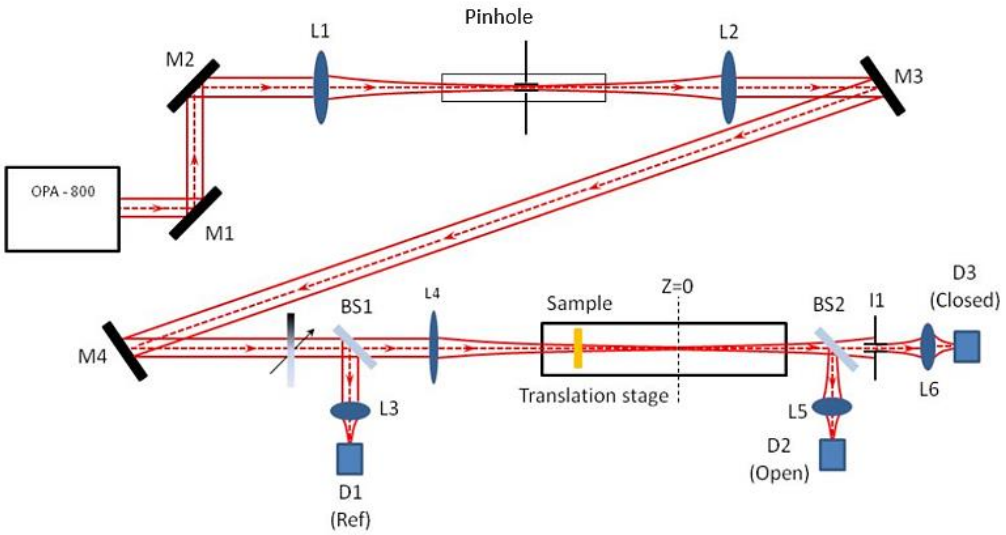

Figure 2.6. Z-scan experimental setup (reproduced from [33])

2.6.2. Detection and data acquisition

For data detection two types of photodiodes were used. For the shorter wavelengths three New Focus (model 2033) amplified germanium detectors with an operating range of 800-1750 nm were employed. While for the measurements at wavelengths longer than 1750 nm three Thorlabs PDA30G-EC PbS amplified detectors were used; these detectors could operate from 1000 to 2900 nm. Both types of detectors were found to have a linear response to signals higher than 1 V. Combinations of neutral density (ND) filters were placed in front of each detector so that their signal levels were kept well below 800 mV for each Z-scan measurement. This assured that the detectors response would be linear to the incident light. A variable ND filter was used to allow for fine adjustment of the incident onto the sample power, this can be seen in figure 2.6 between M4 and BS1. The incident power was measured just before the sample (after L4 in figure 2.6) using a calibrated Laser Probe pyroelectric power meter (RKP-575) connected to a Laser Probe power ratio meter (RK-5720). The sample was mounted on a motorised translation stage (Newport UTM 150 series) which was connected to a Newport MM005 motion controller.

The outputs of the detectors were fed through a peak hold unit to an oscilloscope as well as a data acquisition card, which was connected to a PC. The control software employed is an HP-VEE program which is used to collect the data and control the movement of the translation stage. The control programme was developed by former members of the nonlinear optics (NLO) group. Windowing was used to ensure stable and accurate collection of data. A reference value based on the reading of D1 and a plus-minus percentage, called window, for this reference value are set. For each stage position a certain number of measurements of the reference and corresponding open- and closed-detector signal levels are made; the number of measurements to be made is set by the user. If a number of these values, again set by the user, lie outside the error window of the reference detector, then all the measurements for all three detectors are discarded. This process repeats until the windowing conditions are met. As soon as this happens, the mean values of the reference, open and closed detectors along with the current z-position are saved into a text file. The stage then translates the sample to the next position; the translation distance can be set by the user. Windowed collection of data occurs again at

the new stage position in the same way. This process continues until a ‘stop’ command is entered at the program interface. The reference, open- and closed-detector readings are also plotted in real time allowing the observation of the Z-scan traces as they evolve enabling the quick change of any parameters if required. The user interface of the HP-VEE control software illustrating the windowing procedure is given in figure 2.7.

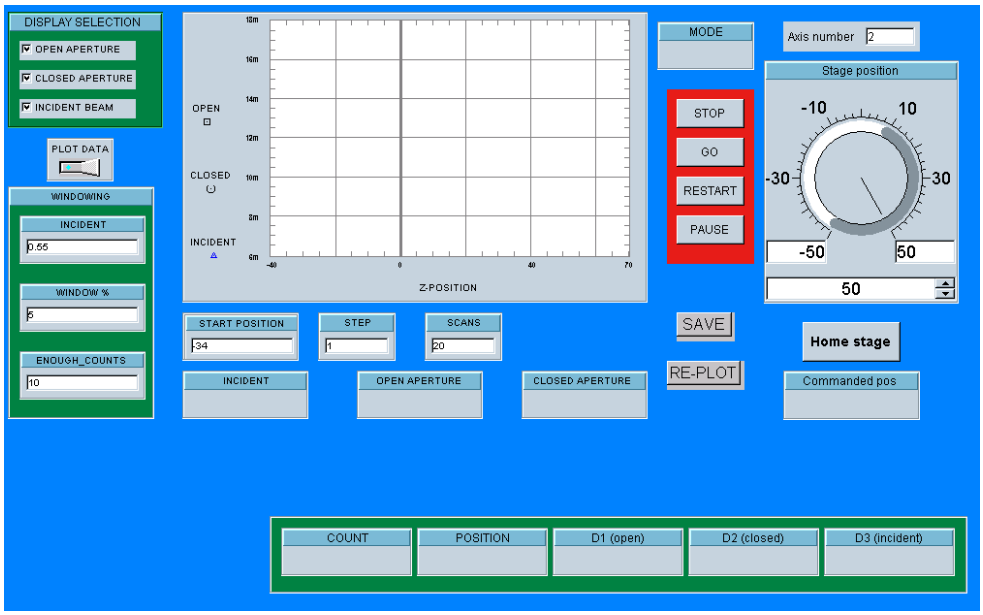

Figure 2.7. Image of the user interface of the HP-VEE Z-Scan control program.

2.7. Ultrafast laser inscription technique

Modern telecommunication systems rely mainly on optical fibres for guiding light. Optical fibres rose to prominence in the 1960’s when Charles Kao and George Hockham theorised that optical fibres could be realised with less than 20 dB·km^{-1} attenuation making them suitable for telecommunications [66]. This work led to Charles Kao receiving a share of the Nobel Prize for Physics in 2009 [67]. However, the rapid evolution of integrated optics during the last decades created the need for the fabrication of guiding structures inside bulk substrates.

With the wide use of ultrafast laser systems during the last 20 years a new technique for direct writing of waveguides in bulk materials has emerged. The ultrafast laser inscription (ULI) technique was first demonstrated in 1996 by Davis et al. [68]. After that original

work, ULI has ascended as a powerful and flexible tool for the fabrication of integrated optical devices and buried waveguides. ULI is based on the nonlinear absorption of sub-bandgap photons to induce permanent structural changes in a material [69]. Ultrashort pulses are focused below the surface of a transparent material. The high field irradiances in the focal volume induce nonlinear absorption processes, resulting in an energy transfer to the material lattice; the material modification is limited to the focal volume inside the substrate. With careful selection of the inscription laser parameters this energy transfer may manifest as a positive refractive index change [68, 69]. Thereby waveguide structures inside a bulk substrate can be realised by simply translating the sample through the laser focus.

Due to their wide availability, early ULI work predominantly employed regeneratively amplified Ti: Sapphire sources; these usually operate at short pulse durations of approximately 100 fs and low repetition rates of 1-5 kHz [70, 71]. However more recently the development and broad use of short pulse mode-locked fibre laser systems enabled the utilisation of higher repetition rate lasers to expedite the fabrication process, with typical pulse widths ranging from 300 fs to 2 ps. This increased freedom in inscription parameters enhanced the capabilities of ULI and most importantly lead to the realisation of low loss waveguides [72, 73].

The most distinct advantage of ULI over other techniques is the truly three-dimensional inscription capabilities it offers. This allows for the fabrication of complex structures making ULI a powerful tool for the development of a range of devices such as; microfluidic devices [74], quantum information processing circuits [75], photonic lanterns for astrophotonics [76] and multi-core fibre couplers [77]. A schematic of a typical ULI rig illustrating its three dimensional capabilities is presented in figure 2.8.

The high flexibility of ULI arises from the fact that it has a large number of variable parameters which can be altered in order to achieve the desired outcome. For the successful fabrication of waveguides or devices with this technique, some key parameters have to be taken into account. The most important inscription parameters are pulse energy, pulse repetition rate, pulse duration, sample translation speed, NA of the focussing optics, wavelength and beam polarisation.

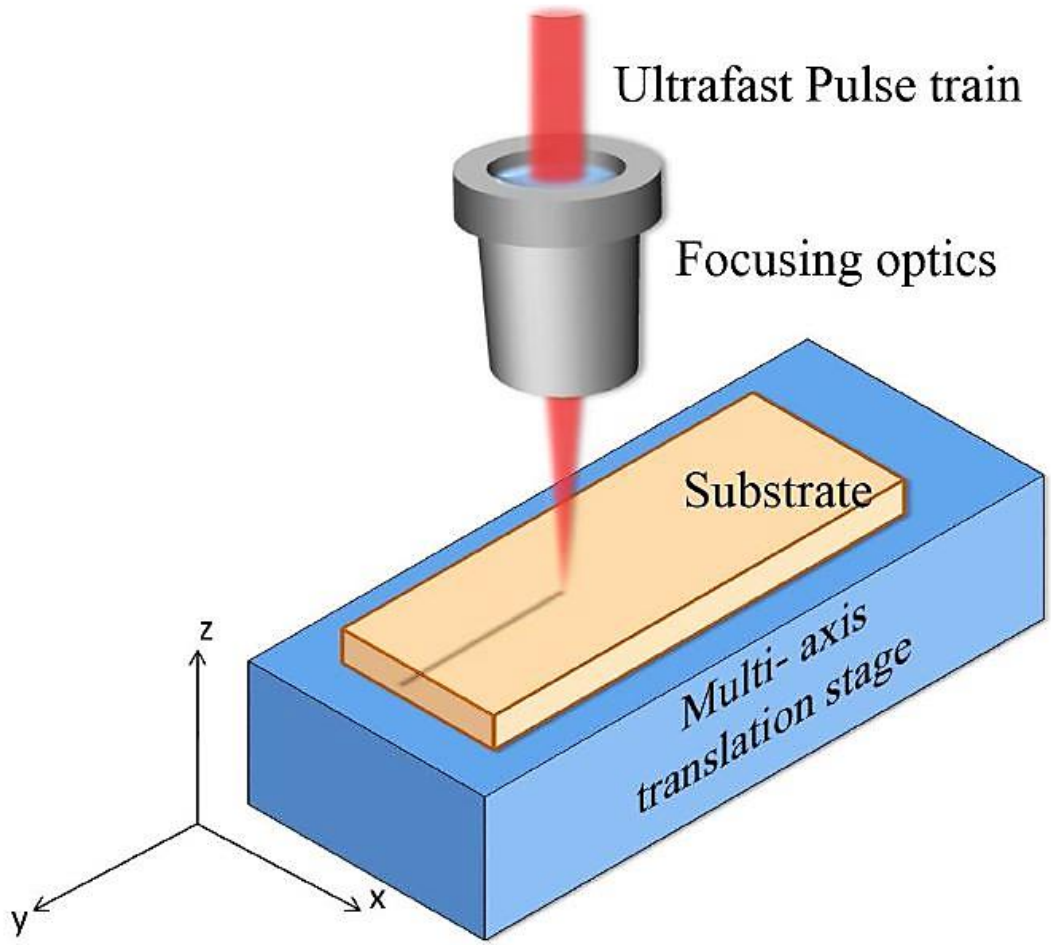

Figure 2.8. Schematic of a typical ULI rig. The setup consists of an objective focussing an ultrafast laser beam inside a bulk substrate and an x-y-z translation stage on which the substrate is held. This allows for the inscription of any three-dimensional structure within the maximum movement range of the translation stage (reproduced from [45]).

As would be expected, the pulse energy is a critical ULI parameter, since it directly determines the amount of energy transferred to the material. This drastically affects the type of modification induced in the material. For instance, at low pulse energies no modification occurs, for higher pulse energies a positive refractive index change can be induced and for even higher pulse energies empty voids can be formed or the substrate can be completely fractured. When inscribing optical waveguides, the optimum pulse energy is the one which induces the required refractive index modification while minimising the generation of scattering and absorption centres which increase waveguide

propagation losses. Of course the optimum pulse energy for a given task will primarily depend on the material and will vary as a function of other inscription parameters [69].

One of the most important ULI parameters is the pulse repetition rate, which is directly related to the thermal accumulation effects in the material. Lower repetition rates mean that the time interval between subsequent pulses is increased allowing heat to diffuse out of the focal region, therefore causing each pulse to interact with cold material. Conversely, the use of high repetition rates allows the temperature of the irradiated material to be driven significantly upward, therefore changing the type of the modification. The use of different repetition rates can drastically alter the shape or size of structures inscribed in a material, particularly those with a low thermal conductivity [78].

The pulse duration has been seen to play a crucial role in the ULI process. In the case of highly nonlinear materials it has been shown that the use of longer pulses reduces the peak power for a given pulse energy, therefore reducing the nonlinear effects such as self-focusing, pulse breakup and filamentation, which reduce the efficiency with which energy can be deposited in the sample [79]. Furthermore altering the pulse duration, in some cases has been seen to have an effect on the propagation losses and the birefringence of the inscribed waveguides [80].

The substrate translation speed is a useful tool for varying the laser fluence on the substrate while keeping the pulse energy fixed. In general, by reducing the translation speed the exposure time of the substrate at the focal region of the laser is increased, subsequently increasing the magnitude of the induced modification. By increasing the translation speed, the opposite effect is achieved. This effect has been shown to be particularly useful for precisely controlling the guided optical modes of the ULI fabricated waveguides [81]. Furthermore, similar to the case of the pulse repetition rate, the translation speed can be used to vary the overlap of subsequent pulses in the material, only on a coarser scale. This is very useful for inscription laser sources that operate on a fixed pulse repetition rate.

The focussing optics also have a significant impact on the material modification. By changing the focussing objective one alters the beam waist at the focus, subsequently

changing the peak irradiance inside the substrate while keeping the average power and pulse energy the same. In practical terms changing the focussing objective affects the cross-section of the modified region.

Due to the fact that ULI relies on nonlinear absorption of sub-bandgap photons, the laser wavelength with respect to the band-gap of the material will govern the order of multi-photon absorption, i.e. the number of photons required in order to overcome the bandgap of the substrate. For laser sources whose wavelength lies far from the material band-edge, the dominant absorption mechanism is not multi-photon absorption but a process known as tunnelling ionisation [69]. The modification of the material will be affected by the nonlinear absorption process occurring in the substrate.

The polarisation of the incident beam will affect the efficiency of the absorbed light, therefore affecting the induced modification in the material. It has been shown that the laser polarisation affects the magnitude of the induced refractive index modification in fused silica [82]. The laser polarisation can also strongly influence the magnitude of the chemical etch-rate. It is demonstrated that ULI induced nanogratings enable hydrofluoric acid to efficiently penetrate into the irradiated material with a dramatic dependence of the etch rate on the laser polarisation [83].

Some of the above fabrication parameters will vary as a function of others, while some others will vary in complete isolation. However, there is a whole range of key inscription parameters that can be altered. Therefore, the limitations of a particular inscription setup, such as fixed emission wavelength or fixed pulse duration, can be overcome by varying other aspects of the inscription in order to reach the desired fabrication. This wide range of inscription parameters is exactly what grants the ULI technique its large flexibility.

2.8. ULI fabrication setup

A description of the ultrafast laser along with the inscription setup used for the fabrication of the waveguides and devices is also given. Figure 2.9 shows the complete inscription apparatus including the ultrafast laser, the steering and focussing optics, the imaging system and the high precision x-y-z translation stages.

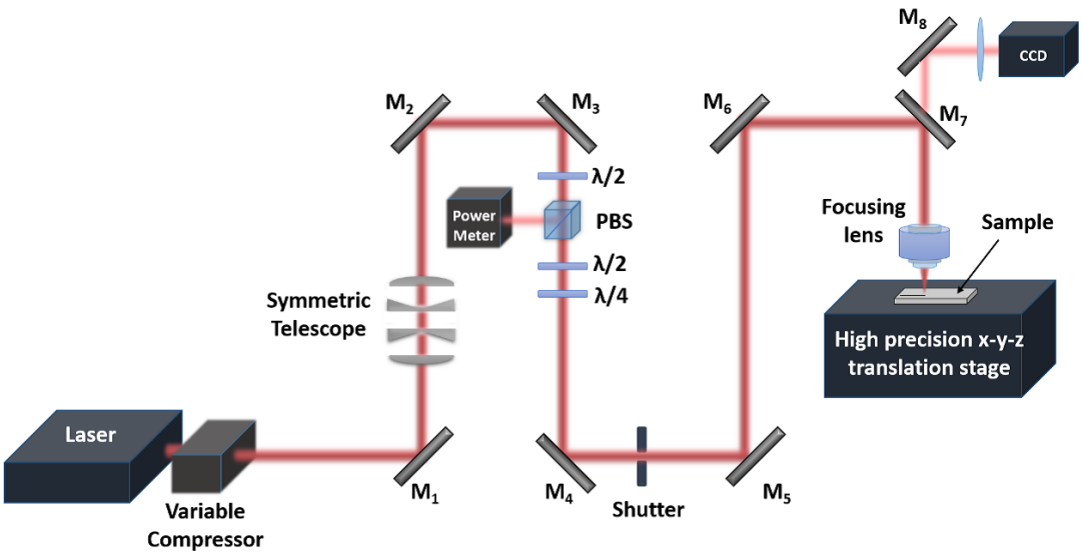

Figure 2.9. Diagram of the ULI experimental setup. The output of the laser is steered using the appropriate optics between mirrors M_1 and M_7 before being focussed in the bulk substrate. The substrate is held on high precision translation Aerotech® stages. The complete setup is computer controlled, including the translation stages, and the power and polarisation control (reproduced from [45]).

2.8.1. IMRA® inscription laser

The inscription laser used for the fabrication of waveguides and devices was a variable repetition rate Yb-doped fibre oscillator power amplifier system, IMRA® FCPA μJewel D400. This laser system allows for the adjusting of the pulse repetition rate within a range from 100 kHz up to 5 MHz. Additionally, the use of an external adjustable compressor allows control over the linear chirp on the laser output. This can be used to change the pulse duration, enabling the achievement of pulse durations in the range of 350 fs to 3 ps. The increased design freedom over the pulse repetition rates and pulse widths, as discussed in the previous section, provides extreme flexibility, therefore making this laser an excellent choice for the fabrication of devices and waveguides via the ULI technique. The laser produces linearly polarised pulses (horizontal) with a centre wavelength of 1045 nm. Also it has the capability of producing average powers ≥350 mW after compression at each pulse repetition rate.

2.8.2. Steering optics

As can be seen from figure 2.9 the output from the compressor is steered via various essential optics between mirrors M_1 and M_7 before being focussed in the bulk substrate. A half-wave plate and polarisation beam splitter combination is utilised for a calibrated control over the average power. Then a second half-wave plate offers the choice of the rotation of the polarisation plane, followed by a quarter-wave plate enabling circularly polarised light if required. The rotation mounts for these optics are controlled via computer, thereby allowing for easy control of the power and polarisation of the inscription beam. The beam is then directed to a vibration insensitive granite gantry through mirrors M_4 to M_7 and focussed within the substrate using the appropriate objective. The substrate is placed on an automated high-precision, air-bearing x-y-z translation stage system, Aerotech® ABL1000. The translation stages and the mechanical shutter shown between mirrors M_4 and M_5 are also controlled by the same computer. Finally, an imaging system indicated by the beam path along M_8 allows for the precise positioning of the sample at the focus of the inscription lens.

2.9. Summary

This chapter has presented the main experimental methods used for the majority of the work presented in this thesis. Particularly, the Z-scan technique was used for nonlinear measurements, while the ULI technique was used for the fabrication of waveguides and photonic devices. The chapter also includes a discussion on the origin of nonlinear optical behaviour. Considering the nonlinear polarisation of a material the third order nonlinear optical coefficients are derived, giving this way insight in the main nonlinear processes involved in the experimental techniques. The femtosecond laser system used for Z-scans was presented followed by a detailed description of the Z-scan technique and experimental setup, illustrating that Z-scan is a fast and elegant way of measuring 3rd order nonlinearities. Finally, the ULI technique was presented and the key experimental parameters were discussed, demonstrating the flexibility of this technology.

Chapter 3. Nonlinear Optical Characterisation of Graphene

3.1. Introduction

This chapter will present the optical characterisation of CVD single and multilayer graphene. First an introduction of graphene's fundamental properties is given and the nonlinear optical properties related to saturable absorption, two-photon absorption and nonlinear refraction are discussed. This leads to the optical characterisation of CVD single and multilayer graphene via the Z-scan technique. The Z-scan measurements revealed a giant negative irradiance-dependent nonlinear refraction for both single and multilayer graphene. A low irradiance regime, where the conventional Kerr nonlinear refractive index n_2 can be deduced, is discriminated from a high irradiance regime where the nonlinear response becomes irradiance dependent. The latter is defined as irradiance-dependent nonlinear refraction and the symbol $\tilde{n}(I)$ is used. Furthermore, the competing saturable absorption and two-photon absorption processes in multilayer graphene are studied over a broad range of wavelengths. The experimental work is followed by a theoretical analysis arising from the conductivity of the graphene monolayer, verifying the irradiance-dependence and negative value of the nonlinear refraction of graphene over a broad range of wavelengths. The experimental results obtained for multilayer graphene were combined with the theoretical analysis and published to Optics Express [10]. Finally the chapter concludes with the optical characterisation of a multilayer graphene saturable absorber, which was used to characterise a graphene based Tm:YAG mode-locked waveguide laser at 2 μm [9].

3.2. Graphene

Carbon is one of the most fascinating elements in the periodic table. It is the base for DNA and can exist in several different forms. The most common form of carbon is graphite, which consists of hexagonal carbon sheets stacked on top of each other. A single sheet of graphite is what we call graphene. Graphene had already been studied theoretically as early as 1947 [1] but it was believed that a single sheet could not be produced in isolated form such that electrical and optical measurements could be performed. Andre Geim, Konstantin Novoselov and their collaborators at the University

of Manchester were the first ones to successfully isolate a single layer of graphene and transfer it to another substrate such that electrical and optical measurements could be performed [2]. This achievement not only got them the Nobel Prize in physics in 2010 [3], but also sparked enormous interest in the graphene research field. The large volume of work dedicated the last decade revealed graphene's many superior properties, leading to its labelling as 'miracle' or 'wonder material'.

Graphene consists of a single layer of carbon atoms arranged in a hexagonal (honeycomb) lattice, with a carbon-carbon distance of 0.142nm. It is the first truly two-dimensional atomic crystal, having a thickness of only one atomic layer of graphite; *thickness=0.35±0.01 nm* [84]. The hexagonal lattice of monolayer graphene is shown in figure 3.1(a).

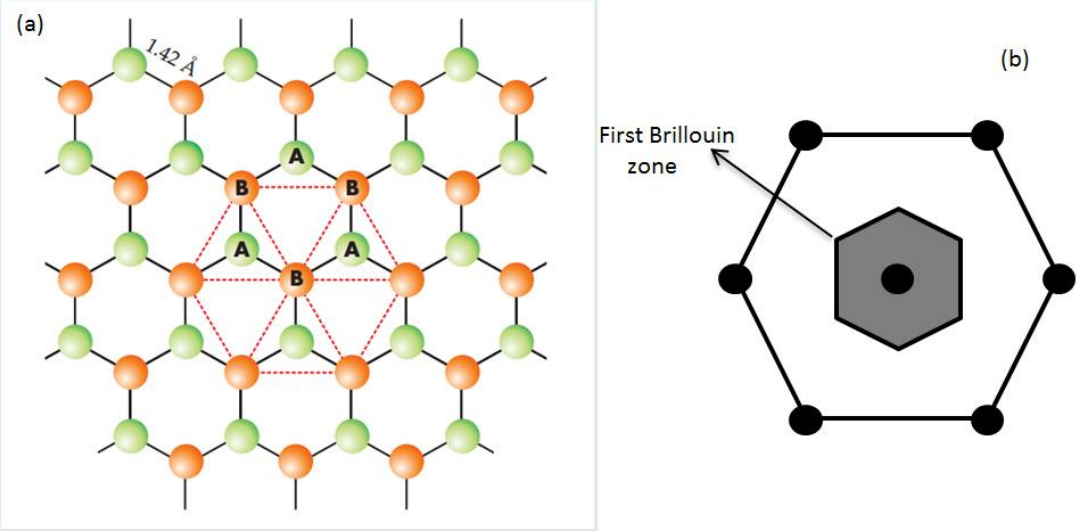

Figure 3.1. (a) Real space hexagonal atomic lattice of graphene consisting of two sub-lattices, represented by atoms in orange and green (reproduced from [85]). (b) The reciprocal lattice of graphene. The shaded region denotes the first Brillouin zone

It can be considered as two interpenetrating triangular sub-lattices, distinguished as green and orange atoms**.** The sites of one sub-lattice (green) are at the centres of triangles defined by the other (orange). The reciprocal lattice of graphene is shown in figure 3.1(b). The reciprocal lattice does not describe any physical object; rather it is a geometrical tool for dealing with problems in the theory of diffraction and electronic structure of solids. A

reciprocal lattice is obtained by taking the Fourier transform of the original lattice wavefunction. The primitive cell in a reciprocal lattice is termed the Brillouin zone, also shown in figure 3.1(b) by the shaded grey area.

The electronic band structure of a solid, also termed as dispersion relation, is derived from its reciprocal lattice using different theoretical models depending upon the type of the material. The band structure of graphene is derived from the reciprocal lattice of figure 3.1(b) and is rather different from usual three-dimensional materials. It consists of two bands, the valence and conduction bands, which touch at 6 points, termed K points or Dirac points and are situated at the edges of the first Brillouin zone in the reciprocal lattice. In the vicinity of the K points the dispersion relation for both the valence and conduction band is linear and given by $E^{\pm}(\kappa) = \pm\hbar v_F|\kappa|$ [86], where κ is the wave vector around the K points and v_F is the Fermi velocity. This linear dispersion relation leads to the formation of a unique band structure; the valence and conduction bands form conic shapes whose tips meet at the K points. This peculiar band structure is shown in figure 3.2.

The linear dispersion relation at the K points implies that the electrons will have zero effective mass, since the effective masses are given by the curvature of the energy bands. The equation describing the propagation of these massless electrons is identical to the Dirac equation for massless fermions which travel at a constant speed close to the speed of light. This is why the connection points of the cones are also called Dirac points. The high conductivity in graphene is a consequence of this property of massless electrons travelling at speeds close to the speed of light.

In the case of undoped graphene the valence band is completely occupied and the conduction band completely empty, therefore the Fermi level is situated at the Dirac points where the two bands meet. Since the valence and conduction bands of graphene touch but do not overlap, graphene is termed as a zero bandgap semiconductor. This implies that irrespective of its energy, an incident photon can be absorbed by graphene.

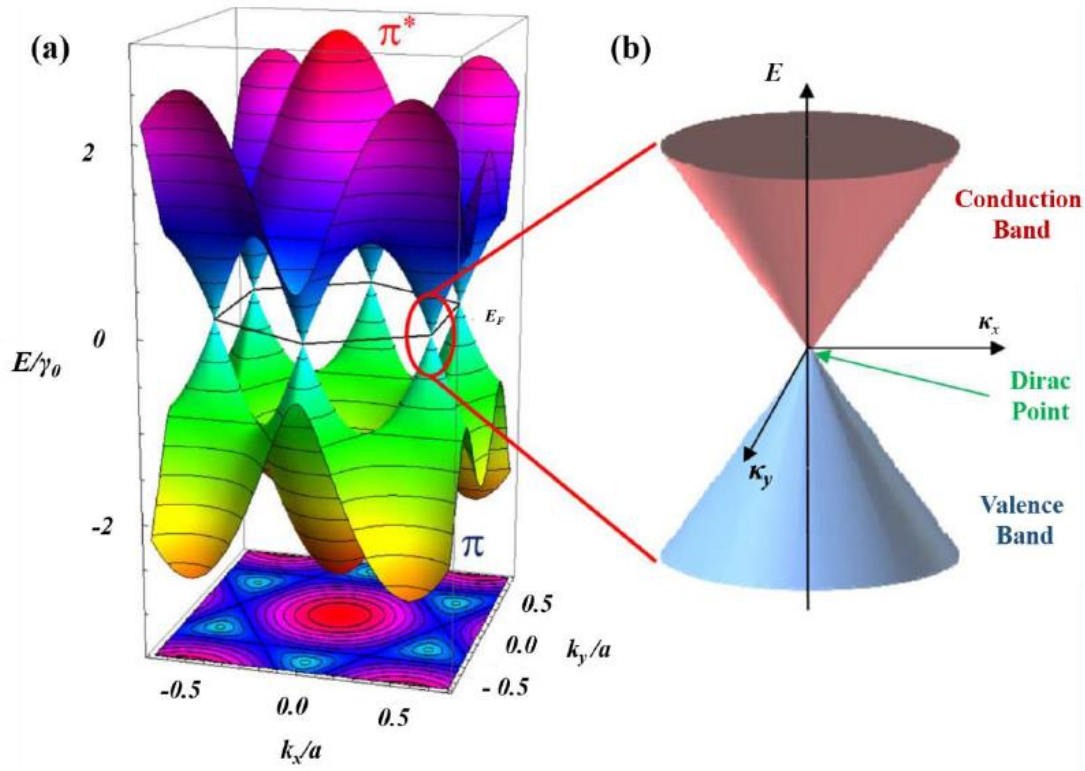

Figure 3.2. Band-structure of graphene. (a) Dispersion relation showing the valence and conduction bands meet at 6 points termed as K points or Dirac points. (b) Zoomed in view of the Dirac point demonstrating the conical shape of the valence and conduction bands (reproduced from [86]).

Graphene has a number of remarkable properties resulting from this unique band-structure. Its tensile strength, mechanical stiffness and elasticity are supreme [87]. It can sustain current densities six orders of magnitude higher than that of copper [88] and shows record thermal conductivity [89]. Despite being only one atom thick, graphene absorbs photons with the same efficiency, $\pi\alpha \approx 2.3\%$ of the incident light, over a wide range of wavelengths spanning from UV to THz [90]. Here α is the fine structure constant and is given by $\alpha = e^2/\hbar c \sim 1/137$ [91]. As can be seen the absorption of ~*2.3%* per graphene layer is universal since it is only determined by the universal physical constants $e, \hbar$ and c.

The aforementioned is only a small number of graphene's exceptional material and optoelectronic properties. The most relevant ones for the realisation of nonlinear optical

devices and applications are the properties associated to saturable absorption, two-photon absorption and nonlinear refraction, therefore they were extensively studied in this thesis.

The saturation in optical absorption makes graphene ideally suited for passive mode-locking of lasers. Therefore, it made graphene very popular amongst nonlinear optics groups since it has led to its utilisation as a saturable absorber medium for mode-locked and Q-switched lasers [8, 9, 86]. The two-photon absorption property of graphene is also of great importance. This property causes the transmission through graphene to decrease, leading to an optical limiting (OL) effect, which can find use in power limiting applications [5], as well as optical sensors and human eye protection [92, 93]. Furthermore, the TPA has to be considered when designing graphene based saturable absorbers for laser mode-locking. More specifically the TPA processes increase the non-saturable losses in the system, reducing the efficiency of the mode-locking. Therefore, the knowledge of the TPA coefficients is essential and must be taken into account for the efficient design of SA devices. Graphene has also been shown to present a giant nonlinear refraction in the orders of $\sim 10^{-13} - 10^{-11} m^2 W^{-1}$ [10, 11]. This extremely high refractive nonlinearity suggests that the figure of merit of graphene for nonlinear optics applications may be highly favourable. Of great interest in the work undertaken in this thesis is the integration of graphene with planar waveguiding structures for the realisation of relevant devices, such as mode-locked waveguide lasers [9], as well as waveguide switching [94] and sensing [95] devices. This motivated the extensive investigation of the nonlinear optical properties of graphene related to saturable absorption, two-photon absorption and nonlinear refraction.

3.2.1. Saturable absorption

Saturable absorption is a nonparametric nonlinear optical process where high field irradiances can decrease the absorption coefficient of a material. This process is irradiance dependent and therefore means that higher irradiances will experience higher transmission through the material. This can often lead to full material transparency. The irradiance dependent absorption coefficient, $\alpha(I)$, for a saturable absorbing material can be defined as [32]:

$$\alpha(I) = \frac{\alpha_0}{1+\frac{I}{I_{sat}}} \tag{3.1}$$

where α_0 is the linear absorption coefficient of the material, I is the field irradiance and I_{sat} is the saturation irradiance of the material. For a two-level saturable absorbing system I_{sat} is defined as:

$$I_{sat} = \frac{h\nu}{\sigma\tau} \tag{3.2}$$

where $h\nu$ is the photon energy, σ is the absorption cross section and τ is the excited state life-time. The most widespread application of saturable absorbing materials is their utilisation in the passive mode-locking of lasers [50]. Here it should be noted that although saturable absorption is a complicated process, it can be described by the behaviour of a simple two-level system which can serve as an analogy to the band structure of a given material, allowing for the individual material's nonlinear properties to become apparent. Moreover, in the case of graphene, due to the analogy between the Dirac equation, which describes the propagation of the electrons near the Dirac points, and two-level systems [96] a big number of models based on two-level systems have been developed to study the saturable absorption behaviour of graphene [97-100].

It is exactly this saturable absorption property of graphene that made it very popular amongst nonlinear optics groups, since it has led to its utilisation as a saturable absorber medium for mode-locked and Q-switched lasers [8, 9, 86]. Saturable absorption in graphene is a consequence of Pauli blocking, when carriers generated because of strong optical excitation lead to the depletion of the valence band and the filling of the conduction band, preventing additional absorption. This process is depicted in figure 3.3.

Figure 3.3(a) shows the linear scaling of the size of the gap between the valence and conduction bands (not the band gap) with respect to the Dirac point, showing that graphene can readily absorb photons over a wide range irrespective of their energy. For an incident photon of energy $h\nu$, there is always an electron-hole pair in resonance leading to absorption and promotion of the electron from the valence to the conduction band. This is depicted in figure 3.3(b). Afterwards, the excited in the conduction band electron loses

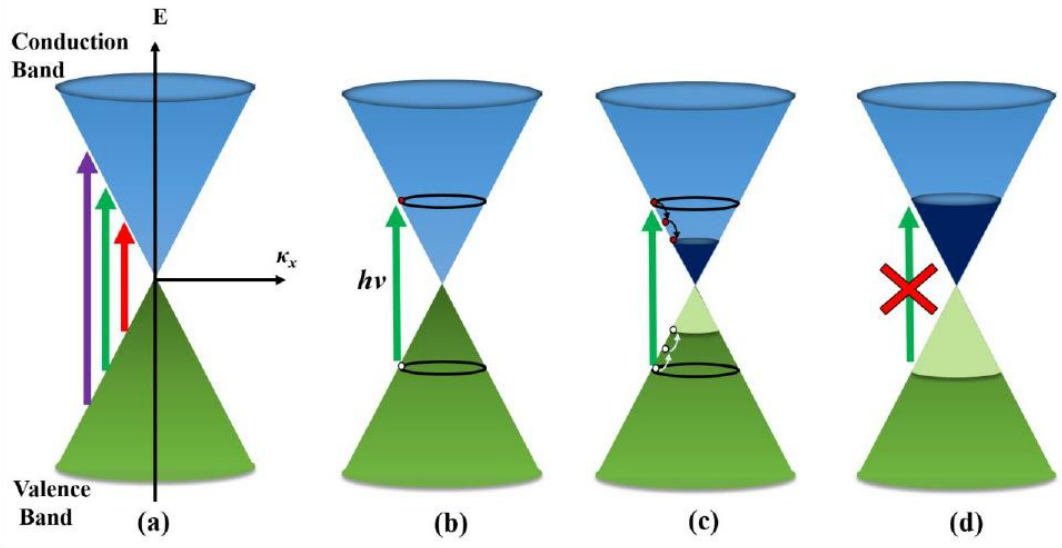

Figure 3.3. The saturable absorption in graphene. The blue and green cones represent the conduction and valence bands respectively. (a) The linear dispersion relation in graphene indicating that graphene can absorb photons in a wide range irrespective of their energy. The solid arrows of different colours indicate different frequencies of incident light. (b) Absorption of an incident photon of energy hv, resulting in the excitation of an electron from the valence to the conduction band. (c) Intraband decay within the valence and conduction bands, therefore leaving room for further absorption of incident photons of the same energy, hv. (d) Absorption saturation in graphene, as a result of the depletion of the valence band and the filling of the conduction band. Consequentially a photon of energy hv, can no longer be absorbed, therefore it will be transmitted through the material (reproduced from [45]).

energy by intraband collisions or intraband decay and migrates to lower energy levels within the same band. A similar process occurs within the valence band for holes. The carriers, electrons and holes, first lose energy by collisions with other carriers. This is then followed by collisions with the lattice, resulting in decay to lower energy levels. This intraband decay process, illustrated in figure 3.3(c), prevents the decay of the excited electrons back into the valence band but meanwhile allows the absorption of more photons of the same energy *hv*, leading to the excitation of more electrons from the valence to the conduction band. When the irradiance is sufficiently increased in order for a substantial number of electrons to be promoted to the conduction band such that all the

lower energy states in the conduction band become full of electrons and all the lower energy states in the valence band become full of holes, the absorption of light at the given photon energy saturates. No further absorption can take place, since by Pauli's exclusion principle no two identical carriers can occupy the same quantum state. This is shown in figure 3.3(d) and in practical terms it means that the photon can no longer be absorbed, therefore it will pass through the graphene causing the transmittance to increase.

The photo-excited ultrafast carrier dynamics in graphene, revealing the ultrafast relaxation phenomena, have been studied extensively. After photo-induced excitation electrons will be promoted from the valence to the conduction band, creating a non-equilibrium ensemble of electrons and holes (figure 3.3 (b)). Thereupon, two timescales are associated with the intraband relaxation of the non-equilibrium photo-generated carriers. An initial fast relaxation time, usually denoted as τ_1, due to electron-electron scattering forming a hot Fermi-Dirac distribution is followed by a slower relaxation time, usually denoted as τ_2, due to electron-phonon scattering which will further cool the thermalized electrons. These intraband relaxations are depicted in figure 3.3 (c). After that, interband relaxations will take place with electron-hole recombination dominating the process until the equilibrium of electron and hole distribution is restored. However, these relaxations describe the case of linear absorption under low excitation irradiance. As the excitation irradiance is increased, the concentration of the photo-generated carriers will increase as well and therefore cause all the lower energy states in the valence and conduction bands to fill, blocking further absorption. This will lead to the transparency of graphene which was phenomenologically described in the previous paragraph and depicted in figure 3.3.

The first report in the intraband relaxation times of graphene was in 2008 by the group of Cornell University. In that work, ultrafast optical pump-probe spectroscopy was used to gain insight and measure the ultrafast carrier dynamics in epitaxial graphene [61]. They measured the fast relaxation times, τ_1, in the range of 70-120 fs, whereas they measured the slow relaxation times, τ_2, in the range of 0.4-1.7 ps range. In a follow up experiment the same group, using optical-pump Terahertz-Probe spectroscopy managed to measure the interband electron-hole recombination times as well [62]. They measured the fast relaxation times, τ_1, of epitaxial graphene in the range of 10-150 fs, whereas they

measured the slow relaxation times, τ_2, in the range of 0.15-1 ps range. The electron-hole recombination times were measured in the range of 1-15 ps and were found to be carrier density dependent. It was also proposed that the mechanisms responsible for electron-hole recombination in graphene could include Plasmon emission, phonon emission, and Auger scattering.

After that initial work, ultrafast optical pump, terahertz [101, 102] or mid-infrared [103, 104] probe spectroscopy was conducted to study the carrier dynamics in epitaxial graphene near the Fermi-Dirac point at different ambient temperatures (10 K – 300 K). Moreover, the ultrafast carrier kinetics in exfoliated and CVD graphene were also studied [105-107]. The results of those studies are relatively consistent with each other, with the fast relaxation times, τ_1, due to carrier-carrier scattering always ranging from some tens to a few hundreds of fs and the slow relaxation times, τ_2, due to carrier-phonon scattering ranging from a few hundreds of fs to 1-2 ps. The discrepancies in the carrier relaxation times between different studies are mainly due to the substrate effect and possibly defects in the graphene lattice induced by the fabrication processes or extensive use of the samples.

3.2.2. Two-photon absorption

Two-photon absorption is another important nonlinear optical process. In the case of TPA the material can simultaneously absorb two photons of identical or different frequencies in order to excite an electron from one state (usually the ground state) to higher electronic states. In the presence of only TPA the irradiance dependent nonlinear absorption coefficient, $\alpha(I)$, presented in equation 2.19 is reduced to

$$\alpha(I) = \alpha + \beta I \tag{3.3}$$

The TPA coefficient β is a macroscopic parameter characterising the TPA properties of a material and is related to the imaginary part of the third order susceptibility by [108]:

$$\chi_{Im}^{(3)} = (n_0^2 \varepsilon_0 c\lambda/3\pi)\beta \tag{3.4}$$

where n_0 is the linear refractive index of the material, ε_0 is the free space electric permittivity and λ is the wavelength.

Under strong laser illumination graphene can present two-photon absorption. This process follows the saturable absorption process in graphene and is presented in figure 3.4, which can be considered as a continuation of figure 3.3.

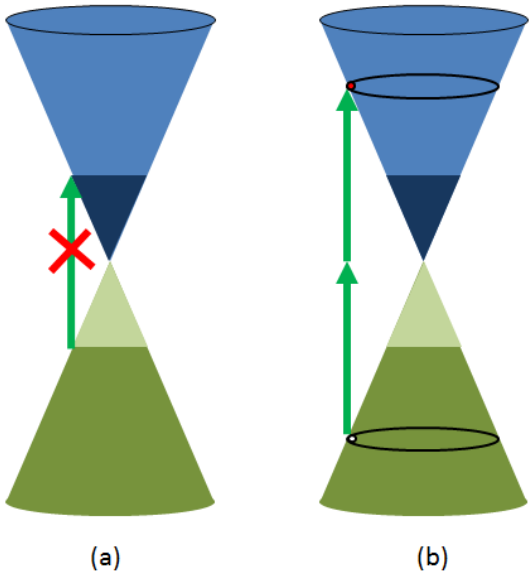

Figure 3.4. The two-photon absorption process in graphene. The blue and green cones represent the conduction and valence bands respectively. (a) The absorption saturation in graphene also presented in figure 3.3(d) and repeated here for purposes of continuity. (b) Two-photon absorption in graphene, showing the simultaneous absorption of two photons in order for an electron to be promoted from the valence to the conduction band.

As already discussed, at a high irradiance regime the absorption saturates due to the depletion of the valence band and the filling of the conduction band; this was presented in figure 3.3(d) and is repeated in figure 3.4(a) for the purposes of continuity. If the irradiance is further increased, two-photon absorption in graphene takes place. This process is illustrated in figure 3.4(b) and as can be seen during the TPA process two photons are absorbed simultaneously combining their photon energies, *hv*, in order to excite an electron from the valence to the conduction band. Thereupon the same intraband decay processes described in the previous section will take place within the valence and

conduction bands, therefore leaving room for further TPA at the same photon energy. This causes the transmission through the sample to decrease leading to an optical limiting effect, which can find use in power limiting applications [5], as well as optical sensors and human eye protection [92, 93].

3.2.3. Nonlinear refraction.

Aside its saturable absorption and two-photon absorption properties, under strong laser illumination graphene also exhibits a nonlinear phase shift due to nonlinear refraction. The concept of the irradiance-dependent refractive index has already been discussed in section 2.3.1 and the nonlinear refractive index coefficient, n_2, has been derived. Furthermore, the effect of the nonlinear refraction property of a material on a focussed beam as this is translated through the focus was discussed in detail in section 2.4.

Interestingly graphene presents giant nonlinear refraction. Z-scan measurements revealed that the nonlinear refraction of few-layer graphene is in the orders of $\sim 10^{-13} - 10^{-11}\, m^2 W^{-1}$ [10, 11]. Furthermore broadband four-wave mixing in few-layer graphene has been reported [6]. That work allowed the determination of the absolute value of the third order susceptibility for a single graphene layer, $\left|\chi_{gr}^{(3)}\right| \simeq 1.5 \times 10^{-7}\ esu$, approximately 8 orders of magnitude larger than bulk dielectrics. This exceptionally large value leads to the irradiance dependence of the nonlinear optical refraction in graphene also reported in [10, 11]. More specifically, at the high irradiance regime and as the irradiance is increased above a certain threshold, aside from $\chi_{gr}^{(3)}$ higher order odd terms of the nonlinear susceptibility, such as $\chi_{gr}^{(5)}$, $\chi_{gr}^{(7)}$ and so on, become significant leading to the irradiance dependence of the nonlinear refraction. Therefore, making the conventional n_2 coefficient unsuitable to describe the nonlinear refraction since it is only related to the $\chi_{gr}^{(3)}$ term of the nonlinear susceptibility. In this case a low irradiance regime can be discriminated, where the conventional Kerr nonlinear refractive index n_2 can be deduced, from a high irradiance regime where the nonlinear response becomes irradiance dependent. In this thesis the latter is defined as irradiance-dependent nonlinear refraction and the symbol $\tilde{n}\ (I)$ is used.

Furthermore, the nonlinear refraction of graphene is proposed to be negative. This negative refraction property is pointed out in [94] by performing a theoretical analysis, but no experimental measurements were made to confirm it. Moreover controllable optical negative refraction in graphite thin films, by performing pump probe experiments has been reported [28]. In that work they illuminated a graphite thin film with two counter-propagating pump beams, and demonstrated the negative refraction of a third probe beam. But due to the complexity of the technique, could not be unambiguously verified whether the negative refraction arose from the graphite films or the two counter-propagating beams forming a phase conjugating surface on the graphite films.

The work undertaken in this thesis unambiguously verified the negative nature of graphene's nonlinear refraction. The negative nonlinear refraction is observed in CVD single and multilayer graphene, as well as graphene poly-vinyl alcohol composites, by exploiting the simplicity of the Z-scan technique which employs a single beam in contrast with reference [28] which involves 3 different beams. Furthermore, as discussed in section 2.4 the sign of the nonlinear refraction can be readily observed with the Z-scan technique by performing a single closed-aperture measurement.

3.3. Z-scan measurements in single layer graphene

The laser system used to perform the Z-scan measurements in single layer graphene (SLG) was the IMRA® FCPA μJewel D400 laser system outlined in section 2.8.1. This was favoured over the OPA system because of the extreme stability it offers regarding the output power. Due to the extremely small thickness of single layer graphene the effect upon the transmittance when performing Z-scan measurements will be very small. Therefore, the OPA system was deemed unsuitable to carry out this delicate and sensitive work due to its output power fluctuations.

The centre wavelength of this system was at 1045 nm. The pulse repetition rate was chosen to be 500 kHz and the pulse width was set to 359 fs. The output was then directed to the Z-scan setup described in section 2.6.1 with the difference of bypassing the spatial filter since the output of the IMRA® was already Gaussian. The beam was focussed with a 25 cm focal length AR coated lens to a spot size of 33 μm. The focal spot size was

measured using the scanning knife-edge technique. This technique allows for the measurement of the beam size in respect to z-position, including the focal spot size, enabling the calculation of the irradiance along the beam path. The calculated spot size of the beam along z and the fitted Gaussian beam profile are shown in figure 3.5.

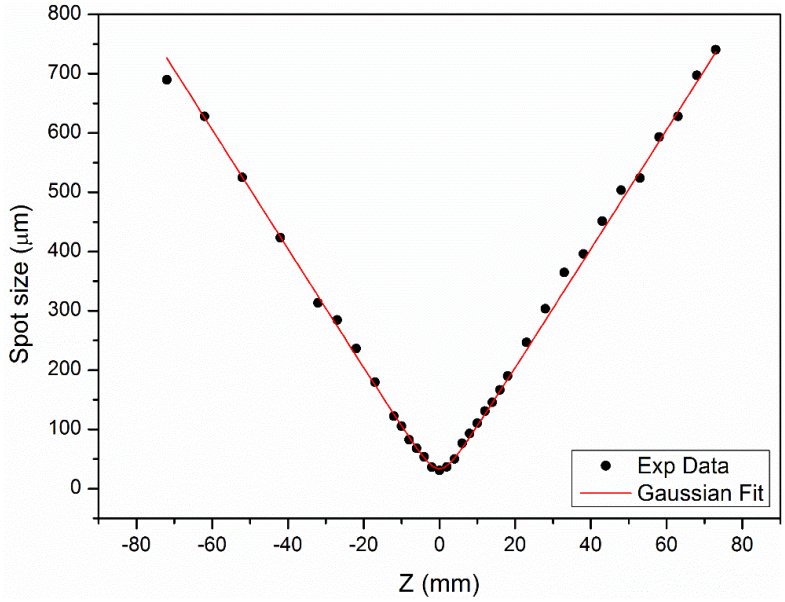

Figure 3.5. Beam width measurements (black data points) measured along z-axis fitted to the equation for a Gaussian curve with a beam waist of 33 ± 2 μm.

The single layer graphene was synthesized by a chemical vapour deposition method (CVD) [109, 110], yielding a high purity and quality oxygen-free SLG sample. This sample was provided by the Department of Physics of the National University of Singapore. Before the Z-scan measurements were performed, Raman spectra of the SLG sample were collected. The Raman spectra were collected on different positions (at least 10) on the SLG sample. The D, G, and 2D peaks of graphene were identified, verifying the quality and homogeneity of the SLG. Figure 3.6 shows two Raman spectra, one of the SLG on the silica substrate and one of only the silica substrate. As can be seen the contribution of the silica substrate (black) is apparent on the Raman spectrum of the SLG (red). Nevertheless, the G and 2D peaks of graphene are clear and easily observable, but the D peak cannot be readily distinguished due to the contribution of the silica substrate. In order to eliminate the contribution of the substrate, the Raman spectrum of the silica

substrate was subtracted point by point from the Raman spectrum of the SLG. This yielded figure 3.7, at which the D, G, and 2D peaks of graphene are easily identified.

At this point it should be noted that the ratio of the I_{2D}/I_G is not equal to 2 which is a standard condition for identifying single-layer defect-free graphene via Raman spectroscopy. This is attributed to the fact that there might be some defects in the graphene lattice from the extensive use of the specific sample, or quite possibly the effect of the silica substrate on the Raman spectra might contribute to this discrepancy. The specific sample was characterised and the single-layer nature of graphene was verified via reflection contrast spectroscopy, micro-Raman spectroscopy and NIR one-photon absorption spectroscopy by our collaborators at the Department of Physics of the National University of Singapore before being provided to us. More details about the characterisation techniques can be found in [111].

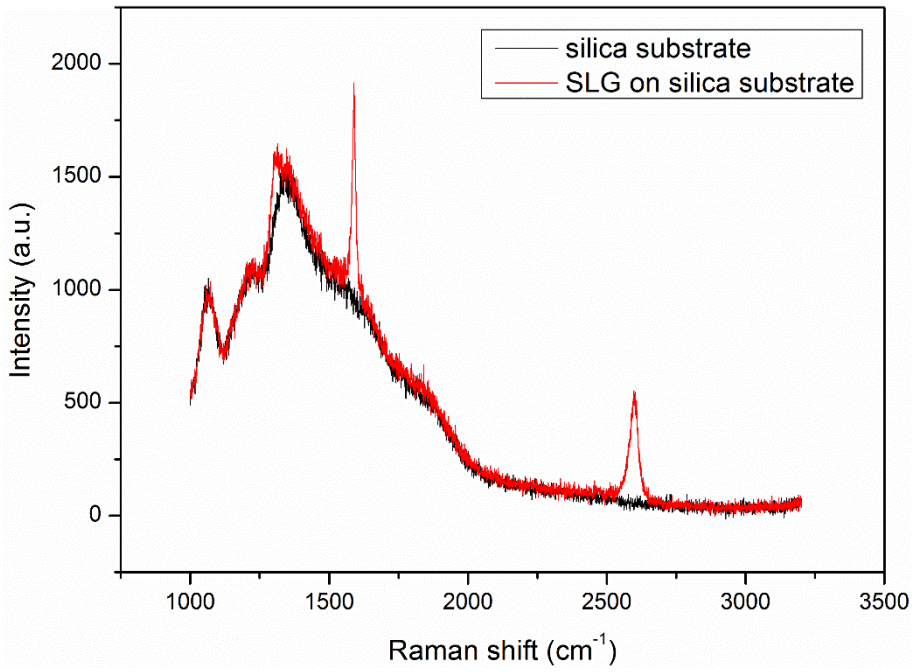

Figure 3.6. Graph showing the Raman spectra of the silica substrate (black) and the SLG on the silica substrate (red), illustrating the contribution of the substrate in the Raman spectrum.

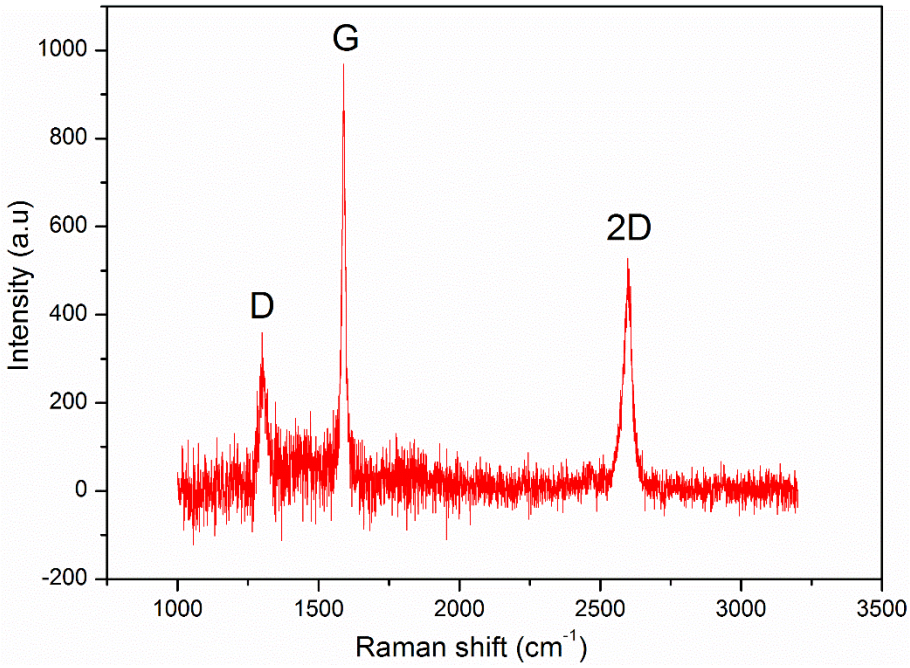

Figure 3.7. Graph showing the Raman spectrum of SLG after the point by point subtraction of the substrate Raman spectrum. The D, G and 2D peaks of graphene are easily observable.

3.3.1 Saturable absorption measurements

The effects of saturable absorption for the SLG were observed for a range of pulse energies spanning from 1 to 540 nJ, corresponding to irradiances of 0.081 to 44 GW/cm^2. The irradiance versus normalised transmittance is plotted in figure 3.8, showing the evolution of saturable absorption with incident on the sample irradiance. This figure was obtained by combining the results from individual open-aperture Z-scan traces performed at different pulse energies and therefore different irradiances. As already mentioned, open-aperture Z-scans were performed in a range of irradiances from 0.081 to 44 GW/cm^2. For each of the Z-scan traces the transmittance rise at the focus was recorded. Thereupon by combining the results from each of these Z-scans, information about the transmittance rise at the focus at different irradiances were obtained, enabling the plot of irradiance versus normalised transmittance, producing figure 3.8. The black dots correspond to the experimental data while the red solid line corresponds to the theoretical fit. As can be seen the magnitude of the saturable absorption is increasing with input irradiance until the transmittance through the sample reaches a constant value of ~1.023

which corresponds to the universal absorption of ~*2.3%* per graphene layer. At the highest irradiances used, ~44 GW/cm^2, there were no evidence of TPA which is in agreement with previous work reporting that TPA in single layer graphene is negligible [112].

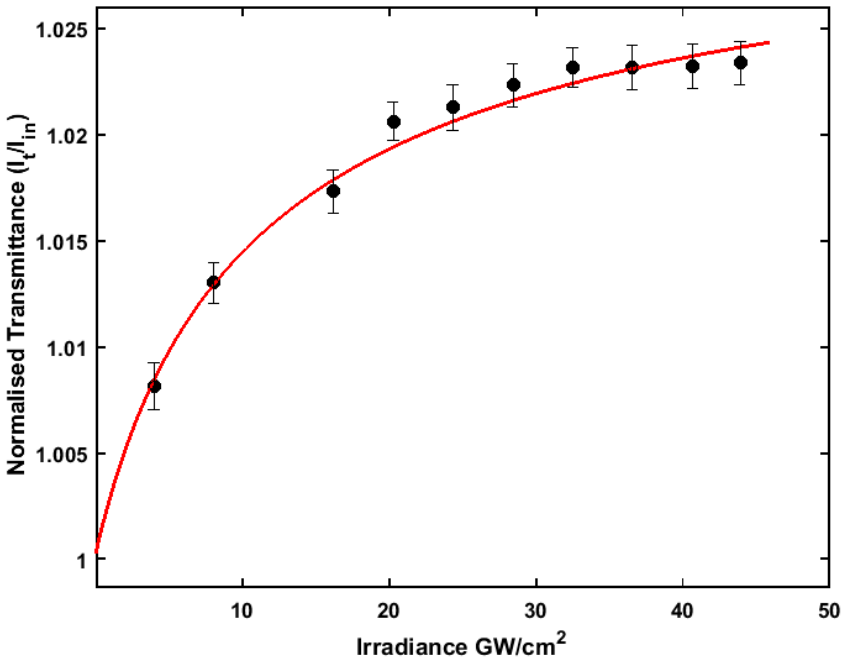

Figure 3.8. Change in transmittance with input irradiance for single layer graphene. The black dots correspond to the experimental data, whereas the solid red line represents the theoretical fit.

The theoretical fit is obtained by solving the differential propagation equation 2.18 after considering the irradiance dependent absorption coefficient, *α(I)*, for a saturable absorbing medium; this is presented in equation 3.1. The propagation equation was solved using the method proposed in [59], where the normalised transmittance is the product of the transmitted over the incident irradiance (I_t/I_{in}). This is also denoted on the y-axis label of figure 3.8. However, in literature it is common practice to label the y-axis just as normalised transmittance. Therefore, from now on the y-axis in figures plotting Z-scan results along the body of the thesis will be labelled as 'Normalised Transmittance'.

The saturation irradiance, I_{sat} is extracted from the transmission numerical fit of figure 3.8. This yielded a saturation irradiance of I_{sat}=5.2 ± 1.7 GW/cm^2 for the graphene

monolayer. The obtained value for the saturation irradiance of the graphene monolayer is in very good agreement with the values reported in [112] for single- and bilayer graphene prepared with the same CVD method as the sample used in this study and investigated via Z-scan. In that work they measured a saturation irradiance of 6 and 1.5 GW/cm^2 at the wavelengths of 780 and 1100 nm respectively for bilayer graphene, whereas the values obtained for single layer graphene at the same wavelengths were 8 and 1.5 GW/cm^2. In another work the saturation irradiances for a range of multilayer CVD graphene samples consisting of 5 to 20 layers were investigated in wavelengths from 435 to 1100 nm via Z-scan and found to range from 2.3 to 21 GW/cm^2 [111]. The saturable absorption of epitaxial graphene was also studied via Z-scan at 800 nm and was measured to be around 4 GW/cm^2 [113].

Due to the extensive use of graphene as a saturable absorber for laser mode-locking there is a large number of reports on the saturation irradiance of graphene. These were acquired for different types of samples and using different methods, with most of them deduced from the pulsed behaviour of the laser which they were used to mode-lock. Therefore, these values vary quite a lot with each other spanning a range from ~0.5 to ~400 MW/cm^2. In [97] they deduced the saturation irradiance of CVD graphene used to mode-lock a fibre laser by adapting a two-level model to the case of graphene. The saturation irradiances were found to vary from 0.61 to 0.71 MW/cm^2 when the number of graphene layers was varied from 3 to 10. In a different work, performing simple transmission measurements in CVD graphene and using a two-level saturation model the saturation irradiances were found to be from 0.585 to 0.75 MW/cm^2 for samples with 1 to 7 layers of graphene [98]. The saturable absorption of exfoliated graphene measured by depositing the graphene layers on a fibre core revealed saturation irradiances from 90 to 380 MW/cm^2 for samples with 8 to 30 graphene layers [114]. In a number of other studies, the saturation irradiances of different graphene products such as graphene oxides, graphene dispersions or graphene-polymer composites were found to range between 7.89 to 266 MW/cm^2 [115-117].

When using graphene as a saturable absorber for laser mode-locking, the pump irradiance must be low in order to ensure that no TPA processes, which would increase the non-saturable losses in the system and impede mode-locking, are taking place. This leads the

saturation irradiances deduced from the mode-locked operation of lasers in literature to be lower than the ones measured in this work via Z-scan where the input irradiances were sufficiently increased in order to measure and quantify the full SA and TPA capabilities of the samples of question.

3.3.2 Nonlinear refraction measurements

Similarly to the case of saturable absorption, the nonlinear refraction properties of the SLG were studied via closed-aperture Z-scans for pulse energies ranging from 1 to 100 nJ, corresponding to irradiances of 0.081 to 8.14 GW/cm^2. The range of pulse energies used enabled the experimental study of the irradiance dependence of the nonlinear refraction of graphene as discussed in section 3.2.3. Furthermore, the closed-aperture Z-scans verified the negative value of the nonlinear refraction property in graphene. Figure 3.9 shows a plot of irradiance versus the irradiance-dependent nonlinear refraction $\tilde{n}(I)$.

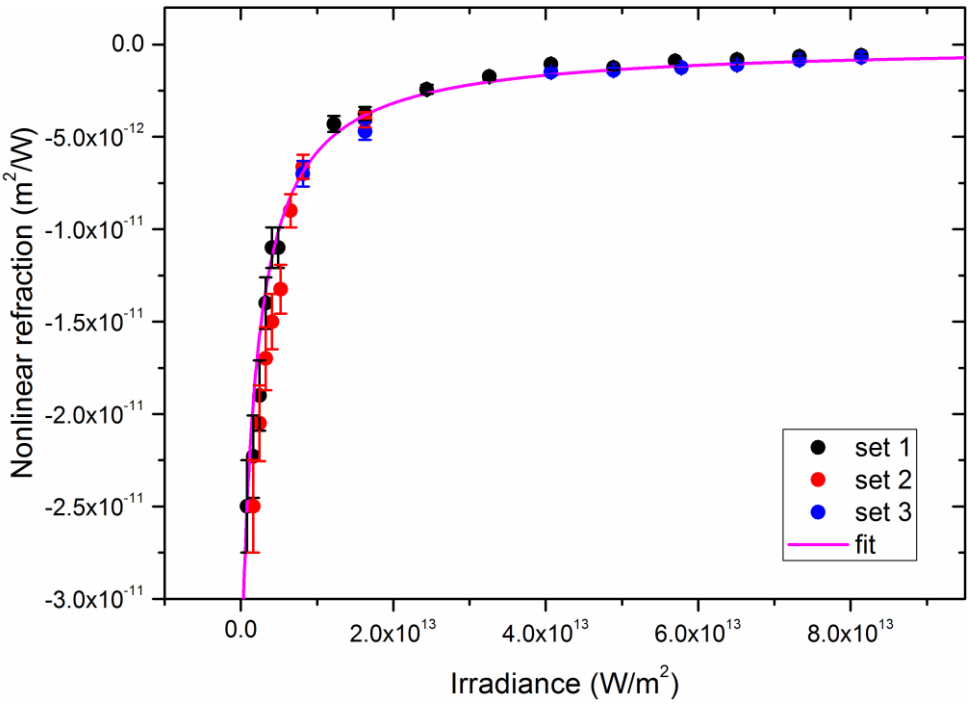

Figure 3.9. Change in nonlinear refraction with input irradiance for single layer graphene. The dots represent the experimental data acquired on three different spots on the graphene monolayer, whereas the solid line represents the theoretical fit. The dashed black line represents the saturation Irradiance I_{sat} for the nonlinear refraction.

The closed-aperture Z-scans performed at different were fitted using equation 2.21 presented in section 2.4. Here it is worth noting that equation 2.21 is a simplified fitting formula derived to calculate n_2 in the case that only $\chi_{gr}^{(3)}$ is present, whereas as discussed in section 3.2.3 the nonlinear refraction in graphene is irradiance-dependent due to the contribution of higher order odd terms of the nonlinear susceptibility. The exact modelling in the high irradiance regime where the nonlinear response becomes irradiance dependent would require us to take into account $\chi_{gr}^{(3)}$ and higher orders of the nonlinear susceptibility, such as $\chi_{gr}^{(5)}$ and so on. However, from the experimental data an effective irradiance-dependent nonlinear refractive index $\tilde{n}(I)$ can be derived by fitting each of the closed-aperture Z-scan traces with the simplified closed-aperture fitting formula of equation 2.21. Thereupon by combining the values obtained from the fitting of each of the closed-aperture Z-scan traces acquired at different irradiances figure 3.9 was created, which can give useful indications about the trend of the nonlinear refraction with increasing irradiance. The same method was used in [11] to investigate the irradiance dependence of 3-layer CVD graphene.

Closed-aperture Z-scans were performed on three different spots on the SLG sample in order to assure the quality and validity of the measurements. These are denoted in figure 3.9 as sets 1 to 3 and are represented with different colours. From the figure it can be seen that the nonlinear refraction increases with increasing irradiance (or decreases if we consider it in absolute values) until it reaches a constant value of $\tilde{n}(I) \approx -9 \times 10^{-13}\ m^2/W$ for $I > 4\ GW/cm^2$. The same irradiance dependence of the nonlinear refraction in 3-layer CVD graphene also investigated via Z-scan was observed in [11].

The Kerr nonlinear refractive index n_2 and the saturation irradiance I_{sat} are deduced by fitting the experimental data of figure 3.9. The irradiance-dependent nonlinear refraction $\tilde{n}(I)$, can be defined as:

$$\tilde{n}(I) = \frac{n_2}{1+\frac{I}{I_{sat}}} \tag{3.5}$$

where n_2 is the nonlinear refractive index, I is the field irradiance and I_{sat} is the saturation irradiance for the nonlinear refraction. This equation results from the semiconductor Bloch equations adapted to the dispersion of graphene [118]. The line of best fit by using equation 3.5 yields $n_2 = (-3.5 \pm 0.6) \times 10^{-11}\ m^2/W$ and $I_{sat} = 0.2 \pm 0.05\ GW/cm^2$. This in practical terms means that at irradiances below $0.2\ GW/cm^2$ the nonlinear phase $\Delta\Phi$ does not saturate, therefore the nonlinear refraction is not irradiance dependent and can be described by the conventional refractive index coefficient; which in this case is $n_2 = -3.5 \times 10^{-11} m^2/W$, in very good agreement with the reported n_2 values for graphene, which are in the order of $\sim 10^{-11} m^2/W$ [11]. In a more recent work investigating the nonlinear refraction of single-layer CVD graphene via two different methods, the optical Kerr effect method and the Z-scan technique, at the telecommunication wavelengths the reported values for the nonlinear refractive index coefficient were $n_2 = -1.1 \times 10^{-13}\ m^2/W$ with the optical Kerr effect method and $n_2 = -2 \times 10^{-12}\ m^2/W$ with the Z-scan technique [119]. More experimental studies performed via Z-scan present discrepancies regarding both the sign and magnitude of n_2 with the reported values spanning a range of two orders of magnitude from $\sim 10^{-13} - 10^{-11}\ m^2/W$ [120, 121]. In addition, disagreements regarding the sign and magnitude of n_2 in graphene also exist in theoretical works. Chatzidimitriou et al. performed a detailed comparison between some theoretical works to conclude that there is a considerable degree of disagreement between them in terms of both the magnitude and the sign of n_2 [122]. It is exactly these discrepancies that create the need for additional experimental works in order to fully understand and quantify the refractive nonlinearity of graphene.

Moving on to discuss the irradiance dependence of the nonlinear refractive index, as the irradiance is increased starting from $I > I_{sat} = 0.2\ GW/cm^2$, the change in nonlinear phase saturates due to the contribution of the higher order odd terms of the nonlinear susceptibility as discussed in section 3.2.3. Therefore, at this high irradiance regime the nonlinear refraction of graphene is described by the irradiance-dependent nonlinear refraction coefficient $\tilde{n}(I)$. The saturation Irradiance I_{sat} for the nonlinear refraction is denoted in figure 3.9 with the straight dashed line and as can be seen only 3 data points are at irradiances $I < I_{sat}$, while the majority of the data points lie in the oversaturation regime. Furthermore, by considering the asymptotic horizontal line that goes through

$n_2 = -3.5 \times 10^{-11} m^2/W$ (not shown on graph), none of the data points lie in the area defined by I_{sat} and n_2.

If one wants to measure the nonlinear refraction before entering the oversaturation regime, Z-scan measurements at lower irradiances must be performed. The closed-aperture Z-scans here were performed at pulse energies as low as 1 nJ and were limited by the detection ability of the instruments. In order to obtain lower irradiances with the specific experimental setup, one must either focus the incident beam to larger focal spots or increase the laser repetition rate. If the choice of increasing the repetition rate is preferred, care must be taken to exclude the contribution of thermal effects that would lead to misleading results.

Here we performed a thermal analysis to verify that no thermal effects manifested at the used repetition rate of 500 kHz. The thermal analysis was performed by Eitan Abraham, a collaborator of the NLO group. The same thermal analysis was also used to study the heat accumulation and thermal damage of the graphene-polymer composites treated in chapter 4, therefore is presented in section 4.4.2 for the purposes of completeness.

3.4. Z-scan measurements in multilayer graphene

Similarly to the case of single layer graphene, the multilayer graphene sample was synthesized by the same CVD method [109, 110] again yielding an oxygen-free sample and was also provided by the Department of Physics of the National University of Singapore. The multilayer graphene was characterised by optical microscopy, Raman and absorption spectroscopy. This work was performed at the Department of Physics of the National University of Singapore; more detailed results and analyses regarding the characterisation of the graphene sample can be found in [111]. The graphene thickness was determined to be 5-7 layers.

Before the Z-scan measurements were performed, Raman spectra of the multilayer graphene sample were collected and the D, G, and 2D peaks of graphene were identified. Due to the multiple layers in this sample, the Raman signal of the graphene was considerably stronger than the case of the single layer graphene, therefore the contribution

of the substrate in this case was negligible. A Raman spectrum of the 5-7 layer graphene is presented in figure 3.10, without performing a substrate subtraction.

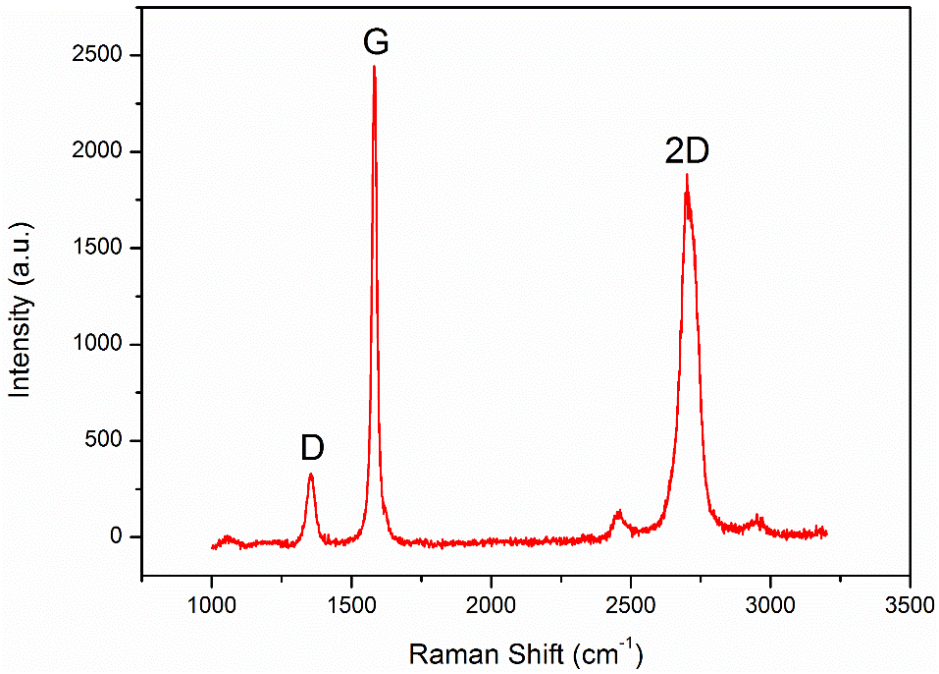

Figure 3.10. Graph showing the Raman spectrum of 5-7layer graphene. The D, G and 2D peaks of graphene are easily observable.

The system used for the Z-scan measurements on the multilayer graphene was the OPA system outlined in section 2.5. Open- and closed-aperture Z-scan measurements were carried out in a broad mid-infrared range spanning ~ 1250 nm, taking advantage of the wide wavelength tuneability of the OPA system. The measurements were carried out at 4 different wavelengths, namely: 1150, 1550, 2000 and 2400 nm. The output of the OPA was directed to the Z-scan setup described previously in section 2.6.1. The beam was focussed with a 20 cm focal length CaF_2 lens and the focal spot size for each wavelength was measured using the scanning knife-edge technique. It was found to be 25 μm at 1150 nm, 26 μm at 1550 nm, 28 μm at 2000 nm and 31 μm at 2400 nm. The estimated error from the fitted Gaussian profile was ± 2 μm for all wavelengths. The calculated spot size of the beam along z and the fitted Gaussian beam profile for the wavelength of 1550 nm are shown in figure 3.11.

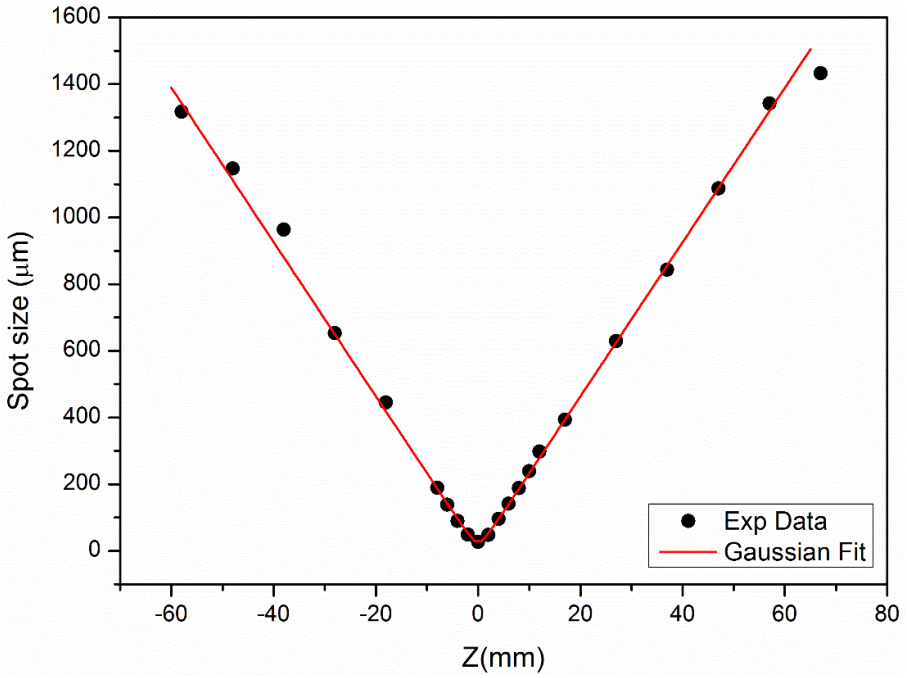

Figure 3.11. Beam width measurements (black data points) measured along z-axis fitted to the equation for a Gaussian curve with a beam waist of 26 ± 2 μm for the wavelength of 1550 nm.

3.4.1 Saturable absorption and two-photon absorption measurements

The effects of saturable and two-photon absorption for the 5-7 layer graphene were observed for pulse energies ranging from 2 to 300 nJ which corresponded to irradiances from ~1 GW/cm^2 to ~100 GW/cm^2. The open-aperture measurements showed that the transmittance had a power dependence characteristic of saturable absorption in the relatively low-irradiance regime. As the input irradiance was increased, a rise in transmittance occurred due to saturable absorption, which was followed by a decrease in transmittance due to TPA.

The competing SA and TPA processes can be seen in figure 3.12 in which five consecutive Z-scans performed at a wavelength of 1550 nm with increasing pulse energies, namely: 50, 75, 100, 150 and 200 nJ, are presented. At the low pulse energy of 50 nJ, as the sample was translated through the focus of the beam, only a rise in transmittance was observed due to SA. However, as the pulse energy was further increased a small valley started to form on top of the transmittance peak indicating the

onset of TPA. At 75 nJ the peak of the transmittance, which was highly confined to the focal region of the beam, started to flatten out suggesting the onset of TPA. Whereas at the higher pulse energies starting from 100 nJ a dip was clearly observed in the transmittance peak verifying the TPA process. As the pulse energy was increased the dip in transmittance became more prominent. The 75 nJ which can be seen as the onset of the TPA corresponds to an irradiance of 35.3 GW/cm^2.

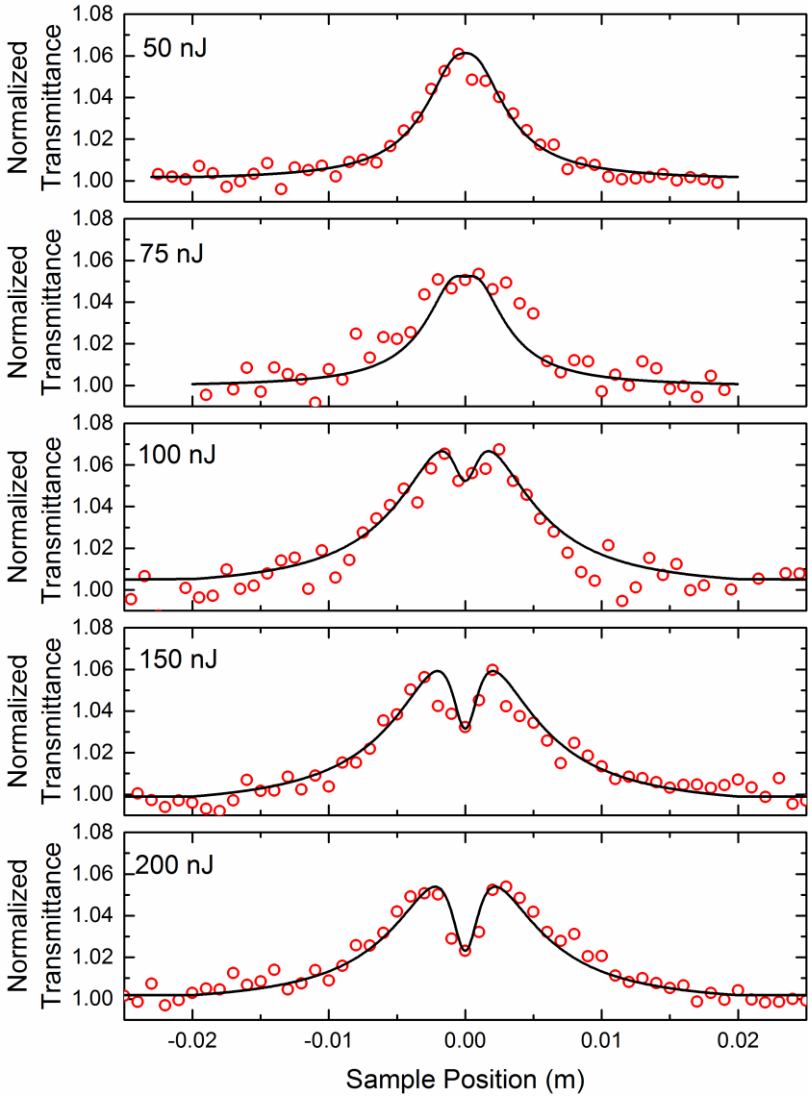

Figure 3.12. Open-aperture Z-scan traces conducted at 5 consecutive pulse energies at a wavelength of 1550 nm showing the competing saturable absorption and two-photon absorption processes. At the low pulse energy of 50 nJ only saturable absorption is present, whereas at the higher pulse energies starting from 75 nJ and onwards the two-photon absorption process is evident.

Figure 3.12 also illustrates one of the main advantages of the Z-scan technique in respect with other experimental methods of measuring optical nonlinearities, such as wave mixing [6] or interferometric [54] techniques. Z-scan is a fast and elegant way to discriminate the SA from TPA process in graphene and investigate the threshold at which SA turns to TPA. This information is essential when designing graphene based saturable absorbers for laser mode-locking because if the TPA threshold is crossed the non-saturable losses in the system increase and therefore mode-locking cannot be achieved.

The irradiance versus normalised transmittance along with the theoretical fits for all wavelengths is shown in figure 3.13. In order to obtain this figure, open-aperture Z-scan traces of different pulse energies, and therefore different irradiances, were combined. More specifically for each of the wavelengths open-aperture Z-scans were performed at a range of pulse energies from 2 to 300 nJ or in terms of irradiance from ~1 GW/cm^2 to ~100 GW/cm^2. Then the ΔT at the focus of each of the traces was recorded and combined in order to create figure 3.13. ΔT is denoted as the difference between the transmittance at the focus where the irradiance is at maximum and sufficiently away from the focus where no nonlinear effects take place, therefore the transmittance is non-varying.

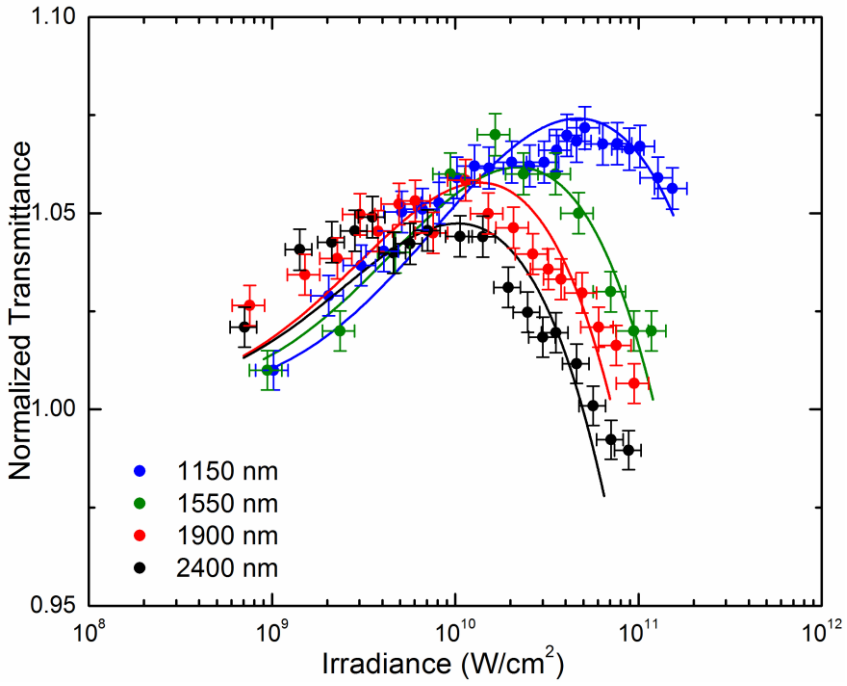

Figure 3.13. Change in transmittance with input irradiance at 1150, 1550, 1900 and 2400nm (dots) with the corresponding theoretical fits (solid lines).

The theoretical fits are obtained by solving the differential propagation equation 2.18 after considering the irradiance dependent absorption coefficient, *α(I)*, for a medium that presents both saturable absorption and two-photon absorption. This is given by the equation [112]:

$$\alpha(I) = \frac{\alpha_0}{1+\frac{I}{I_S}} + \beta I \tag{3.6}$$

where α_0 is the linear absorption coefficient, I_{sat} is the saturation irradiance and β is the TPA coefficient. Inspecting equation 3.6 one can deduce that the first and second terms describe SA and TPA processes respectively. The TPA coefficient β and the saturation irradiance I_{sat} are extracted from the transmission numerical fits of figure 3.13. In the numerical simulation for the best fit, the α_0 parameter used is extracted from the linear transmission spectra of the sample at each of the operating wavelengths. The fitting results are shown in table 3.1.

Table 3.1. Nonlinear coefficients

Wavelength	**α_0 (m^{-1})**	**β (cm/GW)**	**I_{sat} (GW/cm^2)**
1150 nm	5.87×10^7	$(0.38 \pm 0.08)\times10^4$	4.5 ± 1.5
1550 nm	5.64×10^7	$(0.9 \pm 0.23)\times10^4$	3 ± 1
1900 nm	5.59×10^7	$(1.5 \pm 0.37)\times10^4$	2.1 ± 0.7
2400 nm	5.045×10^7	$(1.9 \pm 0.48)\times10^4$	1.9 ± 0.63

The saturation irradiances obtained for multilayer graphene are in very good agreement with the values reported in [111, 112] for bilayer and multilayer CVD graphene, also showing the same decreasing trend with wavelength. A more detailed discussion and comparison regarding the saturation irradiances reported in literature is performed in section 3.3.1.

The 2PA coefficient β shows a small dependence on the wavelength, increasing with longer wavelengths. The same trend was observed in [112] where they reported giant TPA in bilayer graphene in the orders of $1\times10^4 - 2\times10^4$ cm/GW in good agreement with our reported values. In addition, the TPA coefficient of 5-layer CVD graphene was found to be 1.6×10^4 cm/GW at 1100 nm.

From figure 3.13 it can be seen that with increasing wavelength the decrease in transmittance is more prominent, suggesting that there is a more significant contribution from TPA due to the lower photon energy. More specifically, at the highest irradiances investigated in this work, ~100 GWcm^{-2}, the transmittance decreased to about 0.99 for the case of 2400 nm while for the case of 1150 nm the decrease only reached 1.05. This trend is also seen in the coefficients of table 3.1. With increasing wavelength, the saturation irradiance is decreased, whereas the TPA coefficient is increased. As expected this increasing TPA trend with wavelength will lower threshold for the onset of TPA with longer wavelengths. The onset of TPA at each of the wavelengths was found to be:

Table 3.2. Onset of TPA

Wavelength	**Onset of TPA GW/cm^2**
1150 nm	76.4 ± 8.8
1550 nm	35.3 ± 4.6
1900 nm	20.8 ± 3.9
2400 nm	10.2 ± 2.1

3.4.2 Nonlinear refraction measurements

The effects of nonlinear refraction of the 5-7 layer graphene sample were also investigated. The nonlinear refraction trend with irradiance was investigated using the IMRA® laser system outlined in section 2.8.1 exploiting its output power stability and its ability to reach sufficiently low irradiances by tuning the repetition rate. On the other hand, the nonlinear refraction trend with wavelength was investigated with the OPA laser system exploiting its broad wavelength tuneability.

The closed-aperture Z-scan measurements performed with the OPA laser system at four different wavelengths, namely 1150, 1550, 1900 and 2400 nm, at the same irradiance of ~22 GW/cm^2 are presented Figure 3.14. The low repetition rate of the OPA system combined with its output power fluctuations did not allow for reliable closed-aperture Z-scans at sufficiently low irradiances before entering the nonlinear phase shift saturation regime, therefore the Z-scans were performed in the oversaturation regime of the nonlinear phase shift. More specifically the irradiance used here is approximately two

orders of magnitude higher than the nonlinear phase saturation irradiance. Hence the Z-scans performed with the OPA system measure the irradiance-dependent nonlinear refraction. The closed-aperture Z-scans performed here verified the negative value of the nonlinear refraction and most importantly they revealed the trend of the nonlinear refraction with wavelength for the 5-7 layer graphene. The theoretical fits in figure 3.14 use equation 2.21 presented in section 2.4.

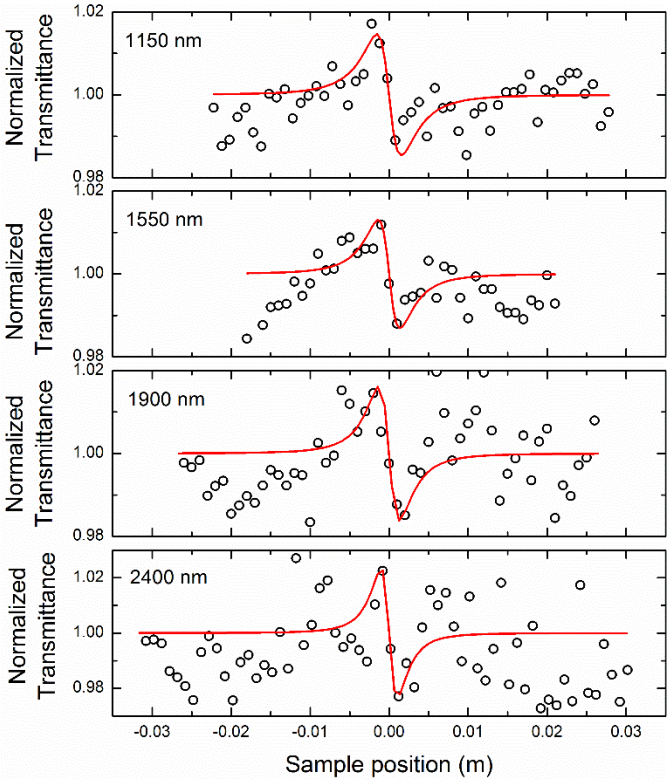

Figure 3.14 Closed-aperture Z-scan traces at 1150, 1550, 1900 and 2400 nm at an irradiance of ~22 GWcm^{-2} with the corresponding theoretical fits.

As can be seen from figure 3.14 the experimental data are quite dispersed, especially at the longer wavelengths of 1900 and 2400 nm. This is attributed to the extremely small thickness of the graphene sample which gives a weak nonlinear response as well as the output power fluctuations of the OPA system, which are more prominent at the longer wavelengths where the conversion efficiency of the BBO crystal is reduced. Therefore, when performing the closed-aperture Z-scan measurements extreme care was taken in order to avoid collecting any unreliable data which would lead to discrepancies in the obtained coefficients from the numerical fitting. First and foremost, the “peak”- “valley”

variation of the experimental data due to nonlinear refraction will lie exactly at the focus of the beam where the irradiance is highest; this behaviour was illustrated graphically in figure 2.4. Hence, any experimental data presenting a "peak"- "valley" behaviour even 1 mm away from the focus were discarded. Moreover, the "peak"- "valley" spatial separation for a closed-aperture Z-scan was deduced by Sheik-Bahae to be $\Delta Z_{p-v} \simeq 1.7 Z_0$, where Z_0 is the Rayleigh range. The closed-aperture Z-scans collected for the graphene sample which did not fulfil this requirement were discarded as well. Therefore, by following the above approach the quality of the experimental data and consequently the validity of the nonlinear coefficients deduced from the numerical fitting were ensured.

The values of the irradiance-dependent nonlinear refraction obtained from the fit for each wavelength are presented in table 3.3. As can be seen graphene presents giant irradiance-dependent nonlinear refraction in the order of $\sim 10^{-13}\ m^2W^{-1}$, which decreases with increasing wavelength. The broad range at which the work was undertaken revealed the trend of the nonlinear refraction in graphene versus wavelength at a wide range spanning ~1250 nm.

Table 3.3. Intensity dependent nonlinear refraction coefficient $\tilde{n}(I)$

Wavelength	$\tilde{n}(I)$ **(cm^2/GW) at 22 GWcm^{-2}**
1150 nm	-0.55 ± 0.06
1550 nm	-0.8 ± 0.07
1900 nm	-1.4 ± 0.13
2400 nm	-2.5 ± 0.26

The irradiance dependence of the nonlinear refraction, which was discussed in section 3.2.3, was studied with the IMRA® laser system for pulse energies ranging from 1 to 90 nJ, which corresponded to irradiances of 0.081 to 7.33 GW/cm^2. This study is shown in figure 3.15 which plots Irradiance versus the irradiance-dependent nonlinear refraction $\tilde{n}(I)$ for the 5-7 layer graphene. This plot demonstrates both the irradiance dependence and negative value of graphene's nonlinear refractive index. From the figure it can be seen that the nonlinear refraction increases with increasing irradiance (or decreases if we consider it in absolute values) until it reaches a constant value of $\tilde{n}(I) \approx -1 \times 10^{-13}\ m^2/W$ for $I > 2\ GW/cm^2$.

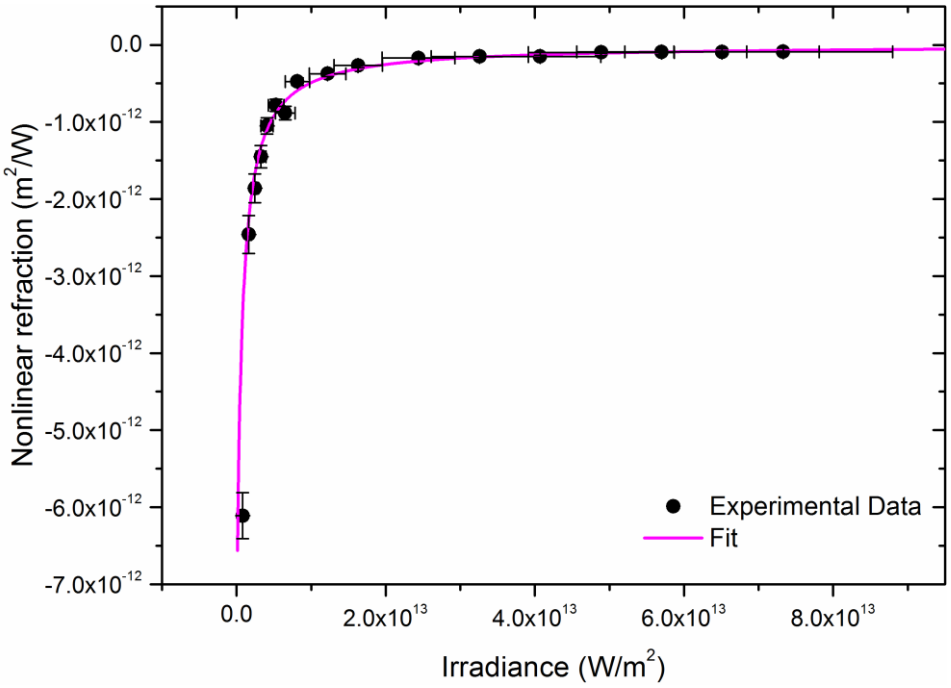

Figure 3.15. Change in nonlinear refraction with input irradiance for 5-7 layer graphene. The dots represent the experimental data, whereas the solid line represents the theoretical fit.

The Kerr nonlinear refractive index n_2 and the saturation irradiance I_{sat} are deduced by fitting the experimental data of figure 3.15 using equation 3.5 presented in section 3.3.2. The line of best fit yields $n_2 = (-7.5 \pm 1.12) \times 10^{-12}\, m^2/W$ and $I_{sat} = 0.07 \pm 0.018\, GW/cm^2$. Similar to the case of the SLG, this means that at irradiances below $0.07\ GW/cm^2$ the nonlinear phase shift $\Delta\Phi$ does not saturate, therefore the nonlinear refraction is described by the conventional n_2 coefficient which is also deduced from the fit. Whereas for irradiances $I > I_{sat} = 0.07\ GW/cm^2$ the nonlinear phase saturates, hence the nonlinear refraction becomes irradiance dependent.

Comparing with the case of the SLG, investigated in section 3.3.2, one can see that both, the saturation irradiance and n_2 coefficient in absolute values are lower for the 5-7 layer graphene. More specifically the I_{sat} and n_2 for the SLG were found to be $I_{sat} = 0.2\ GW/cm^2$ and $n_2 = -3.5 \times 10^{-11}\, m^2/W$, whereas for the 5-7 layer were found to be $I_{sat} = 0.07\ GW/cm^2$ and $n_2 = -7.5 \times 10^{-12} m^2/W$. The differences between the refractive nonlinearities for the two samples can be seen in figure 3.16 which

plots the irradiance versus the irradiance-dependent nonlinear refraction $\tilde{n}(I)$ for both SLG and 5-7 layer graphene on the same axes. Figure 3 .16 (a) plots the measured nonlinear refraction values versus irradiance, whereas figure 3.16 (b) plots the absolute values of the nonlinear refraction in logarithmic scale making the differences between the refractive nonlinearities of the two samples more clear. The error bars have been omitted from these graphs in order to maintain the clarity of presentation and make the comparison between the two samples easier.

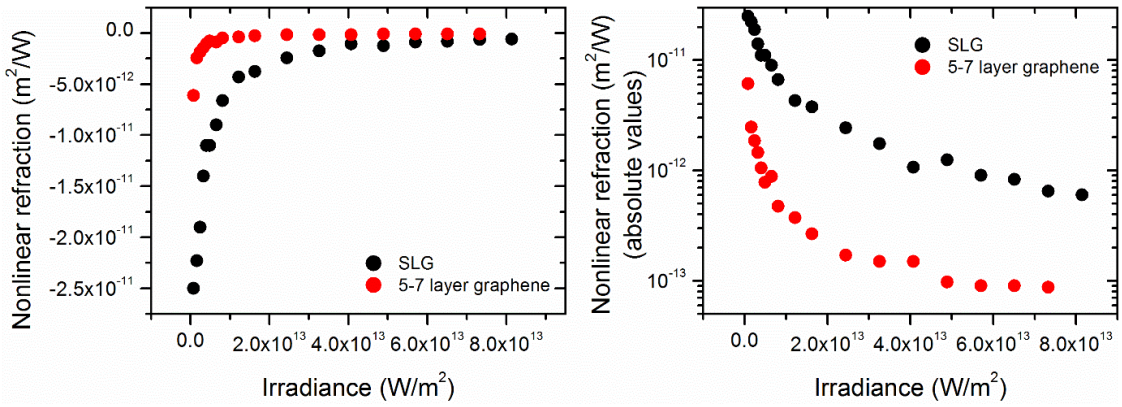

Figure 3.16. (a) Change in nonlinear refraction with input irradiance for SLG (black dots) and 5-7 layer graphene (red dots). (b) Absolute values of nonlinear refraction with input irradiance for SLG (black dots) and 5-7 layer graphene (red dots) plotted in logarithmic scale.

As can be seen from figure 3.16 (a) the irradiance dependent nonlinear refraction presents the same saturating trend for both samples with increasing irradiance, whereas the absolute values of the nonlinear refraction shown in 3.16 (b) are higher for the SLG than the 5-7 layer graphene during the whole range of irradiances used for this investigation. This indicates that the n_2 coefficient will be higher for the SLG sample as well which was verified from the fitting results of the nonlinear refraction for the two samples. Furthermore, the saturation irradiance deduced from the theoretical fits for each case, was found to be lower for the case of the 5-7 layer graphene which means that the 5-7 layer graphene enters the nonlinear phase saturation regime earlier than the SLG. In addition, for comparison purposes, a detailed discussion regarding the nonlinear refraction of graphene reported in literature is performed in section 3.3.2.

3.4.3 Theoretical analysis

The open- and closed-aperture Z-scan measurements revealed some very interesting features of graphene's optical nonlinearities. The most fascinating and novel findings of this study were the irradiance dependent and negative value of graphene's nonlinear refraction. Therefore, we deemed it important to perform a theoretical analysis to support the validity of the experimental findings. The theoretical analysis was performed by Fabio Biancalana and Eitan Abraham, two collaborators of the NLO group, and was adapted to the case of the 5-7 layer graphene sample whose nonlinear optical properties were experimentally investigated via Z-scan and presented in sections 3.4.1 and 3.4.2. Special emphasis was given to the interpretation of the irradiance dependence and negative nature of the nonlinear refraction. Furthermore, the theoretical expression for wavelength dependence of the saturation irradiance is presented and compared with the experimental findings. A theoretical analysis regarding the two-photon absorption trend with wavelength was regarded unnecessary since it has been extensively investigated elsewhere [111, 112].

The theoretical analysis performed here arises from the conductivity of the graphene monolayer which is usually written for monochromatic waves; however, one can perform useful estimates with it, even in the case of short pulses. The analytical expression of the complex linear conductivity $\sigma(\omega)$ of a graphene monolayer is known from Falkovsky's work [123]:

$$\sigma(\omega) = \frac{ie^2(2k_BT)}{\pi\hbar^2(\omega + i\gamma_1)}\left[\frac{E_F}{2k_BT} + \log\left(2e^{-\frac{E_F}{k_BT}} + 1\right)\right]$$
$$+\frac{e^2}{4\hbar}\left\{\frac{1}{2} + \frac{1}{\pi}\arctan\left[\frac{\hbar(\omega+i\gamma_2)-2E_F}{2k_BT}\right]\right\} - \frac{i}{2\pi}\log\left\{\frac{[\hbar(\omega+i\gamma_2)-2E_F]^2}{[\hbar(\omega+i\gamma_2)-2E_F]^2+(2k_BT)^2}\right\} \quad (3.7)$$

where T is the temperature, k_B is the Boltzmann constant, E_F is the Fermi energy (chemical potential), γ_1 and γ_2 are the inverse relaxation times [124]. At zero temperature, $T = 0$, and in the case of photoexcited undoped graphene where $E_F = 0$, the equation for the conductivity is reduced to

$$\sigma(\omega) = \sigma_0 = \frac{e^2}{4\hbar} \tag{3.8}$$

Equation 3.8 is obtained from equation 3.7 simply by setting $T = 0$ and $E_f = 0$, without the requirement of any mathematical iterations or any other form of approximations or simplifications. This is purely real, and equal to the value for the universal conductivity of a monolayer graphene.

Equation 3.7 can be generalised to the nonlinear case and for a multilayer graphene made of *N* layers. The multilayer here was basically treated as a single layer with an effective thickness such that the linear absorption coefficient α_0, which is due to the *N* graphene layers plus the substrate, matches the experimentally observed one over the range of wavelengths at which the Z-scan measurements were performed. Therefore, the values for the inverse relaxation times were taken to be $1/\gamma_1 \approx 400$ fs and $1/\gamma_2 \approx 20$ fs, in order to fit the measured values of the linear absorption coefficient α_0, for the 5-7 layer graphene presented in table 3.1. These values are effective and strongly depend on the number of layers and the type of substrate employed. In the case of photoexcited undoped graphene the Fermi energy vanishes, $E_F = 0$, therefore the relation between the complex linear susceptibility and the conductivity in the multilayer graphene sample is simply taken to be

$$\chi(\omega) = \frac{iN\sigma(\omega)}{\varepsilon_0 \omega d_{\text{eff}}} = \chi' + i\chi'' \tag{3.9}$$

where d_{eff} is the effective thickness of the multilayer, which represents the combined thickness of each graphene layer in the multilayer and the contribution from the substrate. In our estimates we assumed *N=7* layers, since the theoretical analysis was adapted to the case of the multilayer graphene sample which was measured to have 5-7 graphene layers. We found that $d_{eff} \approx 8d$, where *d = 0.33 nm* is the monolayer graphene thickness, fits well with the experimental absorption data.

Using the full nonlinear susceptibility (that can be derived by solving the rate equation of the semiconductor Bloch equations [118]) which is given by:

$$\chi(\omega) = \frac{iN\sigma(\omega)}{\varepsilon_0 \omega d_{\text{eff}}} \frac{1}{(1+\frac{I}{I_{sat}})} \tag{3.10}$$

in which the denominator is common to all rate equations based on two-level systems, the irradiance-dependent nonlinear refractive index was obtained

$$n(I) + i\kappa(I) = \sqrt{1 + \chi(\omega)} \tag{3.11}$$

where $n(I)$ is the irradiance-dependent refractive index and $\kappa(I)$ is the irradiance-dependent extinction coefficient responsible for absorption. The nonlinear refraction coefficient can be defined as $\tilde{n}(I) = {}^{\partial n}/_{\partial I}$. This coefficient has the same physical dimension of the conventionally used nonlinear refractive index n_2, but a different meaning: n_2 is a coefficient in the Taylor expansion of the nonlinear refractive index calculated at $I = 0$, which is independent of the irradiance. However, $\tilde{n}(I)$ is an irradiance-dependent function that gives the slope of the nonlinear refraction versus irradiance diagram, and is not connected to any perturbative expansion. A truncated Taylor expansion is not applicable on $\tilde{n}(I)$ since the experimental measurements of the nonlinear refraction were performed in the over-saturation regime $(I \gg I_{sat})$, where the nonlinearity is non-perturbative. As a consequence, any measurement of the nonlinear refraction in graphene will strongly depend on the particular irradiance used. Thus, under conditions of oversaturation, the nonlinear refractive index coefficients do not decrease, the conventional (truncated) Taylor series diverges, and the interpretation of the nonlinear refraction must be modified to take account for the irradiance dependence.

The calculated nonlinear refraction coefficient $\tilde{n}(I)$, both real and imaginary part, is plotted in figure 3.17 (b) against wavelength at 22 GWcm^{-2} along with the experimental values from table 3.3. It also worth noting that $\chi_{gr}^{(3)}$ and $\tilde{n}(I)$ can in general have the same or opposite signs, depending on the frequency; since $\chi_{gr}^{(3)}$ is complex, the relationship between them is not just a simple proportionality factor. The imaginary part of $\tilde{n}(I)$ is also negative, which is natural since nonlinearity reduces the linear losses due to the saturation process. Despite the fact that the TPA was neglected and the (continuous

wave) CW conductivity of equation 3.9 was used, it is remarkable to observe that the values extracted from the plot of figure 3.17 (b) are in excellent agreement with the experimentally measured nonlinear refraction coefficients presented in table 3.3.

Most importantly the theoretical analysis verified that the nonlinear refraction in graphene is negative for a broad range of wavelengths.

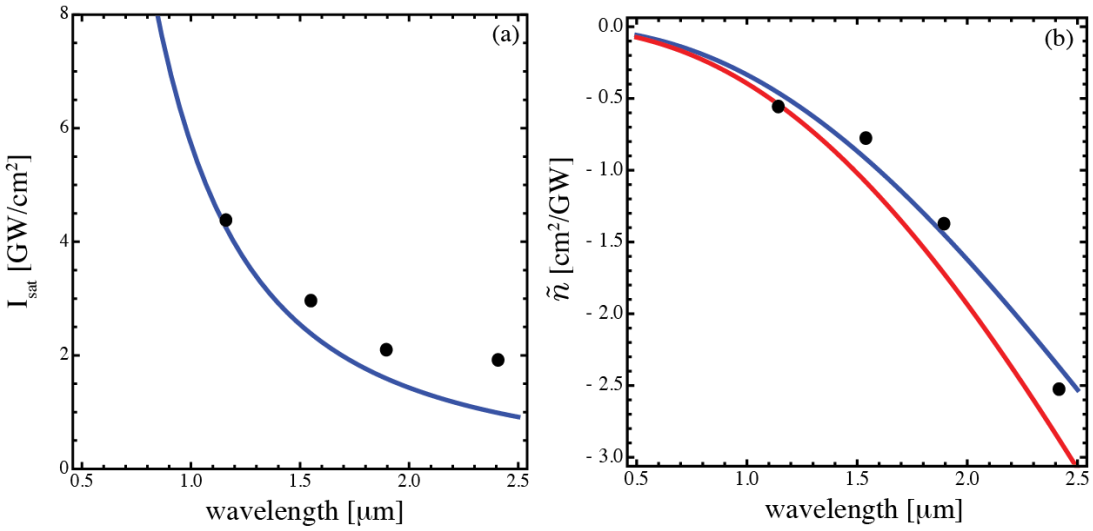

Figure 3.17. (a) Total saturation irradiance I_{sat} versus wavelength, in conditions of room temperature along with the experimental values from table 3.1 (black dots); (b) Real (blue line) and imaginary (red line) parts of the nonlinear refractive index versus wavelength at 22 GWcm^{-2} along with the experimental values from table 3.3 (black dots).

The theoretical expression for wavelength dependence of the saturation irradiance was derived as well. This was found by using the semiconductor Bloch equations [118] adapted to the graphene dispersion, and generalised for *N* layers. In particular, the rate equation (which is identical for the case of semiconductors and graphene, since it does not depend on the electronic dispersion [118]) gives the following formula:

$$I_{\text{sat}} = Nc\varepsilon_0\gamma_1\gamma_2\left(\frac{\hbar\omega}{ev_F}\right)^2 \tag{3.12}$$

where v_F is the Fermi velocity. The theoretical expression for wavelength dependence of I_{sat} is plotted in figure 3.17 (a) and qualitatively agrees well with the experimental values in table 3.1, also presented in figure 3.17 (a). The quantitative discrepancies observed with the experimental values are attributed to the fact that in the theoretical prediction the TPA is neglected and the CW approximation for the conductivity is used.

3.4.4 Laser induced damage in Graphene

The Z-scan measurements performed here also revealed the laser damage threshold of the 5-7 layer graphene with femtosecond pulses. As mentioned earlier in section 3.4.1, open-aperture Z-scan measurements were performed at pulse energies ranging from 2 to 300 nJ, enabling the investigation of SA and TPA. The reason that the open-aperture Z-scans were performed up to 300 nJ and not higher, was that at higher than 300 nJ pulse energies laser induced damage was observed. The laser damage was localised at the focus of the ultrafast beam. The onset of the laser induced damage at 300 nJ corresponds to a pulse fluence of 14.1 mJ/cm^2. This damage threshold is in excellent agreement with previously reported values regarding the femtosecond laser induced damage in CVD graphene [125]. The damage is attributed to the local modification and breaking of the sp^2-carbon bonds due to the ultrafast excitation and no thermal processes are involved in the damage mechanism. The laser damage threshold of graphene is referred in pulse fluence and not irradiance because it has been shown that when operating in the femtosecond regime, changing the pulse width does not show any important effects on the laser damage threshold [126]. Therefore, the irradiance could change even by an order of magnitude for producing similar material damage, while the fluence would remain constant.

Here the damage in graphene was observed while performing open-aperture Z-scan measurements. The damage occurred at high pulse energies starting from 300 nJ up to 650 nJ which corresponded to pulse fluences from 14.1 to 30.6 mJ/cm^2. At the higher pulse fluences used (30.6 mJ/cm^2) the graphene was completely ablated. The damage was verified by collecting Raman spectra from the irradiated with high pulse energy regions and comparing with the Raman spectra of the unirradiated regions. Figure 3.16 shows the Raman spectra from two regions, one outside of the laser-irradiated area and one within

the laser-irradiated, damaged graphene region. The 2nd Raman spectrum (red) was collected within the laser-damaged region of the inset picture of figure 3.16.

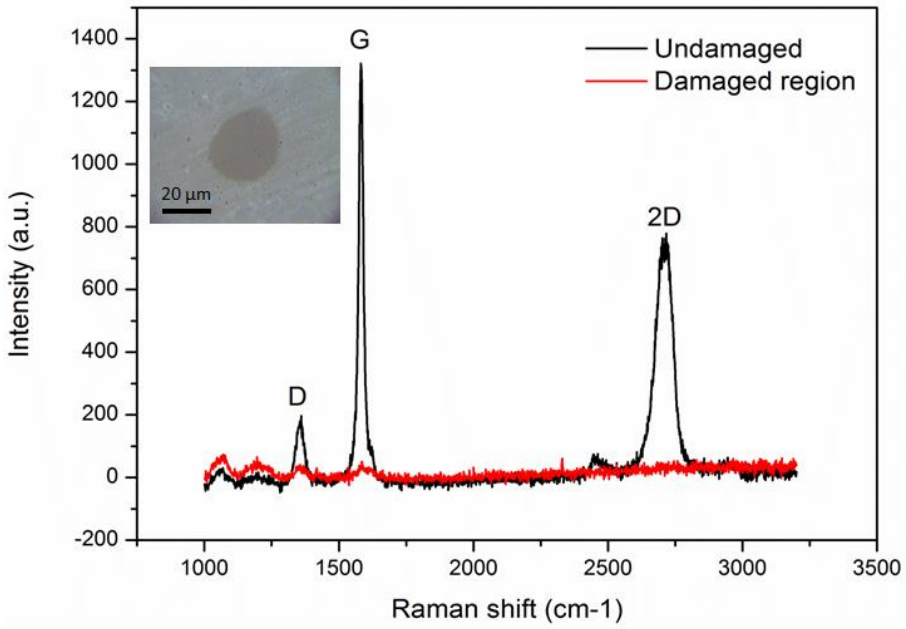

Figure 3.18 Two Raman spectra of 5-7 layer graphene. On unirradiated graphene showing the D, G and 2D peaks (black), on the laser-irradiated damaged region, not showing any of the distinct D, G and 2D peaks of graphene (red). Inset: a microscope picture of a laser-damage spot on graphene. The 2nd Raman spectrum (red) was collected within the laser-damaged region of the inset picture.

All the observed damage spots in the 5-7 layer graphene presented the same circular symmetry as the one depicted in the inset of figure 3.16, suggesting that the damage is well confined within the focal region of the beam. The diameters of the damage spots ranged from ~15 to 35 μm with the biggest damage spot of ~35 μm attributed to the highest pulse energy used, namely 600 nJ.

3.5 Nonlinear optical characterisation of graphene saturable absorber for laser mode-locking.

As outlined earlier in this thesis, the integration of graphene with bulk waveguiding structures for realising relevant devices is of particular interest. The work presented in this section is an ideal example of this synergy. A Tm:YAG waveguide laser was developed by Yingying Ren and Rose Mary, also members of the NLO group by employing the ULI technique. Thereupon mode-locked operation of the laser was demonstrated by integrating it with a graphene saturable absorber. In this section the nonlinear optical characterisation of the graphene saturable absorber used in that work is presented.

The nonlinear optical properties of a saturable absorber provide defining parameters about the absorber such as modulation depth, ΔR, non-saturable loss, ΔR_{ns}, and saturation fluence, F_{sat}. These parameters are very useful for characterising the lasers at which the saturable absorber is used as gain medium for mode-locking. The modulation depth represents the maximum change in optical absorption and is typically expressed in percentage of transmission or reflectivity, depending on the type of the device. The non-saturable loss is the amount of loss in the system, mainly due to scattering and non-saturable absorption. The saturation fluence represents the fluence required to cause significant absorption saturation. These parameters for a saturable absorber medium can be extracted from nonlinear absorption measurements, where the absorption or transmission of the saturable absorber is observed with respect to incident laser pulse fluence [99].

In the case of mirror based saturable absorbers such as Semiconductor Saturable Absorber Mirrors (SESAMs), where transmission studies are not possible, the device is characterised based on its reflectivity, otherwise it can be characterised based on its transmission. The characteristic parameters of the saturable absorber can be deduced by fitting its reflectivity (or transmission) versus pulse fluence curve. The fitting function is based on a travelling wave model that uses the rate equations for a two-level system, and is given as [99]:

$$R(F_p) = R_{ns}\frac{\ln\left[1+\frac{R_{lin}}{R_{ns}}(e^{S}-1)\right]}{S} \quad (3.13)$$

where S is the saturation parameter defined as $S=F_p/F_{sat}$. The modulation depth of the saturable absorber is derived as $\Delta R=R_{ns}-R_{lin}$, where R_{ns} is the reflectivity of the saturable absorber at absorption saturation and R_{lin} is the linear reflectivity. The non-saturable loss is defined as $\Delta R_{ns}=1-R_{ns}$. Equation 3.13 treats the reflectivity of a saturable absorber, but the same relationship can be applied when the transmission is considered.

The above described method was used to characterise a graphene film coated on a quartz substrate. This sample was provided from the Cambridge Graphene Centre, University of Cambridge, UK. The graphene sample was prepared by the Liquid Phase Exfoliation (LPE) method. More details about the preparation method can be found elsewhere in [8, 9].

The OPA laser system outlined in section 2.5 was used to perform the optical characterisation. The characterisation was performed on a transmission mode due to the nature of the sample. The output of the OPA was adjusted in order to produce an output with a central wavelength of 2 μm. The graphene sample was then placed at a fixed position at the focus of the Z-scan setup described in section 2.6.1, taking advantage of its existing alignment to the outputs of the OPA laser system. An AR coated Thorlabs 45:55 pellicle beam splitter was placed in front of the sample, thus enabling the simultaneous observation of the incident and transmitted pulse fluence. Then by using a variable ND wheel filter the incident pulse fluence was varied in incremental steps, enabling the investigation of the saturable absorption property of the sample. The transmittance versus incident pulse fluence is presented in figure 3.17.

The experimental data were fitted using the model function presented in equation 3.13. The line of best fit yields a saturation fluence ~58.97 μJ/cm^2, a modulation depth ~8.36% and non-saturable losses ~ 27.99%. These results were used to characterise a graphene based Tm:YAG waveguide laser at 2 μm and, including the figure, were published in Journal of selected topics in Quantum Electronics [9].

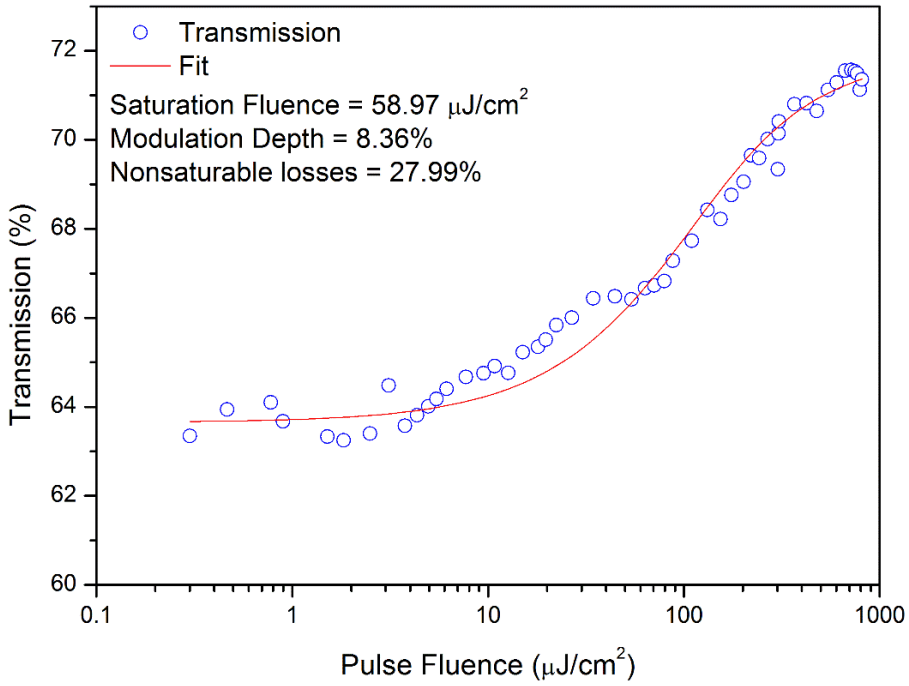

Figure 3.19. Transmittance versus incident pulse fluence for graphene saturable absorber at 2 μm, along with the theoretical fit (red solid line).

3.6 Summary

This chapter has presented the nonlinear optical characterisation of graphene. First an introduction into graphene's fundamental properties was performed and its unique band structure at the Dirac point which gives rise to graphene's remarkable optoelectronic properties was discussed. This lead to the detailed presentation of graphene's nonlinear optical properties related to saturable absorption, two-photon absorption and nonlinear refraction. Thereupon, the optical characterisation of CVD single and multilayer graphene by employing the Z-scan technique followed. The Z-scan measurements revealed a giant negative irradiance-dependent nonlinear refraction for both single and multilayer graphene in the orders of $\sim 10^{-13}\ m^2/W$. The irradiance-dependence of graphene's nonlinear refraction was extensively investigated on single layer graphene. This work enabled the determination of the nonlinear refractive index coefficient n_2 and saturation irradiance I_{sat} for the nonlinear phase shift $\Delta\Phi$. These coefficients were found to be $n_2 = -3.5 \times 10^{-11}\, m^2/W$ and $I_{sat} = 0.2\, GW/cm^2$. The competing saturable absorption and two-photon absorption processes were extensively studied in multilayer graphene over a broad range of wavelengths. The values obtained for the absorption

saturation irradiances of the multilayer graphene were in the order of $\sim 10^{-13}$ m^2/W, whereas the TPA absorption coefficients were in the order of $\sim 10^{-7}$ m$/W$. The experimental work was then followed by a theoretical analysis arising from the conductivity of the graphene monolayer, with special emphasis given to the interpretation of the irradiance-dependence and negative value of the nonlinear refraction. Moreover, the high irradiances employed in this work enabled the investigation of the laser induced damage of graphene. The damage was verified by performing Raman spectroscopy on the laser-irradiated damaged regions, where the absence of the distinct D, G and 2D peaks of graphene was observed. Finally the chapter concluded with the nonlinear optical characterisation of a graphene saturable absorber, which was used to characterise a graphene based Tm:YAG mode-locked waveguide laser at 2 μm.

Chapter 4. Nonlinear Optical Characterisation and Laser Induced Dynamic Thermal Damage in Graphene-Polymer composite films.

4.1. Introduction

This chapter presents the work performed on graphene-polymer composite thin films. It can be seen as consisted of two main sections. In the first section the optical characterisation of a graphene poly-vinyl alcohol (G-PVA) thin film via the Z-scan technique is performed. The relevant nonlinear optical properties related to saturable absorption, two-photon absorption and nonlinear refraction are investigated and the associated coefficients are derived at the operating wavelengths. The second section deals with the laser induced dynamic thermal damage in G-PVA thin films by ultrashort pulses. Two different damage mechanisms, depending on the laser repetition rate, are identified. At a high repetition rate regime, the light absorbed by graphene leads to its temperature rise and consequently to a heat inflow from the embedded graphene into the host polymer. This heat interchange procedure results in a temperature rise and eventually thermal damage of the host polymer. The damage threshold is found to be dependent on the graphene concentration in the host matrix. At the low repetition rate regime, the damage is due to the local modification of the carbon bonds inside the graphene lattice from the ultrafast pulses rather than heat diffusion from the embedded graphene and subsequent thermal damage of the host polymer. The experimental work is followed by a comprehensive thermal analysis, revealing the heat accumulation effects in graphene as a function of the laser repetition rate. Finally, the chapter concludes with the derivation of a heat-interchange model enabling the assessment of the heat transfer at the graphene-polymer interface.

4.2. Graphene-polymer composite materials

The integration of graphene in host matrices to form advanced multifunctional composites is one of the most promising routes in order to take full advantage of its unique properties. This approach enhances the mechanical robustness and durability of the resulting product, while maintaining the strong optical response due to the embedded

graphene. Polymers are a particularly attractive host matrix for integration with graphene. They have been shown to possess good mechanical and thermal properties, as well as improved transparency and stability [127-129]. Moreover, they are low cost, non-toxic and can be easily processed and fabricated into intricately shaped components with excellent preservation of the structure and properties of the embedded graphene using conventional processing methods.

The most popular approach is to embed graphene or carbon nanotubes (CNTs) in host polymers in order to improve the mechanical, thermal and microwave absorption properties of the polymer matrix for applications in the aerospace, automobile, energy and defence industries [128, 130-132]. From an optics point of view, the interest is in exploiting the host polymers to support the embedded graphene in order to take full advantage of its optical properties for realising high-performance light-weight solid thin films for optics and photonic applications. Of interest here are the nonlinear optical properties that arise from the embedded graphene associated to saturable absorption, two-photon absorption and nonlinear refraction with view to utilise such graphene-polymer composites for relevant applications such as saturable absorbers for laser mode-locking [115, 133] and optical limiters for human eye and equipment protection [134, 135]. In order to employ such graphene-polymer composite thin films in optics applications, firstly their nonlinear optical properties must be investigated and characterised. Furthermore, the interaction of the embedded graphene with its host matrix must be considered as well. Here we perform the nonlinear optical characterisation of a G-PVA thin film via the Z-scan technique. We also investigate the heat interchange at the graphene-polymer interface for G-PVA thin films of different graphene concentrations when illuminated with ultrashort pulses at different laser repetition rates. This study reveals interesting information about the heat accumulation effects in graphene with different laser repetition rates as well as the laser induced dynamic thermal damage of the host polymer due to heat diffusion from the embedded graphene.

4.3. Nonlinear optical characterisation of a Graphene – polyvinyl alcohol thin film

The system used for the Z-scan measurements on the G-PVA thin film was the OPA system outlined in section 2.5. Open- and closed-aperture Z-scan measurements were

carried out in a broad mid-infrared range spanning ~ 850 nm, taking advantage of the wide wavelength tuneability of the OPA system. The measurements were carried out at 3 different wavelengths, namely: 1550, 2000 and 2400 nm. The output of the OPA was directed to the Z-scan setup described previously in section 2.6.1. The beam was focussed with a 20 cm focal length CaF_2 lens and the focal spot size for each wavelength was measured using the scanning knife-edge technique. It was found to be 26 μm at 1550 nm, 28 μm at 2000 nm and 31 μm at 2400 nm.

The G-PVA thin film was provided by the Nanomaterials and Spectroscopy Group in the Department of Engineering at The University of Cambridge. The film was prepared by mixing graphene dispersions and polyvinyl alcohol (PVA) solution. A detailed description of the preparation method of the G-PVA thin film is given in [136]. The thickness of the film was measured to be ~ 73 μm and was estimated to have $\sim 30 - 35$ effective graphene layers cross the light path. The transmission spectra for the G-PVA thin film along with a pure PVA film of the same thickness measured with a Perkin Elmer UV/VIS spectrophotometer are presented in figure 4.1.

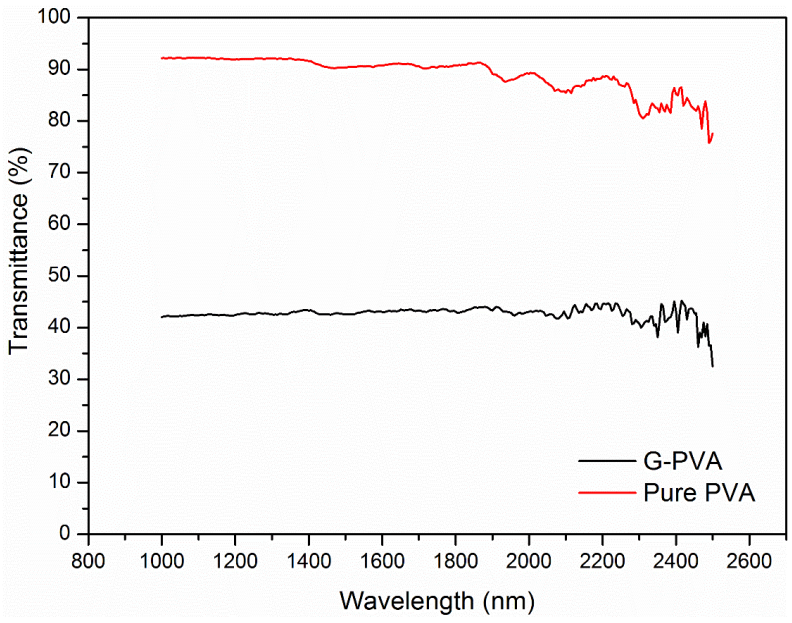

Figure 4.1. Transmission spectra of the G-PVA and pure PVA thin films measured with a Perkin Elmer UV/VIS spectrophotometer.

As can be seen, in the wavelength range of 1-2 μm, the transmittance of the pure PVA is ~90%, whereas the transmittance of the G-PVA composite drops to ~ 42-44% due to the light absorption from graphene. Taking into account that each graphene layer absorbs ~2.3% of the incident light, the estimation of $\sim 30 - 35$ effective graphene layers is consistent with the measured transmission spectra for the G-PVA and the pure PVA thin films.

4.3.1. Saturable absorption and two-photon absorption measurements

The effects of saturable and two-photon absorption for the G-PVA thin film were observed for pulse energies ranging from 2 to 300 nJ which corresponded to irradiances from ~1 GW/cm^2 to ~100 GW/cm^2. The open-aperture measurements showed that the transmittance had a power dependence characteristic of saturable absorption in the relatively low-irradiance regime. As the input irradiance was increased, a rise in transmittance due to saturable absorption occurred, which was followed by a decrease in transmittance due to TPA.

The competing SA and TPA processes can be seen in figure 4.2 in which five consecutive Z-scans performed at a wavelength of 2000 nm with increasing pulse energies, namely: 25, 30, 40, 50 and 60 nJ, are presented. At the low pulse energy of 25 nJ, as the sample was translated through the focus of the beam, only a rise in transmittance was observed due to SA. However, as the pulse energy was increased a small valley started to form on top of the transmittance peak indicating the onset of TPA. At 30 nJ the peak of the transmittance, which was highly confined to the focal region of the beam, started to flatten out suggesting the onset of TPA. Whereas at the higher pulse energies starting from 40 nJ a distinct dip was clearly observed at the focus on top of the transmittance peak verifying the TPA process. As the pulse energy was further increased the dip in transmittance became more prominent. The 30 nJ which can be seen as the onset of the TPA corresponds to an irradiance of 12.2 GW/cm^2. Furthermore, figure 4.2 includes an additional Z-scan trace performed on a graphene-free PVA thin film at the highest pulse energy of 300 nJ used in this work showing a non-varying transmittance, therefore verifying that no absorption effects arise from the host polymer. This trace is depicted with the solid black circles on the same axes as the last Z-scan trace of figure 4.2.

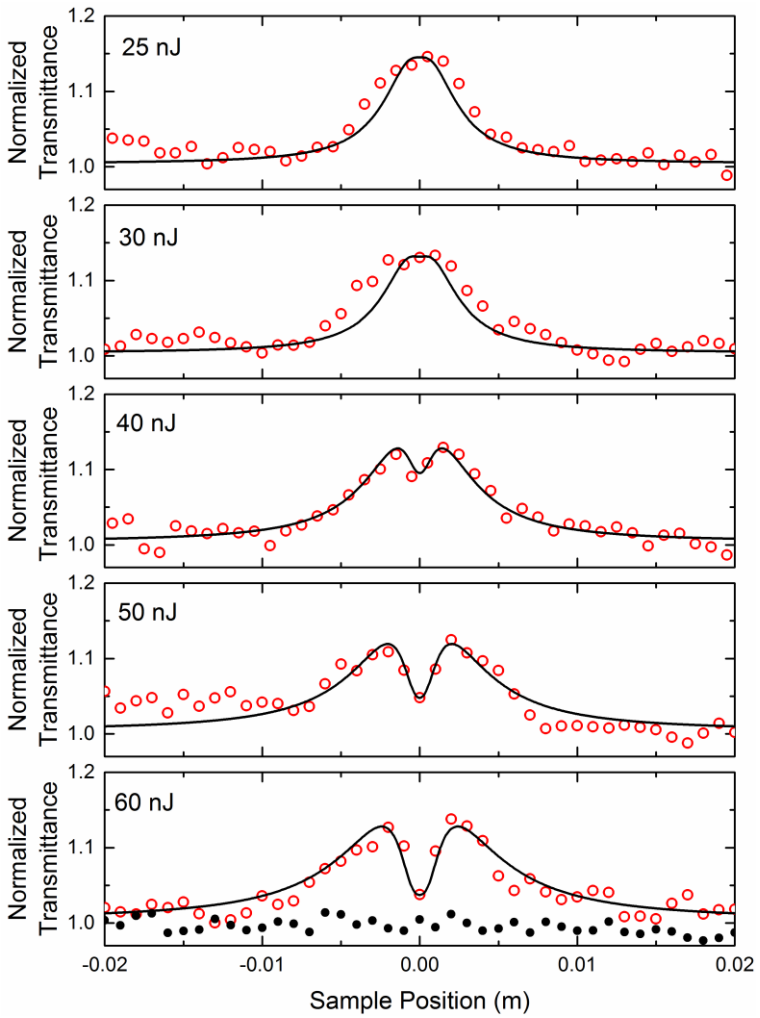

Figure 4.2. Open-aperture Z-scan traces conducted at 5 consecutive pulse energies at a wavelength of 2000 nm showing the competing saturable absorption and two-photon absorption processes. At the low pulse energy of 25 nJ only saturable absorption is present, whereas at the higher pulse energies starting from 30 nJ and onwards the two-photon absorption process becomes evident.

The irradiance versus normalised transmittance along with the theoretical fits for all wavelengths are shown in figure 4.3. In order to obtain this figure, open-aperture Z-scan traces of different pulse energies and therefore different irradiances were combined. More specifically for each of the wavelengths open-aperture Z-scans were performed at a range of pulse energies from 2 to 300 nJ or in terms of irradiances from ~1 GW/cm^2 to ~100 GW/cm^2. Then the ΔT at the focus of each of the traces was recorded and combined in order to construct the plot of irradiance versus normalised transmittance shown in figure 4.3. ΔT is denoted as the difference between the transmittance at the focus, where the

irradiance is at maximum, and sufficiently away from the focus where no nonlinear effects take place, therefore the transmittance is non-varying.

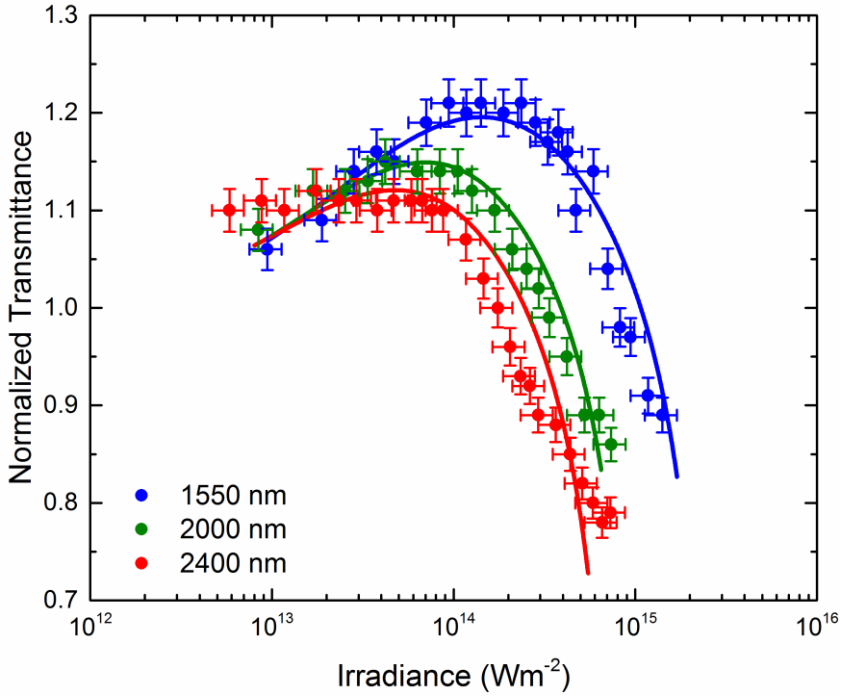

Figure 4.3. Change in transmittance with input irradiance at 1550, 2000 and 2400nm (dots) with the corresponding theoretical fits (solid lines).

The theoretical fits of figure 4.3 are obtained by solving the differential propagation equation 2.18 after considering the irradiance dependent absorption coefficient, $\alpha(I)$, for a medium that presents both saturable and two-photon absorption. This was presented previously in equation 3.6. Both the TPA coefficients β and the saturation irradiances I_{sat} are extracted from the transmission numerical fits of figure 4.3. In the numerical simulation for the best fit, the α_0 parameter used is extracted from the linear transmission spectra of the sample at each of the operating wavelengths. The fitting results are shown in table 4.1, whereas a detailed comparison regarding the saturation irradiances and TPA coefficients of graphene reported in literature is performed in sections 3.3.1 and 3.4.1 respectively.

By observing the trend of the coefficients in table 4.1 it can be seen that the saturation irradiance is decreased with increasing wavelength, whereas the TPA coefficient shows the opposite trend increasing with longer wavelengths. This suggests that there is a more

Table 4.1. Nonlinear coefficients

Wavelength	α_0 (m^{-1})	β_{eff} (cm/GW)	I_{sat} (GW/cm^2)
1550 nm	2.42×10^7	$(0.5 \pm 0.1) \times10^4$	1.2 ± 0.4
2000 nm	2.33×10^7	$(1.25\pm 0.25) \times10^4$	1 ± 0.33
2400 nm	2.06×10^7	$(1.7\pm 0.34) \times10^4$	0.8 ± 0.27

significant contribution from TPA due to the lower photon energy. This trend is also seen in figure 4.3 where the decrease in transmittance is more prominent at the longer wavelengths. As expected this increasing TPA trend with wavelength will lower threshold for the onset of TPA at the longer wavelengths. The onset of TPA at each of the wavelengths was found to be:

Table 4.2. Onset of TPA

Wavelength	Onset of TPA GW/cm^2
1550 nm	28.3 ± 4.6
2000 nm	12.2 ± 2.4
2400 nm	8.3 ± 1.6

Comparing the cases of the G-PVA composite and the CVD 5-7 layer graphene characterised in section 3.4 we can see that the nonlinear coefficients follow the same trend, with the contribution from TPA being more prominent at longer wavelengths. However, the threshold for the onset of the TPA at respective wavelengths is lower for the G-PVA. This is attributed to the stronger nonlinear response of the G-PVA thin film due to its increased number of layers (~30-35). In practical terms it means that the CVD 5-7 layer graphene would be a more suitable saturable absorber for laser mode-locking as it would allow reaching higher irradiances before TPA kicks in and increase the non-saturable losses in the system. In order to overcome this limitation, in the case of G-PVA thin films, the percentage of graphene in the host polymer can be altered during fabrication enabling the tuning of the nonlinear optical response of the resulting composite. If one desires to employ such G-PVA thin films as saturable absorbers for laser mode-locking, this approach can be used for tailoring the absorption properties of the composite and increase the onset threshold for the TPA.

4.3.2. Nonlinear refraction measurements

The effects of the nonlinear refraction of the G-PVA composite were also investigated. As already discussed in section 3.2.3 the nonlinear refraction of graphene is irradiance dependent. This irradiance dependence was investigated for the cases of single and multilayer CVD graphene in sections 3.3.2 and 3.4.2 respectively. However, the low repetition rate of the OPA system combined with its output power fluctuations did not allow for reliable closed-aperture Z-scans at sufficiently low irradiances, *~0.1-10 GW/cm*^{2}. This prevented the investigation of the nonlinear refraction trend with irradiance like the case of single and multilayer CVD graphene. In the case of the G-PVA thin film the closed-aperture Z-scans were performed well in the oversaturation regime of the nonlinear phase shift. More specifically the closed-aperture Z-scans at all three wavelengths were performed at an irradiance of ~ 41 GW/cm^2, approximately two orders of magnitude higher than the nonlinear phase saturation irradiances deduced for the single and multilayer CVD graphene in sections 3.3.2 and 3.4.2 respectively. These are presented in figure 4.4.

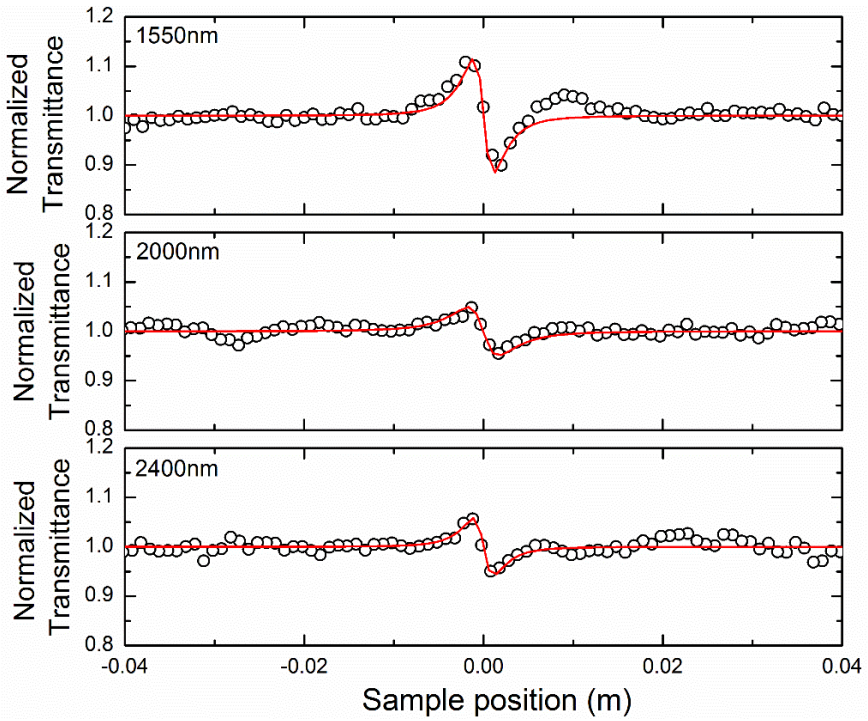

Figure 4.4 Closed-aperture Z-scan traces at 1550, 2000 and 2400 nm at an irradiance of ~41 GWcm^{-2} with the corresponding theoretical fits.

The closed-aperture Z-scans performed here verified the negative value of the nonlinear refraction for the G-PVA composite as well and most importantly they revealed the trend of the nonlinear refraction with wavelength. The theoretical fits in figure 4.4 use equation 2.21 presented in section 2.4. The values for the irradiance-dependent nonlinear refraction obtained from the fit for each wavelength are presented in table 4.3. As can be seen the G-PVA thin film presents giant irradiance-dependent nonlinear refraction in the order of $\sim 10^{-13}\ m^2W^{-1}$, which decreases with increasing wavelength. The broad range at which the work was undertaken revealed the trend of the nonlinear refraction in graphene versus wavelength at a wide range spanning ~850 nm. In addition, a detailed discussion regarding the nonlinear refraction of graphene reported in literature is performed in section 3.3.2.

Table 4.3. Intensity dependent nonlinear refraction coefficient $\tilde{n}(I)$

Wavelength	$\tilde{n}(I)$ **(cm^2/GW) at 41 GWcm^{-2}**
1550 nm	-0.58 ± 0.06
2000 nm	-0.61 ± 0.06
2400 nm	-0.69 ± 0.07

4.4. Laser induced dynamic thermal damage in graphene-polymer composite films.

The interaction of the embedded graphene with the host polymer under laser illumination conditions was also investigated. More specifically when illuminated, the embedded graphene absorbs light leading to its temperature rise and consequently to a heat inflow into the host polymer. If one wishes to employ such graphene-polymer composites for the realisation of relevant applications, the heat interchange at the graphene-polymer interface must be investigated in order to assess whether or not there is the possibility of thermally damaging the host polymer through heat inflow from the embedded graphene. In this work the temperature dynamics of graphene-polymer composite thin films were experimentally investigated. An extensive theoretical thermal analysis was undertaken revealing the heat accumulation effects in graphene with different laser repetition rates and a theoretical model enabling the assessment of the heat interchange at the graphene-polymer interface was derived.

4.4.1 Experimental investigation of the laser induced dynamic thermal damage in G-PVA thin films.

Two G-PVA composites with different graphene concentrations were provided by the centre for research on adaptive nanostructures and nanodevices in the school of physics of the Trinity College of Dublin. The film was prepared by mixing graphene dispersions and polyvinyl alcohol (PVA) solution. A detailed description of the preparation method of the G-PVA composites is given in [137]. For both G-PVA thin films the thickness was measured to be ~ 60 μm. The transmission spectra for the G-PVA thin films along with a pure PVA film of the same thickness measured with a Perkin Elmer UV/VIS spectrophotometer are presented in figure 4.5. The sample with the higher graphene concentration is termed H-G-PVA, whereas the sample with the lower graphene concentration is termed L-G-PVA. As can be seen from the transmission spectra due to the higher graphene concentration H-G-PVA absorbs more of the incident light therefore presenting lower transmission than L-G-PVA. Taking into account that each graphene layer absorbs ~2.3% of the incident light, the transmission spectra of figure 4.5 allowed for the estimation of the effective number of graphene layers for each of the G-PVA thin films. These were estimated to be ~ 27-28 layers for the H-G-PVA and ~ 14-15 layers for the L-G-PVA.

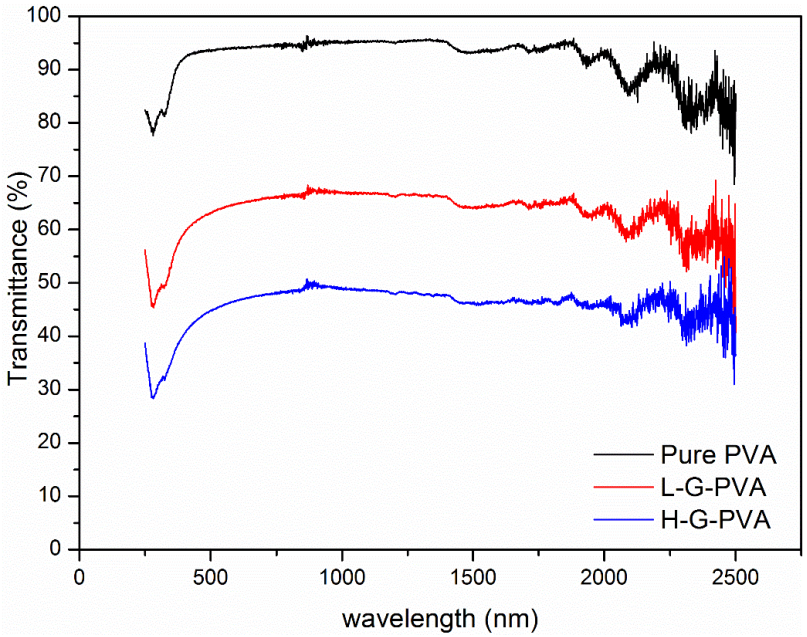

Figure 4.5. Transmission spectra of the G-PVA and pure PVA thin films measured with a Perkin Elmer UV/VIS spectrophotometer.

The temperature dynamics of the G-PVA composite films were investigated in the femtosecond temporal regime at two different laser repetition rates, namely 1 and 500 kHz. The system used for the measurements at the low repetition rate of 1 kHz was the OPA laser system outlined in section 2.5, whereas for the measurements at the high repetition rate of 500 kHz the preferred system was the IMRA® laser system described in section 2.8.1.

The open-aperture Z-scan technique, outlined in section 2.4, was preferred to carry out this work in order to exploit its sensitivity to observe the laser induced damage in the G-PVA composites. The approach for performing this investigation is the following: an open-aperture Z-scan was performed at a low irradiance level observing the characteristic SA trace of graphene which presents a transmittance increase at the focus. Then the irradiance was slowly increased until a different behaviour than the characteristic SA trace was observed. Thereupon another Z-scan was performed on the same position on the sample and at the same low irradiance level as the first Z-scan. The comparison between the two Z-scan traces at the low irradiance regime, before and after the irradiance was increased enabled the study of the laser induced damage. This study can be seen in figures 4.6 and 4.7, which present the cases of 500 and 1 kHz respectively. All Z-scans presented in figures 4.6 and 4.7 were taken in the same order they are listed on the legends and on the same position on the sample.

4.4.1.1 Laser induced damage at a repetition rate of 500 kHz

The open-aperture Z-scan traces at the high repetition rate of 500 kHz with different graphene concentrations showing the laser induced damage are presented in figure 4.6. Figure 4.6 (a) presents the Z-scans performed on the sample with the higher graphene concentration. The first Z-scan trace depicted with the black squares was performed at a low irradiance of 0.57 GW/cm^2 or 7 nJ in terms of pulse energy and presents a transmittance rise at the focus, characteristic of SA. Then the irradiance was increased until a dip of the transmittance at the focus was observed. This behaviour is shown in the 2nd Z-scan trace depicted with the red dots. That Z-scan was performed at an irradiance of 2.44 GW/cm^2 or in terms of pulse energy at 30 nJ and shows a maximum decrease of the normalised transmittance at the focus to about 0.9. Afterwards by increasing the pulse

energy by only 10 nJ reaching the pulse energy of 40 nJ which corresponds to an irradiance of 3.26 GW/cm^2, a giant decrease of the normalised transmittance at the focus to about 0.2 was observed. This behaviour can be seen in the 3rd Z-scan trace depicted with the blue triangles. In order to quantify whether the properties of the G-PVA were permanently altered, a further Z-scan at the same low irradiance of 0.57 GW/cm^2 as the first Z-scan and on the same position on the sample was performed; this is depicted with the pink triangles. As can be seen the first (black squares) and last (pink triangles) Z-scan traces of figure 4.6 (a) at the low irradiance level, before and after the irradiance was increased, present very different behaviour. The first trace presents a transmittance rise at the focus, characteristic of SA, whereas the last trace presents a sharp drop of the transmittance, undoubtedly verifying that the properties of the G-PVA film are permanently altered. This behaviour is attributed to the temperature rise of graphene due to absorption, which leads to a heat inflow from the embedded graphene into the host polymer, resulting in a temperature rise and eventually thermal damage of the host polymer.

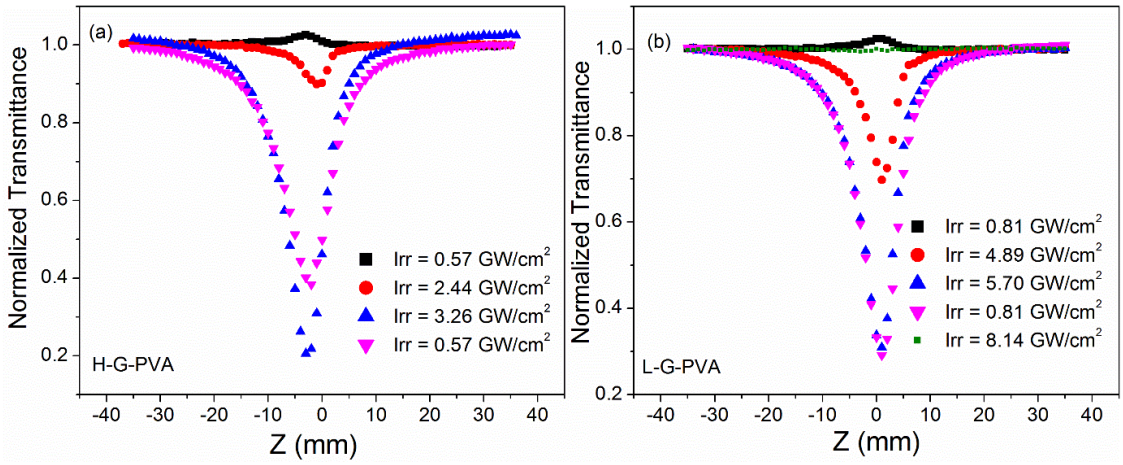

Figure 4.6. (a) Four consecutive open-aperture Z-scan traces at a repetition rate of 500 KHz on the high graphene concentration sample showing the thermal damage of the host polymer. (b) Four consecutive open-aperture Z-scan traces at 500 kHz on the low graphene concentration sample showing the thermal damage of the host polymer, along with a Z-scan trace (green squares) on a graphene-free PVA thin film at an irradiance of 8.14 GW/cm^2 showing a non-varying transmittance.

Figure 4.6 (b) presents the Z-scans performed on the sample with the lower graphene concentration. These were obtained in exactly the same approach as the Z-scans of figure 4.6 (a), where the irradiances of 4.89 and 5.7 GW/cm^2 correspond to pulse energies of 60 and 70 nJ respectively. As can be seen, in the case of the lower graphene concentration, the irradiance threshold for permanently altering the properties of the G-PVA is increased from ~2.44 to ~4.89 GW/cm^2 or in terms of pulse energies from 30 to 60 nJ. This is in accordance with the proposed model for thermally damaging the G-PVA, since lower graphene concentrations in the PVA matrix would require higher irradiances to reach the same temperature rise and thermally damage the host polymer. An additional Z-scan trace performed on a PVA thin film which did not contain any graphene is also presented in figure 4.6 (b). This was performed at a pulse energy of 100 nJ corresponding to an irradiance of 8.14 GW/cm^2 and presents a non-varying transmittance, showing that the graphene-free PVA thin film does not present any nonlinearities or gets damaged by the ultrafast pulses up to irradiances much higher than the ones used to induce the laser damage to the G-PVA thin films at the repetition rate of 500 KHz.

Furthermore, for the last two traces (blue and pink triangles) in both figures 4.6 (a) and (b) the transmittance starts to decrease at about 20 mm away for the focus at both positive and negative directions, which shows that the damage is not confined within the focal region of the beam. The spot size at these positions was measured to be about 200 μm, while the beam waist at the focus was measured to be 33 μm. The fact that the damage was extended to a distance of about six times that of the beam waist at the focus further supports the model for thermal damage of the host polymer due to heat diffusion from the graphene.

4.4.1.2 Laser induced damage at a repetition rate of 1 kHz

Considering now the case of the low repetition rate, the situation is different. The open-aperture Z-scan traces showing the laser induced damage at 1 kHz are presented in figure 4.7. This investigation in the low repetition rate regime was performed in exactly the same approach as the case of the high repetition rate. As can be seen from figure 4.7 in the low repetition rate regime of 1 kHz the properties of the G-PVA thin films, for both

composites regardless of the graphene concentration, were permanently altered at the irradiance of ~212 GW/cm^2 which corresponds to a pulse energy of 450 nJ.

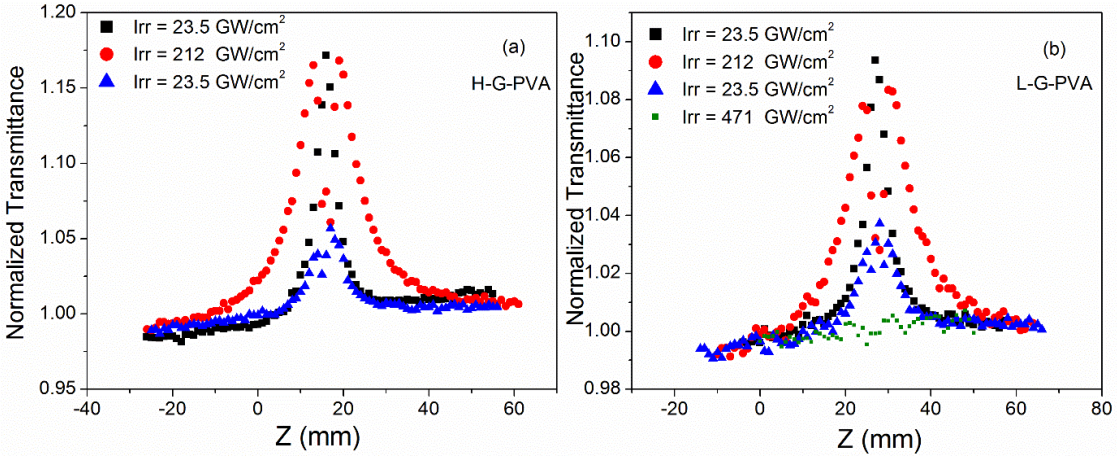

Figure 4.7. (a) Three consecutive open-aperture Z-scan traces at a repetition rate of 1 kHz on the high graphene concentration sample showing the damage before and after the irradiance increase. (b) Three consecutive open-aperture Z-scan traces at 1 kHz on the low graphene concentration sample showing the damage before and after the irradiance increase, along with a Z-scan trace (green squares) on a graphene-free PVA thin film at an irradiance of 471 GW/cm^2 showing a non-varying transmittance.

By inspecting the 2nd trace of each of the figures 4.7 (a) and (b), taken at the high irradiance regime and depicted with the red dots, one can see that as the sample approaches the focus the transmittance is increased showing the characteristics of SA. Then the transmittance is only decreased as the sample is translated through the focus, suggesting that the damage is well confined within the focal region of the beam. The reported damage threshold for graphene with femtosecond pulses is at an optical fluence of 14 mJ/cm^2 [125], and in excellent agreement with the laser damage investigation performed on the 5-7 layer CVD graphene presented in section 3.4.4. The pulse energy of 450 nJ, at which the permanent changes of the G-PVA properties were observed, corresponds to an optical pulse fluence of ~21 mJ/cm^2, slightly higher than the laser damage threshold of the CVD multilayer graphene. This combined with the fact that the damage is confined within the focal region of the beam, indicate that at this low repetition rate regime the optical properties of the G-PVA thin films are permanently altered due to

the local modification of the carbon bonds inside the graphene lattice from the ultrafast pulses [125, 126, 138] rather than heat diffusion from the embedded graphene and thermal damage of the host polymer.

The discrepancy on the damage threshold between CVD graphene and G-PVA films is attributed to the fact the CVD graphene is deposited on a quartz substrate with all the layers on top of each other, whereas in the case of the G-PVA the graphene flakes are randomly distributed in the host matrix which has a thickness of ~60 μm without having any interaction with the outer environment. This suggests that the approach of embedding graphene in host matrices could be used in order to increase the femtosecond laser damage threshold of the resulting composite for low repetition rate applications.

In addition, figure 4.7 (b) includes a Z-scan trace performed on a PVA film which did not contain any graphene. This was taken at a pulse energy of 1 μJ corresponding to an irradiance of 471 GW/cm^2 and presents a non-varying transmittance, showing that the graphene-free PVA does not present any nonlinearities or gets damaged by the ultrafast pulses up to irradiances much higher than the ones used to induce the laser damage to the G-PVA thin films.

In conclusion the ultrafast laser induced dynamic thermal damage in graphene-polymer composites was investigated at two different laser repetition rate regimes, namely 1 and 500 kHZ. Two different damage mechanisms, depending on the laser repetition rate used, were identified. At the high repetition rate regime, the light absorbed by graphene leads to its temperature rise and consequently to a heat inflow from the embedded graphene into the host polymer. This heat interchange procedure results in a temperature rise and eventually thermal damage of the host polymer, with the damage threshold being dependent on the graphene concentration in the host polymer. At the low repetition rate regime the situation is different, the damage threshold is about two orders of magnitude higher than the case of the high repetition rate. The damage mechanism in this regime is due to the local modification of the carbon bonds inside the graphene lattice from the ultrafast pulses [125, 126, 138] rather than heat diffusion from the embedded graphene and subsequent thermal damage of the host polymer.

4.4.2 Thermal analysis

A comprehensive thermal analysis was performed by Eitan Abraham, a collaborator of the NLO group. This analysis can be seen as consisted by two sections. The first section studies the thermal accumulation effects in graphene as a function of the laser repetition rate; whereas the 2nd section treats the heat interchange at the graphene-polymer interface deriving a model which enables the estimation of the polymer temperature rise and the system equilibrium temperature.

4.4.2.1 Heat accumulation effects in graphene

The thermal analysis performed here derives a semi-quantitative model from the heat equation adapted to the case of graphene when irradiated by a train of ultrashort pulses. The heat equation given by [139]:

$$D\nabla^2 T(r,t) - \frac{\partial T(r,t)}{\partial t} = -\frac{Q(r,t)}{\rho c} \tag{4.1}$$

where D is the diffusion coefficient, ρ is the mass density of graphene, c is the specific heat of graphene, r is the radial distance from the centre of the bream and $Q(r,t)$ is the energy absorbed per unit time per unit volume.

In the case of graphene, the energy absorbed per unit time per unit volume is given by:

$$Q(r,t) = \alpha I_0(t) e^{-\frac{r^2}{w^2}} \tag{4.2}$$

where α is the absorption coefficient of graphene and $I_0(t)$ is the peak irradiance at the centre of the beam. Concentrating at the centre of the beam ($r = 0$) where the temperature rise will be maximum, equation 4.2 becomes:

$$Q(0,t) = \alpha I_0(t) \tag{4.3}$$

Given that the laser repetition rates used here are in the orders of KHz while the pulse duration is in the orders of femtoseconds, having about seven orders of magnitude difference, each individual pulse can be treated as an impulse function also known as delta function $\delta(t)$. This delta function can be extended to a train of pulses using the summation $\sum_n \delta(t - n\tau_p)$, where τ_p is the period of the laser repetition rate with n being the number of pulses for a given time *t*.

Considering the above approximation, the peak irradiance at the centre of the beam for a single pulse can be expressed as:

$$I_0(t) = F_0\delta(t) \tag{4.4}$$

where F_0 is pulse fluence.

Furthermore since each pulse is treated as a delta function, the spatial diffusion component of the heat equation can be replaced by a 'heat loss' term with a decay rate assumed to be dominated by the graphene diffusion time τ_g. This 'heat loss' term in essence represents the drop in temperature from the time that the previous pulse stops acting on the sample until the next pulse arrives and imposes a new temperature rise on the sample.

Following the above approximations and substituting equations 4.3 and 4.4, equation 4.1 for the case of a single pulse becomes:

$$\frac{\partial T(0,t)}{\partial t} + \frac{T(0,t)}{\tau_g} = \frac{\alpha F_0}{\rho c}\ \delta(t) \tag{4.5}$$

where the maximum temperature T_0 can be defined as $T_0 = \frac{\alpha F_0}{\rho c}$.

Finally, the model differential equation is obtained by adapting equation 4.5 for a train of pulses:

$$\frac{\partial T}{\partial t} + \frac{T}{\tau_g} = T_0 \sum_{n=0,1,\ldots,\infty} \delta\left(t - n\tau_p\right) H(t - n\tau_p) \tag{4.6}$$

where $H(t - n\tau_p)$ is the Heaviside step function guaranteeing that each pulse will not act on the sample before the corresponding time $t = n\tau_p$ as *H* is zero for negative arguments.

Equation 4.6 can be seen as a semi-quantitative model derived from the heat equation 4.1 and adopted to the case of graphene when irradiated by a train of ultrashort pulses. The analytical solution of 4.6 can be readily obtained by Laplace transformation. Due to the linearity of the heat equation $T(t)$ can be interpreted as an increase from room temperature with the solution given by:

$$T(t) = T_0 \sum_{n=0}^{\infty} H\left(t/\tau_g - n\tau_p/\tau_g\right) \exp[-(t/\tau_g - n\tau_p/\tau_g)] \tag{4.7}$$

Equation 4.7 can be modified to

$$\Theta(t) = T(t)/T_0 = \sum_{n=0}^{N_0} H\left(t/\tau_g - n\tau_p/\tau_g\right) \exp[-(t/\tau_g - n\tau_p/\tau_g)] \tag{4.8}$$

where $\Theta(t)$ is the scaled temperature and represents the relative temperature rise at a high repetition rate regime due to heat accumulation comparing with the case of a low repetition rate regime where no thermal accumulation effects take place. The concept of the scaled temperature will become more easily understood when the plots of $\Theta(t)$ for different laser repetition rates are presented. Furthermore, in equation 4.8, N_0 is the total number of pulses that arrive at the sample. In the following three figures the analytical solution of equation 4.8 is plotted for three different laser repetition rates, namely 50 KHz, 500 KHz and 5 MHz, showing that in the case of 50 KHz no thermal accumulation effects can occur, whereas at the high repetition rates of 500 KHz and 5 MHz the heat accumulation is present. For all three cases the graphene diffusion time is considered to be $\tau_g = 5\mu s$.

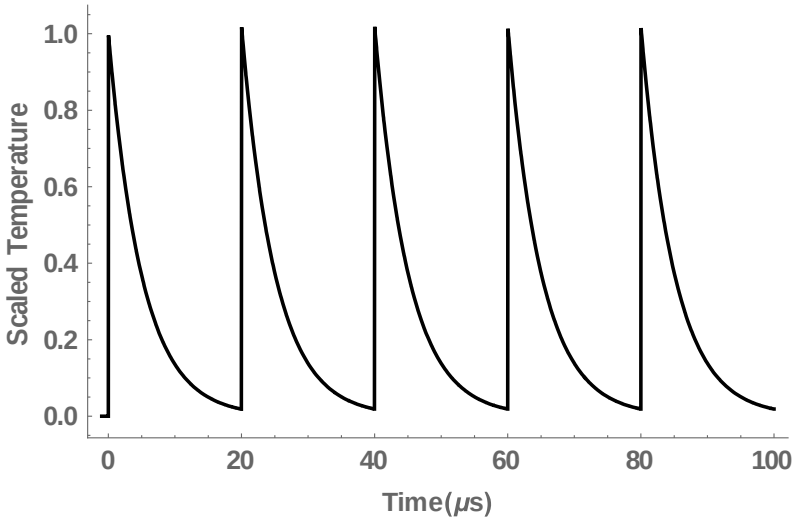

Figure 4.8 The Scaled temperature $\Theta(t)$ at a laser repetition rate of 50 KHz for 5 consecutive pulses ($N_0 = 5$) showing that no thermal accumulation effects can occur.

Figure 4.8 represents the scaled temperature $\Theta(t)$ at a laser repetition rate of 50 KHz for 5 consecutive pulses. Since the laser repetition rate is 50 KHz the period will be $\tau_p = 20\mu s$. As can be seen from the figure, due to the low laser repetition rate, the diffusion is over before the next pulse arrives therefore not allowing for any thermal accumulation effects. By inspecting the figure one can see that the first pulse arrives at $t = 0$ inducing a rise of the scaled temperature $\Theta(t)$ to 1 in normalised units. Then by the time the second pulse arrives at a time of $t = 20\ \mu s$ all the heat will have diffused leading the temperature to drop to 0, therefore the 2nd pulse will induce a temperature rise to 1 but not higher. At this low repetition rate regime this is the case for every successive pulse, therefore the overall temperature rise can never surpass that induced by a single pulse.

However, when the laser repetition rate is increased, the time intervals between successive pulses will decrease not leaving enough room for the heat to completely diffuse before each successive pulse arrives therefore leading to a heat accumulation effect. This case is depicted in figure 4.9 where the scaled temperature $\Theta(t)$ is plotted at a laser repetition rate of 500 KHz.

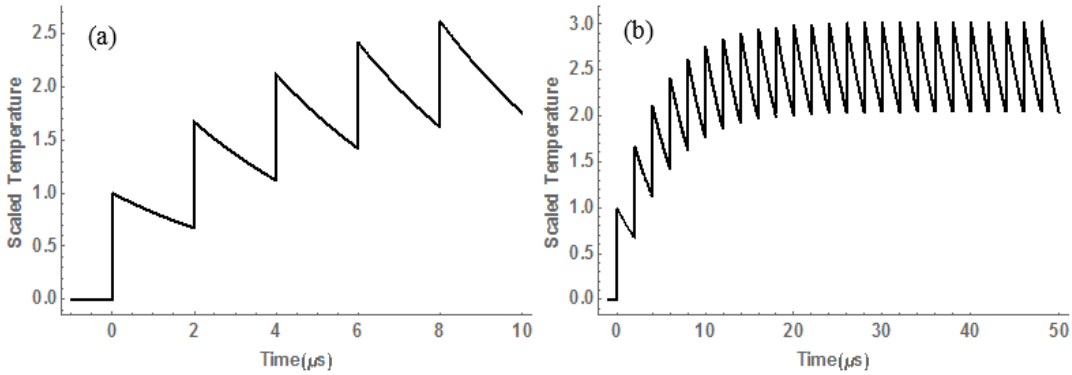

Figure 4.9. (a) The Scaled temperature $\Theta(t)$ at a laser repetition rate of 500 KHz for 5 consecutive pulses ($N_0 = 5$) showing the thermal accumulation in graphene. (b) Same conditions as (a) but considering 25 consecutive pulses.

As can be seen form figure 4.9, due to the high repetition rate, the heat does not completely diffuse before the arrival of each successive pulse, therefore leading to a temperature accumulation effect. More specifically the first pulse arriving at $t = 0$ will induce a rise of the scaled temperature $\Theta(t)$ to 1 in normalised units. Upon the arrival of the 2nd pulse at $t = 2\,\mu s$ the temperature increase induced by the 1st pulse will have decreased to only ~0.65, therefore the contribution of the 2nd pulse will cause the overall temperature to increase to about ~1.65 in normalised units. Then the contribution from each successive pulse will add to the overall temperature rise in the same fashion until this reaches a plateau. This case is shown in figure 4.9 (b) which plots $\Theta(t)$ at a repetition rate of 500 KHz for 25 consecutive pulses. The temperature accumulation will eventually reach a plateau because after a certain number of pulses incident on the sample and as the overall temperature increases the heat loss rate will become proportional to the temperature input not allowing for further increase of the overall temperature. Figure 4.9 (b) in practical terms shows that for a laser repetition rate of 500 KHz the scaled temperature will be increased to about 2.5 times comparing with the case of a lower laser repetition rate where no thermal accumulation effects can occur.

The case of the scaled temperature for an even higher laser repetition rate of 5 MHz is plotted in figure 4.10 showing that as the repetition rate is further increased both the

overall temperature and the number of pulses required to reach the plateau in temperature are also increased.

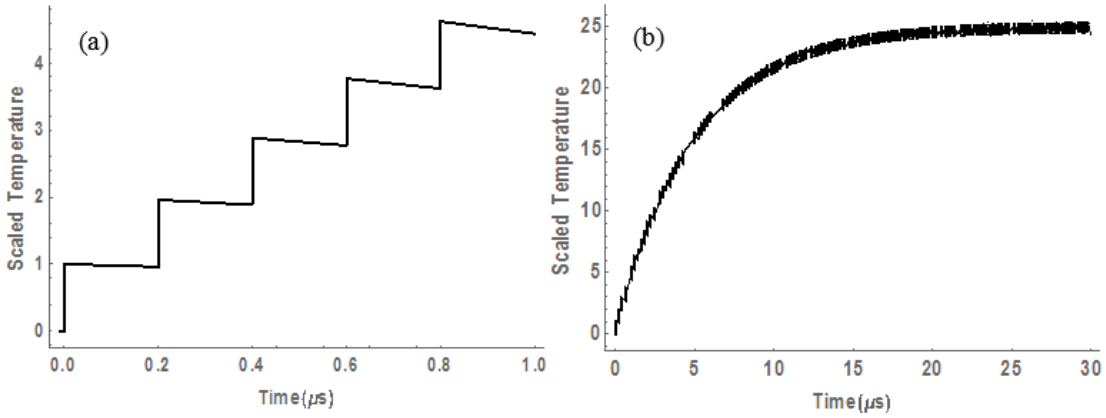

Figure 4.10. (a) The Scaled temperature $\Theta(t)$ at a laser repetition rate of 5 MHz for 5 consecutive pulses ($N_0 = 5$) showing the thermal accumulation. (b) Same conditions as (a) but considering 150 consecutive pulses.

In conclusion, this semi-quantitative model derived from the heat equation and adapted to the case of graphene describes the thermal accumulation effects in graphene as a function of the laser repetition rate. It shows that the heat accumulation is bigger for higher laser repetition rates and regardless of the repetition rate the temperature rise will always saturate eventually reaching a maximum achievable temperature. Furthermore this model enables the accurate estimation of the temperature rise for a given laser repetition rate and number of pulses given that the exact values for the conductivity and the graphene diffusion time, τ_g, are known.

4.4.2.2 Heat interchange at the graphene-polymer interface

The previous section treated the temperature rise and heat accumulation effects solely in graphene, without considering graphene's interaction with the host polymer. In this section the heat interchange between the graphene and the host polymer is investigated. When heat flow is transported across an interface between two different materials there is a temperature discontinuity at the interface [140, 141] which can be expressed as

$$F = G\,\Delta T \tag{4.9}$$

where F is the energy flux density through the interface, G is interfacial thermal conductance and ΔT is the temperature difference at the interface. This was first presented by Pyotr Kapitza for the interface between liquid helium and copper, therefore it is known as Kapitza conductance [142].

If the thickness of the heated polymer is d then the heat power generated in the polymer per unit volume is $G\Delta T / d$. From the 1st law of thermodynamics and in the absence of work done by the system, the change of internal energy per unit volume in the system, ΔQ, is proportional to the change in temperature, dT/dt, that is $\Delta Q = c\rho\frac{dT}{dt}$, where c and ρ are the specific heat capacity and the density respectively. Thus the heat equation for the case of the polymer becomes

$$\rho_p c_p \frac{dT_p}{dt} = \frac{G}{d}\,(\Delta T(t)) \tag{4.10}$$

Dividing both parts of equation 4.10 by the thermal conductivity K_p of the polymer and rearranging we get

$$\frac{dT_p}{dt} = \frac{GD_p}{d\,K_p}\,(\Delta T(t)) \tag{4.11}$$

Similarly for the case of graphene we get

$$\frac{dT_g}{dt} = \frac{-2GD_g}{d\,K_g}\,(\Delta T(t)) \tag{4.12}$$

where the negative sign occurs because graphene is giving temperature to the polymer and the factor 2 is because the heat loss for graphene occurs at the two graphene-PVA interfaces.

Defining the temperature difference $\Delta T(t) = T_g(t) - T_p(t)$ and the quantities $\beta = \frac{GD_p}{d\,K_p}$, $\gamma = \frac{2GD_g}{d\,K_g}$, $\Gamma = \beta + \gamma$ and subtracting equation 4.11 from equation 4.12 we get

$$\frac{d\Delta T(t)}{dt} = -\Gamma\,\Delta T(t) \tag{4.13}$$

with $\Delta T(0) = T_0$. By integrating, equation 4.13 becomes

$$\Delta T(t) = T_0 \exp(-\Gamma\, t) \tag{4.14}$$

Equation 4.14 shows that for long enough times $t >> \Gamma^{-1}$ equilibrium is reached.

By using equation 4.14 in the differential equation 4.11 for the polymer and integrating from $T_p(0) = 0$ to $T_p(t)$ the temporal temperature profile for the polymer becomes

$$T_p(t) = \frac{\beta T_0}{\Gamma}\,[\,1 - \exp(-\Gamma\, t)] \tag{4.15}$$

Similarly for the case of the graphene with $T_g(0) = T_0$ the temporal temperature profile is

$$T_g(t) = \frac{\beta T_0}{\Gamma}\,[\,1 + \frac{\gamma}{\beta}\exp(-\Gamma\, t)] \tag{4.16}$$

Equations 4.15 and 4.16 depict the evolution of the temporal temperature profile for the host polymer and the embedded graphene respectively thus revealing the nature of the temperature interchange between the two materials. Figure 4.11 plots the temperature as a function of time for both the polymer and graphene using equations 4.15 and 4.16 showing that for an initial graphene temperature of $T_0 = 800\ K$ the system reaches to an equilibrium temperature of about 200 K, high enough to induce structural damages to the polymer after 1 ns.

By inspecting equations 4.15 and 4.16 one can see that the equilibrium temperature is $\frac{\beta T_0}{\Gamma}$ which is independent of the polymer thickness *d* and the interfacial thermal conductance *G*, but the decay rate is not. This practically means that the system would reach to the same equilibrium temperature at the interface of the two materials but at different times for different values of *d* and *G*.

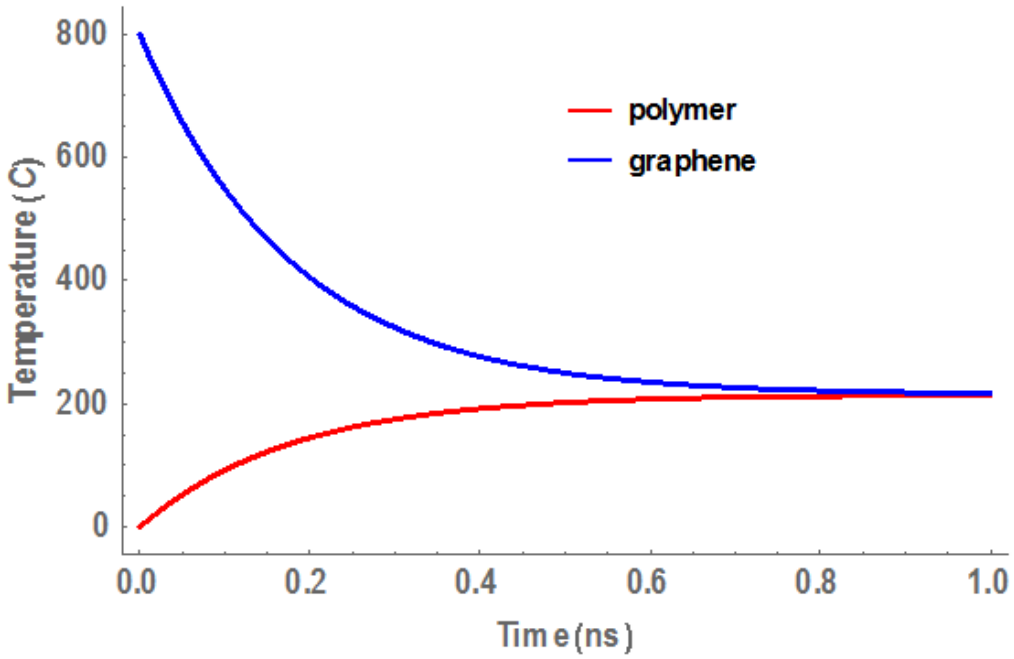

Figure 4.11. Change in temperature with time for the graphene (blue) – polymer (red) system, until equilibrium is reached.

Equations 4.15 and 4.16 emphasize both the novelty and significance of the thermal analysis presented in this section. In this particular situation they were derived for the temporal temperature profiles of the host PVA polymer and embedded graphene respectively but can be generalised in the case of graphene embodied in any host matrix given that the appropriate values for the interfacial conductance *G* and the conductivities are used.

Finally, it is worth noting that by combining the two sections of the theoretical analysis performed here, one can accurately study the temperature dynamics of graphene based composites when irradiated by ultrashort pulses. More specifically the heat accumulation

as a function of the laser repetition rate and the overall temperature rise in graphene can be deduced following the analysis presented in section *4.4.2.1*. Thereupon having the information of the maximum temperature rise in graphene, the temperature rise of the host matrix due to heat diffusion from the embedded graphene along with the system equilibrium temperature and the decay rate can be deduced following the model presented in section *4.4.2.2*.

4.5. Summary

This chapter has presented the work performed on graphene-polymer composite thin films. First the nonlinear optical characterisation of a graphene poly-vinyl alcohol thin film via the Z-scan technique was performed. The relevant nonlinear optical properties related to saturable absorption, two-photon absorption and nonlinear refraction were investigated and the associated coefficients were derived at the operating wavelengths. Thereupon followed the study of the laser induced dynamic thermal damage in G-PVA thin films by ultrashort pulses at two different laser repetition rates, namely 1 and 500 KHz. Two different damage mechanisms were identified. At the high repetition rate regime, the light absorbed by graphene, lead to its temperature rise and consequently to a heat inflow from the embedded graphene into the host polymer. This heat interchange procedure resulted in the temperature rise and eventually thermal damage of the host polymer, whereas the damage threshold was found to be dependent on the graphene concentration. At the low repetition rate regime, the damage threshold was found to be about two orders of magnitude higher than the case of the high repetition rate; the damage mechanism was due to the local modification of the carbon bonds inside the graphene lattice from the ultrafast pulses rather than heat diffusion from the embedded graphene and subsequent thermal damage of the host polymer. The experimental work was then followed by a comprehensive thermal analysis revealing the heat accumulation effects in graphene as a function of the laser repetition rate. Finally, the chapter concluded with the derivation of a heat-interchange model enabling the assessment of the polymer temperature rise due to heat diffusion from the embedded graphene and the equilibrium temperature of the graphene-polymer system. The novel thermal model derived here paves the way for studying the thermal dynamics and heat interchange of graphene embedded into any host matrix.

Chapter 5. Nonlinear optical properties of chalcogenide glasses

5.1. Introduction

The following chapter will present an investigation into the nonlinear optical properties of a series of chalcogenide glasses (ChGs). The chapter starts with an introduction in chalcogenide glasses; their unique properties, which make them very attractive candidates for a range of photonic and optoelectronic applications, are discussed. After that the nonlinear optical measurements of a series of ChGs are presented. These measurements are associated with three different projects. The first project was concerned with the nonlinear optical characterisation of a germanium arsenic selenide ($Ge_{22}As_{20}Se_{58}$) glass known as GASIR-1 provided by Umicore [143] and a gallium lanthanum sulphide glass ($Ga_{26}La_{14}S_{60}$) known as GLS provided by the ORC of Southampton University. If a glass with a high nonlinear switching figure of merit was identified from this study it would be considered for a substrate material for waveguide and device fabrication via ULI, provided that high optical quality samples could be repeatedly produced. After that, and under the second project, the nonlinear optical characterisation of chromium doped zinc selenide (Cr:ZnSe) was performed. Cr:ZnSe is one of the materials extensively studied by the NLO group for the development of active mid-infrared devices, having already published a number of results regarding the realisation of mid-infrared Cr:ZnSe channel waveguide lasers via ULI [144-147]. The next step in this project is to achieve mode-locked operation of the already developed lasers by using the Kerr-lens mode-locking method. The investigation performed here provided the nonlinear refractive index coefficient of Cr:ZnSe, which is necessary upon designing the laser cavity when the KLM method is used for mode-locking. Finally, the chapter concludes with the nonlinear optical characterisation of two novel telluride and phosphate glasses. These glasses were provided by the department of science and technology of the Polytechnic University of Torino under a collaborative project aiming to assess the potential of these novel glasses in the development of near- and mid-infrared optical devices. In this project were also involved the optoelectronics research centre of Southampton University and the Fraunhofer centre for applied photonics. The results obtained for the tellurite glass from this study were combined with thermal as well as spectroscopic characterisation results

from the other partners of this collaborative project and presented at the International Conference on Transparent Optical Networks (ICTON 2015) [148].

5.2 Chalcogenide glasses

The name chalcogenide originates from the Greek word "chalcos" meaning ore and "gen" meaning formation, therefore the term chalcogenide in a broader interpretation is considered to mean ore former [149]. However, the term "chalcogen" is now used to describe the members of group 16 of the periodic table. The group consists of oxygen, sulphur, selenium, tellurium and polonium, though oxygen is not included in the chalcogenide category because oxide materials behave rather differently from other chalcogenides, therefore it has become traditional to treat them separately.

Chalcogenide glasses contain as their main constituent one or more of the chalcogen elements, S, Se and Te covalently bonded to network formers such as As, Ge, Sb, Ga, Si or P [150, 151]. The existence of a broad range of possible glass-forming systems with large composition space provides a high degree of freedom and allows for glasses with optical properties, which can be tailored and optimised for specific photonic applications. The particular nature of the covalent bonds in ChGs gives them unique properties for infrared nonlinear applications. More specifically the vibrational energies of the bonds are low because the constituent atoms are particularly heavy leading to a mid-infrared transparency. As a consequence, their low phonon energies reduce multi-phonon quenching defining them as attractive hosts for rare-earth dopants [14, 152] for lasing applications. This high transmission in the mid-infrared range, especially in the 3-5 μm and the 8-12 μm atmospheric windows, makes them very appealing candidates for military ranging applications [153].

The glass densities of ChGs are high compared to oxide glasses, which combined with their strong polarisability leads to a high linear refractive index of $n \approx 2-3$. For example, recent measurements showed that GLS has a linear refractive index of 2.51 at a wavelength of 0.65 μm, and was found to decrease as a function of increasing wavelength until it reaches the value of 2.28 at a wavelength of 2.15 μm [15]. The high linear refractive index is particularly advantageous for developing photonic crystal fibres, since

the high index contrast compared to air allows for improved confinement. Additionally, according to the empirical Miller's rule [154], a high linear refractive index implies a high nonlinear refractive index as well. This has been confirmed by nonlinear measurements [155, 156], which revealed the ultrafast third-order nonlinearities of ChGs to be up to a thousand times those of silica. These high third-order nonlinearities combined with the low multi-photon absorption [157] and high photosensitivity [158] of ChGs allow for switching devices with shorter interaction lengths, lower switching thresholds and higher figures of merit, making ChGs a very good platform for all-optical signal processing applications [159].

Chalcogenide glasses often have their short wavelength absorption edge in the visible region of the electromagnetic spectrum, however unlike crystalline semiconductors they don't exhibit a sharp absorption edge. Instead, the transmission spectra of chalcogenides exhibit an exponential decrease, usually extending several tens of microns in terms of wavelength, until the transmittance is reduced to zero. This exponential decrease, looking like a tail, was first observed by Frantz Urbach in 1953 [160], therefore it is named Urbach tail. The consequence of this is that photon energies of less than half the band-gap can still cause two-photon absorption to occur [161]. Nevertheless, due to the exponential nature of this Urbach tail, n_2 may increase faster than TPA in this region. Consequently, the best performance in terms of nonlinear index strength versus TPA for switching applications will occur just below the bandgap.

The zero dispersion wavelength of chalcogenide glasses usually lies in the mid-infrared region of the electromagnetic spectrum [29]. This combined with their high mid-infrared transparency, low multiphoton absorption and high optical nonlinearities define ChGs as excellent hosts for supercontinuum generation mid-infrared sources for sensing applications [12, 13, 162, 163].

The aforementioned, unique material and optical properties make chalcogenide glasses very attractive for a range of important optoelectronic and photonic applications. Therefore, the nonlinear optical properties, associated to nonlinear absorption and nonlinear refraction, of a series of ChGs were extensively studied via the Z-scan technique in this thesis. The chalcogenides that provided the most advantageous

nonlinearities were chosen as substrate materials for waveguide and device fabrication via ULI for the realisation of relevant near- and mid-infrared applications.

5.3 Chalcogenide glasses nonlinear measurements

The system used for the Z-scan measurements for all the chalcogenide glasses studied in this thesis was the OPA system outlined in section 2.5. The broad wavelength tuneability of this system enabled the study of the nonlinearities of each of the ChGs at different wavelengths depending on the prospective application.

5.3.1. GLS and GASIR-1 Z-scan measurements

As mentioned in section 5.2, chalcogenide glasses exhibit very high nonlinear refractive indices. This is desirable when designing nonlinear optical switching devices as the high nonlinear refractive index will allow for a large phase change per unit length. On the other hand, multiphoton absorption will limit the effectiveness of a nonlinear optical switching device as the material will absorb energy from the pulse and thus limit the interaction length and phase change within the device. Multiphoton absorption is the nonlinear process during which an atom can simultaneously absorb more than one sub-bandgap photons allowing for an electron to be promoted from the valence to the conduction band. The concept of multiphoton absorption was discussed in depth in the section 2.3.2. The aim of this study was to quantify the nonlinear refraction and absorption properties for each of the two glasses, GLS and GASIR-1, via Z-scan. The results obtained from this investigation are used for the estimation of the nonlinear switching figure of merit for each glass, which will give an indication of the suitability of these glasses for optical switching applications.

5.3.1.1 GLS

The GLS samples were provided by the ORC of Southampton University. These samples were prepared by simultaneously melting batches of homogeneously mixed Ga_2S_3 and La_2S_3 powders of various ratios. The ratio of the Ga_2S_3 and La_2S_3 powders initially melted is used to characterise the resulting GLS glass. For example, when saying 45:55 GLS,

one means that the ratio of the Ga_2S_3 to La_2S_3 powders melted to produce the resulting GLS glass was 45% Ga_2S_3 to 55% La_2S_3. By altering the ratio of the Ga_2S_3 and La_2S_3 powders, some of the properties of the resulting product such as linear absorption or glass transition temperature can be altered [15]. This approach offers a high degree of freedom upon producing a range of GLS glasses of different compositions and therefore different properties, for specific applications.

The normalised closed-aperture Z-scan traces along with the theoretical fits for a 1mm thick 65:35 GLS sample at a wavelength of 1550 nm with incident pulse energies of 50 and 100 nJ corresponding to irradiances of 23.5 and 47.1 GW/cm^2 are shown in in figure 5.1. The theoretical fits use equation 2.21 presented in section 2.4 and yield a nonlinear refractive index coefficient of $(9.7 \pm 0.94) \times 10^{-19}\ m^2W^{-1}$. The aperture transmission was set to 50%, whereas the focussing spot was measured to be 26 μm. The focussing spot was the same, 26 μm, for all the measurements presented in this section, for both GLS and GASIR-1, since the same Z-scan setup at the same wavelength of 1550 nm was used for all the measurements.

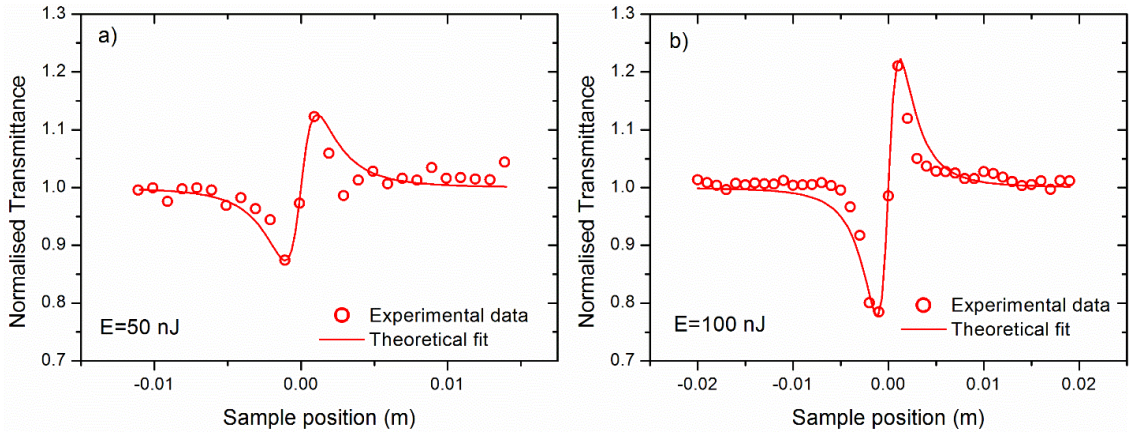

Figure 5.1. Closed-aperture Z-scan traces of 65:35 GLS performed at pulse energies of (a) 50 and (b) 100 nJ, along with the corresponding theoretical fits calculated using an n_2 coefficient of $(9.7 \pm 0.94) \times 10^{-19}\ m^2W^{-1}$.

As the incident pulse energy was increased, the effects of nonlinear absorption were observed on the open-aperture Z-scan traces. GLS has its short absorption edge in the visible region of the electromagnetic spectrum. As discussed in section 5.2, due to the

fact that it doesn't exhibit a sharp edge but an exponential Urbach tail more than one orders of multiphoton absorption are possible. The transmission spectra for a 1 mm thick 65:35 GLS sample, measured with a Perkin Elmer UV/VIS spectrophotometer, illustrating the Urbach tail at the short absorption edge are presented in figure 5.2.

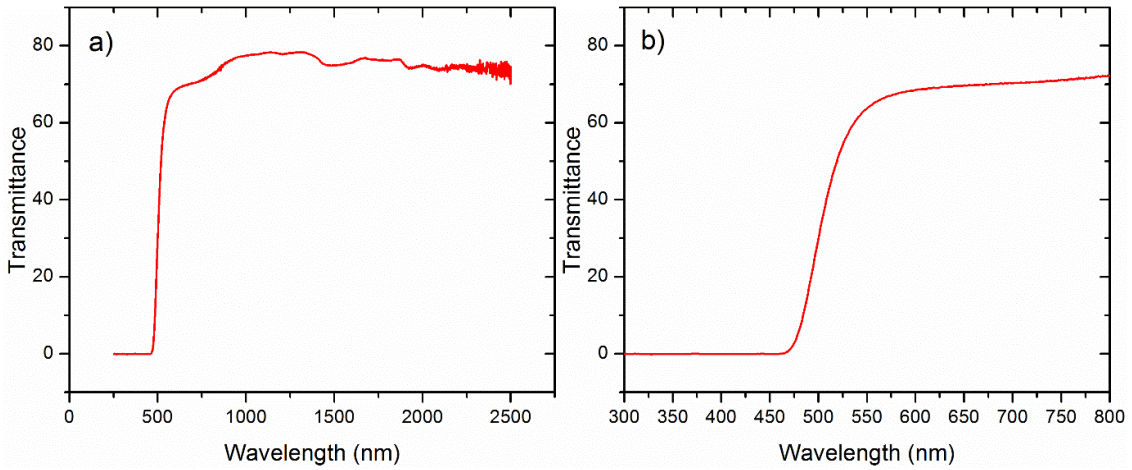

Figure 5.2. (a) Transmission spectrum of 1 mm thick 65:35 GLS extending from 250 to 2500 nm. (b) The same transmission spectrum zoomed-in around the short absorption edge illustrating the Urbach tail of the short wavelength absorption edge in GLS.

GLS presents about 70% transmission at wavelengths longer than ~ 550 nm. Below 550 nm the transmission starts to decrease, but unlike the case of crystalline semiconductors doesn't present a sharp drop rather than gradually decreases until it reaches zero at ~ 475 nm. The wavelength of 550 nm where can be seen as the start of the absorption tail corresponds to a photon energy of $E_{550} = 2.26\ ev$, whereas the wavelength of 475 nm where the transmittance decreases to zero corresponds to a photon energy of $E_{475} = 2.62\ ev$. The wavelength of 1550 nm at which the Z-scan measurements were performed corresponds to a photon energy of $E_{1550} = 0.8\ ev$, therefore the ratios of the edge energies at 550 nm and 475 nm in respect to the incident photon energy are 2.825 and 3.275 respectively. This in practical terms means that for 1550 nm radiation, the dominant nonlinear absorption processes in GLS are expected to be three- and four-photon absorption. The normalised open-aperture Z-scan traces for a 1 mm thick 65:35 GLS at the wavelength of 1550 nm demonstrating the nonlinear absorption processes are presented in figure 5.3.

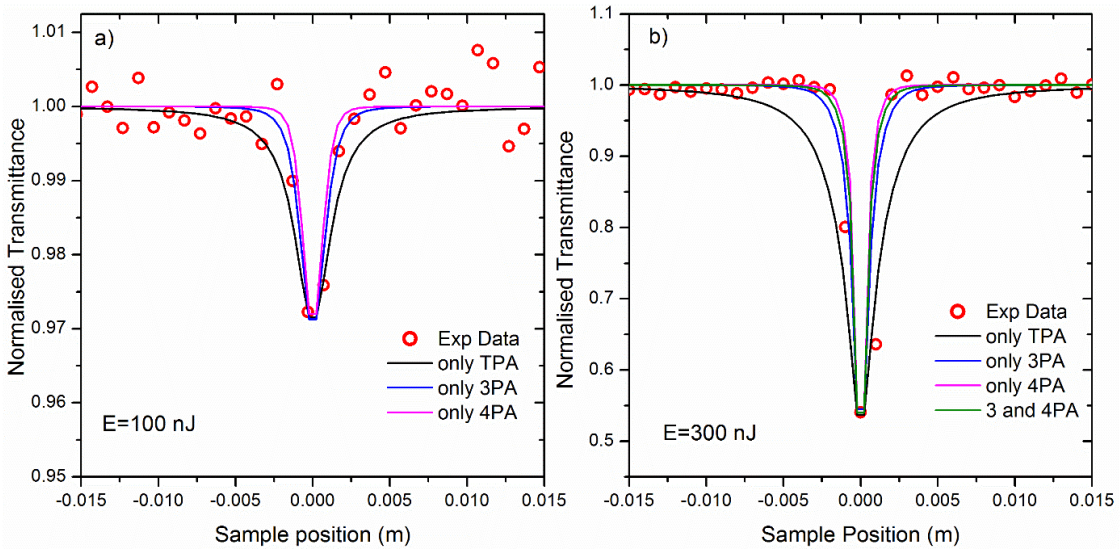

Figure 5.3. Open-aperture Z-scan traces of 65:35 GLS performed at pulse energies of (a) 100 and (b) 300 nJ. The experimental data (red circles) are fitted using two-, three and four-photon absorption processes, represented with the black, blue and pink solid lines respectively. In the case of 300 nJ the experimental data are also fitted using simultaneous three- and four-photon absorption processes, represented with the green solid line.

The spatial resolution of the translation stage used for the open-aperture Z-scan measurements of figure 5.3 was 1mm. As can be seen from the figure, this spatial resolution does not allow the collection of more than three data points as the sample is translated through the focus, which might lead to some uncertainties regarding the order of the predominant multiphoton absorption process. If a translation stage with a higher spatial resolution was available, more data points would be collected in smaller intervals, therefore allowing for a more definite determination of the predominant multiphoton absorption process. Here it should be noted that the limitation in the spatial resolution arises only from the translation stage. The Z-scan experimental technique has not any fundamental limitations regarding its spatial resolution.

The experimental data in figure 5.3 were fitted using either three- or four-photon absorption processes for the reasons discussed above. For comparison purposes the data were also fitted assuming two-photon absorption. The two Z-scans presented in figure 5.3 were performed with incident pulse energies of 100 and 300 nJ corresponding to irradiances of 47.1 and 141.3 GW/cm^2 respectively. As can be seen from the figure the

nonlinear absorption effects start to become apparent at ~100 nJ causing the transmittance to decrease to about 97 %, whereas as the pulse energy is further increased they become more prominent, causing the transmittance to decrease to just above 50 % at 300 nJ.

The theoretical fits for figure 5.3 were obtained by solving the differential propagation equation 2.18 each time, after rearranging the irradiance dependent nonlinear absorption coefficient, *α(I)*, presented in equation 2.19 according to the order of the multiphoton absorption procedure assumed for each fit. For example in the case of only two-photon absorption, equation 2.19 is reduced to $\alpha(I) = \alpha + \beta I$, where β is the TPA coefficient. When assuming only three-photon absorption (3PA), equation 2.19 becomes $\alpha(I) = \alpha + \gamma I^2$, while in the case of only four-photon absorption (4PA) equation 2.19 is reduced to $\alpha(I) = \alpha + \delta I^3$; γ and δ are the 3PA and 4PA coefficients respectively. In the case that simultaneous 3PA and 4PA processes are assumed, equation 2.19 becomes $\alpha(I) = \alpha + \gamma I^2 + \delta I^3$. The nonlinear coefficients obtained from the fits of figure 5.3 are summarised in table 5.1.

Table 5.1 GLS nonlinear absorption coefficients

	Only TPA	Only 3PA	Only 4PA	Simultaneous 3 and 4PA	
Pulse Energy	β $\times 10^{-13}$ m/W	γ $\times 10^{-28}$ m^3/W^2	δ $\times 10^{-43}$ m^5/W^3	γ $\times 10^{-28}$ m^3/W^2	δ $\times 10^{-43}$ m^5/W^3
100 nJ	1.3 ± 0.11	4.5 ± 0.43	13.5 ± 1.27	—	—
300 nJ	8.5 ± 0.81	6.3 ± 0.65	4.4 ± 0.43	2 ± 0.17	3 ± 0.26

Considering first the case of 300 nJ, presented in figure 5.3 (b), there is no significant difference between the experimental data and the theoretical fits obtained for three- (blue solid line) and four-photon (pink solid line) absorption processes, although the 4PA seems to fit the experimental data somewhat better than the 3PA. However, when assuming only TPA processes (solid black line) there is a significant difference between the theoretical fit and the experimental data. This is because as explained earlier, based on the bang-gap to photon energy ratio, for 1550 nm radiation the dominant absorption processes are expected to be three- and four-photon absorption. These high order absorption processes require very high irradiances, which can be achieved only at the focal region of the beam. This is the reason why the open-aperture Z-scan traces present a narrow decrease of the

transmittance localised around the focal region of the beam, causing this way the TPA fit to fail. More specifically, as can be seen in figure 5.3 (b) only three data points, at the focus and 1 mm before and after, present a decreased normalised transmittance lower than 1, whereas the rest of them present a non-varying transmittance indicating that no nonlinear absorption effects occur at distances even as close as 2 mm to the focus.

When assuming simultaneous 3PA and 4PA processes, the theoretical fit lies between the fits of 3PA and 4PA processes occurring separately. In addition, as can be seen from table 5.1, the 3PA and 4PA coefficients for the case of simultaneously occurring three- and four-photon absorption, are in the same order of magnitude and only slightly reduced comparing with the cases of separately occurring 3PA and 4PA processes.

Considering now the case of low pulse energy of 100 nJ, all three theoretical fits for the cases of TPA, 3PA and 4PA do not seem to present any significant differences from the experimental data. By inspecting table 5.1 one can see that the TPA and 3PA coefficients decrease comparing with the case of 300 nJ, which is expected since lower pulse energies would cause weaker absorption, therefore yielding lower absorption coefficients. On the contrary, the 4PA coefficient shows the opposite trend, increasing with lower pulse energies. This disorder implies that at this low pulse energy the dominant procedure is 3PA with probably some contribution from TPA but no 4PA, causing therefore the 4PA fit to fail and give unreasonable and misleading results. This is due to the fact that higher order multiphoton absorption processes like 4PA will require very high irradiances for them to occur, therefore at the low pulse energies, where the nonlinear absorption just starts to become apparent, the irradiance is not sufficiently high to cause any appreciable 4PA effects. However, as the pulse energy is increased the required irradiances are reached and the 3PA and 4PA processes become more prominent with any contribution from TPA becoming negligible.

5.3.1.2 GASIR-1

The GASIR-1 glasses used in this investigation are commercially available and bought by Umicore. Similarly to the case of GLS the nonlinear refraction properties of GASIR-1 were studied with the closed-aperture Z-scan technique at the same wavelength of 1550

nm. Figure 5.4 shows the normalised closed-aperture Z-scan traces along with the theoretical fits for a 1mm thick GASIR-1 sample with incident pulse energies of 10 and 20 nJ corresponding to irradiances of 4.71 and 9.42 GW/cm^2 respectively. The theoretical fits yield a nonlinear refractive index coefficient of $(4.5 \pm 0.38) \times 10^{-18}\ m^2W^{-1}$. This coefficient, is higher comparing with the case of GLS which presented a nonlinear refractive index coefficient of $9.7 \times 10^{-19}\ m^2W^{-1}$. This means that GASIR-1 may have a higher figure of merit than GLS for nonlinear switching applications, although the information about the nonlinear absorption of GASIR-1 are needed for the FOM to be quantified.

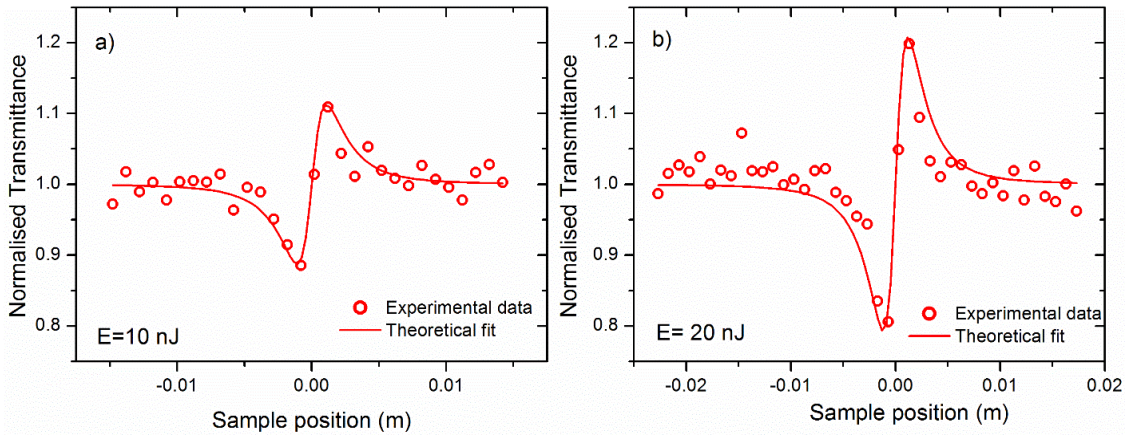

Figure 5.4. Closed-aperture Z-scan traces of GASIR-1 performed at pulse energies of (a) 10 and (b) 20 nJ, along with the corresponding theoretical fits calculated using an n_2 coefficient of $(4.5 \pm 0.38) \times 10^{-18}\ m^2W^{-1}$.

GASIR-1 like GLS has its short absorption edge in the visible region of the electromagnetic spectrum, presenting also the same exponential Urbach tail. This means that more than one orders of multiphoton absorption are possible in the case of GSIR-1 as well. The Urbach tail of GASIR-1 was observed following the same method described for GLS and was found to extend from ~ 800 nm at which the transmission started to decrease until ~ 670 nm at which the transmission reached zero. The two wavelengths of 800 and 670 nm correspond to edge energies of $E_{800} = 1.55$ and $E_{670} = 1.85\ ev$ respectively, therefore comparing with the incident photon energy at 1550 nm ($E_{1550} = 0.8\ ev$) the dominant nonlinear absorption processes in GASIR-1 are expected

to be two- and three-photon absorption. The normalised open-aperture Z-scan traces for a 1 mm thick GASIR-1 sample at the wavelength of 1550 nm are presented in figure 5.5.

The Z-scan traces were fitted using either two- or three-photon absorption processes for the reasons discussed above. For comparison purposes the experimental data were also fitted assuming four-photon absorption. The two Z-scans presented in figure 5.5 were performed with incident pulse energies of 20 and 50 nJ corresponding to irradiances of 9.42 and 23.55 GW/cm^2 respectively. As can be seen from the figure the nonlinear absorption effects start to become apparent at ~20 nJ causing the transmittance to decrease to about 95 %, whereas as the pulse energy is further increased they become more prominent, causing the transmittance to decrease to about 50 % at 50 nJ.

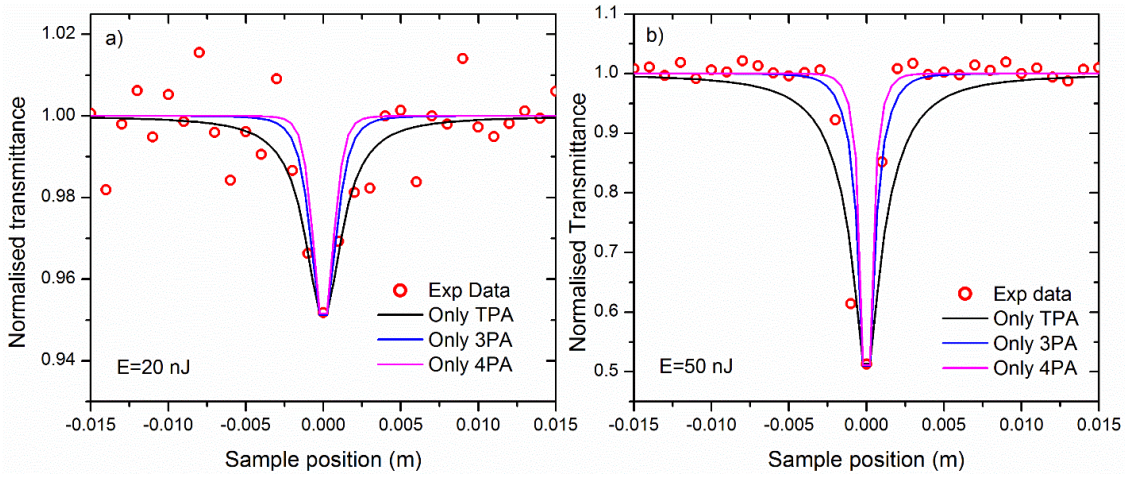

Figure 5.5. Open-aperture Z-scan traces of GASIR-1 performed at pulse energies of (a) 20 and (b) 50 nJ. The experimental data (red circles) are fitted using two-, three- and four-photon absorption processes, represented with the black, blue and pink solid lines respectively.

In the case of GLS the nonlinear absorption effects started to become apparent at pulse energies of ~100 nJ and in order for the transmittance to decrease to about 50% the pulse energies required were just above 300 nJ, much higher than the ones required for GASIR-1. This behaviour demonstrates that GASIR-1 presents much stronger absorptive nonlinearities than GLS. This is not desirable when designing devices for nonlinear

switching applications or continuum generation as any absorption will deplete the pulse propagating through the sample and therefore limit the efficiency.

The theoretical fits for figure 5.5 were obtained by solving the differential propagation equation 2.18 each time, after rearranging the irradiance dependent absorption coefficient, *α(I)*, according to the order of multiphoton absorption procedure assumed for each fit as described in section *5.3.1.1*. The nonlinear coefficients obtained from the fits of figure 5.5 are summarised in table 5.2.

Table 5.2 GASIR-1 nonlinear absorption coefficients

	Only TPA	Only 3PA	Only 4PA
Pulse Energy	β $\times 10^{-12}$ m/W	γ $\times 10^{-26}$ m^3/W^2	δ $\times 10^{-40}$ m^5/W^3
20 nJ	1.13 ± 0.12	2 ± 0.17	3.11 ± 0.26
50 nJ	5.3 ± 0.49	2.36 ± 0.21	0.98 ± 0.1

Considering first the case of 20 nJ, the two- (solid black line) and three-photon (solid blue line) absorption processes fit the experimental data (red circles) better than the four-photon (solid pink line) absorption process, which seems to be narrower than the experimental data around the focus. This is expected, since based on the band edge of GASIR-1 in respect with the incident photon energy at 1550 nm the dominant processes are expected to be two- and three-photon absorption. Additionally, as explained earlier at the low pulse energies when the nonlinear absorption just starts to become apparent, the irradiances are not sufficiently high to cause any appreciable 4PA effects. However, as the irradiance is increased, higher order multiphoton absorption processes come in play. This causes the TPA fit in figure 5.5 (b) to fail, while the 3PA and 4PA processes fit the experimental data very well suggesting that at the high irradiances the dominant processes are 3PA and 4PA. Furthermore, due to GASIR-1's very strong absorptive nonlinearities as the irradiance keeps increasing it is possible for even higher orders of multiphoton absorption to occur.

Similarly to the case of GLS the TPA and 3PA coefficients for GASIR-1 presented in table 5.2 increase with increasing pulse energy due to the stronger absorption from the

sample, whereas the 4PA coefficient shows the opposite trend, decreasing with higher pulse energies. This as explained earlier is due to the fact that at the low pulse energies, when the nonlinear absorption just starts to become apparent, the irradiance is not sufficiently high to cause any appreciable 4PA effects, therefore fitting the experimental data assuming 4PA processes gives misleading and unreasonable values for the 4PA coefficient.

Finally, by comparing the results of tables 5.1 and 5.2 one can see that the nonlinear absorption coefficients for GASIR-1 are higher than the ones for GLS for all nonlinear absorption processes. More specifically the TPA coefficients for GASIR-1 are in the orders of magnitude of 10^{-12} m/W, whereas for GLS are one order of magnitude lower in the range of 10^{-13} m/W. Similarly, the 3PA coefficients are two orders of magnitude higher for GASIR-1; they are in the orders of 10^{-26} m^3/W^2 as opposed to 10^{-28} m^3/W^2 for the case of GLS. Likewise, the 4PA coefficients deduced at the high irradiances used for each sample, where 4PA processes are expected, are in the orders of 10^{-41} m^5/W^3 for GASIR-1 and 10^{-43} m^5/W^2 for GLS. This in practical terms means that GASIR-1 presents much stronger absorptive nonlinearities than GLS, which as discussed earlier is highly undesirable when designing devices for optical switching or continuum generation since any absorption will deplete the propagating through the sample pulse and therefore limit the efficiency.

5.3.1.3 Discussion

The aim of this investigation was to identify a material with a high switching FOM, which would then be used as a substrate material for waveguide and device fabrication via ULI. In order for a material to possess a favourable FOM for nonlinear switching applications it must present high nonlinear refractive index and low multiphoton absorption. A high nonlinear refractive index will allow for a large phase change per unit length, while on the other hand multiphoton absorption will absorb energy from the propagating pulse and therefore limit the interaction length and phase change within the device.

The high nonlinear refractive indices of both GLS and GASIR-1 make them potentially attractive for nonlinear optical switching applications. However, in order to assess their

suitability for such applications the multiphoton absorption processes must be taken into account. A typical figure of merit for optical switching devices for materials that present 3PA can be defined as [164, 165]:

$$FOM = \frac{n_2}{\lambda \gamma I} \tag{5.1}$$

where, n_2 is the nonlinear refractive index, γ is the 3PA coefficient, λ is the operating wavelength and I is the irradiance. The 3PA figure of merit was chosen to characterise the materials since 3PA is among the dominant absorption processes at low and high irradiances for both GASIR-1 and GLS. By using the measured values for the n_2 a 3PA coefficients, for both GASIR-1 and GLS, in equation 5.1 the FOM for each material was calculated. Equation 5.1 gives a FOM of 2.95 for GLS, whereas it yields a FOM of 1.54 for GASIR-1, approximately half of that calculated for GLS. This is due to the fact that GASIR-1 presents very strong absorptive nonlinearities, therefore reducing its FOM. The higher FOM of GLS makes it more favourable for nonlinear optical switching devices. Moreover, GLS is arsenic free, making it safer to handle than the arsenic based GASIR-1. It also means that no changes would be required to the established ULI rig at Heriot-Watt in order to ensure no human contact with airborne particulates in case that GLS was chosen as our host material. The above outlined advantages of GLS over GASIR-1 combined with the fact that high optical quality samples could be repeatedly produced led to the choice of GLS as the host material for waveguide and device fabrication via ULI.

5.3.2. ZnSe and Cr:ZnSe Z-scan measurements

As already discussed the mid-infrared region of the electromagnetic spectrum is of great interest to the NLO group, for the realisation of relevant devices and applications, such as waveguide lasers [145-147] and supercontinuum generation sources [12, 13]. One of the materials that the NLO group extensively uses is chromium doped Zinc Selenide, having already published a number of results regarding the development of mid-infrared Cr:ZnSe channel waveguide lasers fabricated via the ULI technique [145-147]. The next step is to mode-lock these lasers. The most appealing technique to achieve this is Kerr-Lens mode-locking due to the host ZnSe very high nonlinear refractive index comparing

to other chromium hosts like Yttrium aluminium garnet (YAG). The KLM technique which is based on the optical Kerr effect was introduced in section 1.2. According to this effect the spatial properties of a propagating Gaussian beam in a nonlinear medium are altered because the refractive index near the beam axis, where the irradiance is higher, is increased relative to that of the beam periphery. This causes a self-focussing effect which the KLM technique exploits to achieve laser mode-locking. Naturally this self-focussing effect is expected to be stronger in materials with a high n_2 coefficient such as chalcogenides. Therefore, the KLM technique is very promising upon achieving mode-locked operation for our Cr:ZnSe lasers. As can be deduced the nonlinear refractive index of Cr:ZnSe will play a very important role upon designing the laser cavity, since the principle of the KLM technique is based on it. In this study and in consultation with other members of the NLO group who work on the Cr:ZnSe project, the n_2 coefficient of a polycrystalline Cr:ZnSe sample, doped to $8.5 \times 10^{18}\ cm^{-3}$ ions, was measured using the closed-aperture Z-scan technique with aim to use this valuable information upon designing the laser cavity for pulsed operation. For comparison purposes, Z-scan measurements were also performed on an undoped polycrystalline ZnSe sample revealing this way the effects of the chromium dopant on the host ZnSe. Both samples are commercially available and bought by IPG photonics, however the supplier did not reveal the detailed molar composition of the two samples.

Figure 5.6 presents the normalised closed-aperture Z-scan traces along with the theoretical fits for ZnSe and Cr:ZnSe at a wavelength of 2500 nm with incident pulse energies of 110 and 90 nJ respectively, which correspond to irradiances of 36.4 and 29.8 GW/cm^2. The wavelength was chosen to be 2500 nm due to the fact that the operating wavelengths of all the Cr:ZnSe laser sources developed from the NLO group are in the region of 2077 to 2777 nm.

The line of best fit in figure 5.6 (a) yields a nonlinear refractive index coefficient of $(4 \pm 0.36) \times 10^{-19}$ m^2/W for ZnSe, whereas the line of best fit in figure 5.6 (b) yields a nonlinear refractive index coefficient of $(2.8 \pm 0.24) \times 10^{-19}$ m^2/W for the case of Cr:ZnSe. Due to the small difference in the values for the n_2 coefficients for each of the samples, aside the two Z-scan traces presented here, more Z-scans were performed at a range of different pulse energies all showing the similar trend.

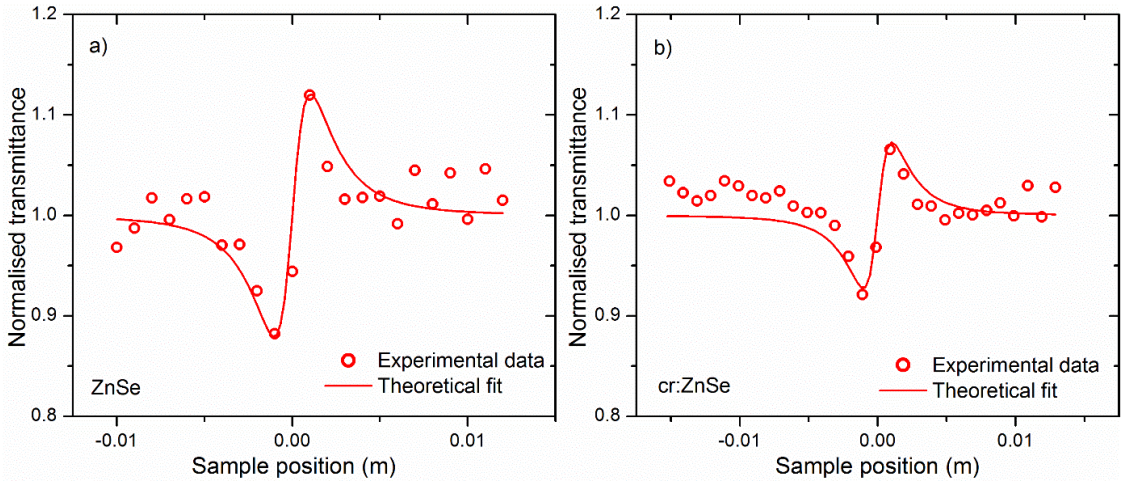

Figure 5.6. Closed-aperture Z-scan traces of (a) ZnSe and (b) Cr:ZnSe, along with the corresponding theoretical fits, showing the effects of the chromium dopant on the refractive nonlinearities of the ZnSe substrate.

The chromium dopant slightly reduces the nonlinear refractive index of the host ZnSe to about 70%. This in practical terms means that a lower doping concentration would allow for a higher nonlinear refractive index, which would be desirable in the case of KLM. On the other hand, a lower chromium concentration would reduce the laser efficiency in regards of output power. Therefore, for optimum pulsed operation, there will have to be a trade-off between nonlinearity and output power. Finally, it is worth noting that the n_2 value obtained for the Cr:ZnSe sample was used in the calculations for the design of the laser cavity.

The effects of the chromium dopant on the absorptive nonlinearities of the host ZnSe were investigated as well. The normalised open-aperture Z-scan traces for the ZnSe and Cr:ZnSe samples at the same wavelength of 2500 nm with an incident pulse energy of 180 nJ which corresponds to an irradiance of $59.6\ GW/cm^2$ are presented in figure 5.7.

As can be seen from the figure, the nonlinear absorption is the same for both the doped and undoped samples. More specifically with the pulse energy of 180 nJ the transmittance decreases to about 87 % for both cases, verifying that the chromium dopant does not have any effect on the absorptive nonlinearities of the host ZnSe substrate. Aside the two traces presented here, more open-aperture Z-scan measurements were performed at a range of

pulse energies always showing the same levels of nonlinear absorption for both samples. The highest pulse energy used for this investigation was 300 nJ or in terms of irradiance *99.4 GW/cm*^{2} and caused the transmittance to decrease to about 74 %.

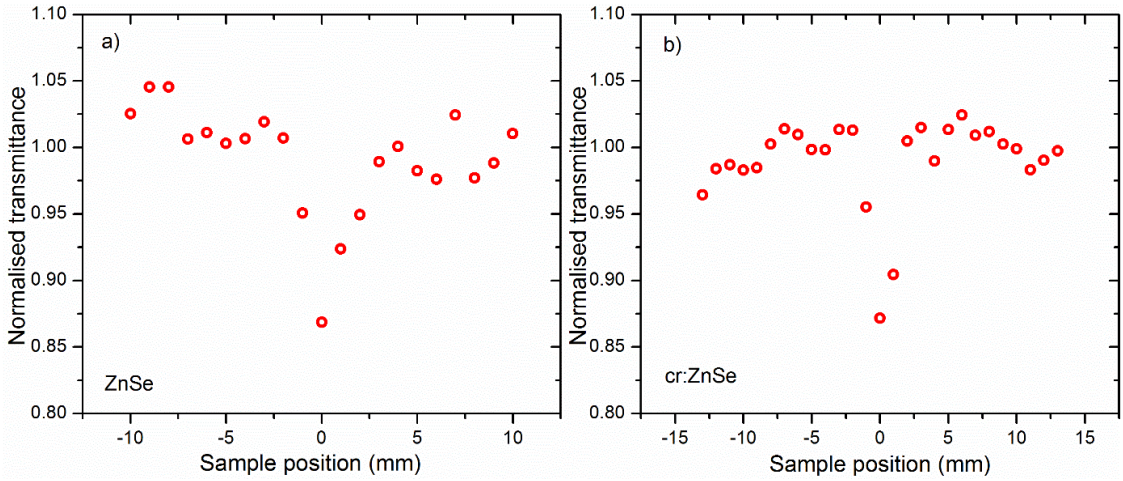

Figure 5.7. Closed-aperture Z-scan traces of (a) ZnSe and (b) Cr:ZnSe at a pulse energy of 180 nJ showing the effects of nonlinear absorption.

This is the expected behaviour since the peak of the absorption cross section for chromium lies at ~1750 nm, about 750 nm away from the wavelength of 2500 nm at which the Z-scan measurements were performed. At 2500 nm the absorption cross section of chromium becomes very small therefore any absorption from the chromium ions at this wavelength will be negligible. The absorption and emission cross sections of a Cr:Znse sample can be found in a previous publication of the NLO group demonstrating an ultrabroad mid-Infrared tunable Cr:Znse channel waveguide laser fabricated via ULI [145]. The specific publication also includes a table with the absorption and emission cross sections of Cr:Znse around the emission wavelengths spanning from 2077 to 3000 nm and concludes that the absorption cross section of Cr:Znse becomes zero for wavelengths above 2600 nm.

The ZnSe and Cr:Znse have their short absorption edge in the visible region of the electromagnetic spectrum presenting the characteristic Urbach tail of chalcogenide glasses. This tail extends from ~550 nm, where the transmission starts to decrease, to ~475 nm at which the transmittance reaches zero. These two wavelengths correspond to

edge energies of $E_{550} = 2.26\, ev$ and $E_{475} = 2.62\, ev$ respectively. Therefore, with an incident wavelength of *2500 nm* which carries a photon energy of $E_{2500} = 0.5\, ev$, the dominant nonlinear absorption processes would expected to be five- and six-photon absorption. However, these high order multiphoton absorption processes would require extremely high irradiance levels to be reached for them to occur. Even at the highest irradiances of *99.4 GW/cm^2* used here the moderate decrease in transmittance to about 74 % indicates that lower order multiphoton procedures take place. If the expected five- and six-photon absorption procedures occurred, then the decrease in transmittance would be expected to be much stronger. This is verified by comparing with the case of GASIR-1 studied in section *5.3.1.2*. As discussed in that section, based on the band edges of GASIR-1 and the incident photon energy, the expected dominant multiphoton processes were two- and three-photon absorption. These are the lowest possible multiphoton absorption processes and require much lower irradiances than the higher order processes, therefore are the ones that occurred in GASIR-1. This caused the transmittance to decrease much faster, requiring much lower pulse energies than the ones used here. More specifically with a pulse energy of only 20 nJ the transmittance decreased to about 95 %, whereas with an increase of only 30 nJ in pulse energy reaching 50 nJ the transmittance rapidly decreased to about 50 %. On the contrary, in the case of Znse and Cr:ZnSe the decrease in transmittance was much slower. For an incident pulse energy of 180 nJ the transmittance decreased to 87%, whereas for an incident pulse energy of 300 nJ the decrease only reached 74 %. This behaviour indicates that the decrease in transmittance is not due to the expected dominant five- and six-photon absorption processes but due to some weak contribution from lower order multiphoton absorption processes. Due to the fact that the irradiances used here were not sufficiently high to trigger the expected high order multiphoton absorption processes, it was deemed purposeful not to try to fit the open-aperture experimental data to avoid any misleading and unreasonable results regarding the nonlinear absorption coefficients.

5.3.3 Tellurite and phosphate glasses Z-scan measurements

In this section the optical characterisation of two novel tellurite and phosphate glasses provided by the department of science and technology of the Polytechnic University of Torino is presented. The main aim of this project was to develop novel nonlinear glasses

with enhanced mechanical, thermal and optical properties for near- and mid-infrared applications. Due to the knowledge and expertise of the NLO group upon measuring optical nonlinearities and the established Z-scan setup at Heriot-Watt University, we were contacted by our collaborators at the Polytechnic University of Torino in order to perform the nonlinear optical characterisation of those glasses at Heriot-Watt. The results obtained for the tellurite glass were combined with thermal and spectroscopic characterisation results obtained from the other partners of this collaborative project and presented at the International Conference on Transparent Optical Networks (ICTON 2015) [148].

5.3.3.1 Tellurite glass

The nonlinear optical properties of the tellurite glass were investigated via the closed-aperture Z-scan technique. The normalised closed-aperture Z-scan traces along with the theoretical fits for a 600 μm thick tellurite sample are presented in figure 5.8. These were performed at a wavelength of 1550 nm with incident pulse energies of 100 and 300 nJ corresponding to irradiances of 47.1 and 141.3 GW/cm^2 respectively. The theoretical fits use equation 2.21 presented in section 2.4 and yield a nonlinear refractive index coefficient of $(4.6 \pm 0.41) \times 10^{-19}$ m^2W^{-1}. The aperture transmission was set to 50%, whereas the focussing spot was measured to be 26 μm.

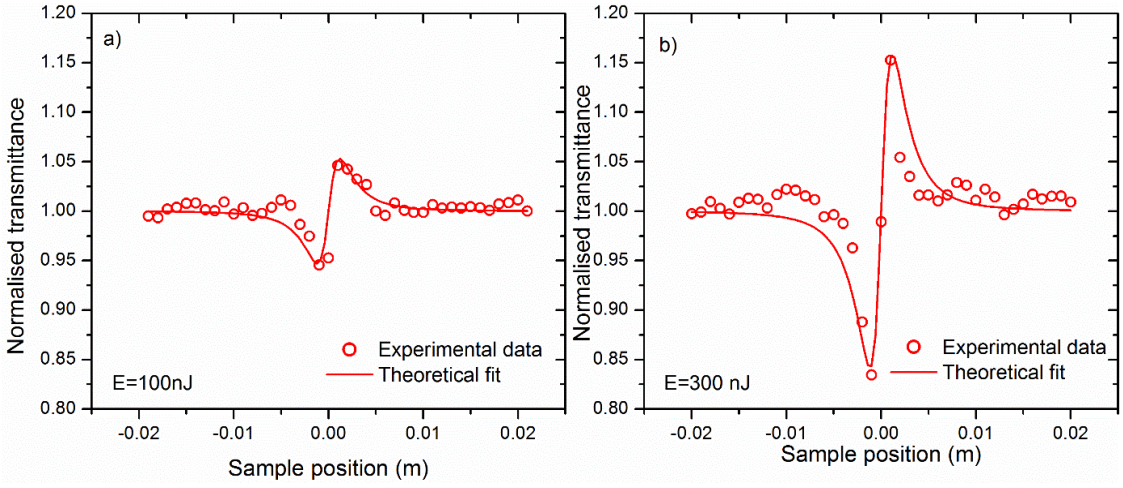

Figure 5.8. Closed-aperture Z-scan traces of the tellurite glass performed at pulse energies of (a) 100 and (b) 300 nJ, along with the corresponding theoretical fits calculated using an n_2 coefficient of $(4.6 \pm 0.41) \times 10^{-19}$ m^2W^{-1}.

5.3.3.2 Phosphate glass

Similarly to the case of the tellurite glass, the nonlinear optical properties of the phosphate glass were studied via the closed-aperture Z-scan technique. Figure 5.9 plots the normalised closed-aperture Z-scan traces along with the theoretical fits for a 300 μm thick phosphate sample. These were also performed at a wavelength of 1550 nm at the same irradiances of 47.1 and 141.3 GW/cm^2. The theoretical fits in this case yield an n_2 coefficient of $(6.5 \pm 0.58) \times 10^{-19}\ m^2W^{-1}$.

As can be seen from the fitting results of figures 5.8 and 5.9, the phosphate glass presents a higher n_2 coefficient than the tellurite glass. Although both glasses possess lower n_2 coefficients than the GLS and GASIR-1 glasses studied in section 5.3.1, which presented the nonlinear refractive index coefficients of $9.7\times10^{-19}\ m^2W^{-1}$ and $4.5\times10^{-18}\ m^2W^{-1}$ respectively. However, no multiphoton absorption effects were observed, in both the phosphate and tellurite glasses, up to the highest irradiances of 141.3 GW/cm^2 outlined above. This means that their figure of merit may be very favourable, and superior to that of GLS and GASIR-1, for nonlinear switching applications and continuum generation. Although, first a number of other properties, such as mechanical and thermal, must be quantified in order to deduce whether there is real potential in these glasses for realising relevant nonlinear infrared applications.

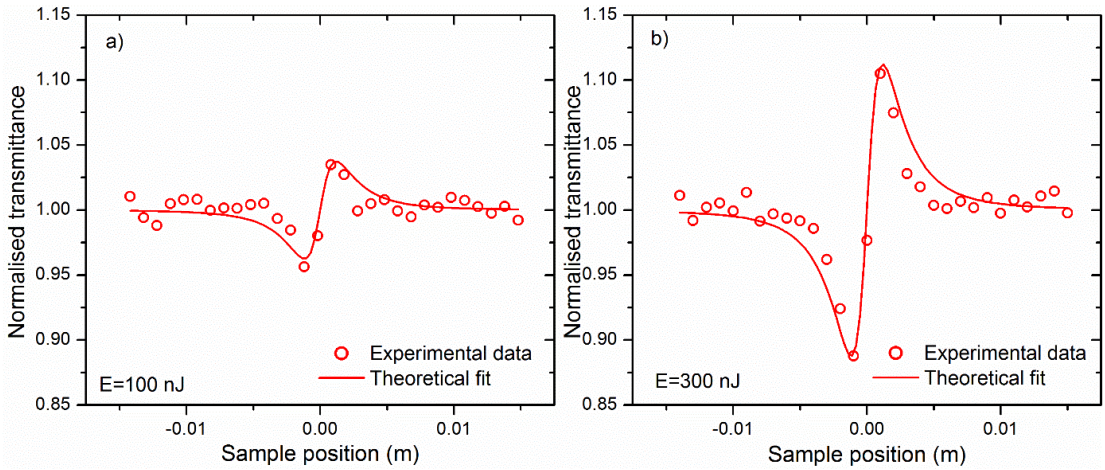

Figure 5.9. Closed-aperture Z-scan traces of the phosphate glass performed at pulse energies of (a) 100 and (b) 300 nJ, along with the corresponding theoretical fits calculated using an n_2 coefficient of $(6.5 \pm 0.58) \times 10^{-19}\ m^2W^{-1}$.

5.4. Summary

This chapter has presented the investigation into the nonlinear optical properties of a series of chalcogenide glasses. First an introduction into the unique material and optical properties of chalcogenide glasses was performed. Thereupon the nonlinear optical characterisation of two chalcogenide glasses, GLS and GASIR-1, followed. The main aim of this project was to determine the optical switching FOM of each glass, which would then give an indication of the suitability of these glasses for optical switching applications. GASIR-1 presented a higher nonlinear refractive index coefficient of 4.5×10^{-18} m^2W^{-1} as opposed to GLS, which presented an n_2 coefficient of 9.7×10^{-19} m^2W^{-1}. However, GASIR-1 presented much stronger absorptive nonlinearities as well, with all the nonlinear absorption coefficients related to two-, three- and four-photon absorption processes being more than one order of magnitude higher than the ones measured for GLS. This led to a lower figure of merit for GASIR-1, which was estimated to be 1.54 as opposed to GLS which presented a FOM of 2.95. Subsequently GLS was chosen as a host material for waveguide and device fabrication via the ULI technique. Afterwards, the nonlinear optical characterisation Cr:ZnSe was presented. This work was performed in consultation with other members of the NLO group who work on a project regarding the development of Cr:ZnSe waveguide lasers. The main aim of this investigation was to obtain the nonlinear refractive index coefficient of Cr:ZnSe. The knowledge of this coefficient is essential for the calculations upon designing the laser cavity in the case the KLM technique is chosen for mode-locking. Finally, the chapter concluded with the nonlinear optical characterisation of two novel telluride and phosphate glasses. This study was conducted in collaboration with the department of science and technology of the Polytechnic University of Torino, the optoelectronics research centre of Southampton University and the Fraunhofer centre for applied photonics. The results obtained for the telluride glass were combined with thermal and spectroscopic characterisation results obtained from the other partners of this collaborative project and presented at the International Conference on Transparent Optical Networks (ICTON 2015) [148].

Chapter 6. Optical characterisation of ultrafast laser inscribed gallium lanthanum sulphide waveguides.

6.1. Introduction

The work presented in this chapter focuses on the fabrication and characterisation of ultrafast laser inscribed waveguides in gallium lanthanum sulphide glasses. The main objective of this investigation was to fabricate and characterise highly nonlinear mid-infrared waveguides, which could then be used as the building block of more advanced mid-infrared devices. As outlined in section 5.3.1, GLS was selected as the substrate material due to its high nonlinear refractive index and low multiphoton absorption, which can lead to a very favourable figure of merit for nonlinear switching applications. The first demonstration of ultrafast laser inscription in GLS was from our collaborators at the ORC of Southampton University [166], where they realised near-infrared waveguides with structures that exhibited a small positive refractive index change. In a different work, previous members of the NLO group demonstrated mid-infrared spectral broadening in ultrafast laser inscribed GLS waveguides spanning over 3500 nm, from 1700 to 5200 nm [12, 13].

The ultrafast laser inscription technique which was introduced in section 2.7 relies on the nonlinear absorption of sub-bandgap photons to induce permanent changes in a material. As already discussed in that section this process involves the use of ultrashort pulses of light tightly focussed within the volume of a dielectric material. These ultrashort pulses generate high optical field irradiances in the focal volume, which trigger nonlinear absorption processes, resulting in an energy transfer to the material lattice. With careful selection of the laser inscription parameters this energy transfer can manifest as a positive refractive index change, which is exploited to fabricate waveguiding structures in bulk substrates. In the case of standard fibres, the refractive index profile (RIP) distribution is step-index due to the fact that the core and cladding are consisted of different materials with very well defined different refractive indices. However, due to the particular nature of ULI the fabricated waveguides are not expected to present the same step-index profile. The laser inscription parameters will have a significant impact on the refractive index profiles of the ULI fabricated waveguides. The knowledge of the RIP distribution of such

ULI waveguides is essential in order to fully comprehend their guiding properties. Most importantly the information regarding the effects the inscription parameters have upon the refractive index profiles will provide extremely useful tools for tailoring the RIPs of ULI fabricated structures for specific applications.

In this investigation high quality optical waveguides were fabricated in GLS substrates via the ULI technique. The optimum inscription parameters which yielded the best quality waveguides are discussed and the morphology of the fabricated waveguides is presented. Afterwards the refractive index profiling, which is the most critical parameter regarding the guiding properties of these waveguides is presented. The effects the inscription parameters have upon the refractive index profiles are investigated and discussed. After that the dispersion measurements, for both the waveguides and bulk substrate, over a wide range of wavelengths in the near- and mid-infrared region of the electromagnetic spectrum spanning from ~1.3 to 4.5 μm are presented. The knowledge of the dispersion at the operating wavelength is essential as it will affect the propagation properties of the beam and it is often desirable for optical devices to operate as close as possible to the zero dispersion wavelength. The wide range at which the dispersion measurements were undertaken enabled the determination of the ZDW for both the waveguides and bulk GLS. The results obtained from the refractive index profiling and dispersion measurements were combined and published in Optics Express [29].

6.2. Ultrafast laser inscription of waveguides in gallium lanthanum sulphide

All the waveguides used in this investigation were fabricated using the ultrafast laser inscription setup outlined in section 2.8. The laser system used was the IMRA® laser presented in section 2.8.1 emitting 360 fs pulses at a pulse repetition rate of 500 kHz. The substrates were mounted on air bearing Aerotech stages and the pulses from the inscription laser were focused inside the substrates to a depth of 240 μm from the top surface using 0.4 NA and 0.6 NA aspheric lenses. The pulse energies incident on the sample varied from 52 to 110 nJ using four different translation speeds, 1, 4, 8 and 12 mm/s with the substrates being moved perpendicular to the laser beam direction. The variation of the inscription parameters, such as focussing objective, inscription pulse energies and sample translation speeds, enabled the investigation of the impact these

parameters have upon the refractive index profiles and dispersion of the waveguides. After fabrication the input and output facets of the substrates were polished to optical quality. The optical quality of all the substrates used was very good; no variations in the waveguide properties were observed between different substrates, which points out one of the major advantages of ULI. The guiding properties of the structures fabricated with this technique are easily and accurately repeatable given that the quality of the substrates is ensured and the same inscription parameters are used.

6.3. Waveguide morphology

The multiscan inscription technique was implemented for the fabrication of the waveguides. This technique uses multiple single-scan modified regions with a small horizontal offset to build up a desired cross-section. The resulting waveguides with this technique present rectangular cross-sections. This process is depicted in figure 6.1. The horizontal offset adds another variable fabrication parameter Δx.

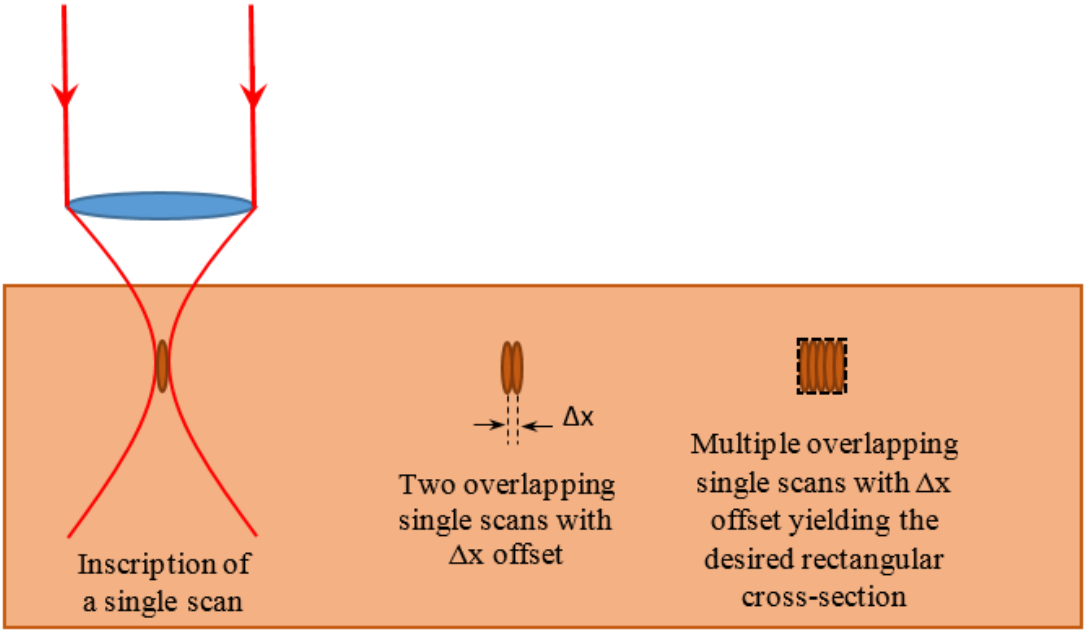

Figure 6.1. Schematic outlining the multiscan inscription process (reproduced from [33]).

In order to determine the best inscription parameters, before the multiscan waveguides are inscribed, a "parameter search" is performed. This means that single scans are inscribed within the substrates varying the inscription parameters and observing the single-scan modified regions each time. Then the single scans that present modified regions that approximate a straight vertical line are chosen for the inscription of the multiscan waveguides. This will become more clear when the inscription of single scans in GLS is presented.

The microscope images viewed in transmission mode showing the modified regions of single-scans inscribed in a GLS substrate using a 0.4 NA aspheric lens at three different pulse energies using five different translation speeds for each pulse energy are presented in figure 6.2.

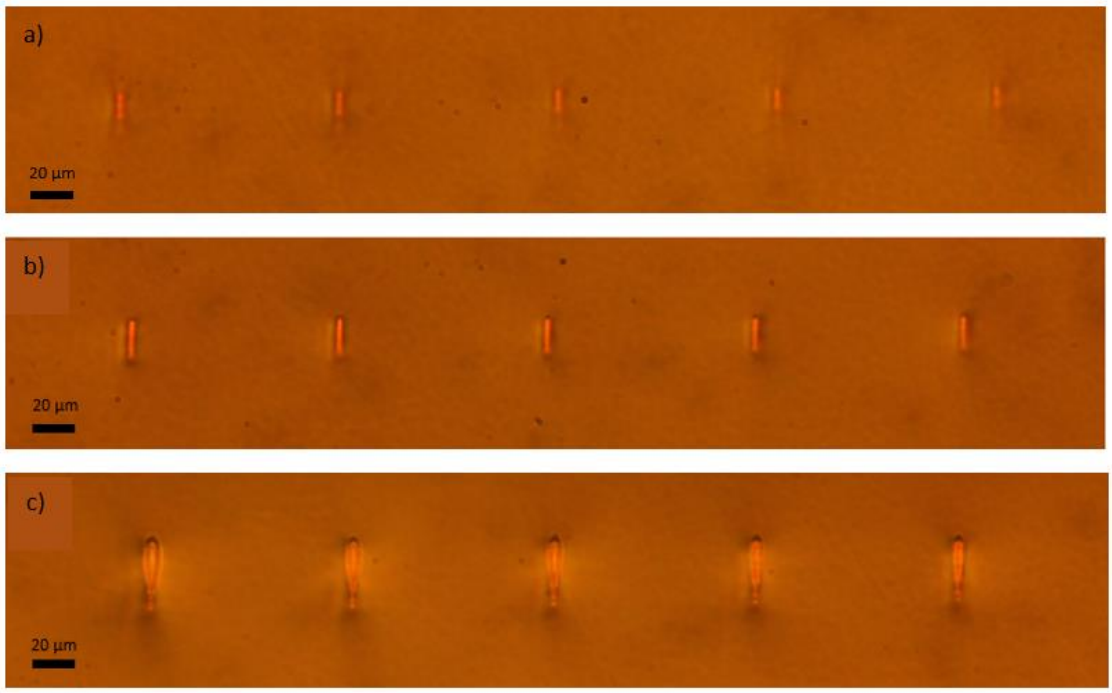

Figure 6.2. (a) Five single scans at a pulse energy of 38 nJ each inscribed with a different translation speed, namely 0.4, 0.8, 1.2, 1.6 and 2 mm/s from left to right. (b) Five single scans at a pulse energy of 58 nJ each inscribed with a different translation speed. (c) Five single scans at a pulse energy of 110 nJ each inscribed with a different translation speed. The translation speeds for the scans presented in (b) and (c) were 4, 8, 12, 16 and 20 mm/s from left to right.

The single scans presented in figure 6.2 (a) were inscribed with a pulse energy of 38 nJ using a different sample translation speed for each scan, namely 0.4, 0.8, 1.2, 1.6 and 2 mm/s from left to right. Figure 6.2 (b) presents five single scans inscribed with a pulse energy of 58 nJ, whereas figure 6.2 (c) presents five single scans inscribed with a pulse energy of 110 nJ. The translation speeds used for the single scans presented in 6.2 (b) and (c) were 4, 8, 12, 16 and 20 mm/s from left to right.

The pulse energy is the inscription parameter with the biggest impact in the modified region. At low pulse energies the modification of the substrate is weaker, leading to a faded modified region when viewed under the microscope. This case is presented in figure 6.2 (a), where the pulse energy of 38 nJ was used for the inscription of the single scans. As the pulse energy is increased the substrate modification becomes stronger, resulting in clear bright modified regions. This can be seen in figure 6.2 (b), where with an increase of 20 nJ comparing with figure 6.2 (a) the single-scan modified regions are much brighter, suggesting that the light confinement with the specific inscription parameters is much better. When the pulse energy is further increased, due to the higher field irradiances inside the substrate, the single-scan modified regions present a teardrop shape; this can be seen in figure 6.3 (c) where the pulse energy of 110 nJ was used for the inscription of the single scans. As the pulse energy keeps increasing the teardrop shaped modified regions become bigger until eventually the substrate gets fractured.

The effect of the sample translation speed on the modified regions, can be seen by inspecting each of the figures 6.2 (a), (b) and (c) separately. The scans inscribed with the low translation speeds and shown on the left of each figure present a brighter modified region, whereas as the translation speed is increased moving towards the right of the figure the modified regions become faded and smaller. This behaviour is more easily seen in the scans inscribed with the low pulse energy in figure 6.2 (a). In figure 6.2 (c) all the scans present the distinct teardrop shape, although the first scan on the left presents a considerably bigger modified region than the last scan on the right. This is because the low translation speeds lead to longer exposure times of the substrate to the focal region of the laser which in turn results in stronger modification. Finally, it is worth mentioning that the translation speeds used for the single scans inscribed with the low pulse energy and presented in figure 6.2 (a) were an order of magnitude lower than the ones used for

the single scans inscribed at the other two pulse energies. Despite the fact that much lower translation speeds were used the modification at this low pulse energy was still very weak. When the same range of translation speeds as the ones used for the case of 58 nJ was used for the pulse energy of 38 nJ, no signs of modification could be observed under the microscope.

The single scans that are the most desirable for the inscription of the multiscan waveguides are the ones that yield modified regions which approximate a straight vertical line at pulse energies and translation speeds just before the point at which the modified regions start to present the teardrop shape. This is because the single scans that approximate a straight line will yield multiscan waveguides with symmetric rectangular cross sections and uniform refractive index distribution which leads to more symmetrical guided modes. If the single scans at the highest possible pulse energies just before the modified region starts to present the teardrop shape are chosen, the modification will be stronger and therefore the multiscan waveguides will present higher refractive index contrast between the core and cladding which will lead to better confinement of the guided light. Following the criteria outlined above, from all the single scans presented in figure 6.2 the best one for multiscan waveguide inscription would be the one inscribed with a pulse energy of 58 nJ and sample translation speed of 4 mm/s.

The waveguide structures fabricated via the multiscan inscription technique in a GLS substrate using a 0.4 NA aspheric lens at a pulse energy of 64 nJ and a sample translation speed of 12 mm/s are presented in figure 6.3. For the inscription of the waveguides presented in this figure multiple single scans with an offset of 0.36 μm were used. By altering the number of scans each time the cross section of the waveguides can be controlled. The number of single scans used for the waveguides presented in this figure was 6, 12, 18, 24, 30, 36 and 42 scans from left to right. When a small number of single scans is used the waveguides still approximate a vertical straight line but as the number of scans is increased the waveguides present a rectangular cross-section which is desirable for having more symmetrical guided modes.

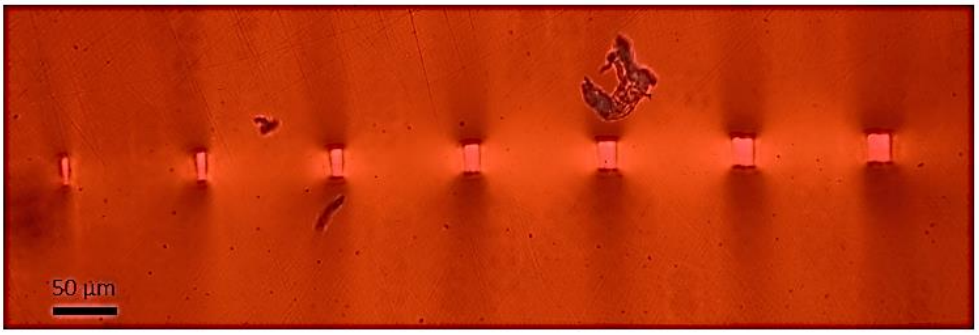

Figure 6.3 Microscope images of multiscan waveguide structures inscribed using different number of scans each time. The number of scans used was 6, 12, 18, 24, 30, 36 and 42 scans from left to right.

Studies in the origins of the propagation losses in ULI fabricated waveguides showed that the principal loss mechanism is scattering [167], with some cases reporting more than 90% of the propagation losses due to scattering [168]. The main effects proposed to cause the scattering in the ULI structures are laser-induced colour centres [169], broken bonds and/or extended defects [170] caused by the inscription process. Another mechanism proposed to contribute to the propagation losses is the signal radiation from the leaky modes from the waveguide core [171] which becomes more prominent when a small refractive index contrast is chosen. However, although the ULI field has grown rapidly over the last two decades, the investigation in the origins of the propagation losses in ULI fabricated waveguides has not attracted much interest and there is still a significant volume of work to be done to fully understand the origin of the propagation losses and how the various inscription parameters affect them.

Regarding the magnitude of the propagation losses in ULI fabricated waveguides, low propagation losses in the orders of ~ 0.1 dB/cm have been reported in silica and borosilicate glasses [172, 173], with the lowest to date propagation loss value of 0.027 dB/cm reported in gorilla glass [174]. In the case of GLS, propagation losses in ULI fabricated waveguides have been reported in the orders of ~ 0.8 dB/cm [175].

Propagation loss measurements performed by other members of the NLO group in straight waveguides fabricated in GLS substrates using the cut-back technique revealed

propagation losses as low as ~ 0.6 dB/cm, slightly lower than the reported values in literature, and total insertion losses in the orders of ~ 1.1 dB/cm. In addition, there is ongoing work within the NLO group upon investigating how the various laser inscription parameters affect the propagation losses of waveguides inscribed in both GLS and Er^{3+}:GLS substrates, which will probably lead in achieving even lower propagation losses than 0.6 dB/cm in such ULI waveguides in GLS.

6.4. Refractive index profile measurements

The refractive index profile measurements of the GLS waveguides were performed by our collaborators at the COPL of Laval University. The refractive index profiles of the waveguides were obtained by using the quantitative phase microscopy (QPM) method [176]. This method is able to extract a corresponding phase image from slightly defocussed bright field images of the waveguides. Thereupon, by applying an inverse Abel transformation on this phase image [177], the refractive index profiles of the waveguides can be retrieved. Figure 6.4 (a) shows the refractive index profiles of 5 different waveguides, fabricated in the same substrate, obtained with the method described above. The refractive index profiles for each waveguide were measured along line L1 shown in figure 6.4 (c), which shows a top view of a GLS waveguide.

The waveguides were inscribed with a pulse energy of 72 nJ and a sample translation speed of 12 mm/s using a 0.6 NA aspheric lens. Each waveguide was fabricated with different number of scans thus yielding waveguides of different sizes with waveguide 1 having the smallest cross-section and waveguide 5 having the biggest cross-section. Waveguide 1 was measured to have a width of about 4 μm and every subsequent waveguide was 0.66 μm wider than the previous one so that the widest waveguide had a width of about 6.6 μm. The effect of different widths for each of the waveguides is evident on the measured refractive index profiles of figure 6.4 (a). The height was the same for all waveguides, about 18μm.

Although the geometrical widths of the waveguides were measured to be 4-6.6 μm, the refractive index profiles present a small oscillation beyond this geometrical limit, going below and then above the asymptotic bulk refractive index ($\Delta n = 0$), leading the total

refractive index variation to extend up to ~16 μm. This variation beyond the modified by the laser area is attributed to residual stresses induced in the bulk GLS by the ULI technique. The main mechanisms considered responsible for the refractive index increase, observed in femtosecond-laser-written waveguides are densification [178] and stress [179] induced by the inscription laser in the glass substrate. Therefore, the high stress modified area will inevitably impose a certain amount of stress to its adjacent regions even though unmodified by the laser, causing the refractive index variation to extend beyond the modified region.

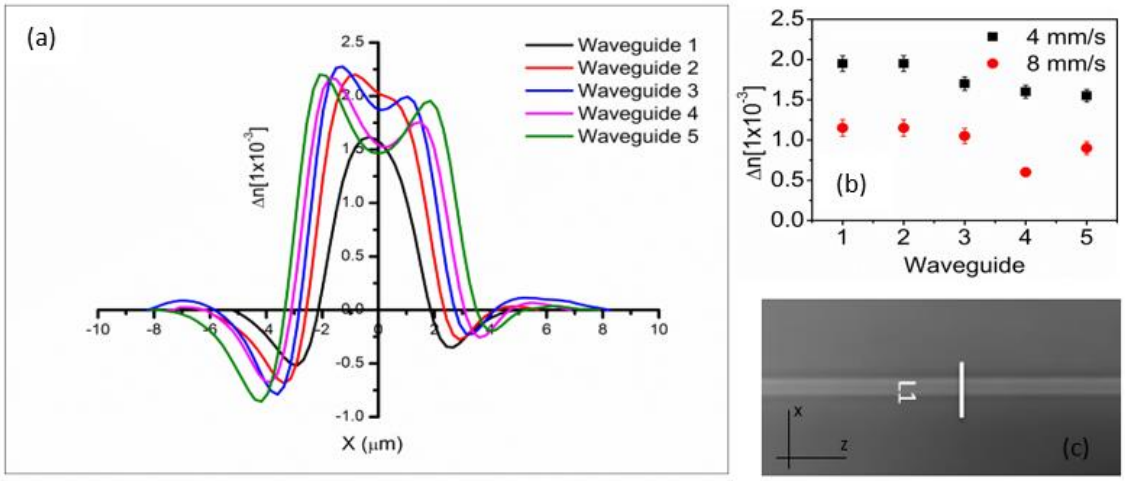

Figure 6.4 (a) Refractive index profiles along the line L1 shown in (c) of 5 waveguides of different widths inscribed with a pulse energy of 72 nJ and translation speed of 12 mm/s using a 0.6 NA aspheric lens. (b) Maximum Refractive index increase of two sets of waveguides (red and black) inscribed with different translation speeds using again a 0.6 NA aspheric lens and a pulse energy of 94 nJ. (c) Top view of a GLS waveguide with the line L1 along which the refractive index profile Δn(x) is measured.

Figure 6.4 (b) shows the maximum refractive index increase Δn of two different sets of waveguides, which were inscribed with different translation speeds and keeping all other inscription parameters the same. The waveguides were inscribed with a pulse energy of 94 nJ using a 0.6 NA aspheric lens in the same substrate as the waveguides of figure 6.4 (a). The set inscribed with a sample translation speed of 4 mm/s presented a higher maximum refractive index increase than the set inscribed with a translation speed of 8 mm/s. This, as discussed in section 6.3 is attributed to the longer exposure time of the

substrate at the focal region of the laser, which leads to stronger modification and therefore higher increase of the refractive index. Following the discussion performed in section 6.3 regarding the choice of the best inscription parameters, the measured refractive index profiles verify that the best parameters for the fabrication of the multiscan waveguides are the ones that yield single-scan modified regions that approximate a straight line just before the point at which the modified regions start to present the teardrop shape. These parameters yield multiscan waveguides with symmetric cross-sections and symmetric guided modes having as high refractive index increase as possible. If higher pulse energies or lower translation speeds are chosen, even though the refractive index increase will be higher, the guided modes will become more asymmetrical.

In order to better understand the confinement properties of our waveguides, the measured x-axis refractive index profile of waveguide 3 presented in figure 6.4 (a) was imported into the commercially available Comsol Multiphysics software. This is shown in figure 6.5 (a).

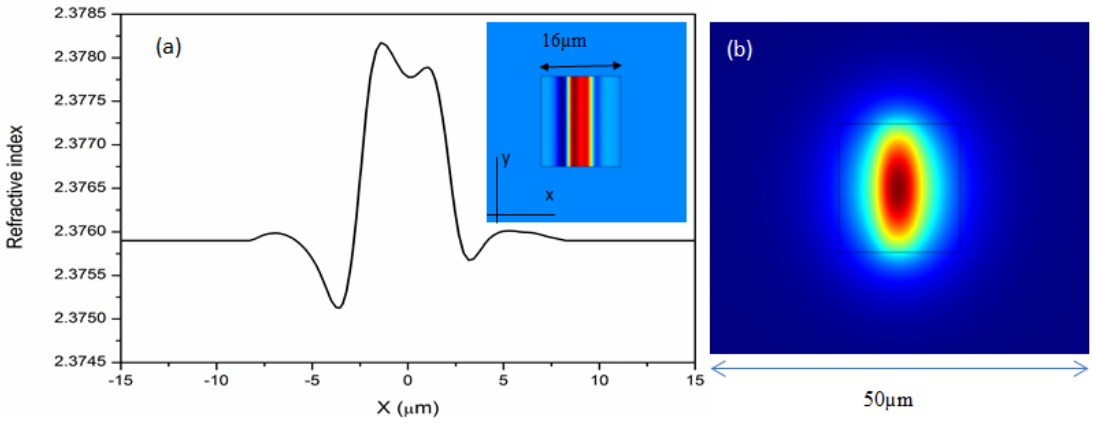

Figure 6.5 (a) Measured refractive index profile along the x-axis of waveguide 3 in figure 6.4 (a) imported in Comsol, inset shows the modelled x,y refractive index distribution at 1.55 µm. (b) Calculated mode profile of the fundamental mode at 1.55 µm for the imported waveguide geometry generated with Comsol.

The modelling was performed by Deepak Jain a member of the fibre sensors and supercontinuum group in the department of photonics engineering of the Technical University of Denmark under the supervision of professor Ole Bang. For the y-axis a uniform step-index profile was assumed. The inset shows the modelled x,y refractive index distribution at the wavelength of 1.55 µm, where the refractive index of bulk GLS at 1.55 µm was taken to be 2.3759. The calculated electric field profile of the fundamental mode at 1.55 µm which exhibited single mode operation is shown in figure 6.5 (b). The theoretical $1/e^2$ mode field diameters (MFDs) yielded by Comsol for the imported refractive index profile of waveguide 3 of figure 6.4 (a) for 1.55 µm operation were 10.08 µm in the x-direction and 18 µm in the y-direction.

In order to support the validity of the theoretically simulated MFDs and subsequently the refractive index profile of waveguide 3, its guiding properties were experimentally investigated by coupling 1.55 µm light and observing the mode profiles at the output facet.

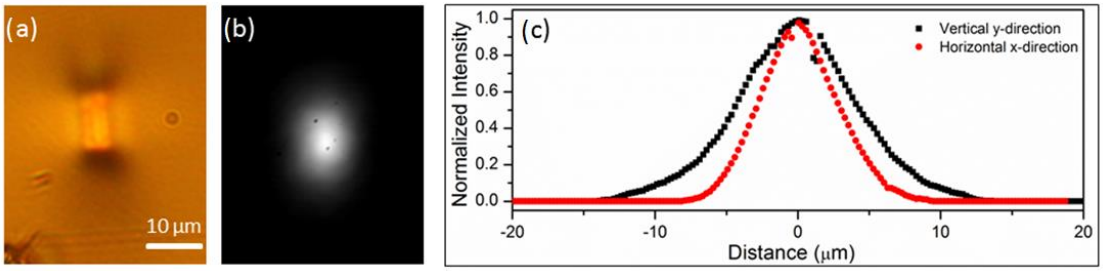

Figure 6.6 (a) End facet image of waveguide 3 taken in transmission mode, (b) corresponding mode profile image for waveguide 3 pumped at 1.55 µm and (c) the associated mode cross-sections at 1.55 µm in the vertical and horizontal directions.

Figure 6.6 (a) shows the end facet image of the waveguide when viewed under a microscope in transmission mode. Figure 6.6 (b) shows the imaged output facet of the waveguide whilst coupling 1.55 µm light into it, exhibiting single mode guiding, whereas the waveguide mode cross-sections are shown in figure 6.6 (c). The mode profile was imaged using a 40× (0.65 NA) aspheric lens and captured using a Hamamatsu InGaAs infrared camera. The experimentally measured $1/e^2$ mode field diameters for the

waveguide were found to be 10.98 ± 1.15 μm in the x-direction and 17.68 ± 2 μm in the y-direction. These are in very good agreement with the theoretically simulated MFDs which were calculated to be 10.08 μm in the x-direction and 18 μm in the y-direction, thereby validating the measurements of the refractive index profiles.

The guiding properties of the waveguides were also studied at longer wavelengths by calculating in Comsol the electric field profiles of the fundamental mode at 2, 3, 4 and 5 μm for the imported refractive index profile of waveguide 3 from figure 6.4 (a). These are shown in figure 6.7.

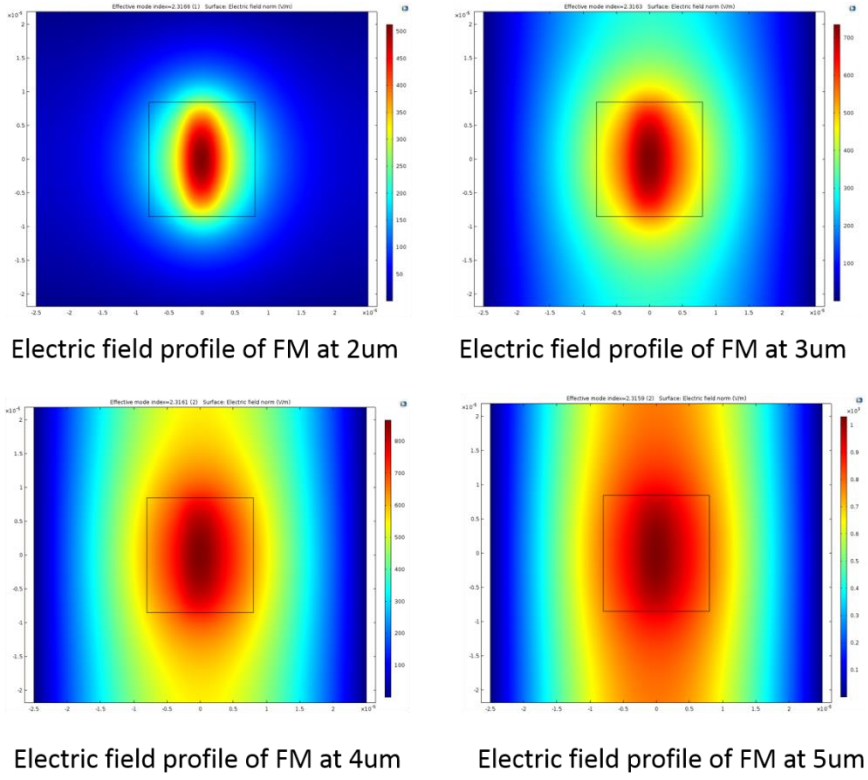

Figure 6.7 Calculated mode profile of the fundamental mode at 2, 3, 4 and 5 μm for the imported refractive index geometry of waveguide 3 from figure 6.4 (a) generated with Comsol. This shows that the electric field is spreading out of the core with increasing wavelength of operation.

As can be seen from the figure, the electric field is spreading out of the core with increasing wavelength of operation. This in practical terms means that the confinement

at longer wavelengths is weak, leading the fundamental mode to leak out of the waveguide. The information regarding the guiding properties obtained from the modelling can be very useful upon tailoring the refractive indices and cross-sections of the waveguides in order to achieve stronger index contrast and therefore improved light confinement at longer wavelengths.

6.5. Dispersion measurements

The dispersion measurements were carried out by Christian Petersen, a member of the fibre sensors and supercontinuum group in the photonics engineering department of Technical University of Denmark under the supervision of Professor Ole Bang. The material dispersion of the bulk substrate and the total dispersion of a series of inscribed waveguides was measured using white-light spectral-domain interferometry. The experimental setup for measuring the dispersion is shown in figure 6.8 (a).

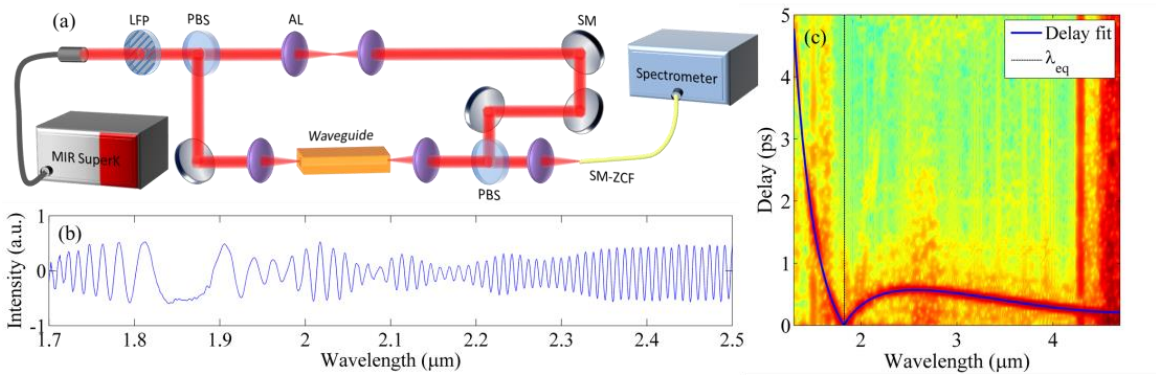

Figure 6.8 (a) Experimental setup for measuring waveguide dispersion using a mid-infrared supercontinuum source and a balanced Mach-Zehnder interferometer (LFP: Linear film polariser, PBS: Plate beam splitter, AL: Aspheric lens, SM: Silver mirror, SM-ZCF: Single-mode ZBLAN collecting fibre). (b) Example interference spectrum with clearly resolved interference fringes. The gap at 1.85 μm marks the phase equalisation wavelength (λ_{eq}) of the test and reference beams. (c) Short-time Fourier transform analysis of the interference spectrum displaying the differential delay of the test and reference beams, showing only a single guided mode.

It comprises a broadband mid-infrared supercontinuum source (~1.3-4.5 μm), a balanced Mach-Zehnder free-space interferometer, and a scanning spectrometer (0.4-5.0 μm). Light was coupled to and collimated from the waveguides by aspheric lenses, and the two interfering beams were collected using a single-mode ZBLAN optical fibre. Interference fringes, like the ones seen in figure 6.8 (b) were visible throughout the entire spectrum, providing around 600-700 interference extrema. These extrema were fitted to a fringe counting function using a modified Cauchy dispersion formula to model the wavelength dependence of the effective refractive index from which the dispersion was calculated [180]. The calculated dispersion for the bulk GLS along with a series of waveguides is shown in figure 6.9.

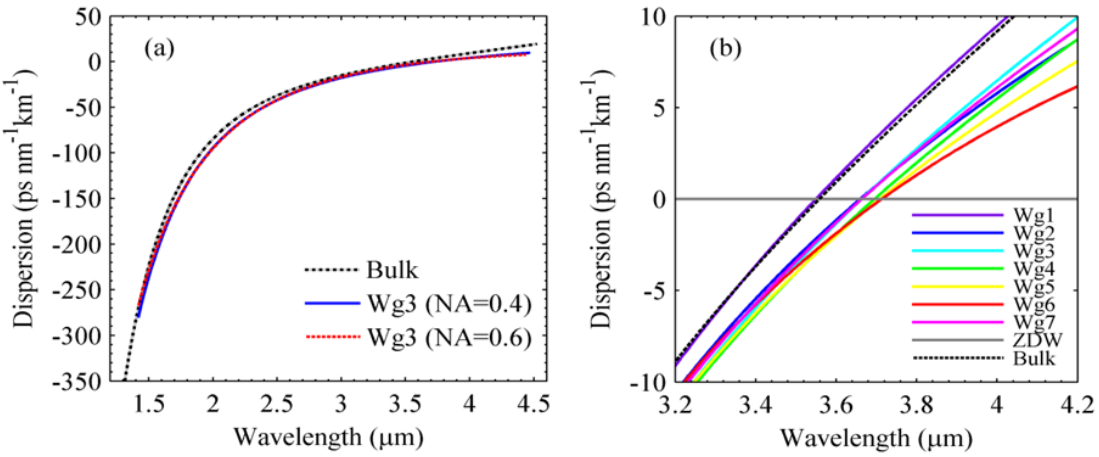

Figure 6.9 (a) Comparison of the measured dispersion of the bulk glass and two waveguides of identical dimensions but fabricated using different NA focusing lenses and different pulse energy. (b) Zoomed-in view of the dispersion around the ZDW of the bulk glass and seven waveguides inscribed with the same parameters but having increasing cross-sections with waveguide 1 having the smallest cross section and waveguide 7 having the largest one.

Figure 6.9 (a) shows the measured dispersion of the bulk glass substrate along with the dispersion of two waveguides with the same dimensions but fabricated using different NA inscription lenses and different pulse energy. For the waveguide inscribed with the 0.4 NA aspheric lens the pulse energy was 64 nJ with a sample translation speed of 12 mm/s, while for the waveguide inscribed with the 0.6 NA aspheric lens the pulse

energy was 110 nJ with a sample translation speed of 12mm/s. From figure 6.9 (a) it is seen that the dispersion of the waveguides is very similar to that of the bulk glass, with negligible impact from changing the inscription parameters, such as, the NA of the inscription lens and the pulse energy. This implies that the total waveguide dispersion will be dominated by material dispersion.

Figure 6.9 (b) shows a zoomed-in view of the ZDW region of seven different waveguides, which all, except for waveguide 1, are seen to have almost identical dispersion curves. The waveguides were inscribed with a pulse energy of 110 nJ and a sample translation speed of 12 mm/s using a 0.6 NA aspheric lens, but they were chosen to have increasing widths with waveguide 1 being the narrowest and waveguide 7 being the widest. Waveguide 1 was measured to have a width of about 3 μm and every subsequent waveguide was 1.98 μm wider than the previous one so that the widest waveguide had a width of about 15 μm. The height was the same for all waveguides, about 18 μm. The bulk glass ZDW was identified to be around 3.61 μm, and for waveguide 1 the ZDW was at 3.55 μm, whereas the other six waveguides had a measured ZDW between 3.66 and 3.71 μm. The discrepancy regarding the ZDW between waveguide 1 and waveguides 2-7 is attributed to the fact that the index contrast of waveguide 1 is very weak so its dispersion should be very close to that of the bulk material.

The waveguide dispersion was investigated also theoretically by importing the measured refractive index profiles in Comsol. The modelling revealed that the waveguide dispersion is indeed very small, hence the total dispersion in the waveguides will be dominated by material dispersion, which is in agreement with the experimental measurements. The waveguide dispersion over a range of wavelengths yielded by Comsol for the imported refractive index profile of waveguide 3 from figure 6.4 (a) is shown in figure 6.10. As can be seen from the figure, the modelled waveguide dispersion is very small ranging from about -3.3 to 0.5 ps $nm^{-1}km^{-1}$ for wavelengths spanning from 2 to 5 μm, whereas the measured dispersion for the waveguides and bulk GLS presented in figure 6.9 (a) is ranging from -350 to about 10 ps $nm^{-1}km^{-1}$ for wavelengths from 1.3 to 4.5 μm. The small value of the calculated waveguide dispersion shows that the total dispersion in the waveguides will be dominated by material dispersion.

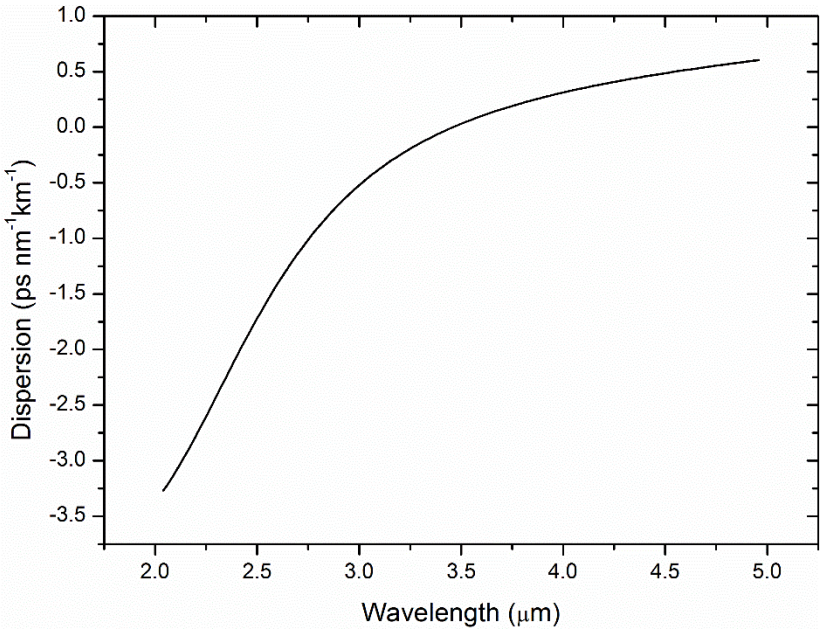

Figure 6.10 Calculated waveguide dispersion for the imported refractive index geometry of waveguide 3 from figure 6.4 (a) generated with Comsol.

6.6. Summary

This chapter has presented an investigation in the key properties, such as refractive index profiles and dispersion, of GLS waveguides fabricated via ULI. First the optimum inscription parameters which yielded the best quality waveguides were discussed and the morphology of the fabricated waveguides was presented. The refractive index profiles of a series of waveguides fabricated with different inscription parameters were measured using quantitative phase microscopy. This enabled the investigation of the effects the inscription parameters have upon the refractive index profiles. The guiding properties of the waveguides over a range of wavelengths were modelled by importing the measured refractive index profiles in the commercially available software Comsol. The modelling showed weaker guiding at longer wavelengths providing the required information for tailoring the refractive indices and cross-sections of the waveguides in order to achieve stronger index contrast and improved light confinement at longer wavelengths. The simulated mode field diameters of the waveguides for 1.55 μm operation were in excellent agreement with the experimentally measured MFDs when guiding 1.55 μm light in the waveguides, thereby supporting the validity of the measured refractive index profiles. After that, the dispersion of the waveguides and the bulk GLS was measured over a broad

range of wavelengths in the near- and mid-infrared region of the electromagnetic spectrum spanning from ~1.3 to 4.5 μm. The broad range at which the dispersion measurements were undertaken enabled the determination of the ZDW for both the waveguides and bulk GLS, which was found to be between 3.66 and 3.71 μm for the waveguides and about 3.61 μm for the bulk. Furthermore, the origin of the dispersion in the waveguides was investigated by importing the measured refractive index profiles into Comsol. The modelling revealed low waveguide dispersion, implying that the full dispersion in the waveguides is dominated by material dispersion, which was in agreement with the experimental observations.

Chapter 7. Ultrafast all-optical switching in ultrafast laser inscribed gallium lanthanum sulphide directional couplers

7.1. Introduction

The work presented in this chapter focuses on the fabrication of optical directional couplers in gallium lanthanum sulphide via the ultrafast laser inscription technique. The high Kerr nonlinearities of GLS were exploited to realise an ultrafast all-optical nonlinear switching device with main objective to determine the nonlinear refractive index coefficient, n_2, of the modified by the laser area from the switching parameters. The direct measurement of the n_2 coefficient of the modified region was also attempted by trying to inscribe a large area in GLS with aim to perform closed-aperture Z-scan measurements upon it. However, this task was proven to be very challenging due to the shattering of the substrates due to the high stresses imposed by the large area modified regions. Therefore, the alternative of calculating the n_2 coefficient for the modified area of the waveguides from the switching parameters of the directional couplers was preferred. Due to its high Kerr nonlinearity, GLS is a very attractive candidate for a range of nonlinear optical applications such as all-optical switching or Kerr-lens mode locking. For the optimum design of such nonlinear applications the knowledge of the exact value of the n_2 coefficient is required. Therefore, for the realisation of nonlinear devices and applications in GLS via ULI, the information regarding the n_2 coefficient of the modified by the laser area and the effect the inscription parameters have upon it are very important.

The chapter begins by introducing the basic operating principles of coupled modes in optical directional couplers, followed by a discussion on how the irradiance dependent refractive index can be exploited to achieve all-optical switching (AOS). After that the optical directional couplers fabricated in GLS substrates are presented and the optimum inscription parameters are discussed. This is then followed by the demonstration of ultrafast all-optical switching in the developed directional couplers. Finally, the nonlinear refractive index coefficient, n_2, of the modified by the laser area is calculated, by making use of the switching parameters. The knowledge of this coefficient allowed for comparison with the n_2 coefficient of bulk GLS, giving valuable information regarding the effects the ULI technique has on the nonlinear refractive index which as discussed

above is very important for the design and optimisation of nonlinear photonic devices in GLS via ULI.

7.2. Basic operating principles of coupled modes in optical directional couplers

A directional coupler is a device that operates by coupling together two modes travelling in the same direction. To achieve that, optical directional couplers consist of two parallel dielectric waveguides positioned very close to each other. When propagating light in any dielectric waveguide there is an evanescent field extending outside the core. If the two parallel waveguides that form the directional coupler are placed sufficiently close to each other the parts of the evanescent fields that extend outside the cores will overlap spatially. This will lead to an energy transfer process between the overlapping evanescent tails of the guided modes enabling the mode coupling upon which directional couplers are based. This is illustrated in figure 7.1, which shows the overlapping electric field distributions of two adjacent parallel waveguides for two different waveguide separation distances. The electric field distribution of each waveguide is presented below its cross-section. The extent of overlap between the evanescent tails of the guided modes is depicted with the shaded grey areas whereas the separation distance between the waveguides is denoted with s.

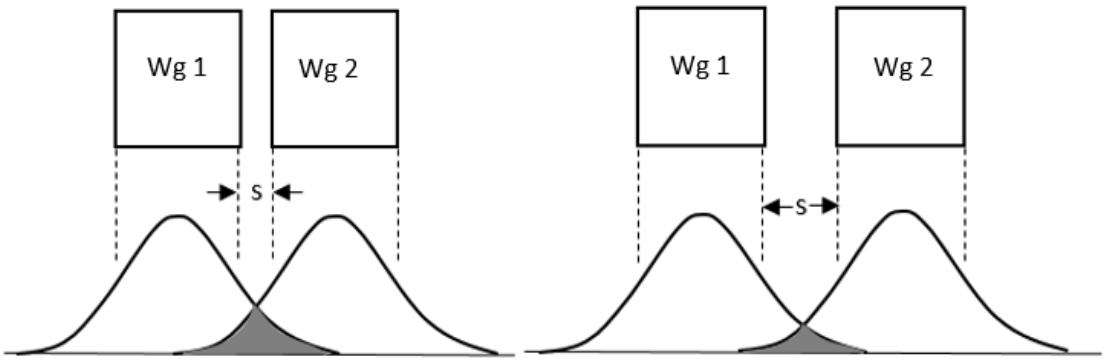

Figure 7.1. Overlap of the evanescent fields of two adjacent parallel waveguides for two different separation distances. The extent of the overlap is depicted with the shaded grey areas. For smaller separation distances (left hand side), the extend of overlap is greater, whereas as the separation distance increases (right hand side) the extend of overlap reduces.

For a small separation distance between the waveguides, shown in the left hand side of figure 7.1, the extend of overlap of the electric field distributions will be greater leading to a bigger energy transfer between the two guided modes. As the separation distance is increased, the extend of overlap reduces leading to a weaker interaction between the two guided modes; this is depicted in the right hand side of figure 7.1.

The conventional coupled-mode theory can be used to describe the mode coupling and energy transfer between the two waveguides that form the directional coupler. First, the guided modes in the individual waveguides are considered. If the two waveguides are infinitely far apart the modes will propagate independently and will obey the propagation equations

$$\frac{d\alpha_1}{dz} = -j\beta_1\alpha_1 \tag{7.1a}$$

$$\frac{d\alpha_2}{dz} = -j\beta_2\alpha_2 \tag{7.1b}$$

where α_1 and α_2 are the mode amplitudes, with β_1 and β_2 being the corresponding propagation constants for each of the two waveguides. When the waveguides are brought into close proximity for the modes to couple together, the spatial dependences of one mode will be modified by the existence of the other and vice versa. The coupled propagation equations will then take the form

$$\frac{d\alpha_1}{dz} = -j(\beta_1 + K_{11})\alpha_1 - jK_{12}\alpha_2 \tag{7.2a}$$

$$\frac{d\alpha_2}{dz} = -j(\beta_2 + K_{22})\alpha_2 - jK_{21}\alpha_1 \tag{7.2b}$$

where K_{12}, K_{21} and K_{11}, K_{22} are the mutual and self-coupling coefficients respectively. In the case of symmetric directional couplers $K_{12} = K_{21} = \kappa$. Moreover, if the system is assumed to be lossless and the waveguide modes are assumed to be orthogonal, self-consistency requires that the law of power conservation is satisfied. Then equations 7.2 are recast to

$$\frac{d\alpha_1}{dz} = -j\delta\alpha_1 - j\kappa\alpha_2 \quad (7.3a)$$

$$\frac{d\alpha_2}{dz} = -j\delta\alpha_2 - j\kappa\alpha_1 \quad (7.3b)$$

where $\delta = \frac{\beta_1 + K_{11} - \beta_2 - K_{22}}{2}$ is called the detuning or mismatch coefficient and describes the mismatch of the propagating modes in the two waveguides arising from the differences in their propagation constants.

When only one of the waveguides is excited at the input, i.e., $\alpha_1(0) = 1$ and $\alpha_2(0) = 0$, the general solutions of equations 7.3 for the guided powers in waveguides 1 and 2 are given by

$$P_1(z) = cos^2(Sz) + cos^2(n)sin^2(Sz) \quad (7.4a)$$

$$P_2(z) = sin^2(n)sin^2(Sz) \quad (7.4b)$$

where $S = \sqrt{\delta^2 + \kappa^2}$ and the parameter n is defined by $\tan(n) = \frac{\kappa}{\delta}$.

As can be seen from equations 7.4, the guided power in the waveguides is a function of the propagation distance, z. The distance along the propagation direction at which the two waveguides extend in parallel and sufficiently close to each other for the guided modes to interact is called interaction length. Equations 7.4 also demonstrate that the energy transfer process between the two waveguides becomes periodic with distance. More specifically when light is coupled in one of the waveguides it cumulatively transfers to the other waveguide as it travels in the propagation direction. For long interaction lengths it is possible for the energy interchange to reach 100 % and all of the light to transfer into the second waveguide. The light then starts coupling back in the first waveguide until it reaches 100 % return, at which point it again starts to transfer in the second waveguide starting a new cycle for the energy-interchange process which keeps repeating along the interaction length. This process is illustrated in figure 7.2 which plots two parallel

waveguides showing the energy transfer process to waveguide 2 and back as a function of distance when light is coupled in waveguide 1.

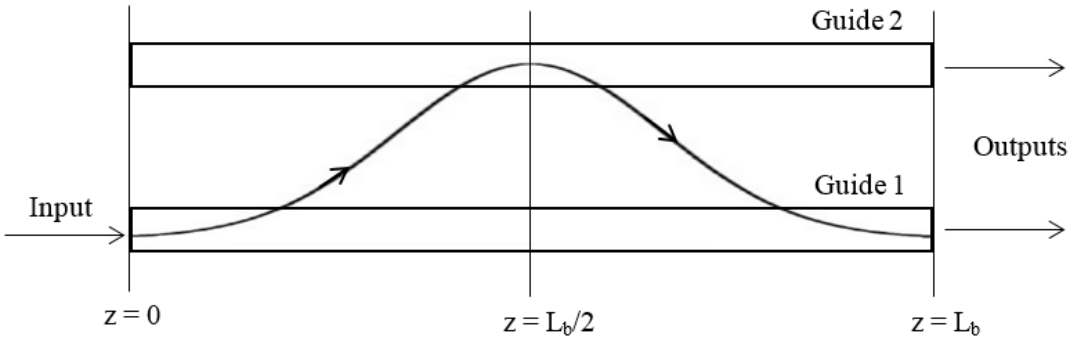

Figure 7.2. Conceptual representation of the energy interchange process between two parallel waveguides. The light is coupled in waveguide 1 at z = 0; as it propagates down the waveguide the energy transfers cumulatively to waveguide 2 until the transfer reaches 100 % at distance z = L_b/2. Then the light starts to transfer back in the input waveguide, reaching 100 % return at distance z = L_b.

The distance over which the light completely transfers to waveguide 2 and then back to waveguide 1 completing a full cycle is called beat length and is denoted as L_b in figure 7.2. Subsequently the distance over which the maximum amount of power transfers to waveguide 2 is called half beat length and is denoted as $L_b/2$ in figure 7.2. From equations 7.4 for maximum power transfer at waveguide 2 the half beat length must be:

$$z = \frac{L_b}{2} = \frac{\pi}{2S} \tag{7.5}$$

where the maximum power is equal to:

$$P_{2|max} = sin^2(n) \tag{7.6}$$

By observing equations 7.4 and figure 7.2 it can be easily deduced that by choosing different interaction lengths, directional couplers with different output ratios can be realised. An output ratio *r* can be defined as the output power at waveguide 2, normalised

to the total output power at both waveguides when the input is applied in waveguide 1 and is given by [181]:

$$r = \frac{P_2}{P_1+P_2} = \frac{\kappa^2}{S^2} sin^2(Sz) \tag{7.7}$$

In the ideal case the propagation constants of the two waveguides are equal, therefore $\delta = 0$ and S which is given by the relationship $S = \sqrt{\delta^2 + \kappa^2}$ reduces to κ. Then equation 7.7 reduces to $r = sin^2(\kappa z)$ and 100 % transfer to waveguide 2 is possible. However, if β_1 and β_2 deviate from each other, δ will be nonzero therefore leading S to always be larger than κ. Subsequently the fraction $\frac{\kappa^2}{S^2}$ in equation 7.7 will always be smaller than unity not allowing 100 % transfer to waveguide 2 regardless what interaction length is chosen.

In conclusion the coupled mode theory presented in this section, and more specifically the derived equations 7.4 and 7.7, show that when designing optical directional couplers, the two parameters that will have the biggest impact on the coupler output ratios will be the coupling coefficient which is dictated by the separation distance between the waveguides and the interaction length. Moreover, it is pointed out that if the two waveguides which form the directional coupler possess different propagation constants there will be a phase mismatch in the propagating modes and 100 % power transfer to the 2nd waveguide is not possible.

7.3. All-optical switching principle in optical directional couplers

An optical directional coupler can be operated as an optical switch by employing a control method to direct light from one output port to the other in a controlled fashion. In the case that the control method uses only an optical signal to switch the light from one output port to the other without any mechanical, electrical or other components involved, the switching procedure is called all-optical switching. The irradiance dependent refractive index introduced in section 2.3.1 is exploited to achieve all-optical switching in optical directional couplers fabricated in GLS substrates via ULI. The high nonlinear refractive index coefficient, n_2, of GLS makes this approach for AOS very appealing.

For a generic switching device, switching occurs when the relative path length of the light changes by half a wavelength. Thus for a device of interaction length L, the refractive index change required to switch from one state to another is given by [182]:

$$\Delta nL = \lambda/2 \tag{7.8}$$

The directional couplers are designed in such way that when a low power input is applied in waveguide 1, a maximum amount of power transfers to waveguide 2 in the output. To achieve this and taking into account the discussion performed in section 7.2 the interaction length of the directional couplers must be chosen to be half beat length. Then, as the input power is increased the refractive index of waveguide 1, following equation 2.16, will start to increase. As soon as the input power is sufficiently increased so that the required Δn in waveguide 1 is reached and equation 7.2 is satisfied, the output will completely transfer from waveguide 2 to waveguide 1; therefore all-optical switching is achieved. This switching process is also evident in equation 7.7. As already mentioned, the increasing input power will cause the refractive index of waveguide 1 to increase. This will in turn alter the waveguide's propagation constant, β_1, and therefore increase the mismatch coefficient δ between the two propagating modes. Therefore, the fraction $\frac{\kappa^2}{S^2}$ in equation 7.7 will decrease reducing this way the output ratio, *r*, of waveguide 2.

7.4. Ultrafast laser inscription of directional couplers in gallium lanthanum sulphide

All the directional couplers used in this work had the same geometric layout. They were formed from two waveguides. Each of the waveguides was consisted of straight lead-in and lead-out sections linked to s-bends which led to a straight interaction region of length L. A schematic of the directional couplers is shown in figure 7.3.

When the input is in the lead-in section of waveguide 1, its lead-out section is denoted as bar port, whereas the lead-out section of waveguide 2 is denoted as cross port. The interaction length is denoted as L, while the separation distance between the two waveguides along the interaction length, from now on called core-to-core separation, is denoted as s. The directional couplers were chosen to have the particular structure in order

to avoid evanescent coupling in any other sections of the waveguides apart from the interaction length. For this reason, the transverse to the propagation direction displacement of the waveguides, denoted as x-offset in figure 7.3, was chosen to be 50 μm for each waveguide leading to a total separation distance of more than 100 μm for the lead-in, lead-out sections, big enough to ensure that no evanescent coupling would occur in these regions.

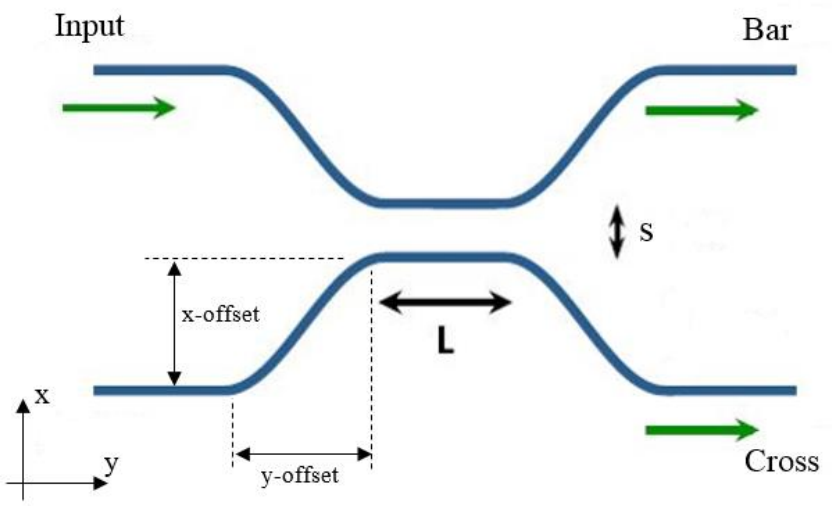

Figure 7.3 Schematic of the directional coupler structure. L is the interaction length, where s is the separation distance between the two waveguides along the interaction length.

Prior to fabricating the directional couplers, an investigation in the optimum parameters which minimised the bend losses in the s-bend regions was performed. From this investigation it was found that s-bends with a waveguide displacement of 5 mm along the propagation direction, denoted as y-offset in figure 7.3, and a radius of curvature 110 μm presented zero bend losses. This investigation was performed by inscribing a straight waveguide followed by waveguides with s-bend regions, keeping all the other inscription parameters the fixed and varying only the y-offset and bend radii of the waveguides with the s-bends. Then loss measurements were performed on all the waveguides and the waveguides with the s-bend regions that presented the same losses as the straight waveguide, therefore presenting zero bend losses, were identified. The x-offset during this investigation was always kept at 50 μm.

The s-bends and directional couplers were fabricated using the ultrafast laser inscription setup outlined in section 2.8 with the IMRA® laser system, presented in section 2.8.1, set to emit 360 fs pulses at a pulse repetition rate of 500 kHz. The pulses from the inscription laser were focused inside the substrates using a 0.4 NA aspheric lens. The pulse energy incident on the samples was chosen to be 58 nJ and the translation speed was set to 12 mm/s. The directional couplers were fabricated by using the multiscan technique introduced in section 6.3. Ten scans with a scan-to-scan horizontal offset of 0.36 μm were used, yielding waveguides with rectangular cross sections of about 4.6-18 μm for each coupler. The above parameters used for the inscription of the directional couplers are the optimal ULI parameters identified in chapter 6 for realising high quality waveguides for 1550 nm single mode operation.

7.4.1 All-optical switching in ULI directional couplers fabricated in GLS

As already discussed in section 7.3, a directional coupler is suitable to be operated as an all-optical switch when for a low irradiance input a maximum amount of power transfers to the cross port in the output. Therefore, before carrying out the switching experiment, the directional couplers that presented a higher cross than bar output for a low irradiance input and hence being suitable to be operated as all-optical switches were identified. This was done by employing a 1550 nm CW fibre laser as input, whilst recording the output cross-to-bar ratio for each of the couplers. The use of the CW laser ensured that no nonlinearities were excited whilst propagating light in the directional couplers, therefore the output ratio was measured at the low irradiance regime before any switching occurs.

After identifying the directional couplers that presented a higher cross than bar output, a single beam experiment was performed to examine their operation as all-optical switches. The femtosecond OPA laser system, introduced in section 2.5, centred at 1550 nm was used as an input while the output cross-to-bar ratio of the directional couplers was measured as a function of the input irradiance. The high peak powers made available from the OPA laser system (~0.8 GW at 1550 nm) enabled the excitation of the nonlinear refraction property of GLS and therefore trigger the irradiance dependence of the refractive index upon which the operation of the directional couplers as optical switches is based. Figure 7.4 shows a plot of the output relative transmission for the bar and cross

ports as a function of the input irradiance for two directional couplers inscribed with the same core-to-core separation of 7.5 μm but chosen to have different interaction lengths. Coupler 1 was chosen to have an interaction length of 3.7 mm, whereas for coupler 2 the interaction length was set to 3.8 mm. The bar and cross output ratios, recorded with the 1550 nm CW laser as an input, prior the switching experiment was performed are shown in the same axes system with pink and blue circles.

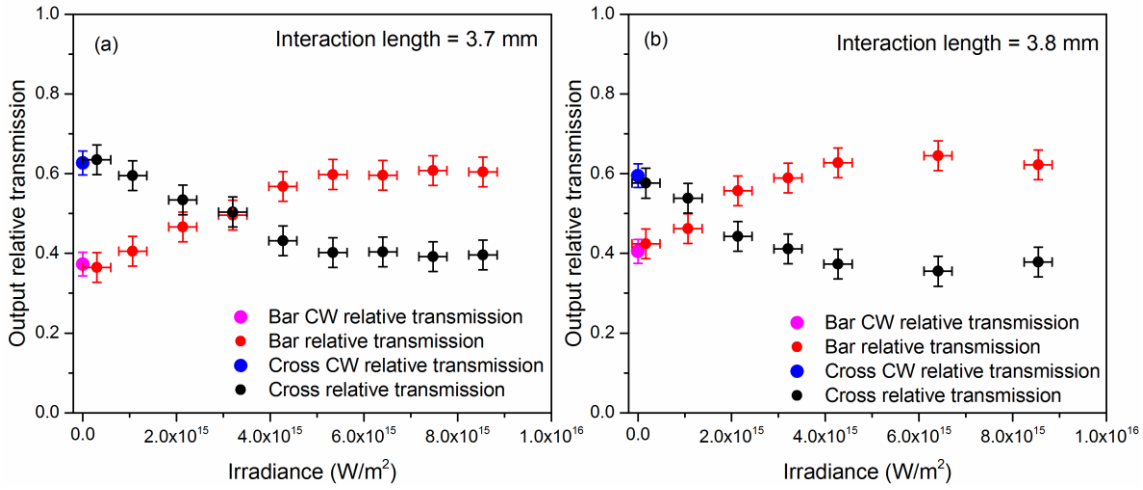

Figure 7.4. (a) Output relative transmission for the bar (red) and cross ports (black) as a function of the input irradiance for a directional coupler with an interaction length of 3.7 mm. (b) Output relative transmission for the bar (red) and cross ports (black) as a function of the input irradiance for a directional coupler with an interaction length of 3.8 mm. The pink and blue circles in both graphs represent the bar and cross output ratios respectively in the linear regime when a CW 1550 nm laser is used as an input.

As can be seen from figure 7.4, for a low irradiance input, about 60 % of the light was in the cross port in the output. Then, as the irradiance started increasing the refractive index of the bar waveguide increased as well. This caused its propagation constant to change which in turn detuned the output cross to bar ratio following equation 7.1. As soon as the input irradiance was sufficiently increased for the required Δn in the bar waveguide to be reached and equation 7.2 to be satisfied, the output completely reversed to about 60-40 % bar to cross ratio. The incident irradiance required for the coupler 1 presented in figure 7.4 (a) to completely switch from the cross to the bar state was about 5.34×10^{15} W/m^2, whereas the incident irradiance required for the second coupler

presented in figure 7.4 (b) to completely switch from the cross to the bar state was about 4.27×10^{15} W/m^2. Coupler 1 required a higher irradiance than coupler 2 to completely switch from the cross to the bar state due to its shorter interaction length. More specifically the accumulated contribution from the nonlinear refractive index coefficient, n_2, to the overall increase of the refractive index will be smaller with shorter interaction lengths. Therefore, a coupler with a shorter interaction length will need higher irradiances to reach the required Δn for equation 7.2 to be satisfied and switching to be achieved. This is a common dilemma when designing optical directional couplers for AOS applications, where there will have to be a trade of between switching irradiance and device dimensions.

For a low irradiance input before any switching occurs, the power transfer in the cross port for the directional couplers presented in figure 7.4 was about 60 %. This transfer ratio would be unlikely to reach 100 % regardless of the sampling of the interaction length. This behaviour is characteristic of differences in the propagation constants of the two waveguides that form the directional couplers, which arise from the fabrication procedure. The refractive index profiling of the GLS waveguides presented in section 6.4 revealed that the total refractive index variation induced by ULI can extend beyond the geometrical structure of the waveguides up to ~16 μm. Therefore, in the case of the directional couplers presented in figure 7.4, where the core-to-core separation was chosen to be 7.5 μm, the optical properties (e.g. mode index) of the first waveguide for each coupler were directly affected by the inscription of the second waveguide and vice versa leading to different propagation constants for the two waveguides. A possible solution to this problem would be to choose core-to-core separations bigger than ~20 μm, although in this case the coupling coefficient would be greatly decreased and would therefore require very long interaction lengths for the maximum amount of power to transfer to the cross waveguide. Another possible source of the mismatch in the propagation constants of the two waveguides might be the temperature variations in the lab during the inscription process, where variations as small as ~ ± 1^o C might be sufficient to change the ULI parameters over the course of the experiment [175].

The output relative transmission for the bar and cross ports as a function of the input irradiance for a directional coupler inscribed with a core-to-core separation of 15 μm and an interaction length of 7.95 mm is shown in figure 7.5.

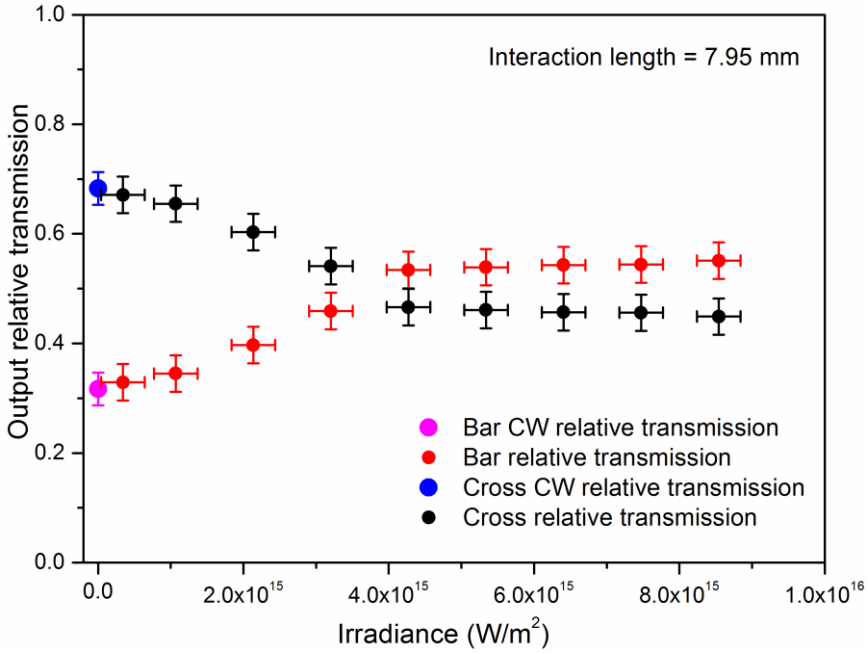

Figure 7.5. Output relative transmission for the bar (red) and cross ports (black) as a function of the input irradiance for a directional coupler with a core-to-core separation of 15 μm and interaction length of 7.95 mm. The pink and blue circles represent the bar and cross output ratios respectively in the linear regime when a CW 1550 nm laser is used as an input.

The choice of the bigger core-to-core separation for this coupler helped decrease the effect each waveguide has on the optical properties of the other waveguide through the inscription process. This reduced the differences in the propagation constants of the two waveguides leading to an increase of the transferred power in the cross waveguide to about 70 % in the low irradiance input regime. However, the choice of a bigger core-to-core separation also decreased the coupling coefficient between the waveguides, leading to a requirement for a longer interaction length for maximum amount of power to transfer to the cross waveguide. The longer interaction length impedes complete switching, reducing the switching contrast for high irradiance inputs. This is evident in figure 7.5; for low irradiance inputs the output ratio is about 67-33 % cross to bar, whereas for high

irradiance inputs the switching ratio only reaches about 55-45 % bar to cross. This is because of the irradiance dependence of the nonlinear phase shift. For high irradiance inputs where MPA is present, the pulse gets depleted as it propagates through the directional coupler. Therefore, for a given irradiance input the irradiance at the beginning of the interaction length will be higher than the one in the end leading to different switching conditions along the interaction length of the directional coupler limiting the switching efficiency.

Another effect that reduces the switching contrast is intermodal dispersion [183]. As already discussed above due to the particular nature of ULI the two waveguides which form the directional coupler will have different propagation constants. This will lead to a group-delay difference since the modes in the two waveguides will travel at slightly different speeds. It is easily deduced that the group-delay difference will increase with increasing interaction length. As this group-delay difference increases, the period of time over which the two modes overlap becomes shorter and shorter, therefore power transfer between the two waveguides can take place only in a small part of the pulse period. This causes pulse distortion and the pulses that evolve from the two waveguides can have different shapes. In the case that the group-delay difference becomes comparable to or larger than the pulse width, two separate pulses of equal amplitudes evolve from each waveguide, regardless of the splitting ratio of the coupler [183].

Even though longer interaction lengths might allow for lower switching irradiances and higher power transfer to the cross waveguide for low irradiance inputs, they will also cause the effects outlined above to become very prominent completely jeopardising the function of the directional couplers as optical switches. In order to avoid these problems, usually directional couplers of shorter interaction lengths are preferred, having to pay the price of higher switching irradiances.

7.4.2 Determination of the nonlinear refractive index coefficient, n_2, of the ULI modified area from the switching conditions.

The all-optical switching experiments presented in section 7.5 enabled the calculation of the nonlinear refractive index coefficient, n_2, of the modified by the laser area from the

switching parameters. As already discussed in section 7.1, the knowledge of this coefficient is very important for the optimisation of photonic devices in GLS via ULI.

The phase change $\Delta\Phi$ due to nonlinear refraction was introduced in equation 2.22 and is repeated here for purposes of completeness:

$$\Delta\Phi = \frac{2\pi L n_2 I}{\lambda} \tag{7.3}$$

where in this case L is the interaction length of the directional coupler, λ is the operating wavelength and I is the irradiance.

The phase change, $\Delta\Phi$, required to switch a nonlinear directional coupler, is in the order of 4π [184]. By substituting this into equation 7.3 and solving for n_2 equation 7.3 transforms to:

$$n_2 = \frac{2\lambda}{IL} \tag{7.4}$$

Using the switching irradiances, after accounting for the losses due to Fresnel reflection at the input facet, along with the corresponding interaction lengths for each of directional couplers presented in figure 7.4 in equation 7.4, the n_2 of the modified region was estimated. The yielded n_2 for coupler 1 was 1.89×10^{-19} m^2/W whereas the yielded value for coupler 2 was 2.30×10^{-19} m^2/W.

In a work demonstrating all-optical switching in an Aluminium Gallium Arsenide (AlGaAs) directional coupler [185] a critical irradiance, I_c, was defined as the irradiance required to switch a directional coupler with an interaction length L to the condition where equal output powers emerge from the bar and cross waveguides. This critical irradiance was given by:

$$I_c = \frac{\lambda}{L n_2} \tag{7.5}$$

The critical irradiance for coupler 1 of figure 7.4 is 3.2×10^{15} W/m^2, whereas the critical irradiance for the 2nd coupler of figure 7.4 is about 1.49×10^{15} W/m^2. Using the corresponding critical irradiances and interaction lengths in equation 7.5 for the calculation of the nonlinear refractive index coefficient for each of the directional couplers, the yielded n_2 values are 1.58×10^{-19} m^2/W and 3.29×10^{-19} m^2/W for couplers 1 and 2 respectively in good agreement with the values calculated with equation 7.4.

The calculated values for the nonlinear refractive index coefficient of the modified area are between 3 to 6 times lower than the one measured via the Z-scan technique for the bulk GLS and was found to be 9.7×10^{-19} m^2/W. The n_2 of the modified area was also estimated by other members of the NLO group in a previous work where they demonstrated spectral broadening in ultrafast laser inscribed GLS waveguides [13]. In that work they derived the nonlinear phase change from the SPM peaks and calculated the n_2 coefficient by using equation 7.3. The estimated n_2 coefficient for the modified region of the waveguides was approximately 5 times lower than the one for bulk GLS, in very good agreement with the obtained results in this investigation. The results of both studies indicate that the ULI technique can cause changes to the nonlinear refractive index of GLS, decreasing the nonlinear refractive indices of the modified regions comparing with the bulk substrate.

Finally, it is worth mentioning that since the guided modes extend outside the geometrical limits of the waveguides, the part of the mode that propagates in the unmodified region will contribute in the estimation of the n_2 coefficient for the modified region. This yields an increased n_2 coefficient comparing with the case at which the guided mode propagates entirely within the geometrical limits of the modified region. Therefore, the reduction of the n_2 coefficient for the modified region is probably higher than the one calculated in the two studies mentioned above. An accurate calculation of the n_2 coefficient for the modified region is not possible when using methods which consider propagating modes, since these modes will always extend outside the modified region of the waveguides. As already discussed in section 7.1, to overcome this problem the inscription of a large area in GLS was attempted with aim to study the n_2 coefficient via the closed-aperture Z-scan technique. However, other problems arose, such as the shattering of the substrates due to the high stresses imposed by the large area modified regions.

7.5 Summary

In summary, this chapter has presented the ultrafast all-optical switching achieved in GLS directional couplers fabricated via the ULI technique. The basic operating principles of coupled modes in directional couplers were introduced, followed by a discussion on how the irradiance dependent refractive index can be exploited to achieve all-optical power switching. Then the directional couplers fabricated in GLS substrates were presented and the optimum fabrication parameters were discussed. Ultrafast all-optical switching was demonstrated and the nonlinear refractive index coefficient, n_2, of the modified by the laser area was calculated from the switching parameters. The experimental findings showed that the ULI technique can induce changes to the nonlinear refractive index of GLS, decreasing the nonlinear refractive indices of the modified regions up to approximately 4-5 times comparing with the bulk substrate.

Chapter 8. Waveguides in erbium doped gallium lanthanum sulphide: potential for mid-infrared waveguide lasing applications

8.1. Introduction

This chapter will present the fabrication of ultrafast laser inscribed optical waveguides in erbium doped gallium lanthanum sulphide glasses. The main objective of this study was to explore the potential for mid-infrared waveguide Er^{3+}: GLS lasing applications. First an introduction into erbium doped gallium lanthanum sulphide is performed, pointing out the advantages of GLS as a rare earth host. The absorption spectrum of Er^{3+}: GLS along with the energy levels of Er^{3+} indicating the possible mid-infrared transitions are introduced. After that, the waveguides inscribed in Er^{3+}: GLS are presented and the optimum fabrication parameters are discussed. The chapter finally closes with the demonstration of fluorescence for the infrared transitions at 1550 and 2750 nm, detected after exciting the Er^{3+} ions at 980 nm. The initial results obtained here, revealing the promising potential of GLS as a rare earth host, were presented at the CLEO 2015 conference [14].

8.2. Erbium doped gallium lanthanum sulphide glass

The potential of GLS for nonlinear switching applications, was extensively studied in chapters 5, 6 and 7. Gallium lanthanum sulphide also offers promise as a host material for optically active applications. As already discussed in chapter 5, their low phonon energies reduce multi-phonon quenching which leads to a mid-infrared transparency, therefore allowing for mid-infrared transitions in this important wavelength region. The presence of lanthanum as a glass former in the GLS glass matrix offers a distinct advantage. GLS can be readily doped with rare earth ions simply by substitution of the lanthanum ion in the glass matrix. This allows for high dopant concentrations without observing any rare earth ion clustering [186]. For example, in silica glasses rare earth ion clustering limits the dopant concentrations to a few hundred parts per million, where in GLS, concentrations of hundreds of thousands parts per million have been reported [187].

Additionally, the high refractive index of GLS enhances the absorption and emission cross sections of the rare earth ions in the matrix [187].

The aforementioned properties make GLS a very attractive host for rare earth dopants. The most widely studied rare-earth dopant is the trivalent erbium ion (Er^{3+}) due to the success of the erbium doped fibre amplifier (EDFA) in silica based glasses [188]. EDFA's make use of the 1.55 μm transition from the first energy level to the ground state to amplify emission in the ~1.5 μm wavelength region. However, the high phonon energy of the silica host leads to mid-infrared opacity making the mid-infrared transitions from the higher laying levels at longer wavelengths inaccessible. By changing the host material from silica to GLS, these mid-infrared transitions can be accessed due to the host GLS better mid-infrared transparency. This blend of mid-infrared transparency and excellent rare earth solubility offers great potential upon realising Er^{3+} doped GLS mid-infrared lasing applications. The absorption spectrum of Er^{3+} doped GLS along with the Er^{3+} energy levels indicating the possible infrared transitions is shown in figure 8.1.

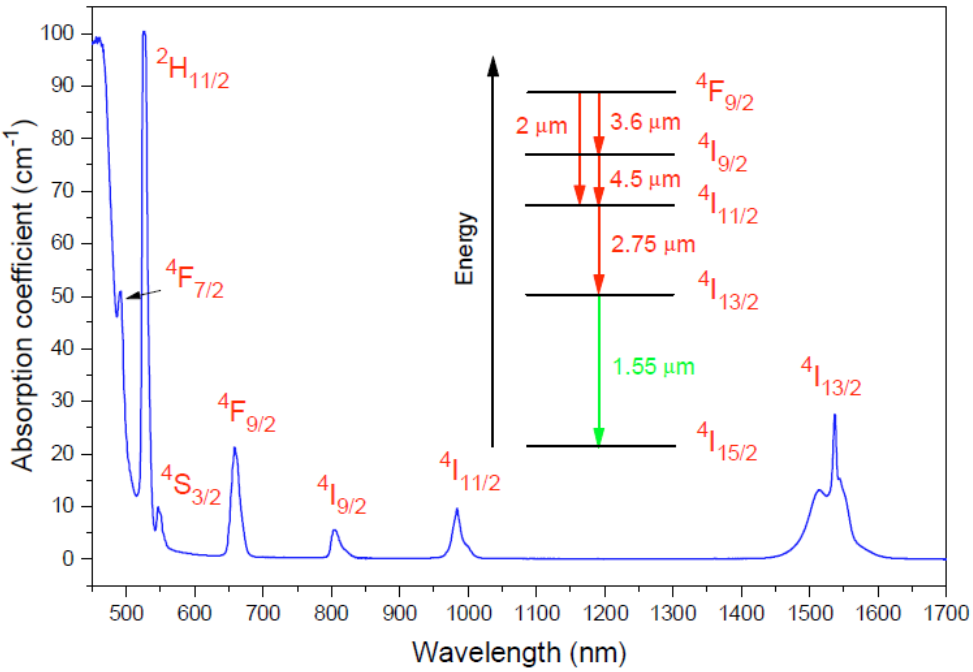

Figure 8.1. Absorption spectrum of Er^{3+} doped GLS glass along with the Er^{3+} energy levels indicating the infrared transitions (reproduced from [152]).

In the work presented in this chapter, the ULI technique was used to fabricate waveguides in Er^{3+}: GLS substrates. The Er^{3+} ions were excited at the 2nd energy level ($^4I_{11/2}$) using a 980 nm fibre laser and the infrared transitions at 2.75 μm from the 2nd to the 1st energy level and at 1.55 μm from the 1st energy level to the ground state were detected.

8.3. Ultrafast laser inscription of waveguides in erbium doped gallium lanthanum sulphide

Two samples with different Er^{3+} concentrations, namely 1% and 2% of Er^{3+} ions in the GLS host matrix, were used for the fabrication of the waveguides. These samples were provided from our collaborators at the ORC of Southampton University. The waveguides were fabricated using the ultrafast laser inscription setup outlined in section 2.8 with the IMRA® laser system, presented in section 2.8.1, set to emit 360 fs pulses at a pulse repetition rate of 500 kHz. The pulses from the inscription laser were focused inside the substrates using a 0.4 NA aspheric lens. The pulse energies incident on the samples were ranging from 72 down to 40 nJ, whereas the translation speeds varied from 0.5 to 20 mm/s. The waveguides were fabricated by using the multiscan inscription technique introduced in section 6.3. Three different scan-to-scan horizontal offsets were used, namely 0.3, 0.33 and 0.36 μm. In order to realise waveguides for 1.55 μm single mode operation the number of single scans was varied from 9 to 15 scans, yielding waveguides with rectangular cross sections of about 3.7-6.5 μm width and 15-18 μm height. For the realisation of waveguides for 2.75 μm single mode operation the number of scans was chosen to vary from 25 to 38 scans, yielding waveguides with cross sections of about 8.5-13.7 μm width and 15-18 μm height. Six waveguides fabricated in a 1% Er^{3+}: GLS substrate at a pulse energy of 52 nJ using a sample translation speed of 4 mm/s are shown in figure 8.2.

The first three waveguides of figure 8.2 were inscribed with a scan-to-scan horizontal offset of 0.3 μm but using different number of scans for each waveguide, namely 28, 31 and 34 scans from left to right. The last three waveguides were inscribed with a scan-to-scan horizontal offset of 0.33 μm and using the same number of single scans as the first three waveguides again from left to right.

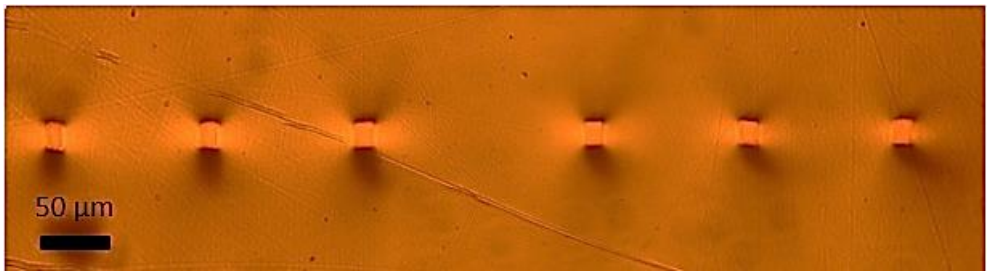

Figure 8.2. Microscope images of six waveguides inscribed in a 1% Er^{3+}: GLS substrate.

8.4. Fluorescence in Er^{3+} doped GLS waveguides

The Er^{3+} ions in the waveguides were excited at the second energy level ($^4I_{11/2}$) using a fibre laser operating at 980 nm as a pump. The pump laser was collimated with a 10X aspheric lens and then focussed in the sample with another 10X aspheric lens. The fluorescence spectra were collected with a CaF_2 lens and captured by focussing in a Thorlabs optical spectrum analyser (OSA205) operating at the wavelength region of 1.0 to 5.6 µm. A long pass filter which cut off at 1.4 µm was used in front of the spectrum analyser to block the pump wavelength. The collected fluorescence spectra for the 1% and 2% Er^{3+}: GLS samples are shown in figures 8.3 and 8.4 respectively.

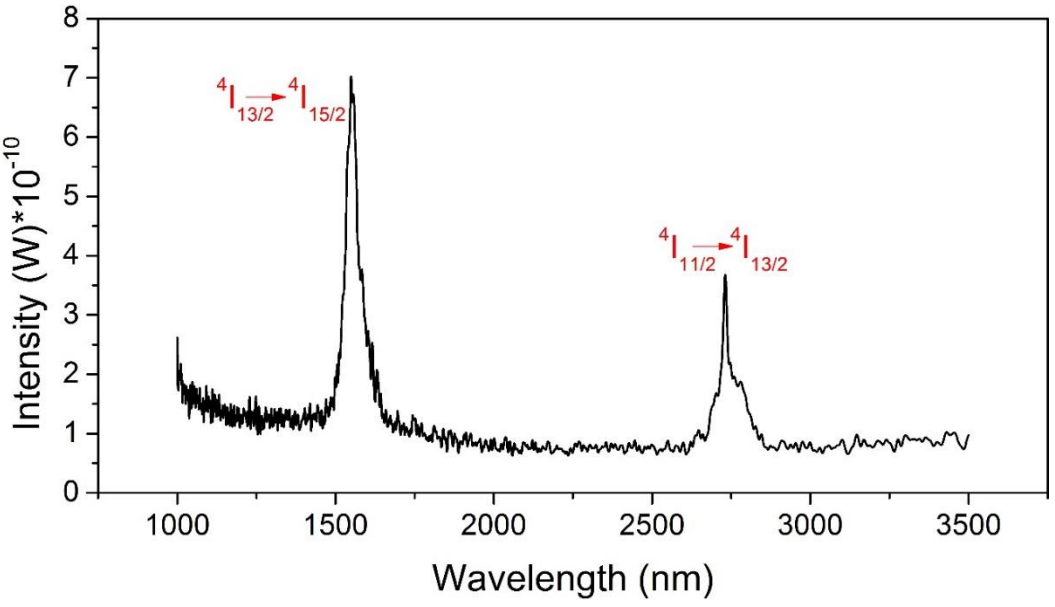

Figure 8.3. Fluorescence spectra of a 1% Er^{3+}: GLS glass showing the emissions at 1.55 and 2.75 µm after exciting the Er^{3+} ions at 980 nm.

The fluorescence spectra of figure 8.3 were collected from a waveguide inscribed with a pulse energy of 48 nJ at a sample translation speed of 8 mm/s. For this waveguide 27 scans with a scan-to-scan horizontal offset of 0.3 μm were used, yielding a waveguide with rectangular cross sections of about 8.7-18 μm.

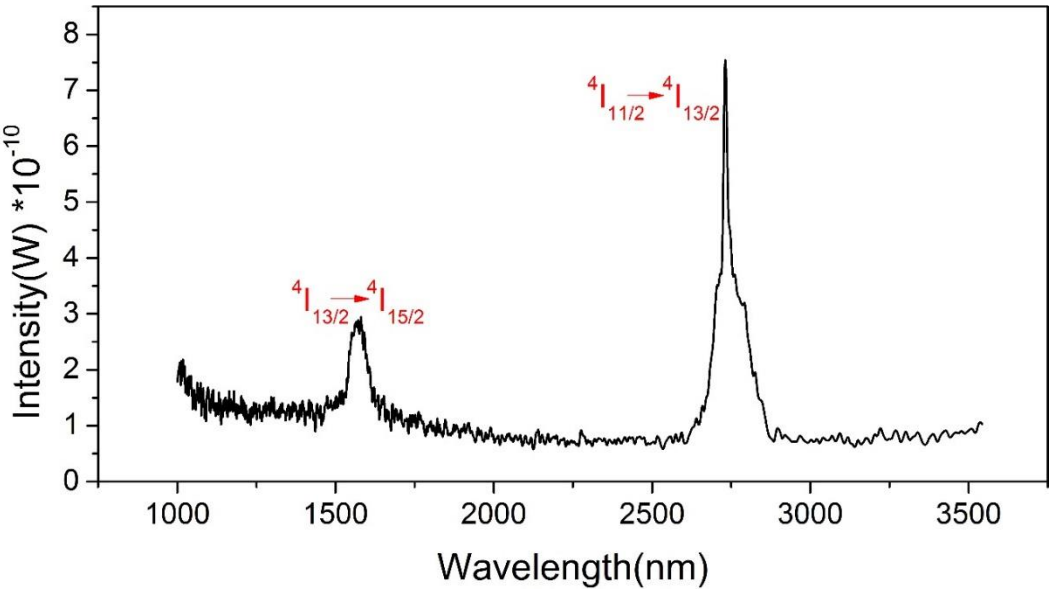

Figure 8.4. Fluorescence spectra of a 2% Er^{3+}: GLS glass showing the emissions at 1.55 and 2.75 μm after exciting the Er^{3+} ions at 980 nm.

The fluorescence spectra of figure 8.4 were collected from a waveguide inscribed with a pulse energy of 52 nJ at a sample translation speed of 4 mm/s. For this waveguide 28 scans with a scan-to-scan horizontal offset of 0.3 μm were used, yielding a waveguide with rectangular cross sections of about 9-18 μm.

The waveguides in the two samples presented in figures 8.3 and 8.4 had the same length of 20 mm, whereas the pump level in both occasions was at 1 watt. From the figures it can be seen that the fluorescence peak at 1.55 μm is suppressed for the sample with the higher Er^{3+} concentration, whereas the fluorescence peak at 2.75 μm shows the opposite trend, being enhanced with increasing Er^{3+} concentration. This behaviour is attributed to the fact that the first energy level ($^4I_{13/2}$) suffers from concentration quenching. This practically means that the fluorescent lifetimes of this level decrease with increasing Er^{3+} concentrations, therefore quenching emission. On the contrary, the 2nd energy level ($^4I_{11/2}$)

does not present any concentration quenching. As a result, the fluorescent lifetimes remain unaltered and emission from this level is increased with increasing Er^{3+} concentrations. Similar dependencies of the two energy levels, $^4I_{13/2}$ and $^4I_{11/2}$, on the Er^{3+} concentration were also observed for Er:YAG samples [189]. However, so far there has not been any reported work investigating the fluorescent life times as a function of Er^{3+} concentration in Er^{3+}: GLS glasses. The NLO group is working in close proximity with our collaborators at the ORC of Southampton University to fabricate a range of Er^{3+}: GLS glasses with varying Er^{3+} concentrations and perform an extensive investigation on the spectral properties and energy level lifetimes dependencies on the Er^{3+} concentration.

The mode profiles of the fluorescence were captured with a FLIR SC7000 camera. The fluorescence mode profile for the 1.55 μm transition was isolated using a 1.55 μm bandpass filter in front of the camera to block both the 2.75 μm fluorescence and the pump wavelength. The fluorescence mode profile for the 2.75 μm transition was isolated using a long pass filter which cut off at 2 μm in front of the camera. The fluorescence mode profiles for the 1.55 and 2.75 μm transitions are shown in figures 8.5 and 8.6 respectively.

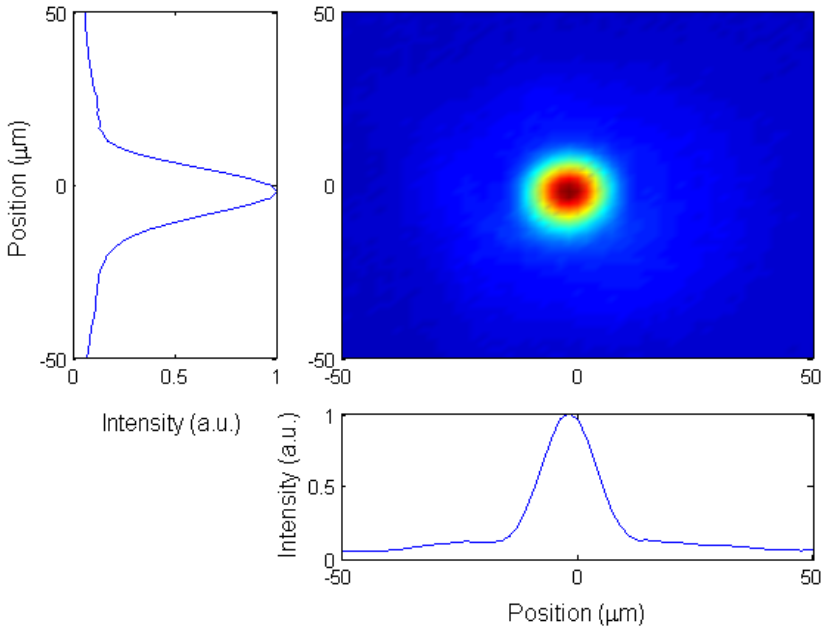

Figure 8.5. Fluorescence mode profile for the 1.55 μm transition along with the associated mode cross-sections in the vertical and horizontal directions.

The fluorescence mode profile, presented in figure 8.5, for the 1.55 μm infrared transition was collected from a waveguide inscribed with a pulse energy of 52 nJ at a sample translation speed of 4 mm/s. Nine scans with a scan-to-scan horizontal offset of 0.33 μm were used, yielding a waveguide with rectangular cross sections of about 3.6-18 μm. This waveguide exhibited single mode guiding for the 1.55 μm fluorescence. The experimentally measured $1/e^2$ mode field diameters for the waveguide were found to be 14.46 ± 1.55 μm in the horizontal direction and 17.84 ± 1.55 μm in the vertical direction.

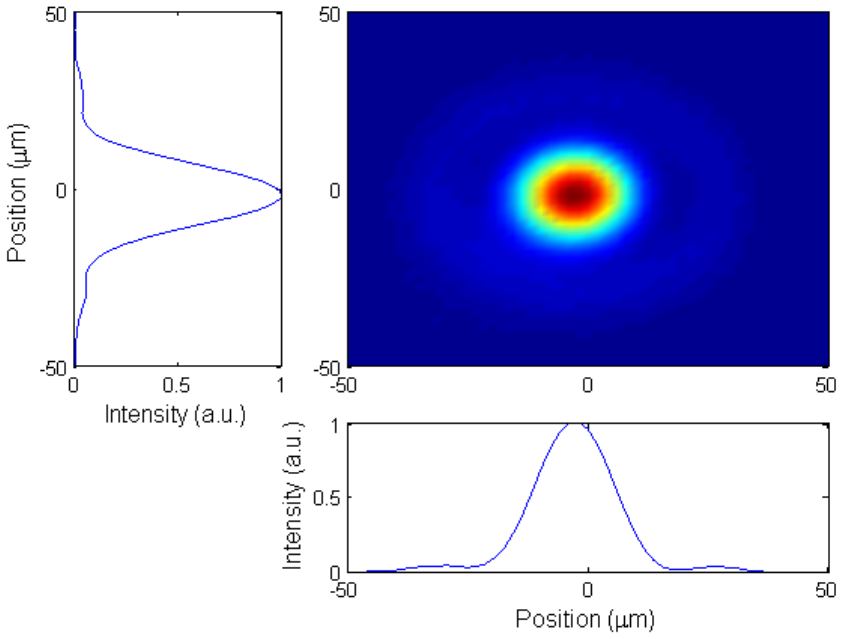

Figure 8.6. Fluorescence mode profile for the 2.75 μm transition along with the associated mode cross-sections in the vertical and horizontal directions.

The fluorescence mode profile, presented in figure 8.6, for the 2.75 μm infrared transition was collected from a waveguide inscribed with a pulse energy of 58 nJ at a sample translation speed of 4 mm/s. Twenty-eight scans with a scan-to-scan horizontal offset of 0.36 μm were used, yielding a waveguide with rectangular cross sections of about 10.7-18 μm. This waveguide exhibited single mode guiding for the 2.75 μm fluorescence. The experimentally measured $1/e^2$ mode field diameters for the waveguide were found to be 18.13 ± 1.55 μm in the horizontal direction and 19.51 ± 1.55 μm in the vertical direction.

The mode profile for the waveguide presented in figure 8.6 is more symmetrical in regards of the MFDs in the horizontal and vertical directions comparing with the mode profile of the waveguide presented in figure 8.5. This is due to fact that the width of the waveguide of figure 8.6 is bigger, since it was designed for 2.75 μm single mode operation. This points out that if the geometrical cross sections are tailored so that the width of the waveguides is equal to their height, waveguides with entirely symmetrical Gaussian mode profiles can be realised.

8.5. Summary

This chapter has presented the preliminary results regarding the fabrication of ultrafast laser inscribed waveguides in erbium doped gallium lanthanum sulphide glasses exploring the potential for mid-infrared waveguide Er^{3+}: GLS lasing applications. The advantages of GLS as a rare earth host were discussed and the absorption spectrum of Er^{3+} doped GLS along with the energy levels of Er^{3+} indicating the possible mid-infrared transitions were introduced. After that, the waveguides fabricated in Er^{3+}: GLS substrates were presented and the optimum fabrication parameters were discussed. Fluorescence for the 1.55 and 2.75 μm infrared transitions was demonstrated after exciting the Er^{3+} ions at 980 nm. The initial results obtained here, revealing the potential of GLS as a rare earth host, were presented at the CLEO 2015 conference [14].

Chapter 9. Conclusions and future work

9.1. Conclusions

The work presented in this thesis has focused on the ultrafast nonlinear optics of bulk chalcogenides and two-dimensional materials in the near- and mid-infrared. Special emphasis was given to the investigation of the nonlinear optical properties of graphene aiming for its integration with nonlinear bulk chalcogenides for the realisation of relevant nonlinear devices and applications. Chapters 3 and 4 were concerned with the investigation of the fundamental nonlinear absorption and refraction properties of graphene via the Z-scan technique. The saturable absorption, two-photon absorption and nonlinear refraction of CVD single- and multi-layer graphene were studied over a broad range of wavelengths. The nonlinear optical properties of graphene poly-vinyl alcohol composite films which can be advantageous over multilayer graphene for specific applications were investigated. The thermal damage of the G-PVA composites due to heat diffusion from the embedded graphene and subsequent thermal damage of the host polymer was assessed. Chapter 5 focussed in the investigation of the nonlinear optical properties of a series of chalcogenide glasses via Z-scan with aim to identify a suitable host material for waveguide and device fabrication, whereas chapters 6 to 8 concentrated in the fabrication and characterisation of waveguides and devices in gallium lanthanum sulphides via ULI. High quality waveguides were realised in GLS and their fundamental properties, such as refractive index profiles and dispersion over a broad range of wavelengths which also enabled the determination of the ZDW of GLS, were measured. The ultrafast all-optical switching achieved in directional couplers fabricated in GLS allowed for the calculation of the nonlinear refractive index coefficient, n_2, of the modified by the laser area from the switching parameters. Optical waveguides were successfully fabricated in Er^{3+} doped GLS and the infrared transitions at 1550 and 2750 nm were detected after exciting the Er^{3+} ions at 980 nm revealing the potential for mid-infrared Er^{3+}: GLS waveguide lasing applications.

The nonlinear optical properties of all the materials investigated in this thesis are summarised in table 9.1 and compared under a general discussion which allows for useful conclusions regarding the relationship between the materials nature and the nonlinearity.

Table 9.1 Summary of the nonlinear optical coefficients

	Nonlinear refractive index coefficient (m^2/W)	Saturable absorption coefficient (W/m^2)	Two-photon absorption coefficient (m/W)	Three-photon absorption coefficient (m^3/W^2)	Four-photon absorption coefficient (m^5/W^3)
Single layer Graphene (1045 nm)	-3.5×10^{-11}	5.2×10^{13}	—	—	—
Multilayer Graphene					
1150 nm	-0.55×10^{-13}	4.5×10^{13}	0.38×10^{-7}	—	—
1550 nm	-0.8×10^{-13}	3×10^{13}	0.9×10^{-7}		
2000 nm	-1.4×10^{-13}	2.1×10^{13}	1.5×10^{-7}		
2400 nm	-2.5×10^{-13}	1.9×10^{13}	1.9×10^{-7}		
G-PVA composite					
1550 nm	-0.58×10^{-13}	1.2×10^{13}	0.5×10^{-7}	—	—
2000 nm	-0.61×10^{-13}	1×10^{13}	1.25×10^{-7}		
2400 nm	-0.69×10^{-13}	0.8×10^{13}	1.7×10^{-7}		
GLS (1550 nm)	9.7×10^{-19}	—	$\sim 10^{-13}$	$\sim 10^{-28}$	$\sim 10^{-43}$
GASIR-1 (1550 nm)	4.5×10^{-18}	—	$\sim 10^{-12}$	$\sim 10^{-26}$	$\sim 10^{-40}$
ZnSe (2500 nm)	4×10^{-19}	—	—	—	—
Cr:ZnSe (2500 nm)	2.8×10^{-19}	—	—	—	—
Tellurite (1550 nm)	4.6×10^{-19}	—	—	—	—
Phosphate (1550 nm)	6.5×10^{-19}	—	—	—	—

The nonlinear optical properties of all the materials investigated in this thesis along with the operating wavelength are summarised in table 9.1. These materials can be divided between two main categories; graphene allotropes which during the last decade emerged as novel materials with superior nonlinear optical properties baring the promise of implementation in a range of applications and chalcogenide glasses which are more well-known and already used in a range of mid-infrared applications due to their excellent mid-infrared transparency and high optical nonlinearities.

As can be seen graphene fulfils the expectations as a highly nonlinear material since all the graphene products present at least six orders of magnitude higher nonlinear refractive index coefficients than the chalcogenide glasses, with single layer graphene presenting the highest nonlinear refractive index of them all in the orders of ~10^{-11} m^2/W. Moreover, the TPA coefficients of graphene were measured to be at least five orders of magnitude higher than the ones measured for the two chalcogenide glasses, GLS and GASIR-1. The investigation of graphene's nonlinearities at different wavelengths revealed the trend of the nonlinear coefficients. The nonlinear refraction (in absolute values) and two-photon absorption increase with increasing wavelength, whereas the saturable absorption presents the opposite trend decreasing with increasing wavelength. This is due to the fact that longer wavelengths possess lower photon energies, therefore exciting electrons positioned closer to the Dirac point which are more nonlinear than the ones positioned further away [190].

The chalcogenide glasses investigated in this study present comparable nonlinear refractive index coefficients in the orders of ~10^{-19} m^2/W, with only GASIR-1 presenting a nonlinear refractive index in the orders of ~10^{-18} m^2/W about an order of magnitude higher than the rest of them. However, GASIR-1 also presents much higher nonlinear absorption coefficients which combined with the presence of Arsenic in the glass matrix make it unattractive for nonlinear switching applications. Comparing the results obtained for ZnSe and Cr:ZnSe it was deduced that the chromium dopant slightly reduces the nonlinear refractive index coefficient of Cr:ZnSe comparing with ZnSe, whereas its contribution to the nonlinear absorption was negligible due to the fact that the peak of the absorption cross section of chromium lies far away from the operating wavelength of 2500 nm. Finally, the tellurite and phosphate glasses might be of particular interest. Although their nonlinear refractive index coefficients were slightly lower than the one obtained for GLS, they did not present any nonlinear absorption effects up to the highest irradiances of 141.3 GW/cm^2 used in this study, implying that their figure of merit for nonlinear switching applications maybe very favourable and superior to that of GLS. Therefore, a deeper investigation in the potential of these glasses for nonlinear optical applications might reveal very interesting information.

In the following paragraphs overall conclusions regarding the worked performed in each chapter are drawn.

In chapter 3 the Z-scan experimental technique was used to study the saturable absorption, two-photon absorption and nonlinear refraction properties of CVD single- and multi-layer graphene. The graphene samples were provided by the Department of Physics of the National University of Singapore. The closed-aperture Z-scan measurements revealed a giant value for the nonlinear refraction of graphene in the orders of $\sim 10^{-13}\ m^2/W$. This nonlinear refraction property of graphene was found to have a negative sign and also be irradiance-dependent, therefore it was discriminated from the conventional nonlinear refractive index coefficient, n_2, which is irradiance independent. The irradiance dependence was extensively investigated in the single layer graphene, leading to the determination of the nonlinear refractive index coefficient, n_2, and the irradiance, I_{sat}, at which the nonlinear phase shift $\Delta\Phi$ saturates, which were found to be $n_2 = -3.5 \times 10^{-11}\ m^2/W$ and $I_{sat} = 0.2\ GW/cm^2$. The wavelength dependence of the nonlinear refraction was studied in the multi-layer graphene sample. The negative value and wavelength dependence of the nonlinear refraction were supported with a theoretical analysis arising from the conductivity of the graphene monolayer. The open-aperture Z-scan measurements revealed that under laser illumination multilayer graphene exhibits a transmittance increase due to saturable absorption, followed by optical limiting due to two-photon absorption. The saturation irradiances, I_{sat}, and two-photon absorption coefficients, β, were measured and the threshold at which SA turns to TPA was defined for each of the operating wavelengths. At the highest irradiances used in this study, laser induced damage was observed in graphene. The damage was verified by Raman spectroscopy and the femtosecond laser induced damage threshold in graphene was found to be at 14.1 mJ/cm^2.

Chapter 4 presented the work performed on graphene-polymer composite thin films which for some applications can be advantageous over multilayer graphene. The Z-scan technique was used for the nonlinear optical characterisation of a G-PVA thin film, provided by the Nanomaterials and Spectroscopy Group in the Department of Engineering at the University of Cambridge. The closed-aperture Z-scans showed the same negative irradiance-dependent nonlinear refraction as the CVD graphene. The

saturable and two-photon absorption properties of the G-PVA were investigated via open-aperture Z-scans and the associated nonlinear coefficients were derived at the operating wavelengths. The laser induced dynamic thermal damage in G-PVA thin films by ultrashort pulses was also considered. The G-PVA composites were provided by the centre for research on adaptive nanostructures and nanodevices in the school of physics of the Trinity College of Dublin. Two different damage mechanisms, depending on the laser repetition rate, were identified. At a high repetition rate regime of 500 kHz, the light absorbed by graphene led to its temperature rise and consequently to a heat inflow from the embedded graphene into the host polymer. This heat interchange procedure resulted in a temperature rise and eventually thermal damage of the host polymer. The damage threshold was found to be dependent on the graphene concentration in the host matrix. At the low repetition rate regime of 1 kHz, the damage was found to be due to the local modification of the carbon bonds inside the graphene lattice from the ultrafast pulses rather than heat diffusion from the embedded graphene and thermal damage of the host polymer. A comprehensive thermal analysis enabled the study of the heat accumulation effects in graphene as a function of the laser repetition rate. A heat-interchange model allowing for the assessment of the heat transfer at the graphene-polymer interface and the equilibrium temperature of the graphene-polymer system was derived. This novel heat-interchange model paves the way for studying the thermal dynamics and heat interchange of graphene embedded into any host matrix.

In chapter 5 the Z-scan experimental technique was used to study the nonlinear absorption and refraction properties of a range of chalcogenide glasses. A germanium arsenic selenide ($Ge_{22}As_{20}Se_{58}$) glass known as GASIR-1 provided by Umicore and a gallium lanthanum sulphide glass provided by the ORC of Southampton University were investigated with aim to choose a suitable host material for waveguide and device fabrication via ULI. GASIR-1 presented a higher nonlinear refractive index coefficient than GLS. The n_2 coefficient for GASIR-1 was measured to be 4.5×10^{-18} m^2W^{-1}, whereas the one for GLS was found to be 9.7×10^{-19} m^2W^{-1}. However, GASIR-1 presented much stronger absorptive nonlinearities as well, with all the nonlinear absorption coefficients related to two-, three- and four-photon absorption processes being more than one order of magnitude higher than the ones measured for GLS. This led to a lower figure of merit for GASIR-1, which was estimated to be 1.54 as opposed to GLS which presented a FOM

of 2.95. The high FOM combined with the fact that GLS is an arsenic-free chalcogenide led to its choice as a substrate material for waveguide and device fabrication. The nonlinear refraction properties of a Cr:ZnSe sample were studied via closed-aperture Z-scans with aim to use the n_2 coefficient to optimise the design of the laser cavity for mode-locking a Cr:ZnSe waveguide laser via KLM. Finally, the nonlinear optical characterisation of two novel telluride and phosphate glasses was performed with main objective to assess their potential for mid-infrared nonlinear applications.

Chapter 6 presented the fabrication and characterisation of ultrafast laser inscribed waveguides in gallium lanthanum sulphide glasses. The refractive index profiles of a series of waveguides fabricated with different inscription parameters were measured using quantitative phase microscopy. The variation of the inscription parameters enabled the investigation of the effects they have upon the refractive index profiles. From this study it was found that the refractive index increase of the modified by the laser area of the waveguides varied from about 1×10^{-3} to 4×10^{-3} with inscription parameters presenting a strong dependence on the fabrication pulse energy. The material dispersion of bulk GLS and the total dispersion of a series of inscribed waveguides was measured using white-light spectral-domain interferometry. The measurements were performed over a broad range of wavelengths in the near- and mid-infrared region of the electromagnetic spectrum spanning from ~1.3 to 4.5 μm. This study revealed that the total dispersion in the waveguides is dominated by material dispersion. The wide range at which the dispersion measurements were undertaken enabled the determination of the zero dispersion wavelength for both the waveguides and bulk GLS. The ZDW was found to be between 3.66 and 3.71 μm for the waveguides and about 3.61 μm for the bulk.

The work presented in chapter 7 focussed in the fabrication of optical directional couplers in gallium lanthanum sulphide via the ultrafast laser inscription technique. The high Kerr nonlinearities of GLS were exploited to achieve ultrafast all-optical switching in the fabricated directional couplers. The incident irradiances required to completely switch the couplers from the cross to the bar state were in the orders of $\sim 10^{15}\ W/m^2$. The nonlinear refractive index coefficient, n_2, of the modified by the laser area was calculated from the switching parameters. The experimental findings showed that the ULI technique can cause changes to the nonlinear refractive index of GLS, decreasing the nonlinear

refractive indices of the modified regions up to approximately 4-5 times comparing with the bulk substrate.

Chapter 8 presented fabrication of ultrafast laser inscribed waveguides in erbium doped gallium lanthanum sulphide. Fluorescence for the infrared transitions at 1550 and 2750 nm was detected after exciting the Er^{3+} ions at 980 nm. Samples with different Er^{3+} concentrations were treated. It was found that the 2750 nm fluorescence was enhanced with increasing Er^{3+} concentration, whereas the fluorescence at 1550 nm presented the opposite trend, decreasing with increasing Er^{3+} concentration. The mode profiles obtained for the fluorescence at both 1550 and 2750 nm showed good symmetry. The $1/e^2$ mode field diameters for the 1550 nm fluorescence were measured to be 14.46 ± 1.55 μm in the horizontal direction and 17.84 ± 1.55 μm in the vertical direction, whereas the ones obtained for the 2750 nm fluorescence were found to be 18.13 ± 1.55 μm in the horizontal direction and 19.51 ± 1.55 μm in the vertical direction. These preliminary results obtained here revealed the promising potential of GLS as a rare earth host.

9.2. Future work

From the study into the nonlinear optical properties of chalcogenide glasses, GLS emerged as a very promising material mid-infrared nonlinear applications. Its large nonlinear refractive index coupled with its low multiphoton absorption not only lead to a large FOM for switching applications but also make GLS a very attractive candidate for supercontinuum generation sources for sensing applications. The NLO group has already demonstrated mid-infrared spectral broadening in ultrafast laser inscribed GLS waveguides spanning over 3500 nm, from 1700 nm to 5200 nm [12, 13]. The results obtained from the refractive index profiling and dispersion measurements of GLS waveguides, presented in chapter 6, are already being utilised to tailor the guiding properties and extend the spectral broadening further into the infrared. Following the optimisation of the supercontinuum generation, the highly evanescent guiding nature of the GLS waveguides could be exploited to realise an embedded sensor device. Such a device would consist of a single mode waveguide written inside GLS allowing for the generation of a broad supercontinuum. Then by taking advantage of the inherent 3D writing capabilities offered by ULI, the waveguide will split into two waveguides one of

which will be raised close to the substrate surface in order for the evanescent field to interact with the surface, while the other will remain 'buried' into the substrate acting as reference. Fundamental molecular absorption lines that lie inside the bandwidth of the supercontinuum spectrum will therefore manifest as a dip in the supercontinuum transmission which will be monitored by comparing with the second embedded reference waveguide.

Moreover, the propagation loss measurements revealed propagation losses in the orders of 0.6 dB/cm. A deeper investigation in the origins of these propagation losses and the various mechanisms that contribute to the loss, as well as how the various laser inscription parameters affect the propagation losses of waveguides inscribed in GLS substrates should be performed. These studies will provide useful insight in better understanding the structure of the material and most importantly they will potentially lead to achieving even lower than 0.6 dB/cm propagation losses.

Additionally, the ultrafast laser inscription technique is an ideal candidate for the fabrication of tapered waveguides. The cross sections of such waveguides will vary along the waveguide length. These waveguides can find application as photonic lanterns; light from a multimode fibre can be coupled in the waveguide facet with the large cross section and collected with a single mode fibre from the facet with the small cross section. The 3D capabilities of ULI can be exploited to accurately tailor the waveguide cross sections to match the input and output fibre cross sections, minimising coupling losses which would otherwise be significant if the two fibres were coupled together without the use of the tapered waveguide.

The tapered waveguides would be extremely beneficial in the case of rare earth doped materials for lasing applications, serving two different purposes. Firstly, they would allow for high pump powers to couple in the sample by focussing on waveguide facets with larger cross sections, therefore preventing input facet ablation while maintaining the ability of single mode operation in the output. Secondly they would greatly favour mode-locking via KLM, due to the fact that the irradiance will increase as the beam propagates in a waveguide with decreasing cross sections. Subsequently, this increasing irradiance

along the waveguide length will enhance the optical Kerr effect causing tighter self-focussing of the beam and therefore enable the generation of ultrashort pulses.

As mentioned earlier the low phonon energies, mid-infrared transparency and excellent rare earth solubility make GLS a very attractive host for rare earth dopants. The initial results obtained here in Er^{3+}: GLS ultrafast laser inscribed waveguides reveal very promising potential for mid-infrared rare earth doped GLS waveguide lasers via ULI. The NLO group is already working in close proximity with our collaborators at the ORC of Southampton University to prepare a range of Er^{3+}: GLS samples of different Er^{3+} concentrations with view to perform an extensive investigation on the dependencies of the spectral properties and energy level lifetimes on the Er^{3+} concentration. Furthermore, other rare earth dopants are considered. The preparation of holmium (Ho^{3+}) doped GLS is scheduled in order to explore the possibilities for Ho^{3+} doped GLS waveguide lasers via ULI. Moreover, it is planned to perform a spectroscopic analysis on the modified by the laser area of the waveguides to investigate whether the ULI technique has an effect on the spectral properties and energy level lifetimes of rare earth doped gallium lanthanum sulphides.

The two tellurite and phosphate glasses investigated in section 5.3.3 might be of particular interest. Although their nonlinear refractive index coefficients were slightly lower than the one obtained for GLS, they did not present any nonlinear absorption effects up to the highest irradiances of 141.3 GW/cm^2 used in this study, implying that their figure of merit maybe very favourable and superior to that of GLS for nonlinear switching applications and supercontinuum generation. Although, first a number of other properties, such as mechanical and thermal, must be quantified in order to deduce whether there is real potential in these glasses for realising relevant nonlinear infrared applications a deeper investigation in their nonlinear optical properties, which might reveal very interesting information, should be performed.

The in-depth investigation in graphene's nonlinear optical properties, performed in single- multilayer and embedded in polymer graphene, provides all the necessary information, such as Saturation irradiance and TPA thresholds, for using graphene based materials as saturable absorbers for laser mode-locking. Moreover, it reveals their

advantages or disadvantages for certain applications. The graphene-PVA composites cannot be employed in high repetition rate applications due to the low thermal damage threshold of the host polymer from heat diffusion from the embedded graphene. Advantages could be taken from the nonlinear optical characterisation of deposited graphene. Graphene could be coated on the output facet of rare earth doped substrates after waveguide fabrication, therefore eliminating the need of a substrate to support the graphene saturable absorber and subsequently decrease the losses in the laser cavity. The giant two-photon absorption observed in multilayer graphene and G-PVA composites can lead to their utilisation as optical limiters for human eye and sensor protection, enabling the realisation of devices that operate over the entire visible and infrared range of the electromagnetic spectrum.

Additionally, ultrafast optical pump-probe spectroscopy can be performed to gain insight and measure the ultrafast carrier dynamics of the single- multilayer and embedded in polymer graphene characterised in this thesis via Z-scan. The information regarding the ultrafast relaxation phenomena of these samples combined with the nonlinear optical coefficients acquired via Z-scan will provide all the necessary information for fully understanding and characterising the photo-induced processes in these graphene samples.

References

1. P. R. Wallace, "The Band Theory of Graphite," Physical Review **71**, 622-634 (1947).
2. K. S. Novoselov, A. K. Geim, S. V. Morozov, D. Jiang, Y. Zhang, S. V. Dubonos, I. V. Grigorieva, and A. A. Firsov, "Electric Field Effect in Atomically Thin Carbon Films," Science **306**, 666-669 (2004).
3. NobelPrize.org, "The Nobel Prize in Physics 2010 " (2016, 14 March), retrieved http://www.nobelprize.org/nobel_prizes/physics/laureates/2010/.
4. A. Martinez and Z. Sun, "Nanotube and graphene saturable absorbers for fibre lasers," Nat Photon **7**, 842-845 (2013).
5. J. Wang, Y. Hernandez, M. Lotya, J. N. Coleman, and W. J. Blau, "Broadband Nonlinear Optical Response of Graphene Dispersions," Advanced Materials **21**, 2430-2435 (2009).
6. E. Hendry, P. J. Hale, J. Moger, A. K. Savchenko, and S. A. Mikhailov, "Coherent Nonlinear Optical Response of Graphene," Physical Review Letters **105**, 097401 (2010).
7. M. Dragoman, D. Neculoiu, G. Deligeorgis, G. Konstantinidis, D. Dragoman, A. Cismaru, A. A. Muller, and R. Plana, "Millimeter-wave generation via frequency multiplication in graphene," Applied Physics Letters **97**, 093101 (2010).
8. R. Mary, G. Brown, S. J. Beecher, F. Torrisi, S. Milana, D. Popa, T. Hasan, Z. Sun, E. Lidorikis, S. Ohara, A. C. Ferrari, and A. K. Kar, "1.5 GHz picosecond pulse generation from a monolithic waveguide laser with a graphene-film saturable output coupler," Opt. Express **21**, 7943-7950 (2013).
9. R. Yingying, G. Brown, R. Mary, G. Demetriou, D. Popa, F. Torrisi, A. C. Ferrari, C. Feng, and A. K. Kar, "7.8-GHz Graphene-Based 2-μm Monolithic Waveguide Laser," Selected Topics in Quantum Electronics, IEEE Journal of **21**, 395-400 (2015).
10. G. Demetriou, H. T. Bookey, F. Biancalana, E. Abraham, Y. Wang, W. Ji, and A. K. Kar, "Nonlinear optical properties of multilayer graphene in the infrared," Opt. Express **24**, 13033-13043 (2016).
11. H. Zhang, S. Virally, Q. Bao, L. Kian Ping, S. Massar, N. Godbout, and P. Kockaert, "Z-scan measurement of the nonlinear refractive index of graphene," Opt. Lett. **37**, 1856-1858 (2012).
12. J. McCarthy, H. Bookey, S. Beecher, R. Lamb, I. Elder, and A. K. Kar, "Spectrally tailored mid-infrared super-continuum generation in a buried waveguide spanning 1750 nm to 5000 nm for atmospheric transmission," Applied Physics Letters **103**, 151103 (2013).
13. J. E. McCarthy, H. T. Bookey, N. D. Psaila, R. R. Thomson, and A. K. Kar, "Mid-infrared spectral broadening in an ultrafast laser inscribed gallium lanthanum sulphide waveguide," Opt. Express **20**, 1545-1551 (2012).
14. G. Demetriou, F. Thorburn, A. Lancaster, C. Craig, E. Weatherby, D. W. Hewak, and A. Kar, "Fluorescence in Erbium Doped Gallium Lanthanum Sulphide: Potential for mid-IR Waveguide Laser," in *CLEO: 2015*, OSA 2015), STh1G.2.
15. P. Bastock, C. Craig, K. Khan, E. Weatherby, J. Yao, and D. W. Hewak, "Properties of Gallium Lanthanum Sulphide Glass," in *CLEO: 2015*, OSA 2015), STh1G.1.
16. J. Kerr, "XL. A new relation between electricity and light: Dielectrified media birefringent," Philosophical Magazine Series 4 **50**, 337-348 (1875).
17. M. Göppert-Mayer, "Über Elementarakte mit zwei Quantensprüngen," Annalen der Physik **401**, 273-294 (1931).
18. P. A. Franken, A. E. Hill, C. W. Peters, and G. Weinreich, "Generation of Optical Harmonics," Physical Review Letters **7**, 118-119 (1961).
19. D. E. Spence, P. N. Kean, and W. Sibbett, "60-fsec pulse generation from a self-mode-locked Ti:sapphire laser," Opt. Lett. **16**, 42-44 (1991).
20. U. Morgner, F. X. Kärtner, S. H. Cho, Y. Chen, H. A. Haus, J. G. Fujimoto, E. P. Ippen, V. Scheuer, G. Angelow, and T. Tschudi, "Sub-two-cycle pulses from a Kerr-lens mode-locked Ti:sapphire laser," Opt. Lett. **24**, 411-413 (1999).

21. R. Kingston, "Parametric amplification and oscillation at optical frequencies," (1962), pp. 472-&.
22. J. A. Giordmaine and R. C. Miller, "Tunable Coherent Parametric Oscillation in $LiNbO_3$ at Optical Frequencies," Physical Review Letters **14**, 973-976 (1965).
23. L. E. Myers, W. R. Bosenberg, G. D. Miller, R. C. Eckardt, M. M. Fejer, and R. L. Byer, "Quasi-phase-matched 1.064-μm-pumped optical parametric oscillator in bulk periodically poled LiNbO3," Opt. Lett. **20**, 52-54 (1995).
24. D. Feng, N. B. Ming, J. F. Hong, Y. S. Yang, J. S. Zhu, Z. Yang, and Y. N. Wang, "Enhancement of second-harmonic generation in LiNbO3 crystals with periodic laminar ferroelectric domains," Applied Physics Letters **37**, 607-609 (1980).
25. J. Peng, "Developments of mid-infrared optical parametric oscillators for spectroscopic sensing: a review," OPTICE **53**, 061613-061613 (2014).
26. C. Ding, R. Yu, J. Li, X. Hao, and Y. Wu, "Formation and ultraslow propagation of infrared solitons in graphene under an external magnetic field," Journal of Applied Physics **115**, 234301 (2014).
27. Y. V. Bludov, D. A. Smirnova, Y. S. Kivshar, N. M. R. Peres, and M. I. Vasilevskiy, "Discrete solitons in graphene metamaterials," Physical Review B **91**, 045424 (2015).
28. H. Harutyunyan, R. Beams, and L. Novotny, "Controllable optical negative refraction and phase conjugation in graphite thin films," Nat Phys **9**, 423-425 (2013).
29. G. Demetriou, J.-P. Bérubé, R. Vallée, Y. Messaddeq, C. R. Petersen, D. Jain, O. Bang, C. Craig, D. W. Hewak, and A. K. Kar, "Refractive index and dispersion control of ultrafast laser inscribed waveguides in gallium lanthanum sulphide for near and mid-infrared applications," Opt. Express **24**, 6350-6358 (2016).
30. H. Bookey, "Linear and nonlinear optics of chalcogenide bulk glasses and fibre for ultrafast all-optical switching," (Heriot Watt University, Edinburgh, February 2004).
31. G. New, *Introduction to Nonlinear Optics* (Cambridge University Press, 2011).
32. R. W. Boyd, "Chapter 1 - The Nonlinear Optical Susceptibility," in *Nonlinear Optics (Third Edition)* (Academic Press, Burlington, 2008), pp. 1-67.
33. J. E. McCarthy, "Nonlinear Optical Processes in Bulk and Waveguide Structures in the Infrared," (Heriot Watt University, Edinburgh, 2013).
34. R. W. Boyd, "Chapter 2 - Wave-Equation Description of Nonlinear Optical Interactions," in *Nonlinear Optics (Third Edition)* (Academic Press, Burlington, 2008), pp. 69-133.
35. S. L. Chuang, S. Schmitt-Rink, B. I. Greene, P. N. Saeta, and A. F. J. Levi, "Optical rectification at semiconductor surfaces," Physical Review Letters **68**, 102-105 (1992).
36. M. Bass, P. A. Franken, J. F. Ward, and G. Weinreich, "Optical Rectification," Physical Review Letters **9**, 446-448 (1962).
37. Y. B. Band, C. Radzewicz, and J. S. Krasinski, "Sum- and difference-frequency generation for broadband input fields," Physical Review A **49**, 517-529 (1994).
38. T. Suhara and M. Fujimura, "Optical Parametric Amplifiers and Oscillators," in *Waveguide Nonlinear-Optic Devices* (Springer Berlin Heidelberg, Berlin, Heidelberg, 2003), pp. 271-281.
39. G. K. Kitaeva and A. N. Penin, "Spontaneous parametric down-conversion," Journal of Experimental and Theoretical Physics Letters **82**, 350-355 (2005).
40. T. Y. F. Tsang, "Optical third-harmonic generation at interfaces," Physical Review A **52**, 4116-4125 (1995).
41. M. Cronin-Golomb, B. Fischer, J. White, and A. Yariv, "Theory and applications of four-wave mixing in photorefractive media," IEEE Journal of Quantum Electronics **20**, 12-30 (1984).
42. S. Carusotto, G. Fornaca, and E. Polacco, "Two-Photon Absorption and Coherence," Physical Review **157**, 1207-1213 (1967).
43. G. S. He, L.-S. Tan, Q. Zheng, and P. N. Prasad, "Multiphoton Absorbing Materials: Molecular Designs, Characterizations, and Applications," Chemical Reviews **108**, 1245-1330 (2008).
44. R. W. Boyd, "Chapter 4 - The Intensity-Dependent Refractive Index," in *Nonlinear Optics (Third Edition)* (Academic Press, Burlington, 2008), pp. 207-252.

45. R. Mary, "Compact Near-Infrared 3-Dimensional Channel Waveguide Lasers," (Heriot Watt University, Edinburgh, september 2014).
46. R. L. Sutherland, *Handbook of nonlinear optics* (CRC press, 2003).
47. R. W. Boyd, "Chapter 7 - Processes Resulting from the Intensity-Dependent Refractive Index," in *Nonlinear Optics (Third Edition)* (Academic Press, Burlington, 2008), pp. 329-390.
48. F. W. Wise and J. Moses, "Self-focusing and Self-defocusing of Femtosecond Pulses with Cascaded Quadratic Nonlinearities," in *Self-focusing: Past and Present: Fundamentals and Prospects*, R. W. Boyd, S. G. Lukishova, and Y. R. Shen, eds. (Springer New York, New York, NY, 2009), pp. 481-506.
49. G. P. Agrawal, "Chapter 4 - Self-Phase Modulation," in *Nonlinear Fiber Optics (Fourth Edition)* (Academic Press, San Diego, 2006), pp. 79-119.
50. H. A. Haus, "Theory of mode locking with a fast saturable absorber," Journal of Applied Physics **46**, 3049-3058 (1975).
51. F. He, Y. Liao, J. Lin, J. Song, L. Qiao, Y. Cheng, and K. Sugioka, "Femtosecond Laser Fabrication of Monolithically Integrated Microfluidic Sensors in Glass," Sensors **14**, 19402 (2014).
52. S. Hughes, J. M. Burzler, and T. Kobayashi, "Modeling of picosecond-pulse propagation for optical limiting applications in the visible spectrum," J. Opt. Soc. Am. B **14**, 2925-2929 (1997).
53. H. B. Liao, R. F. Xiao, H. Wang, K. S. Wong, and G. K. L. Wong, "Large third-order optical nonlinearity in Au:TiO_2 composite films measured on a femtosecond time scale," Applied Physics Letters **72**, 1817-1819 (1998).
54. R. Quintero-Torres and M. Thakur, "Measurement of the nonlinear refractive index of polydiacetylene using Michelson interferometry and z-scan," Journal of Applied Physics **85**, 401-403 (1999).
55. M. Sheik-Bahae, A. A. Said, T. H. Wei, D. J. Hagan, and E. W. Van Stryland, "Sensitive measurement of optical nonlinearities using a single beam," Quantum Electronics, IEEE Journal of **26**, 760-769 (1990).
56. J. T. Gopinath, M. Soljačić, E. P. Ippen, V. N. Fuflyigin, W. A. King, and M. Shurgalin, "Third order nonlinearities in Ge-As-Se-based glasses for telecommunications applications," Journal of Applied Physics **96**, 6931-6933 (2004).
57. S. Hughes, J. M. Burzler, G. Spruce, and B. S. Wherrett, "Fast Fourier transform techniques for efficient simulation of Z-scan measurements," J. Opt. Soc. Am. B **12**, 1888-1893 (1995).
58. G. Adomian, "A review of the decomposition method in applied mathematics," Journal of Mathematical Analysis and Applications **135**, 501-544 (1988).
59. J. Wang, B. Gu, H.-T. Wang, and X.-W. Ni, "Z-scan analytical theory for material with saturable absorption and two-photon absorption," Optics Communications **283**, 3525-3528 (2010).
60. G. Stock and W. Domcke, "Detection of ultrafast molecular-excited-state dynamics with time- and frequency-resolved pump-probe spectroscopy," Physical Review A **45**, 3032-3040 (1992).
61. J. M. Dawlaty, S. Shivaraman, M. Chandrashekhar, F. Rana, and M. G. Spencer, "Measurement of ultrafast carrier dynamics in epitaxial graphene," Applied Physics Letters **92**, 042116 (2008).
62. P. A. George, J. Strait, J. Dawlaty, S. Shivaraman, M. Chandrashekhar, F. Rana, and M. G. Spencer, "Ultrafast Optical-Pump Terahertz-Probe Spectroscopy of the Carrier Relaxation and Recombination Dynamics in Epitaxial Graphene," Nano Letters **8**, 4248-4251 (2008).
63. L. Caspani, R. P. M. Kaipurath, M. Clerici, M. Ferrera, T. Roger, J. Kim, N. Kinsey, M. Pietrzyk, A. Di Falco, V. M. Shalaev, A. Boltasseva, and D. Faccio, "Enhanced Nonlinear Refractive Index in $\ensuremath{\epsilon}$-Near-Zero Materials," Physical Review Letters **116**, 233901 (2016).

64. R. M. Kaipurath, M. Pietrzyk, L. Caspani, T. Roger, M. Clerici, C. Rizza, A. Ciattoni, A. Di Falco, and D. Faccio, "Optically induced metal-to-dielectric transition in Epsilon-Near-Zero metamaterials," Scientific Reports **6**, 27700 (2016).
65. P. Maine, D. Strickland, P. Bado, M. Pessot, and G. Mourou, "Generation of ultrahigh peak power pulses by chirped pulse amplification," IEEE Journal of Quantum Electronics **24**, 398-403 (1988).
66. K. C. Kao and G. A. Hockham, "Dielectric-fibre surface waveguides for optical frequencies," Electrical Engineers, Proceedings of the Institution of **113**, 1151-1158 (1966).
67. NobelPrize.org, "Nobel Prize in Physics 2009" (2016, 24th February), retrieved http://www.nobelprize.org/nobel_prizes/physics/laureates/2009/.
68. K. M. Davis, K. Miura, N. Sugimoto, and K. Hirao, "Writing waveguides in glass with a femtosecond laser," Opt. Lett. **21**, 1729-1731 (1996).
69. R. R. Thomson and G. Cerullo, "Ultrafast Laser Inscription of Photonic Devices in Bulk Dielectrics," in *Ultrafast Nonlinear Optics*, R. Thomson, C. Leburn, and D. Reid, eds. (Springer International Publishing, Heidelberg, 2013), pp. 323-350.
70. G. Li, X. Baoxi, and C. Tow Chong, "Microstructure in lithium niobate by use of focused femtosecond laser pulses," Photonics Technology Letters, IEEE **16**, 1337-1339 (2004).
71. R. R. Thomson, S. Campbell, I. J. Blewett, A. K. Kar, and D. T. Reid, "Optical waveguide fabrication in z-cut lithium niobate (LiNbO3) using femtosecond pulses in the low repetition rate regime," Applied Physics Letters **88**, 111109 (2006).
72. N. D. Psaila, R. R. Thomson, H. T. Bookey, A. K. Kar, N. Chiodo, R. Osellame, G. Cerullo, G. Brown, A. Jha, and S. Shen, "Femtosecond laser inscription of optical waveguides in Bismuth ion doped glass," Opt. Express **14**, 10452-10459 (2006).
73. H. T. Bookey, R. R. Thomson, N. D. Psaila, A. K. Kar, N. Chiodo, R. Osellame, and G. Cerullo, "Femtosecond Laser Inscription of Low Insertion Loss Waveguides in Z-Cut Lithium Niobate," Photonics Technology Letters, IEEE **19**, 892-894 (2007).
74. D. Choudhury, W. T. Ramsay, R. Kiss, N. A. Willoughby, L. Paterson, and A. K. Kar, "A 3D mammalian cell separator biochip," Lab on a chip **12**, 948-953 (2012).
75. G. D. Marshall, A. Politi, J. C. F. Matthews, P. Dekker, M. Ams, M. J. Withford, and J. L. O'Brien, "Laser written waveguide photonic quantum circuits," Opt. Express **17**, 12546-12554 (2009).
76. R. R. Thomson, T. A. Birks, S. G. Leon-Saval, A. K. Kar, and J. Bland-Hawthorn, "Ultrafast laser inscription of an integrated photonic lantern," Opt. Express **19**, 5698-5705 (2011).
77. R. R. Thomson, H. T. Bookey, N. D. Psaila, A. Fender, S. Campbell, W. N. MacPherson, J. S. Barton, D. T. Reid, and A. K. Kar, "Ultrafast-laser inscription of a three dimensional fan-out device for multicore fiber coupling applications," Opt. Express **15**, 11691-11697 (2007).
78. S. M. Eaton, H. Zhang, M. L. Ng, J. Li, W.-J. Chen, S. Ho, and P. R. Herman, "Transition from thermal diffusion to heat accumulation in high repetition rate femtosecond laser writing of buried optical waveguides," Opt. Express **16**, 9443-9458 (2008).
79. J. R. Macdonald, R. R. Thomson, S. J. Beecher, N. D. Psaila, H. T. Bookey, and A. K. Kar, "Ultrafast laser inscription of near-infrared waveguides in polycrystalline ZnSe," Opt. Lett. **35**, 4036-4038 (2010).
80. H. Zhang, S. M. Eaton, and P. R. Herman, "Low-loss Type II waveguide writing in fused silica with single picosecond laser pulses," Opt. Express **14**, 4826-4834 (2006).
81. W.-J. Chen, S. M. Eaton, H. Zhang, and P. R. Herman, "Broadband directional couplers fabricated in bulk glass with high repetition rate femtosecond laser pulses," Opt. Express **16**, 11470-11480 (2008).
82. D. J. Little, M. Ams, P. Dekker, G. D. Marshall, J. M. Dawes, and M. J. Withford, "Femtosecond laser modification of fused silica: the effect of writing polarization on Si-O ring structure," Opt. Express **16**, 20029-20037 (2008).

83. C. Hnatovsky, R. S. Taylor, E. Simova, V. R. Bhardwaj, D. M. Rayner, and P. B. Corkum, "Polarization-selective etching in femtosecond laser-assisted microfluidic channel fabrication in fused silica," Opt. Lett. **30**, 1867-1869 (2005).
84. A. Gupta, G. Chen, P. Joshi, S. Tadigadapa, and Eklund, "Raman Scattering from High-Frequency Phonons in Supported n-Graphene Layer Films," Nano Letters **6**, 2667-2673 (2006).
85. A. K. Geim and A. H. MacDonald, "Graphene: Exploring carbon flatland," Physics Today **60**, 35-41 (2007).
86. S. Yamashita, "A Tutorial on Nonlinear Photonic Applications of Carbon Nanotube and Graphene," Journal of Lightwave Technology **30**, 427-447 (2012).
87. K. S. Novoselov, V. I. Falko, L. Colombo, P. R. Gellert, M. G. Schwab, and K. Kim, "A roadmap for graphene," Nature **490**, 192-200 (2012).
88. J. Moser, A. Barreiro, and A. Bachtold, "Current-induced cleaning of graphene," Applied Physics Letters **91**, 163513 (2007).
89. A. A. Balandin, S. Ghosh, W. Bao, I. Calizo, D. Teweldebrhan, F. Miao, and C. N. Lau, "Superior Thermal Conductivity of Single-Layer Graphene," Nano Letters **8**, 902-907 (2008).
90. J. M. Dawlaty, S. Shivaraman, J. Strait, P. George, M. Chandrashekhar, F. Rana, M. G. Spencer, D. Veksler, and Y. Chen, "Measurement of the optical absorption spectra of epitaxial graphene from terahertz to visible," Applied Physics Letters **93**, 131905 (2008).
91. R. R. Nair, P. Blake, A. N. Grigorenko, K. S. Novoselov, T. J. Booth, T. Stauber, N. M. R. Peres, and A. K. Geim, "Fine Structure Constant Defines Visual Transparency of Graphene," Science **320**, 1308 (2008).
92. F. Bonaccorso, Z. Sun, T. Hasan, and A. C. Ferrari, "Graphene photonics and optoelectronics," Nat Photon **4**, 611-622 (2010).
93. M. Bass, C. DeCusatis, J. Enoch, V. Lakshminarayanan, G. Li, C. Macdonald, V. Mahajan, and E. V. Stryland, *Handbook of Optics, Third Edition Volume II: Design, Fabrication and Testing, Sources and Detectors, Radiometry and Photometry* (McGraw-Hill, Inc., 2010), p. 1264.
94. K. J. A. Ooi, L. K. Ang, and D. T. H. Tan, "Waveguide engineering of graphene's nonlinearity," Applied Physics Letters **105**, 111110 (2014).
95. H. Li, Y. Anugrah, S. J. Koester, and M. Li, "Optical absorption in graphene integrated on silicon waveguides," Applied Physics Letters **101**, 111110 (2012).
96. F. Fillion-Gourdeau and S. MacLean, "Time-dependent pair creation and the Schwinger mechanism in graphene," Physical Review B **92**, 035401 (2015).
97. Q. Bao, H. Zhang, Y. Wang, Z. Ni, Y. Yan, Z. X. Shen, K. P. Loh, and D. Y. Tang, "Atomic-Layer Graphene as a Saturable Absorber for Ultrafast Pulsed Lasers," Advanced Functional Materials **19**, 3077-3083 (2009).
98. F. Zhang, S. Han, Y. Liu, Z. Wang, and X. Xu, "Dependence of the saturable absorption of graphene upon excitation photon energy," Applied Physics Letters **106**, 091102 (2015).
99. M. Haiml, R. Grange, and U. Keller, "Optical characterization of semiconductor saturable absorbers," Applied Physics B **79**, 331-339 (2004).
100. R. Côté, M. Barrette, and É. Bouffard, "Electromagnetic absorption and Kerr effect in quantum Hall ferromagnetic states of bilayer graphene," Physical Review B **92**, 125426 (2015).
101. J. H. Strait, H. Wang, S. Shivaraman, V. Shields, M. Spencer, and F. Rana, "Very Slow Cooling Dynamics of Photoexcited Carriers in Graphene Observed by Optical-Pump Terahertz-Probe Spectroscopy," Nano Letters **11**, 4902-4906 (2011).
102. H. Choi, F. Borondics, D. A. Siegel, S. Y. Zhou, M. C. Martin, A. Lanzara, and R. A. Kaindl, "Broadband electromagnetic response and ultrafast dynamics of few-layer epitaxial graphene," Applied Physics Letters **94**, 172102 (2009).
103. D. Sun, Z.-K. Wu, C. Divin, X. Li, C. Berger, W. A. de Heer, P. N. First, and T. B. Norris, "Ultrafast Relaxation of Excited Dirac Fermions in Epitaxial Graphene Using Optical Differential Transmission Spectroscopy," Physical Review Letters **101**, 157402 (2008).

104. D. Sun, C. Divin, C. Berger, W. A. de Heer, P. N. First, and T. B. Norris, "Spectroscopic Measurement of Interlayer Screening in Multilayer Epitaxial Graphene," Physical Review Letters **104**, 136802 (2010).
105. R. W. Newson, J. Dean, B. Schmidt, and H. M. v. Driel, "Ultrafast carrier kinetics in exfoliated graphene and thin graphite films," Opt. Express **17**, 2326-2333 (2009).
106. P. A. Obraztsov, M. G. Rybin, A. V. Tyurnina, S. V. Garnov, E. D. Obraztsova, A. N. Obraztsov, and Y. P. Svirko, "Broadband Light-Induced Absorbance Change in Multilayer Graphene," Nano Letters **11**, 1540-1545 (2011).
107. J. Shang, T. Yu, J. Lin, and G. G. Gurzadyan, "Ultrafast Electron−Optical Phonon Scattering and Quasiparticle Lifetime in CVD-Grown Graphene," ACS Nano **5**, 3278-3283 (2011).
108. R. del Coso and J. Solis, "Relation between nonlinear refractive index and third-order susceptibility in absorbing media," J. Opt. Soc. Am. B **21**, 640-644 (2004).
109. X. Li, W. Cai, J. An, S. Kim, J. Nah, D. Yang, R. Piner, A. Velamakanni, I. Jung, E. Tutuc, S. K. Banerjee, L. Colombo, and R. S. Ruoff, "Large-Area Synthesis of High-Quality and Uniform Graphene Films on Copper Foils," Science **324**, 1312-1314 (2009).
110. S. Bae, H. Kim, Y. Lee, X. Xu, J.-S. Park, Y. Zheng, J. Balakrishnan, T. Lei, H. Ri Kim, Y. I. Song, Y.-J. Kim, K. S. Kim, B. Ozyilmaz, J.-H. Ahn, B. H. Hong, and S. Iijima, "Roll-to-roll production of 30-inch graphene films for transparent electrodes," Nat Nano **5**, 574-578 (2010).
111. W. Chen, Y. Wang, and W. Ji, "Two-Photon Absorption in Graphene Enhanced by the Excitonic Fano Resonance," The Journal of Physical Chemistry C **119**, 16954-16961 (2015).
112. H. Yang, X. Feng, Q. Wang, H. Huang, W. Chen, A. T. S. Wee, and W. Ji, "Giant Two-Photon Absorption in Bilayer Graphene," Nano Letters **11**, 2622-2627 (2011).
113. G. Xing, H. Guo, X. Zhang, T. C. Sum, and C. H. A. Huan, "The Physics of ultrafast saturable absorption in graphene," Opt. Express **18**, 4564-4573 (2010).
114. A. Martinez, K. Fuse, and S. Yamashita, "Mechanical exfoliation of graphene for the passive mode-locking of fiber lasers," Applied Physics Letters **99**, 121107 (2011).
115. Z. Sun, T. Hasan, F. Torrisi, D. Popa, G. Privitera, F. Wang, F. Bonaccorso, D. M. Basko, and A. C. Ferrari, "Graphene Mode-Locked Ultrafast Laser," ACS Nano **4**, 803-810 (2010).
116. J. Xu, J. Liu, S. Wu, Q.-H. Yang, and P. Wang, "Graphene oxide mode-locked femtosecond erbium-doped fiber lasers," Opt. Express **20**, 15474-15480 (2012).
117. Z. Zheng, C. Zhao, S. Lu, Y. Chen, Y. Li, H. Zhang, and S. Wen, "Microwave and optical saturable absorption in graphene," Opt. Express **20**, 23201-23214 (2012).
118. E. Malic and A. Knorr, *Graphene and Carbon Nanotubes: Ultrafast Optics and Relaxation Dynamics* (Wiley, Berlin, 2013).
119. E. Dremetsika, B. Dlubak, S.-P. Gorza, C. Ciret, M.-B. Martin, S. Hofmann, P. Seneor, D. Dolfi, S. Massar, P. Emplit, and P. Kockaert, "Measuring the nonlinear refractive index of graphene using the optical Kerr effect method," Opt. Lett. **41**, 3281-3284 (2016).
120. W. Chen, G. Wang, S. Qin, C. Wang, J. Fang, J. Qi, X. Zhang, L. Wang, H. Jia, and S. Chang, "The nonlinear optical properties of coupling and decoupling graphene layers," AIP Advances **3**, 042123 (2013).
121. L. Miao, Y. Jiang, S. Lu, B. Shi, C. Zhao, H. Zhang, and S. Wen, "Broadband ultrafast nonlinear optical response of few-layers graphene: toward the mid-infrared regime," Photon. Res. **3**, 214-219 (2015).
122. D. Chatzidimitriou, A. Pitilakis, and E. E. Kriezis, "Rigorous calculation of nonlinear parameters in graphene-comprising waveguides," Journal of Applied Physics **118**, 023105 (2015).
123. L. A. Falkovsky, "Optical properties of graphene," Journal of Physics: Conference Series **129**, 012004 (2008).
124. T. Gu, N. Petrone, J. F. McMillan, A. van der Zande, M. Yu, G. Q. Lo, D. L. Kwong, J. Hone, and C. W. Wong, "Regenerative oscillation and four-wave mixing in graphene optoelectronics," Nat Photon **6**, 554-559 (2012).

125. M. Currie, J. D. Caldwell, F. J. Bezares, J. Robinson, T. Anderson, H. Chun, and M. Tadjer, "Quantifying pulsed laser induced damage to graphene," Applied Physics Letters **99**, 211909 (2011).
126. A. Roberts, D. Cormode, C. Reynolds, T. Newhouse-Illige, B. J. LeRoy, and A. S. Sandhu, "Response of graphene to femtosecond high-intensity laser irradiation," Applied Physics Letters **99**, 051912 (2011).
127. M. Tanahashi, "Development of Fabrication Methods of Filler/Polymer Nanocomposites: With Focus on Simple Melt-Compounding-Based Approach without Surface Modification of Nanofillers," Materials **3**, 1593 (2010).
128. J. Du and H.-M. Cheng, "The Fabrication, Properties, and Uses of Graphene/Polymer Composites," Macromolecular Chemistry and Physics **213**, 1060-1077 (2012).
129. Y. Hou, J. Tang, H. Zhang, C. Qian, Y. Feng, and J. Liu, "Functionalized Few-Walled Carbon Nanotubes for Mechanical Reinforcement of Polymeric Composites," ACS Nano **3**, 1057-1062 (2009).
130. G. Williams, R. Trask, and I. Bond, "A self-healing carbon fibre reinforced polymer for aerospace applications," Composites Part A: Applied Science and Manufacturing **38**, 1525-1532 (2007).
131. G. Mittal, V. Dhand, K. Y. Rhee, S.-J. Park, and W. R. Lee, "A review on carbon nanotubes and graphene as fillers in reinforced polymer nanocomposites," Journal of Industrial and Engineering Chemistry **21**, 11-25 (2015).
132. Y. Sun and G. Shi, "Graphene/polymer composites for energy applications," Journal of Polymer Science Part B: Polymer Physics **51**, 231-253 (2013).
133. Z. Sun, D. Popa, T. Hasan, F. Torrisi, F. Wang, E. R. Kelleher, J. Travers, V. Nicolosi, and A. Ferrari, "A stable, wideband tunable, near transform-limited, graphene-mode-locked, ultrafast laser," Nano Res. **3**, 653-660 (2010).
134. S. Husaini, J. E. Slagle, J. M. Murray, S. Guha, L. P. Gonzalez, and R. G. Bedford, "Broadband saturable absorption and optical limiting in graphene-polymer composites," Applied Physics Letters **102**, 191112 (2013).
135. A. Midya, V. Mamidala, J.-X. Yang, P. K. L. Ang, Z.-K. Chen, W. Ji, and K. P. Loh, "Synthesis and Superior Optical-Limiting Properties of Fluorene-Thiophene-Benzothiadazole Polymer-Functionalized Graphene Sheets," Small **6**, 2292-2300 (2010).
136. M. Zhang, E. J. R. Kelleher, F. Torrisi, Z. Sun, T. Hasan, D. Popa, F. Wang, A. C. Ferrari, S. V. Popov, and J. R. Taylor, "Tm-doped fiber laser mode-locked by graphene-polymer composite," Opt. Express **20**, 25077-25084 (2012).
137. Y. Feng, N. Dong, G. Wang, Y. Li, S. Zhang, K. Wang, L. Zhang, W. J. Blau, and J. Wang, "Saturable absorption behavior of free-standing graphene polymer composite films over broad wavelength and time ranges," Opt. Express **23**, 559-569 (2015).
138. H. O. Jeschke, M. E. Garcia, and K. H. Bennemann, "Theory for the Ultrafast Ablation of Graphite Films," Physical Review Letters **87**, 015003 (2001).
139. D. V. Widder, *The heat equation* (Academic Press, 1976), Vol. 67.
140. R. J. Stoner and H. J. Maris, "Kapitza conductance and heat flow between solids at temperatures from 50 to 300 K," Physical Review B **48**, 16373-16387 (1993).
141. E. T. Swartz and R. O. Pohl, "Thermal boundary resistance," Reviews of Modern Physics **61**, 605-668 (1989).
142. P. Kapitza, "The study of heat transfer in helium II," J. Phys.(USSR) **4**, 181-210 (1941).
143. "GASIR-1 Infrared transmitting Glass" (2016, 4th May), retrieved http://eom.umicore.com/en/infrared-optics/blanks/GASIR-for-infrared-optics.pdf.
144. S. A. McDaniel, A. Lancaster, J. W. Evans, A. K. Kar, and G. Cook, "Power scaling of ultrafast laser inscribed waveguide lasers in chromium and iron doped zinc selenide," Opt. Express **24**, 3502-3512 (2016).
145. J. R. Macdonald, S. J. Beecher, A. Lancaster, P. A. Berry, K. L. Schepler, and A. K. Kar, "Ultrabroad Mid-Infrared Tunable Cr:ZnSe Channel Waveguide Laser," IEEE Journal of Selected Topics in Quantum Electronics **21**, 375-379 (2015).

146. J. R. Macdonald, S. J. Beecher, P. A. Berry, G. Brown, K. L. Schepler, and A. K. Kar, "Efficient mid-infrared Cr:ZnSe channel waveguide laser operating at 2486 nm," Opt. Lett. **38**, 2194-2196 (2013).
147. J. R. Macdonald, S. J. Beecher, P. A. Berry, K. L. Schepler, and A. K. Kar, "Compact mid-infrared Cr:ZnSe channel waveguide laser," Applied Physics Letters **102**, 161110 (2013).
148. D. Milanese, J. Lousteau, D. Pugliese, P. Janicek, N. G. Boetti, E. Ceci-Ginistrelli, G. Demetriou, A. K. Kar, and H. T. Bookey, "Novel tellurite core and cladding glasses for high numerical aperture optical fibre: Prospects for a supercontinuum optical fibre source," in *Transparent Optical Networks (ICTON), 2015 17th International Conference on*, 2015), 1-4.
149. W. B. Jensen, "A Note on the Term "Chalcogen"," Journal of Chemical Education **74**, 1063 (1997).
150. B. J. Eggleton, B. Luther-Davies, and K. Richardson, "Chalcogenide photonics," Nat Photon **5**, 141-148 (2011).
151. A. Zakery and S. R. Elliott, "Optical properties and applications of chalcogenide glasses: a review," Journal of Non-Crystalline Solids **330**, 1-12 (2003).
152. T. Schweizer, D. Brady, and D. W. Hewak, "Fabrication and spectroscopy of erbium doped gallium lanthanum sulphide glass fibres for mid-infrared laser applications," Opt. Express **1**, 102-107 (1997).
153. V. Moizan, V. Nazabal, J. Troles, P. Houizot, J.-L. Adam, J.-L. Doualan, R. Moncorgé, F. Smektala, G. Gadret, S. Pitois, and G. Canat, "Er3+-doped GeGaSbS glasses for mid-IR fibre laser application: Synthesis and rare earth spectroscopy," Optical Materials **31**, 39-46 (2008).
154. C. C. Wang, "Empirical Relation between the Linear and the Third-Order Nonlinear Optical Susceptibilities," Physical Review B **2**, 2045-2048 (1970).
155. J. M. Harbold, F. O. Ilday, F. W. Wise, and B. G. Aitken, "Highly nonlinear Ge-As-Se and Ge-As-S-Se glasses for all-optical switching," Photonics Technology Letters, IEEE **14**, 822-824 (2002).
156. C. Quémard, F. Smektala, V. Couderc, A. Barthélémy, and J. Lucas, "Chalcogenide glasses with high non linear optical properties for telecommunications," Journal of Physics and Chemistry of Solids **62**, 1435-1440 (2001).
157. K. S. Bindra, H. T. Bookey, A. K. Kar, B. S. Wherrett, X. Liu, and A. Jha, "Nonlinear optical properties of chalcogenide glasses: Observation of multiphoton absorption," Applied Physics Letters **79**, 1939-1941 (2001).
158. K. Shimakawa, A. Kolobov, and S. Elliott, "Photoinduced effects and metastability in amorphous semiconductors and insulators," Advances in Physics **44**, 475-588 (1995).
159. M. D. Pelusi, V. G. Ta'eed, F. Libin, E. Magi, M. R. E. Lamont, S. Madden, C. Duk-Yong, D. A. P. Bulla, B. Luther-Davies, and B. J. Eggleton, "Applications of Highly-Nonlinear Chalcogenide Glass Devices Tailored for High-Speed All-Optical Signal Processing," Selected Topics in Quantum Electronics, IEEE Journal of **14**, 529-539 (2008).
160. F. Urbach, "The Long-Wavelength Edge of Photographic Sensitivity and of the Electronic Absorption of Solids," Physical Review **92**, 1324-1324 (1953).
161. J. S. Sanghera, L. B. Shaw, P. Pureza, V. Q. Nguyen, D. Gibson, L. Busse, I. D. Aggarwal, C. M. Florea, and F. H. Kung, "Nonlinear Properties of Chalcogenide Glass Fibers," International Journal of Applied Glass Science **1**, 296-308 (2010).
162. C. R. Petersen, U. Møller, I. Kubat, B. Zhou, S. Dupont, J. Ramsay, T. Benson, S. Sujecki, N. Abdel-Moneim, Z. Tang, D. Furniss, A. Seddon, and O. Bang, "Mid-infrared supercontinuum covering the 1.4–13.3 μm molecular fingerprint region using ultra-high NA chalcogenide step-index fibre," Nat Photon **8**, 830-834 (2014).
163. N. D. Psaila, R. R. Thomson, H. T. Bookey, S. Shen, N. Chiodo, R. Osellame, G. Cerullo, A. Jha, and A. K. Kar, "Supercontinuum generation in an ultrafast laser inscribed chalcogenide glass waveguide," Opt. Express **15**, 15776-15781 (2007).

164. F. Yoshino, S. Polyakov, and G. I. Stegeman, "All-optical multiphoton absorption figures of merit: Polydiacetylene poly (bis para-toluene sulfonate) of 2,4-hexadiyne-1,6diol," Applied Physics Letters **84**, 5362-5364 (2004).
165. J. U. Kang, A. Villeneuve, M. Sheik-Bahae, G. I. Stegeman, K. Al-hemyari, J. S. Aitchison, and C. N. Ironside, "Limitation due to three-photon absorption on the useful spectral range for nonlinear optics in AlGaAs below half band gap," Applied Physics Letters **65**, 147-149 (1994).
166. M. Hughes, W. Yang, and D. Hewak, "Fabrication and characterization of femtosecond laser written waveguides in chalcogenide glass," Applied Physics Letters **90**, 131113 (2007).
167. S. M. Eaton, W. J. Chen, H. Zhang, R. Iyer, J. Li, M. L. Ng, S. Ho, J. S. Aitchison, and P. R. Herman, "Spectral Loss Characterization of Femtosecond Laser Written Waveguides in Glass With Application to Demultiplexing of 1300 and 1550 nm Wavelengths," Journal of Lightwave Technology **27**, 1079-1085 (2009).
168. L. Tong, R. R. Gattass, I. Maxwell, J. B. Ashcom, and E. Mazur, "Optical loss measurements in femtosecond laser written waveguides in glass," Optics Communications **259**, 626-630 (2006).
169. S. M. Eaton and P. R. Herman, "Passive Photonic Devices in Glass," in *Femtosecond Laser Micromachining: Photonic and Microfluidic Devices in Transparent Materials*, R. Osellame, G. Cerullo, and R. Ramponi, eds. (Springer Berlin Heidelberg, Berlin, Heidelberg, 2012), pp. 155-195.
170. B. McMillen, B. Zhang, K. P. Chen, A. Benayas, and D. Jaque, "Ultrafast laser fabrication of low-loss waveguides in chalcogenide glass with 0.65 dB/cm loss," Opt. Lett. **37**, 1418-1420 (2012).
171. D. Choudhury, J. R. Macdonald, and A. K. Kar, "Ultrafast laser inscription: perspectives on future integrated applications," Laser & Photonics Reviews **8**, 827-846 (2014).
172. Y. Nasu, M. Kohtoku, and Y. Hibino, "Low-loss waveguides written with a femtosecond laser for flexible interconnection in a planar light-wave circuit," Opt. Lett. **30**, 723-725 (2005).
173. S. M. Eaton, H. Zhang, P. R. Herman, F. Yoshino, L. Shah, J. Bovatsek, and A. Y. Arai, "Heat accumulation effects in femtosecond laser-written waveguides with variable repetition rate," Opt. Express **13**, 4708-4716 (2005).
174. J. Lapointe, M. Gagné, M.-J. Li, and R. Kashyap, "Making smart phones smarter with photonics," Opt. Express **22**, 15473-15483 (2014).
175. A. Arriola, S. Mukherjee, D. Choudhury, L. Labadie, and R. R. Thomson, "Ultrafast laser inscription of mid-IR directional couplers for stellar interferometry," Opt. Lett. **39**, 4820-4822 (2014).
176. A. Roberts, E. Ampem-Lassen, A. Barty, K. A. Nugent, G. W. Baxter, N. M. Dragomir, and S. T. Huntington, "Refractive-index profiling of optical fibers with axial symmetry by use of quantitative phase microscopy," Opt. Lett. **27**, 2061-2063 (2002).
177. M. Kalal and K. Nugent, "Abel inversion using fast Fourier transforms," Appl. Opt. **27**, 1956-1959 (1988).
178. C. W. Ponader, J. F. Schroeder, and A. M. Streltsov, "Origin of the refractive-index increase in laser-written waveguides in glasses," Journal of Applied Physics **103**, 063516 (2008).
179. V. R. Bhardwaj, P. B. Corkum, D. M. Rayner, C. Hnatovsky, E. Simova, and R. S. Taylor, "Stress in femtosecond-laser-written waveguides in fused silica," Opt. Lett. **29**, 1312-1314 (2004).
180. P. Hlubina, D. Ciprian, and M. Kadulová, "Measurement of chromatic dispersion of polarization modes in optical fibres using white-light spectral interferometry," Measurement Science and Technology **21**, 045302 (2010).
181. S. M. Eaton, W. Chen, L. Zhang, H. Zhang, R. Iyer, J. S. Aitchison, and P. R. Herman, "Telecom-Band Directional Coupler Written With Femtosecond Fiber Laser," IEEE Photonics Technology Letters **18**, 2174-2176 (2006).

182. D. M. Beggs, T. P. White, L. O'Faolain, and T. F. Krauss, "Ultracompact and low-power optical switch based on silicon photonic crystals," Opt. Lett. **33**, 147-149 (2008).
183. K. S. Chiang, "Propagation of short optical pulses in directional couplers with Kerr nonlinearity," J. Opt. Soc. Am. B **14**, 1437-1443 (1997).
184. V. Mizrahi, M. A. Saifi, M. J. Andrejco, K. W. DeLong, and G. I. Stegeman, "Two-photon absorption as a limitation to all-optical switching," Opt. Lett. **14**, 1140-1142 (1989).
185. J. S. Aitchison, A. H. Kean, C. N. Ironside, A. Villeneuve, and G. I. Stegeman, "Ultrafast all-optical switching in $Al_{0.18}Ga_{0.82}As$ directional coupler in 1.55 μm spectral region," in *Electronics Letters,* (Institution of Engineering and Technology, 1991), pp. 1709-1710.
186. C. C. Ye, D. W. Hewak, M. Hempstead, B. N. Samson, and D. N. Payne, "Spectral properties of Er^{3+}-doped gallium lanthanum sulphide glass," Journal of Non-Crystalline Solids **208**, 56-63 (1996).
187. Y. D. West, T. Schweizer, D. J. Brady, and D. W. Hewak, "Gallium Lanthanum Sulphide Fibers for Infrared Transmission," Fiber and Integrated Optics **19**, 229-250 (2000).
188. P. Urquhart, "Review of rare earth doped fibre lasers and amplifiers," IEE Proceedings J - Optoelectronics **135**, 385-407 (1988).
189. W. Q. Shi, M. Bass, and M. Birnbaum, "Effects of energy transfer among Er3+ ions on the fluorescence decay and lasing properties of heavily doped $Er:Y_3Al_5O_{12}$," J. Opt. Soc. Am. B **7**, 1456-1462 (1990).
190. J. B. Khurgin, "Graphene—A rather ordinary nonlinear optical material," Applied Physics Letters **104**, 161116 (2014).